



SCUOLA INTERNAZIONALE  
SUPERIORE di STUDI AVANZATI  
International School  
for Advanced Studies

An analytic Kerr-accretion model  
as a test solution for a new GR SPH code

Thesis submitted for the degree of  
“Doctor Philosophiæ”

CANDIDATE

SUPERVISORS

Emilio Tejeda Rodríguez

John C. Miller and Stephan Rosswog

International School for Advanced Studies  
Via Bonomea 265, 34136 Trieste, Italy



# Abstract

This thesis discusses several aspects of the implementation and testing of a new general relativistic computer code based on the smoothed particle hydrodynamics (SPH) method. The code, which has been called SPHINCS (SPH IN Curved Spacetime), is still at the development stage and this is a progress report on some parts of the project. SPHINCS is intended for use in studying various astrophysical applications concerning accretion processes onto black holes (BHs) including: the tidal disruption of a star by a BH; study of the collapsing interiors of massive, rapidly rotating stars within the so-called collapsar scenario; and the interaction of a rotating BH with the inner parts of an accretion disc around it.

In the first part of this thesis we present the mathematical formulation on which SPHINCS is based. Using the language of the so-called 3+1 formalism, we show how the numerical variables and the corresponding evolution equations used in SPHINCS can be derived self-consistently from the Lagrangian of a perfect fluid. We then discuss the implementation of SPHINCS in Kerr spacetime and give explicit expressions for the acceleration terms due to the spacetime metric that enter into the evolution equations.

In the second part of the thesis, we introduce an analytic toy model which is intended to be used as a test solution for benchmarking SPHINCS (and possibly other GR hydro codes). This model describes the steady and axisymmetric flow of a rotating gas cloud of non-interacting particles infalling towards a Kerr BH. We demonstrate the utility of the model as a test solution by showing some results of comparing it with several SPH simulations of an idealised collapsar-like setup that implement pseudo-Newtonian potentials for mimicking the effects of Kerr and Schwarzschild spacetimes. Besides its use as a test solution for numerical codes, we also demonstrate that this model is a useful tool for highlighting purely general relativistic effects in hydrodynamic flows. Finally, we discuss its potential use as a tool for exploring the parameter space in applications where the assumptions of the model are approximately valid.



# Collaborations

The research presented in this thesis is the result of the author's own work, as well as the outcome of the scientific collaborations mentioned below, except where explicit reference is made to the results of others. This work forms part of a larger collaborative project involving S. Rosswog, E. Gafton, J. C. Miller, and the author, aimed at developing the new SPHINCS code. The thesis is partially based on the following research papers:

Tejeda E., Mendoza S. and Miller J. C.

*Analytic solutions to the accretion of a rotating finite cloud towards a central object - II. Schwarzschild spacetime*

Mon. Not. R. Astron. Soc, 419:1431, 2012

Tejeda E., Taylor P. A. and Miller J. C.

*An analytic toy model for relativistic accretion in Kerr spacetime*

arXiv:1207.0733 (accepted for publication in MNRAS)

Rosswog S., Tejeda E., Gafton E. and Miller J. C.

*The SPHINCS code: Smoothed Particle Hydrodynamics IN Curved Spacetime*  
(in preparation)



# Acknowledgements

I would like to thank my supervisors, John Miller and Stephan Rosswog, for their mentorship and continuous support during these last four years, and for the discussions and their suggestions that greatly contributed to this dissertation. I would also like to thank Paul Taylor for valuable discussions and for carefully reading this manuscript and providing useful comments that helped improve it. I am grateful to Sergio Mendoza, William Lee, Zdenek Stuchlík and Vladimír Karas for their very helpful inputs along different stages of my PhD. Special thanks go to my family and friends (both in Trieste and back home) for having been supportive in spite of the distance. Finally, I thank Manuel Draicchio for his encouragement and support during this last year.



# Contents

<b>Abstract</b>	<b>iii</b>
<b>Collaborations</b>	<b>v</b>
<b>Acknowledgements</b>	<b>vii</b>
<b>1 Introduction</b>	<b>1</b>
1.1 Brief history of the concept of black hole . . . . .	1
1.2 Astrophysical black holes . . . . .	3
1.3 Accretion discs . . . . .	4
1.4 Numerical tool . . . . .	6
1.5 Structure of the thesis . . . . .	10
1.6 Notation, conventions and units . . . . .	11
<b>2 Smoothed particle hydrodynamics in a curved spacetime</b>	<b>13</b>
2.1 Basics of general relativistic hydrodynamics . . . . .	13
2.2 3+1 decomposition of the metric . . . . .	16
2.2.1 Local Eulerian observers . . . . .	18
2.3 Conservation laws in the 3+1 formalism . . . . .	20
2.3.1 Continuity equation . . . . .	21
2.3.2 Spatial part of the stress-energy equation . . . . .	22
2.3.3 Temporal part of the stress-energy equation . . . . .	23
2.3.4 Non-relativistic limit . . . . .	23
2.4 SPHINCS . . . . .	24
2.4.1 SPH interpolation and density estimate . . . . .	25
2.4.2 Canonical momentum . . . . .	29
2.4.3 Canonical energy . . . . .	32
2.4.4 Recovery of primitive variables . . . . .	35
2.4.5 Geodesic motion limit . . . . .	37
2.4.6 Special relativistic limit . . . . .	38
2.4.7 Non-relativistic limit . . . . .	38
2.5 Summary . . . . .	39

<b>3</b>	<b>SPHINCS implementation for Kerr spacetime</b>	<b>43</b>
3.1	Boyer-Lindquist coordinates . . . . .	44
3.2	Locally non-rotating frames . . . . .	48
3.3	Kerr-Schild coordinates . . . . .	49
3.4	Cartesian-like form of the KS coordinates . . . . .	51
3.5	SPHINCS in Kerr spacetime . . . . .	54
3.6	SPHINCS in Schwarzschild spacetime . . . . .	55
3.7	Summary . . . . .	56
<b>4</b>	<b>Timelike geodesics in Kerr spacetime</b>	<b>59</b>
4.1	Constants of motion . . . . .	60
4.2	Equations of motion . . . . .	62
4.3	Circular orbits in the equatorial plane . . . . .	64
4.4	Radial motion . . . . .	67
4.5	Polar motion . . . . .	73
4.6	Summary . . . . .	76
<b>5</b>	<b>Toy model for relativistic accretion</b>	<b>79</b>
5.1	Model description and boundary conditions . . . . .	80
5.2	Velocity field . . . . .	83
5.3	Streamlines . . . . .	84
5.3.1	Radial solution . . . . .	85
5.3.2	Polar angle solution . . . . .	89
5.3.3	Timelike geodesics in the $r$ - $\theta$ plane . . . . .	92
5.4	Density field . . . . .	93
5.5	Applications of the analytic model . . . . .	95
5.6	Comparison with numerical simulations . . . . .	98
5.6.1	Schwarzschild case . . . . .	101
5.6.2	Kerr case . . . . .	104
5.7	Summary and discussion . . . . .	106
<b>6</b>	<b>Final remarks and conclusions</b>	<b>111</b>
<b>A</b>	<b>Appendix A: Catalogue of test particle orbits</b>	<b>115</b>
A.1	Orbits in the equatorial plane I . . . . .	115
A.2	Orbits in the equatorial plane II . . . . .	123
A.3	Orbits off the equatorial plane I . . . . .	130
A.4	Orbits off the equatorial plane II . . . . .	138
A.5	Orbits off the equatorial plane III . . . . .	141
<b>B</b>	<b>Appendix B: Jacobi elliptic functions</b>	<b>143</b>
	<b>References</b>	<b>149</b>

# List of Figures

3.1	Important radial locations in Kerr spacetime . . . . .	46
3.2	Radial and polar coordinate surfaces . . . . .	47
4.1	Energy and angular momentum of circular orbits . . . . .	66
4.2	Radii of special circular orbits . . . . .	67
4.3	Radial effective potentials . . . . .	70
4.4	Variation of the radial effective potential with $\ell$ . . . . .	71
4.5	Representative off-equatorial orbits . . . . .	72
4.6	Polar effective potential . . . . .	74
4.7	Representative polar orbits for $\ell_z \neq 0$ . . . . .	76
4.8	Representative polar orbits for $\ell_z = 0$ . . . . .	77
5.1	Schematic illustration of the toy model . . . . .	81
5.2	Streamline tube used for calculating the density field . . . . .	93
5.3	Examples of accretion flows within the toy model . . . . .	96
5.4	Radius of the disc plotted against $a$ and $\ell$ . . . . .	97
5.5	Parameter domain for the toy model . . . . .	98
5.6	Comparison between the toy model and an SPH simulation for a non-rotating BH . . . . .	102
5.7	Comparison of the streamlines of the toy model and a ballistic SPH simulation . . . . .	103
5.8	Comparison between ballistic and fluid streamlines . . . . .	105
5.9	Comparison between the toy model and an SPH simulation for a rotating BH . . . . .	107
5.10	Comparison between analytic and ballistic streamlines . . . . .	108
5.11	Comparison between ballistic and fluid streamlines . . . . .	108
A.1	Orbits in the equatorial plane I . . . . .	116
A.2	Co-rotating elliptical-like trajectory . . . . .	118
A.3	Co-rotating parabolic-like trajectory . . . . .	119
A.4	Co-rotating hyperbolic-like trajectory . . . . .	120
A.5	Co-rotating unstable circular trajectory . . . . .	121
A.6	Co-rotating plunging trajectory . . . . .	122

---

A.7	Orbits in the equatorial plane II . . . . .	123
A.8	Counter-rotating elliptical-like trajectory . . . . .	125
A.9	Counter-rotating parabolic-like trajectory . . . . .	126
A.10	Counter-rotating hyperbolic-like trajectory . . . . .	127
A.11	Counter-rotating unstable circular trajectory . . . . .	128
A.12	Counter-rotating plunging trajectory . . . . .	129
A.13	Orbits off the equatorial plane I . . . . .	130
A.14	Stable spherical trajectory . . . . .	132
A.15	Elliptical-like trajectory . . . . .	133
A.16	Parabolic-like trajectory . . . . .	134
A.17	Hyperbolic-like trajectory . . . . .	135
A.18	Unstable spherical trajectory . . . . .	136
A.19	Plunging trajectory . . . . .	137
A.20	Orbits off the equatorial plane II . . . . .	138
A.21	Evolution of the polar angle for plunging trajectories . . . . .	139
A.22	Plunging orbits projected onto the $R$ - $z$ plane . . . . .	139
A.23	Plunging orbits projected onto the equatorial plane . . . . .	140
A.24	Orbits off the equatorial plane III . . . . .	141
A.25	Evolution of the polar angle for plunging trajectories . . . . .	142
A.26	Spatial projections of plunging orbits . . . . .	142

# Chapter 1

## Introduction

### 1.1 Brief history of the concept of black hole

The origin of the concept of a black hole (BH) can be traced back to the end of the 18th century when Michell (1784) and Laplace (1796), using Newtonian gravity, first theorised the existence of a massive body with a gravitational field strong enough to prevent light reaching infinity from its surface. Nevertheless, the formal study of these objects had to wait until, using the recently formulated theory of general relativity (Einstein, 1915), Schwarzschild (1916) found a first analytic solution of Einstein's field equations describing the empty spacetime around a static and spherically symmetric point particle of mass  $M$ . The solution given by Schwarzschild featured two singularities: one at the origin of coordinates  $r = 0$  (where  $r$  is a radial coordinate) and a second one located at the so-called Schwarzschild radius  $r_s = 2GM/c^2$  (where  $G$  is the gravitational constant and  $c$  is the speed of light). The first one is a true physical singularity characterised by infinite curvature of the spacetime, while Lemaître (1933) showed that the latter is not a physical singularity but rather a coordinate one. For several decades, BHs were considered mainly as theoretical entities rather than real physical objects that could exist in nature.

From the point of view of theory, the first three major breakthroughs in the development of the concept of a BH came with the discovery of an upper limit to the mass of a (non-rotating) white dwarf (Chandrasekhar, 1931),<sup>(1)</sup> the postulation of the existence of objects as compact as a neutron star (Baade & Zwicky, 1934), and the first suggestion that the continued gravitational collapse of a spherically symmetric and sufficiently massive body will inevitably lead to the formation of a BH (Oppenheimer & Volkoff, 1939; Oppenheimer & Snyder, 1939).

Nevertheless, the true revolution in the concept of BHs came after the continuing progress with observational techniques gave the first hints that BHs could actually be found in nature. The development of radio astronomy from the late 1940s onwards led to the discovery and eventual identification of quasars and other active galactic nuclei

---

<sup>(1)</sup>This mass is known as the Chandrasekhar limit and is around  $1.4 M_\odot$ , where  $M_\odot = 1.99 \times 10^{33}$  g is the solar mass.

(AGN) as extremely powerful extragalactic sources (Schmidt, 1963), as well as to the discovery of the first pulsars by Hewish, Bell et al. 1968 (which were identified as rapidly rotating neutron stars by Gold, 1968). On the other hand, with the advent of X-ray and gamma-ray astronomy in the 1960s, the first X-ray binary (Sco X-1) was discovered by Shklovsky (1967) while the first observations of gamma-ray bursts (GRBs) were reported by Klebesadel et al. (1973). The observed variability in the spectra of several of these sources and the inferred spatial dimensions of the emitting regions led to the conclusion that extremely compact sources had to be involved.

These discoveries triggered the beginning of a series of rapid developments in the theoretical aspects of BHs. An important change in the physical interpretation of the coordinate singularity at  $r_s$  came with the concept of an event horizon introduced by Finkelstein (1958). It was realised that the surface defined by this radius behaves as a one-way membrane through which massive particles and photons can only pass inward. In other words, the event horizon causally disconnects the region of spacetime in its interior (including the true physical singularity) from the rest of the universe. Nevertheless, it was still expected that some kind of mechanism would be able to prevent the formation of a physical singularity until Penrose (1965) showed that the result found by Oppenheimer & Snyder (1939) was not only generic but also the necessary outcome of continued gravitational collapse. In those years a more general solution to Einstein's field equations was found by Kerr (1963) and extended by Newman et al. (1965). The so-called Kerr-Newman family of spacetimes are characterised by being axisymmetric and depending on just three parameters describing the BH: the mass  $M$ , the specific angular momentum  $a$  (also called spin parameter), and the electric charge  $q$ . Moreover, as followed from the results of Israel (1967); Carter (1971); Robinson (1975), it constitutes the unique solution representing the spacetime external to the event horizon for idealised stationary vacuum BHs which is consistent with the requirements that the spacetime should be asymptotically-flat and have no singularities external to the event horizon. The result that the solution depends on just three parameters is known as the 'no-hair' theorem. The Kerr-Newman metrics only represent BHs, with the central singularity hidden behind an event horizon, when the parameters satisfy the condition  $a^2 + q^2 \leq M^2$ .<sup>(2)</sup>

In recent years, the development of space-based X-ray observatories has allowed a detailed measurement of the gravitational broadening of the Fe  $K\alpha$  emission line in the spectra of AGN (as reviewed in Miller, 2007). Moreover, observations using infrared techniques with extremely high resolution have made it possible to follow the proper motion of individual stars, revealing the presence of a supermassive BH at the centre of our galaxy (see e.g. Ghez et al., 2008; Gillessen et al., 2009). Another major breakthrough in the study of BHs came with the association of (long) GRBs with the rather energetic Type Ic (core-collapse) supernovae (see e.g. Galama et al., 1998). Now, dozens of strong BH candidates have been discovered (see e.g. Narayan, 2005). The measured masses of these objects are above (and, for several, well above) what is likely to be a secure upper

---

<sup>(2)</sup>Note that this inequality is expressed in geometric units for which  $c = G = 1$ . This same relation in standard units is  $c^2 a^2 + G q^2 \leq G^2 M^2$  (with  $q$  measured in electrostatic units).

limit to the mass of a neutron star, which is around  $3 M_{\odot}$  (Rhoades & Ruffini, 1974). Only in the last year, the first evidence of the tidal disruption of an ordinary star by a supermassive BH was observed as a X-ray flare (see e.g. Burrows et al., 2011). In the near future, it is expected that the first gravitational waves will start to be detected by one of the several already operational gravitational wave ground-based interferometers (such as LIGO, VIRGO, and others). In this context, merging BHs are expected to be among the most copious sources of gravitational waves (see e.g. Hughes, 2009). The beginning of gravitational wave astronomy should open up a whole new channel of information that will be crucial for our understanding of general relativity and BH physics.

Thanks to this continuous progress on the theoretical and observational fronts, BHs are now considered as fairly common objects related to some of the most powerful astrophysical phenomena in the universe (see e.g. Blandford, 1987; Celotti et al., 1999).

## 1.2 Astrophysical black holes

Due to the no-hair theorem, it is expected that relatively isolated BHs, independently of how they were created, should eventually settle down as Kerr-Newman BHs. In most of the astrophysical applications though, we can neglect the charge of the BH since any significant net charge present at formation would be expected to be quickly neutralised in practice. We cannot do the same with the spin parameter since, in any realistic scenario, a physical BH will necessarily possess some amount of intrinsic angular momentum, either because it was born with it or because it acquired it as a result of matter with angular momentum that subsequently fell into it (Bardeen, 1970; Blandford, 1987). Therefore, for astrophysical BHs in an environment in which the mass of the surrounding matter is negligible as compared to their own mass, the exterior spacetime should be well approximated by the Kerr solution with  $|a| \leq M$ .

The masses of astrophysical BHs span a range that goes from the stellar mass BHs ( $\sim 3\text{-}30 M_{\odot}$ ) that originate from the death of massive stars in supernova explosions and from the coalescence of stellar binaries (Shapiro & Teukolsky, 1983); passing through intermediate mass BHs ( $10^3\text{-}10^4 M_{\odot}$ ) that are thought to reside in the centre of globular clusters, although there are still few observational candidates (e.g. Gebhardt et al., 2005; Noyola et al., 2008); and up to the supermassive BHs ( $10^6\text{-}10^9 M_{\odot}$ ) at the centre of (possibly all) galaxies (King, 2003). The existence of primordial BHs with an even broader mass range (from  $\sim 10^{14}$  g upwards) was first hypothesised by Carr & Hawking (1974) as a result of the gravitational collapse of over-density regions within the large-scale density fluctuations present in the early stages of the expansion of the universe. However, firm observational evidence of primordial BHs with masses  $M \lesssim M_{\odot}$  is still missing, while more massive ones might constitute the seeds of today's supermassive BHs.

Just as the BH masses are spread over many orders of magnitude, the radiation that systems associated with them emit also spans a large range. For typical X-ray binaries, energy is emitted mainly through photons in the X-ray part of the spectrum, while the energy spectrum coming from AGN spans from the ultraviolet to gamma-ray

frequencies. On the other hand, for phenomena such as supernova explosions and binary star coalescence it is expected that, given the high temperatures and densities found in the stellar interiors, in many cases the fluid will become optically thick to photons and the only efficient cooling mechanism will be through neutrino emission.

### 1.3 Accretion discs

Given that no kind of information can come out from within the event horizon, we cannot really make direct observations of a BH. However, the properties of the spacetime around them are inferred from their effects on nearby matter. In particular, the process known as accretion in which matter falls onto a BH has been a topic of intense research since the pioneering work by Bondi (1952), and today it is considered as one of the most efficient mechanisms for transforming rest mass energy into radiation (with an efficiency factor of  $\sim 10\%$  of the rest mass energy of the accreted matter for astrophysical BHs), second only to the process of matter-antimatter annihilation (see e.g. Frank et al., 2002). Moreover, the study of accretion processes onto BHs (and also onto neutron stars) offers a unique opportunity for testing and validating the theory of general relativity, since it is only in the strong-field regime that prevails in the immediate vicinity of these objects that we find the largest departures between the Einstein and the Newtonian descriptions of gravity.

Even though accretion onto BHs can be highly efficient at extracting gravitational potential energy, it is important to note that, due to the absence of a hard surface at which to decelerate the infalling gas, purely radial infall onto a BH will not be an efficient mechanism in general (Shapiro, 1974). Traditionally, rotation of the accreting matter has been invoked as the means to provide centrifugal support to give time for different dissipative processes to take place and release part of the potential energy. Gas rotation can lead to the formation of a disc-like structure (Prendergast & Burbidge, 1968) in which centrifugally balanced material slowly spirals inwards under the action of dissipative mechanisms. These transfer angular momentum outwards, drive the flow of matter inwards, and transform the gravitational potential energy into kinetic energy, heat, and, ultimately, radiation. Among the various different mechanisms for driving accretion that have been considered in the literature for modelling accretion discs we have, e.g.: viscous stresses originated by a turbulent flow, as proposed in the thin-disc model of Shakura & Sunyaev (1973) and extended to the relativistic domain by Novikov & Thorne (1973); cooling by advection of hot matter, as in the Polish-doughnut model of Jaroszyński et al. (1980) and in the slim-disc model of Abramowicz et al. (1988); extraction of angular momentum by large-scale magnetic fields, as in Blandford & Payne (1982); transportation of angular momentum driven by the magnetorotational instability, as modelled by Balbus & Hawley (1991); cooling dominated by neutrino emission, as proposed by Popham et al. (1999); accretion driven by a purely relativistic effect in low angular momentum flows, leading to the small-scale inviscid disc model of Beloborodov & Illarionov (2001); and angular momentum transfer due to a dynamical instability leading to the formation of spiral arms and related shock fronts in the accretion flow, as

in the GRB model of Taylor et al. (2011) and references therein.

It is believed that, at least at some point in their evolution, many accretion disc systems are related to the existence of highly collimated jets in which plasma is accelerated to relativistic speeds (with associated Lorentz factors  $\Gamma \sim 10$ -1000). In the case of jets coming from AGN, the degree of collimation is such that they can extend over several kiloparsecs depositing huge amounts of thermal energy into the intergalactic medium. Although the exact mechanism connecting the disc and the jet is not fully understood, in the case of jets related to BHs, it is commonly believed that strong magnetic fields and a rapidly rotating BH play a fundamental role in launching and accelerating the jet via, e.g. the Blandford-Znajek mechanism (Blandford & Znajek, 1977).

Besides its role in connection with relativistic jets, any substantial value for the angular momentum of the BH will significantly affect the innermost region of an accretion disc around it, exactly where one expects to find the highest densities, temperatures and luminosities in the flow. For instance, the inner radius of a Keplerian-like accretion disc around a maximally rotating BH (defined as a BH for which  $|a| = M$ ) is around six times closer to the central accretor than it would be for a non-rotating BH (see e.g. Novikov & Thorne, 1973), while the binding energy for the innermost stable circular orbit increases from  $\sim 5.7\%$  of the rest-mass energy for a non-rotating BH up to  $\sim 42\%$  for a maximally rotating one. This increase in both the surface area of the emitting disc and the binding energy released can substantially boost the overall efficiency of the system. Moreover, the BH angular momentum may exert a restoring torque on an accretion disc which happens to be tilted with respect to the BH rotation axis (see e.g. Bardeen & Petterson, 1975; Lodato & Pringle, 2006).

The predictive power of the different accretion disc models has allowed us to interpret most of the astrophysical phenomena that we have mentioned in Sections 1.1 and 1.2. Accretion models form today the basis of our understanding of astrophysical systems such as:

- AGN, which are thought to be powered by long-term accretion onto a supermassive BH in the centre of the host galaxy (for a review see, e.g. Rees, 1984). Moreover, they are thought to play a fundamental role in the cosmological evolution and growth of galaxies, as is inferred from the strong correlations between the BH mass and the mass of the central bulge of the hosting galaxy (see e.g. King, 2003).
- X-ray binaries, the emission from which is considered to originate in a hot accretion disc around a neutron star or a BH. These discs are fed with material from a companion ordinary star either via a stellar wind (wind-fed binaries) or when the outer surface of the companion fills up the Roche-lobe and then loses matter through the inner Lagrangian point (Roche-lobe overflow). For general reviews see, e.g. King (1995); McClintock & Remillard (2006).
- X-ray flares, some of which (as the source Swift J1644+57 detected last year, see e.g. Burrows et al., 2011) are thought to originate following the tidal disruption of a star by a central BH (for a review see, e.g. Rees, 1988).

- Long-duration GRBs, which are thought to originate when the core of a massive, rapidly-rotating star exhausts its nuclear fuel and collapses to a BH. The subsequent infall of the rest of the deep stellar interior towards the newborn BH forms a massive accretion disc which launches a pair of powerful relativistic jets (see e.g. Woosley, 1993; Piran, 2004).
- Short-duration GRBs, some of which are expected to originate after the coalescence of two neutron stars or, of a neutron star and a BH, in a close binary system. The result of this merger is expected to be qualitatively similar to that in the case of long GRBs (for a review see, e.g. Nakar, 2007).

We have seen that the process of accretion onto a BH is considered to be the fundamental mechanism behind some of the most powerful astrophysical phenomena. However, proper modelling of these systems requires input from almost all of the branches of physics in order to account for: self-gravitating fluids in the presence of strong gravitational and magnetic fields; spatial, temporal and density scales spanning many orders of magnitude; hydrodynamic flows with complex geometries, in which turbulence and strong shocks can develop; an accurate microphysical description of dissipative processes such as physical viscosity and cooling by neutrino emission; radiative transfer (for both photons and neutrinos); realistic equations of state describing in some cases matter at nuclear densities; nuclear burning of matter; etc. It is clear, then, that a comprehensive analysis of these systems requires full-scale numerical simulations. Nevertheless, given that no numerical method can perform equally well at each of these requirements simultaneously, it is also clear that we need to decide which are the dominant effects that we want to model in a particular problem and then choose the most suitable numerical approach. In the following section we present the particular numerical tool with which we intend to study some of these systems.

## 1.4 Numerical tool

The first assumption that we shall make in the present discussion is that the matter surrounding the BH is well described by the fluid approximation. Within this description, matter, which is composed of a large number of particles, is considered as a continuous field and its properties are described in terms of various dynamic and thermodynamic quantities (e.g. density, pressure, velocity, etc.). These variables are defined as local averages over spatial volumes that are small as compared to a typical length scale of the whole system but still large enough so as to contain a large number of particles. We shall refer to these volumes as fluid elements and consider that the particles enclosed within each of these are in local thermodynamic equilibrium.

The numerical techniques that exist for solving the hydrodynamic equations can be divided broadly into two types of approach: the so-called Eulerian approach, in which observers sitting in a fixed coordinate system describe the fluid as it passes by them; and the so-called Lagrangian approach, in which the description is made in terms of observers

that move along with the fluid.<sup>(3)</sup> Each of these approaches has its own advantages and disadvantages. However, the built-in adaptivity of a Lagrangian approach makes it particularly well-suited for studying physical scenarios without obvious symmetries or with a complex and/or changing geometry, as we have seen is typically the case for many astrophysical situations. In the present work we shall consider the Lagrangian technique known as smoothed particle hydrodynamics (SPH) originally developed by Lucy (1977) and Gingold & Monaghan (1977). General reviews of this method are given in Monaghan (1992, 2005); Rosswog (2009); Springel (2010); Price (2012).

The core of the SPH method consists of sampling the fluid properties at a finite set of interpolation points. These points are then moved according to the hydrodynamic equations in such a way that their updated positions can be used to interpolate back the properties of the fluid at any future time. Since each of these interpolation points is assigned a fixed mass, they are usually referred to as SPH particles. The interpolation in SPH is done in terms of weighted sums over the SPH particles in the vicinity of the point of interest. The so-called smoothing kernel weights the relative contribution of each neighbouring particle to the target point as a function of the distance between them. The sort of kernels used in SPH typically have a compact support whose width is characterised by the so-called smoothing length. Within this method, the derivatives involved in the evolution equations are calculated as exact derivatives of the interpolated values, i.e. derivatives are discretised as sums over particle properties, weighted now with the gradient of the smoothing kernel.

Another important procedure in SPH is the implementation of an efficient algorithm to search for the neighbours entering the kernel estimate. This procedure is closely related to the techniques used in N-body simulations for calculating gravitational forces in Newtonian and post-Newtonian simulations. Common approaches are the so-called tree methods (particles are organised in a hierarchical structure of nested cells, see e.g. Barnes & Hut, 1986; Hernquist & Katz, 1989) and particle-mesh methods (particles are mapped onto a mesh, see e.g. Dubinski et al., 2004).

Modern formulations of the SPH method use a set of evolution equations derived from a variational principle, as first proposed by Gingold & Monaghan (1982). This approach ensures, in the absence of dissipative processes, exact conservation of momentum (linear and angular), energy and entropy. Another important development is the introduction of a time-varying smoothing length that adapts to the local density in such a way that the total mass contained within the compact support of the kernel remains approximately constant. This makes SPH fully adaptive and is much easier to implement in practice than the usual adaptive mesh refinement approach used in grid-based methods. Nevertheless, if a varying smoothing length is used but the evolution equations are not modified in a self consistent way, then exact conservation of physically conserved quantities is no longer guaranteed (Nelson & Papaloizou, 1994). The necessary corrective terms, usually referred to as ‘grad- $h$ ’ terms, can also be derived self consistently from a Lagrangian (see e.g. Springel, 2010).

---

<sup>(3)</sup>There are also mixed approaches such as the so-called Adaptive Lagrangian Eulerian scheme, see e.g. Margolin (1997); Loubère et al. (2010).

The Lagrangian nature of the SPH approach makes it inherently adaptive, providing higher resolutions in regions in which the fluid is densest, while computational resources are not wasted on empty regions of space. This property makes SPH an ideal tool for dealing with astrophysical scenarios in which temporal, spatial and density scales may vary over many orders of magnitude. And, indeed, it has been extensively used for studying many astrophysical problems such as: cosmological expansion of the universe (see e.g. Springel et al., 2005b), galactic dynamics and galaxy mergers (see e.g. Springel et al., 2005a), fragmentation of self-gravitating gas clouds and star formation (see e.g. Price & Bate, 2009), tidal disruption of stars by BHs (see e.g. Kobayashi et al., 2004; Rosswog et al., 2009), stellar mergers of white dwarfs (see e.g. Dan et al., 2012) and of neutron stars (see e.g. Oechslin et al., 2002; Price & Rosswog, 2006), and the collapsing interiors of massive stars as GRB progenitors (see e.g. Lee & Ramírez-Ruiz, 2006; López-Cámara et al., 2009; Taylor et al., 2011).

Most of the astrophysical simulations using SPH are based on non-relativistic formulations. Nevertheless, there have been several extensions of the method to the relativistic context. Formulations within special relativity (relevant for the study of jets) have been made by Mann (1993); Chow & Monaghan (1997); Siegler & Riffert (2000); Rosswog (2010a). The SPH method has also been combined with different approximations to general relativity such as pseudo-Newtonian potentials (López-Cámara et al., 2009; Taylor et al., 2011), and the conformally flat approximation (Oechslin et al., 2002). Full general relativistic formulations of SPH have also been proposed (see e.g. Kheyfets et al., 1990; Laguna et al., 1993; Siegler & Riffert, 2000; Taylor, 2008) in which derivatives in the evolution equations are approximated by using SPH interpolation. GR formulations derived from a Lagrangian have been given by Monaghan & Price (2001); Aguiar et al. (2001) and Rosswog (2010b). This last work in particular also considered the corrective ‘grad- $h$ ’ terms directly in its derivation.

The work presented in this thesis forms part of a larger collaboration dealing with the development of a new general relativistic SPH code called SPHINCS: Smoothed Particle Hydrodynamics IN Curved Spacetime (to be presented in Rosswog et al., 2012). The code is still at the development stage and the following are the current elements of the SPHINCS work-plan:

1. The special relativistic SPH code introduced in Rosswog (2010a). The code is derived from a perfect-fluid Lagrangian and, in the absence of dissipative effects, features exact conservation of mass, energy, linear and angular momentum. The code has been successfully benchmarked against a series of standard tests for relativistic fluid dynamics such as supersonic advection, one and two-dimensional relativistic shock tubes, ultra-relativistic wall shocks, and the relativistic simple waves.
2. A new formulation of a density-balanced binary tree presented in Gafton & Rosswog (2011) which has proven to be highly efficient and accurate for the neighbour search and gravitational force calculation involved in the SPH method.
3. The already mentioned new general relativistic SPH formulation given by Rosswog

(2010b). Under appropriate symmetry conditions for the spacetime metric, this formulation recovers exact conservation of physically conserved quantities.

4. Explicit expressions for the terms associated with the spacetime curvature in the SPHINCS evolution equations for Schwarzschild and Kerr spacetimes. (This thesis)
5. An orbit catalogue of representative test particle trajectories in both Schwarzschild and Kerr spacetimes for benchmarking the ability of the new code to recovering geodesic motion. (This thesis)
6. An analytic toy model for the accretion flow of a rotating cloud of non-interacting particles infalling towards a central BH recently introduced in Tejeda et al. (2012a) for Schwarzschild spacetime and extended in Tejeda et al. (2012b) for Kerr spacetime. This analytic solution has already been used as a benchmark for testing the accuracy of two distinct SPH codes (Lee & Ramírez-Ruiz, 2006; Taylor et al., 2011) in dealing with purely general relativistic effects. (This thesis)

In principle, a full, general relativistic hydrodynamics code should solve simultaneously for the general relativistic hydrodynamic equations and the Einstein field equations. However, for applications in which it is safe to neglect the contribution of the mass-energy content of the fluid to the overall spacetime curvature, we can consider the spacetime metric as a fixed background and use the SPHINCS equations to evolve the fluid configuration in time. This is the first step in our programme for the development of SPHINCS, for which we shall also neglect the self-gravity of the fluid as well as non-adiabatic processes such as viscosity or radiative transfer.

As we shall discuss in this thesis, the equations of motion in the SPHINCS formulation not only reduce to the special relativistic ones in the flat spacetime limit, but also they naturally split into two terms: a first one involving the gradient of the fluid pressure (calculated via SPH interpolation), and a second one involving derivatives of the metric tensor and depending only on the position of the target particle. Furthermore, we shall also show that, for a spacetime metric that allows the introduction of Cartesian-like coordinates (as the Kerr metric does) and due to the particular kernel estimate that we use here, the first term in the equations of motion is formally identical to the special relativistic one. Given that the special relativistic version of SPHINCS has already been tested, the first version of the new code (fixed metric + inviscid flow) should be useful mainly for testing all of the different aspects of the implementation that are specific to a curved spacetime. For this, it will be particularly relevant to test for recovery of geodesic motion in the limit of vanishing hydrodynamic forces but other useful tests should also be considered, e.g. the general relativistic extension of the Bondi (1952) model given by Michel (1972) (which describes the steady spherical accretion of a perfect fluid onto a Schwarzschild BH) and the Bondi-Hoyle accretion model (where an initially homogeneous fluid is accreted onto a central object moving through it, Hoyle & Lyttleton, 1939; Bondi & Hoyle, 1944) extended by Font et al. (1999) to consider a Kerr BH as central accretor.

Once these features of the code are well tested, in the second stage of the project we will introduce a treatment of the fluid self-gravity as a small perturbation on top of the underlying fixed metric. As a first approximation, we can model the fluid self-gravity using a Newtonian approach, for which we will benefit from the binary tree of Gafton & Rosswog (2011). Moreover, at this stage we will consider more general equations of state and introduce the artificial viscosity prescription used by Rosswog (2010a) for handling relativistic shocks. This code will be used to study several astrophysical applications such as: the study of tidal disruptions of stars by BHs, the gravitational collapse of massive stars within the collapsar scenario, the accretion flow feeding supermassive BHs, and the numerical study of the effect of a rotating BH on the inner regions of an accretion disc around it.

With further development, SPHINCS could also be used to study more general situations in which the effect of the mass-energy of the fluid on the spacetime metric must be taken into account. In order to guarantee that the solution obtained is fully consistent with the Einstein field equations, in this case the SPHINCS code should be coupled with a metric solver (e.g. one of the several included in the publicly-available software collection for numerical relativity called the Einstein Toolkit, Löffler et al., 2012) that, at every time step, would take as input the mass-energy distribution coming from the SPHINCS evolution and calculate numerically updated values for the components of the spacetime metric.

## 1.5 Structure of the thesis

In this thesis we devote special attention to discussing the aspects of the project in which we have contributed with original work up to now. This contribution has been mainly focused on the points 4, 5 and 6 mentioned above, although we have also contributed with a relatively simple scheme for recovering the physical variables from the numerically evolved ones (which is a necessary procedure given the form of the SPHINCS evolution equations). There is also an original contribution to point 3, for which we have re-derived the SPHINCS evolution equations using the language of the so-called 3+1 formalism (Arnowitt et al., 1959). This formalism is particularly suitable for numerical implementations solving an initial value problem in which a physical system is evolved in time starting off from known initial data. The adoption of the 3+1 formalism should be especially useful if, at a future stage of development, we couple SPHINCS with a metric solver, since most of those codes are written in terms of this formalism.

This thesis is organised as follows:

In Chapter 2 we give a general review of general relativistic hydrodynamics as well as of the 3+1 formalism. Based on these tools, we show how the SPHINCS equations can be derived from the Lagrangian of a perfect fluid. We then show that, in the flat spacetime limit, SPHINCS reduces to the special relativistic formulation given by Rosswog (2010a). We also show that in the limit of vanishing hydrodynamic forces, the SPHINCS equations naturally reproduce geodesic motion. Finally we discuss a simple scheme for recovering the physical variables in terms of the numerically evolved ones.

In Chapter 3 we discuss the implementation of the SPHINCS evolution equations in Kerr spacetime. We start this chapter with a general overview of the Kerr metric, introducing two different coordinate systems and discussing the relation between them and their connection with the 3+1 formalism. At the end of this chapter we provide explicit expressions for the acceleration terms due to the spacetime metric that enter in the evolution equations.

In Chapter 4 we explore in detail the timelike geodesics of Kerr spacetime. This study allows us to gain deeper insight into the dynamic properties of this spacetime and to present a catalogue of representative test particle trajectories (included in Appendix A). We show how the symmetries of the Kerr metric lead to the existence of four first integrals of the motion that ultimately allow us to partially decouple the geodesic equations and to reduce them to a system of first order, ordinary differential equations. We devote special attention to the discussion of circular trajectories restricted to the equatorial plane, since these play an important role in the context of accretion discs. Then we discuss the more general case of trajectories off the equatorial plane. For this study we introduce the concepts of radial and polar effective potentials and, in terms of these tools, we analyse in detail the differential equations dictating the radial and latitudinal motions.

In Chapter 5 we construct an analytic toy model for the accretion flow of a rotating gas cloud infalling towards a Kerr BH. The model is based on the assumptions of stationarity, axisymmetry and ballistic trajectories of the gas particles, i.e. they follow timelike geodesics of Kerr spacetime. We introduce a novel approach for solving the radial and latitudinal parts of the motion in terms of a single analytic formula, which also serves for describing all of the different streamlines of the model. Furthermore, we show how the density field can be computed using a simple numerical scheme based on finite differences. The main purpose of this analytic model is to use it as a test solution for benchmarking general relativistic hydrodynamic codes. We show the results of the comparisons of the toy model with several SPH numerical simulations of an idealised collapsar-like setup that implement pseudo-Newtonian potentials for mimicking effects of Kerr and Schwarzschild spacetimes. Besides its use as a test solution, we also argue that the toy model constitutes a useful tool for highlighting purely general relativistic effects in hydrodynamic flows. It should also be useful for exploring the parameter space preceding the execution of full numerical simulations in applications in which the stationarity and axisymmetry conditions are approximately valid.

Finally, in Chapter 6 we give a general discussion, prospects of future work and our conclusions.

## 1.6 Notation, conventions and units

Unless otherwise stated, throughout the present work we use geometric units for which  $G = c = 1$ . We adopt a signature  $(-1, 1, 1, 1)$  for the spacetime metric, using Greek indices to denote spacetime components (running from 0 to 3) and Latin indices for spatial components only (running from 1 to 3). We shall reserve Latin subscripts starting

with the first letters of the alphabet ( $a, b, c$ ) for labelling SPH particles. We follow Einstein's convention of summation over repeated spacetime indices but not over labels of SPH particles. Four-vectors will be denoted with bold-faced symbols (e.g.  $\mathbf{v}$ ) while an over-arrow will be used to distinguish three-vectors (e.g.  $\vec{v}$ ).

## Chapter 2

# Smoothed particle hydrodynamics in a curved spacetime

In this chapter we present SPHINCS, a new formulation of the SPH method for solving the general relativistic hydrodynamic equations. The spacetime metric is taken as a known, but otherwise arbitrary function of the spatial coordinates (which can be given either analytically or numerically). In other words, we are considering here a fixed background metric and neglecting any kind of backreaction due to the motion of the fluid. This formulation has its origins in a relativistic derivation of the SPH evolution equations, starting from the Lagrangian of a perfect fluid, made by Monaghan & Price (2001) and then extended by Rosswog (2010b) to account self-consistently for a varying smoothing length.

We start this chapter with a brief review of some basic results of general relativistic hydrodynamics which will be useful for the present discussion. Then we introduce the so-called 3+1 decomposition of spacetime (Arnowitt et al., 1959), in which a global time direction is singled out and its level sets are used to foliate the spacetime into a family of three-dimensional, spatial hypersurfaces. Next we show how the SPHINCS numerical variables and corresponding evolution equations can be derived from the Lagrangian of a perfect fluid. Since the resulting evolution equations demand explicit knowledge of both the numerical and the physical variables, we shall introduce a simple scheme for recovering the primitive variables from the updated numerical ones after every time step. Then, we consider the limit of vanishing hydrodynamic forces and show that the SPHINCS formulation naturally reduces to the geodesic equations. Next we take the special relativistic limit of the SPHINCS equations and show that this recovers the expressions given in Rosswog (2010a), and finally, we show that in the non-relativistic limit, the usual expressions for the evolution equations in standard SPH are recovered.

### 2.1 Basics of general relativistic hydrodynamics

In general relativity, gravity is considered as an intrinsic property of the spacetime embodied in the curvature of its geometry. Within this framework, the geometry of the

spacetime and its mass-energy content are mixed together as a dynamic four-dimensional entity: on the one hand, the geometry of the spacetime sets the arena for the motion of particles and the evolution of physical fields, while, on the other hand, the mass-energy content in the spacetime determines the curvature.

Given that the spacetime is a curved four-dimensional manifold, the language of differential geometry is particularly suitable for describing its properties. Then, the key ingredient for characterising the geometry of the spacetime is the metric tensor  $g_{\mu\nu}$ . Given two spacetime events separated by an infinitesimal coordinate displacement  $dx^\mu$ , the metric tensor is used to define, in an invariant way (i.e. independently of any coordinate system), the square of the length of the interval of spacetime between the two events as

$$ds^2 = g_{\mu\nu} dx^\mu dx^\nu. \quad (2.1.1)$$

A spacetime interval is called spacelike if  $ds^2 > 0$ , timelike if  $ds^2 < 0$  and null if  $ds^2 = 0$ . The inverse of the metric tensor  $g^{\mu\nu}$ , is defined by

$$g^{\mu\lambda} g_{\lambda\nu} = \delta_\nu^\mu, \quad (2.1.2)$$

where  $\delta_\nu^\mu$  is a tensor whose elements are the Kronecker deltas. In addition to calculating spacetime intervals, the metric tensor also allows us to introduce a scalar product between vectors. For instance, given two arbitrary four-vectors  $\mathbf{A}$  and  $\mathbf{B}$ , we define their scalar product as

$$\mathbf{A} \cdot \mathbf{B} = g_{\mu\nu} A^\mu B^\nu = A_\nu B^\nu, \quad (2.1.3)$$

where  $A_\nu = g_{\mu\nu} A^\mu$  are the covariant components of  $\mathbf{A}$ .

We define a test particle as an ideal point particle whose rest mass  $m_0$  has a negligible effect on the whole spacetime curvature. Its four-velocity  $\mathbf{U}$  is defined as the vector tangent to its worldline and normalised as  $\mathbf{U} \cdot \mathbf{U} = -1$ , while its four-momentum is defined as  $\mathbf{p} = m_0 \mathbf{U}$ . The contravariant components of  $\mathbf{U}$  are given as  $U^\mu = dx^\mu/d\tau$ , where  $d\tau^2 = -ds^2$  is the square of the proper time (i.e. time measured in the comoving reference frame). Under the only action of the gravitational field, the motion of the test particle is determined by the spacetime curvature through the so-called geodesic equations

$$U^\mu U_{;\mu}^\sigma = 0, \quad (2.1.4)$$

where a semicolon represents the covariant derivative which is defined in terms of the ordinary partial differentiation  $U_{;\mu}^\sigma \equiv \partial U^\sigma / \partial x^\mu$  as

$$U_{;\mu}^\sigma \equiv U_{,\mu}^\sigma + \Gamma_{\mu\nu}^\sigma U^\nu, \quad (2.1.5)$$

and where  $\Gamma_{\mu\nu}^\sigma$  are the Christoffel symbols which can be expressed in terms of the metric as

$$\Gamma_{\mu\nu}^\sigma = \frac{1}{2} g^{\sigma\lambda} (g_{\mu\lambda,\nu} + g_{\nu\lambda,\mu} - g_{\mu\nu,\lambda}). \quad (2.1.6)$$

Using Eq. (2.1.5) together with the identity  $d/d\tau = U^\mu \partial / \partial x^\mu$ , we can rewrite the geodesic equation in Eq. (2.1.4) as

$$\frac{dU^\sigma}{d\tau} + \Gamma_{\mu\nu}^\sigma U^\mu U^\nu = 0. \quad (2.1.7)$$

Note that the covariant derivative of an arbitrary mixed second rank tensor  $A^\mu_\nu$  is given by

$$A^\mu_{\nu;\lambda} = A^\mu_{\nu,\lambda} + \Gamma^\mu_{\sigma\lambda} A^\sigma_\nu - \Gamma^\sigma_{\nu\lambda} A^\mu_\sigma, \quad (2.1.8)$$

while the covariant derivative of a scalar reduces simply to partial differentiation, i.e.  $f_{;\mu} = f_{,\mu}$ , where  $f$  is any arbitrary scalar function. Moreover, from the definition of the Christoffel symbols in Eq. (2.1.6), it is easy to check that

$$g_{\mu\nu;\lambda} = 0. \quad (2.1.9)$$

In a general case, the spacetime under consideration will contain more than just test particles, and so we need to introduce the stress-energy tensor  $\mathbf{T}$  in order to describe the distribution of mass-energy. This is a symmetric tensor that includes the contribution of all of the physical fields present in the spacetime (e.g., matter field, electromagnetic fields, etc.) and its component  $T^{\mu\nu}$  gives the flux of four-momentum  $p^\mu$  in the direction of  $x^\nu$ . The stress-energy tensor acts as a source of spacetime curvature in the Einstein field equations which consist of the following system of second order differential equations in  $g_{\mu\nu}$

$$R_{\mu\nu} - \frac{1}{2} g_{\mu\nu} R = 8\pi T_{\mu\nu}, \quad (2.1.10)$$

where  $R_{\mu\nu}$  is the Ricci tensor and  $R \equiv R^\mu_\mu$  the Ricci scalar. The Ricci tensor is defined as  $R_{\mu\nu} \equiv R^\lambda_{\mu\lambda\nu}$ , where

$$R^\lambda_{\mu\sigma\nu} = \Gamma^\lambda_{\mu\nu,\sigma} - \Gamma^\lambda_{\mu\sigma,\nu} + \Gamma^\lambda_{\alpha\sigma} \Gamma^\alpha_{\mu\nu} - \Gamma^\lambda_{\alpha\nu} \Gamma^\alpha_{\mu\sigma} \quad (2.1.11)$$

is the Riemann tensor.

In the present chapter we shall assume that the only mass-energy of the spacetime is coming from a perfect fluid of neutral matter which is characterised by zero viscosity and no heat conduction. A thorough discussion of general relativistic hydrodynamics involving more general fluids can be found in Font (2008). A local description of the state of the fluid is given in terms of the fluid element velocity field  $\mathbf{U}$ , the baryon number density  $n$ , the specific internal energy  $u$  (or internal energy per unit rest mass), the specific entropy  $s$ , and the pressure  $P$ . These last four variables represent scalar quantities measured in a reference frame comoving with the fluid element. Introducing the average baryonic rest mass  $m_0$  of the fluid, we can express the rest mass density of the fluid as  $\rho = m_0 n$ . As discussed in Chapter 1, we know that for a perfect fluid the entropy of each fluid element is a conserved quantity along the worldline of the element, although it can, in principle, be different for different fluid elements. The rest of the thermodynamic variables are related through an equation of state (EoS) of the form  $f(n, u, P) = 0$ , which can be used to express any of them in terms of the other two, e.g.  $P = P(n, u)$  or  $u = u(n, P)$ . Expressing all energies and the pressure  $P$  in units of the baryonic rest mass  $m_0$ , the stress-energy tensor for a perfect fluid is given by

$$T^{\mu\nu} = n \omega U^\mu U^\nu + P g^{\mu\nu}, \quad (2.1.12)$$

where  $\omega = 1 + u + P/n$  is the relativistic specific enthalpy. In general relativity local conservation of energy-momentum is expressed by

$$T_{;\mu}^{\mu\nu} = 0, \quad (2.1.13)$$

and the conservation of baryon number is expressed as

$$(n U^\mu)_{;\mu} = 0. \quad (2.1.14)$$

This last result is also known as the continuity equation.

A further useful relation between the thermodynamic variables can be obtained by calculating the scalar product of Eq. (2.1.13) with the four-velocity, i.e.

$$U_\nu T_{;\mu}^{\mu\nu} = -n U^\mu \omega_{;\mu} - \omega (n U^\mu)_{;\mu} + n \omega U_\nu U^\mu U_{;\mu}^\nu + U^\nu P_{;\nu} = 0 \quad (2.1.15)$$

where we have used the normalisation condition  $U_\nu U^\nu = -1$  and Eq. (2.1.9). Note that the second term in Eq. (2.1.15) vanishes by virtue of Eq. (2.1.14), while the third term also vanishes since

$$U_\nu U^\mu U_{;\mu}^\nu = \frac{1}{2} U^\mu (U_\nu U^\nu)_{;\mu} = 0. \quad (2.1.16)$$

Now, using the identity  $d/d\tau = U^\mu \partial/\partial x^\mu$  and substituting  $\omega = 1 + u + P/n$  into Eq. (2.1.15) we finally get

$$\frac{du}{d\tau} = \frac{P}{n^2} \frac{dn}{d\tau}, \quad (2.1.17)$$

or, in terms of total differentials,

$$du = \frac{P}{n^2} dn, \quad (2.1.18)$$

which is nothing more than the first law of thermodynamics when only adiabatic processes are considered (consistent with the fact that in the perfect fluid description there is no entropy generation).

Before exploring Eqs. (2.1.13) and (2.1.14) in further detail, we introduce in the next section some useful concepts of the so-called 3+1 decomposition of the spacetime, which is a practical tool for the numerical evolution of a fluid.

## 2.2 3+1 decomposition of the metric

In general relativity the four dimensions of spacetime are treated on an equal footing. This allows for the use of a fully covariant language with which there is no need to make any distinction between temporal and spatial coordinates. However, in several circumstances (and especially for numerical implementations), it becomes extremely useful to identify a clear temporal direction along which one can evolve a given physical system starting off from a known initial configuration. This is the spirit of the so-called 3+1 decomposition of spacetime or ADM formalism (Arnowitt et al., 1959; Alcubierre, 2008), which consists of two basic steps: First, we need to choose a scalar function  $t(x^\mu)$  whose level sets  $t(x^\mu) = \text{const.}$  serve to foliate the spacetime into hypersurfaces  $\Sigma_t$ . Provided

that the spacetime is globally hyperbolic,<sup>(1)</sup> it is always possible to find a function  $t$  such that each slice  $\Sigma_t$  is spacelike. Once a particular foliation has been chosen, the second step is to introduce a spatial coordinate system  $(x^i)$  for each slice  $\Sigma_t$ . In this way, the coordinates of any given point of the spacetime are split as  $(x^\mu) = (t, x^i)$ . The spatial coordinates  $(x^i)$  can be introduced in a continuous fashion by setting them once at an arbitrary slice  $\Sigma_t$  and then describing the way in which they should be propagated to future (or past) slices. This description is usually made in terms of four auxiliary functions, the lapse  $\alpha$  and the shift  $\beta^i$ , that can be freely designated due to the gauge freedom of Einstein's field equations. Using these auxiliary functions, the spacetime metric  $g_{\mu\nu}$  is split as

$$\begin{aligned} ds^2 &= g_{\mu\nu} dx^\mu dx^\nu \\ &= -\alpha^2 dt^2 + \gamma_{ij} (dx^i + \beta^i dt) (dx^j + \beta^j dt), \end{aligned} \quad (2.2.1)$$

where  $\gamma_{ij}$  is the induced spatial metric on each hypersurface  $\Sigma_t$  which is determined once a particular time function  $t(x^\mu)$  is chosen. From Eq.(2.2.1) it is clear that the spatial intervals within a given hypersurface  $\Sigma_t$  are calculated as

$$ds^2|_{\Sigma_t} = \gamma_{ij} dx^i dx^j. \quad (2.2.2)$$

We also use  $\gamma_{ij}$  for lowering and raising indices and for calculating inner products of pure spatial tensors living in the three dimensional hypersurfaces  $\Sigma_t$ . For instance, using the three shift functions  $\beta^i$  to define the contravariant components of a three-vector  $\vec{\beta} \in \Sigma_t$ , we can calculate its covariant components as  $\beta_i \equiv \gamma_{ij} \beta^j$  while its magnitude is given by  $\|\vec{\beta}\|^2 \equiv \vec{\beta} \cdot \vec{\beta} = \gamma_{ij} \beta^i \beta^j = \beta_i \beta^i$ . Using this notation, we can read off from Eq.(2.2.1) the components of the four-metric  $g_{\mu\nu}$  as

$$(g_{\mu\nu}) = \begin{pmatrix} -\alpha^2 + \|\vec{\beta}\|^2 & \beta_i \\ \beta_j & \gamma_{ij} \end{pmatrix}, \quad (2.2.3)$$

and it is easy to check that the components of the inverse metric  $g^{\mu\nu}$  are given by

$$(g^{\mu\nu}) = \begin{pmatrix} -1/\alpha^2 & \beta^i/\alpha^2 \\ \beta^j/\alpha^2 & \gamma^{ij} - \beta^i \beta^j/\alpha^2 \end{pmatrix}, \quad (2.2.4)$$

where the inverse of the spatial metric satisfies  $\gamma^{ik} \gamma_{kj} = \delta_j^i$ . The determinants of the four- and three-metrics,  $g$  and  $\gamma$ , respectively, are related through the following identity

$$\sqrt{-g} = \alpha \sqrt{\gamma}. \quad (2.2.5)$$

---

<sup>(1)</sup>A given spacetime is called globally hyperbolic if it admits the existence of a null or spacelike hypersurface (Cauchy surface) such that, by fixing initial data on it, one can determine the whole past and future history of the spacetime

We note here the following basic result from the theory of determinants (see e.g. Landau & Lifshitz, 1975) that will allow us to calculate derivatives of  $\gamma$  and  $g$  at several points in the present discussion, i.e.

$$dg = g g^{\mu\nu} dg_{\mu\nu}, \quad d\gamma = \gamma \gamma^{ij} d\gamma_{ij}. \quad (2.2.6)$$

Once the spacetime has been foliated into spatial slices  $\Sigma_t$ , at every point of the spacetime we can define two types of observer: one who moves along constant spatial coordinate lines ( $x^i = \text{const.}$ ) and another one who remains at rest with respect to the slices  $\Sigma_t$ . The former one is called a coordinate observer while the latter is called a local Eulerian observer.<sup>(2)</sup> In the next subsection we discuss some special properties of these observers.

### 2.2.1 Local Eulerian observers

Saying that a local Eulerian observer (LEO) remains at rest with respect to any given  $\Sigma_t$ , means that, at any given point ( $x^i$ ) on a slice  $\Sigma_t$ , the LEO is moving along the normal direction to  $\Sigma_t$  at ( $x^i$ ). Since the hypersurfaces  $\Sigma_t$  are spacelike, it then follows that the LEO moves along a timelike trajectory (not necessarily geodesic). In other words, the LEO corresponds to a physical observer (not necessarily an inertial one) with respect to whom we can make local measurements to describe physical properties of, for instance, a fluid passing by the LEO.

Both the coordinate observer and the LEO carry with them a set of tetrad vectors spanning their local reference frames. We call  $\{\mathbf{e}_{(\mu)}\}$  the set of basis vectors of the coordinate observer frame and  $\{\mathbf{e}^{(\mu)}\}$  the associated basis for the contravariant components of the vectors. On the other hand, denoting with a bar coordinates referred to the LEO, i.e.  $(\bar{x}^\mu) = (\bar{t}, \bar{x}^i)$ , we call the corresponding bases for the covariant and contravariant components of vectors  $\{\bar{\mathbf{e}}_{(\mu)}\}$  and  $\{\bar{\mathbf{e}}^{(\mu)}\}$ , respectively.<sup>(3)</sup> The transformation rule between these two coordinate systems is given by

$$d\bar{t} = \alpha dt, \quad (2.2.7)$$

$$d\bar{x}^i = dx^i + \beta^i dt, \quad (2.2.8)$$

from where we see that  $\alpha$  can be interpreted as a measure of the difference between the rates of the LEO and the coordinate times, while  $\vec{\beta}$  measures the relative velocity between the LEO and the lines of constant spatial coordinates. Using Eqs. (2.2.7) and (2.2.8) it is simple to check that the two sets of basis vectors are related by

$$\begin{aligned} \bar{\mathbf{e}}^{(t)} &= \alpha \mathbf{e}^{(t)}, & \bar{\mathbf{e}}_{(t)} &= (\mathbf{e}_{(t)} - \beta^i \mathbf{e}_{(i)}) / \alpha, \\ \bar{\mathbf{e}}^{(i)} &= \mathbf{e}^{(i)} + \beta^i \mathbf{e}^{(t)}, & \bar{\mathbf{e}}_{(i)} &= \mathbf{e}_{(i)}. \end{aligned} \quad (2.2.9)$$

<sup>(2)</sup>Note that the coordinate observer does not necessarily correspond to a physical observer since, in principle, the shift can be superluminal which would make the coordinates ( $x^i$ ) to change superluminally from one slice to the next.

<sup>(3)</sup>It is important to note that the coordinate system associated with the LEO frame is a local one and, in general, cannot be extended to cover a region of spacetime of finite extent.

The Jacobian of the transformation law between the LEO and coordinate observer frames is the matrix  $\partial\bar{x}^\mu/\partial x^\nu$ , while  $\partial x^\mu/\partial\bar{x}^\nu$  is the Jacobian of the inverse transformation. From Eq. (2.2.9) we can immediately read off the components of the two Jacobian matrices as

$$\left(\frac{\partial\bar{x}^\mu}{\partial x^\nu}\right) = \begin{pmatrix} \alpha & 0 & 0 & 0 \\ \beta^1 & 1 & 0 & 0 \\ \beta^2 & 0 & 1 & 0 \\ \beta^3 & 0 & 0 & 1 \end{pmatrix}, \quad (2.2.10)$$

and

$$\left(\frac{\partial x^\mu}{\partial\bar{x}^\nu}\right) = \begin{pmatrix} 1/\alpha & 0 & 0 & 0 \\ -\beta^1/\alpha & 1 & 0 & 0 \\ -\beta^2/\alpha & 0 & 1 & 0 \\ -\beta^3/\alpha & 0 & 0 & 1 \end{pmatrix}. \quad (2.2.11)$$

Using these Jacobian matrices, we can transform any vector or tensor back and forth between the LEO and coordinate observer frames. For example, by applying Eq. (2.2.11) twice to the metric tensor we obtain that its components in the LEO frame are given by

$$(\bar{g}_{\mu\nu}) = \begin{pmatrix} -1 & 0 \\ 0 & \bar{\gamma}_{ij} \end{pmatrix}, \quad (2.2.12)$$

from where it follows that the differential line element in the LEO reference frame is given by

$$ds^2 = -d\bar{t}^2 + \bar{\gamma}_{ij} d\bar{x}^i d\bar{x}^j. \quad (2.2.13)$$

Denoting by  $\mathbf{N}$  the four-velocity of a LEO, it is clear that, referred to their own coordinate system, the components of  $\mathbf{N}$  are simply given by  $(\bar{N}^\mu) = (1, 0, 0, 0)$  and  $(\bar{N}_\mu) = (-1, 0, 0, 0)$ . Using the Jacobian tensors, we find that the components of  $\mathbf{N}$  in the global (i.e. unfoliated) coordinate system are given by

$$(N^\mu) = (1/\alpha, -\beta^i/\alpha), \quad (2.2.14)$$

while its covariant components are

$$(N_\mu) = (-\alpha, 0, 0, 0). \quad (2.2.15)$$

Consider now a particle moving with four-velocity  $\mathbf{U}$ . The covariant and contravariant components of  $\mathbf{U}$  in the LEO reference frame can be written as

$$\begin{aligned}(\bar{U}^\mu) &= (\Gamma, \Gamma \bar{V}^i), \\ (\bar{U}_\mu) &= (-\Gamma, \Gamma \bar{V}_i),\end{aligned}\tag{2.2.16}$$

where  $\Gamma \equiv -\mathbf{N} \cdot \mathbf{U} = \bar{U}^0$  is the Lorentz factor between the particle and the LEO, and  $\bar{V}^i = d\bar{x}^i/d\bar{t}$  is the  $i$ -th component of the three-velocity  $\vec{V}$  of the particle relative to the LEO. By using the normalisation condition  $\mathbf{U} \cdot \mathbf{U} = -1$  in Eq. (2.2.16), it is simple to check that  $\Gamma$  can also be expressed as

$$\Gamma = (1 - \vec{V} \cdot \vec{V})^{-1/2}.\tag{2.2.17}$$

Making use of the Jacobian matrices, it follows that the covariant and contravariant components of  $\mathbf{U}$  in the global coordinate system are given by

$$\begin{aligned}(U^\mu) &= (\Gamma/\alpha, \Gamma [V^i - \beta^i/\alpha]) \\ &= (\Gamma/\alpha, \Gamma v^i/\alpha), \\ (U_\mu) &= \left( -\Gamma[\alpha - \vec{\beta} \cdot \vec{V}], \Gamma V_i \right),\end{aligned}\tag{2.2.18}$$

where  $v^i = dx^i/dt$  is the  $i$ -th component of the coordinate three-velocity  $\vec{v}$ . From Eq. (2.2.18), we see that the three-velocities  $\vec{v}$ ,  $\vec{V}$  and  $\vec{\beta}$  are related by

$$\vec{V} = (\vec{v} + \vec{\beta})/\alpha.\tag{2.2.19}$$

It is important to note that only  $\vec{V}$  corresponds to a physical three-velocity, and thus it satisfies  $\|\vec{V}\|^2 < 1$ , while there is nothing to prevent  $\vec{v}$  and  $\vec{\beta}$  from being superluminal under certain circumstances.

Finally, we note that the normal vector  $\mathbf{N}$  can be used to introduce the projection tensor

$$\gamma_{\mu\nu} = g_{\mu\nu} + N_\mu N_\nu,\tag{2.2.20}$$

that, when applied to any arbitrary four-tensor, removes the part of it which is normal to  $\Sigma_t$  at any given point ( $x^i$ ). Note that from Eqs. (2.2.15) and (2.2.20) it follows that the spatial metric  $\gamma_{ij}$  corresponds to the spatial part of the projection tensor.

### 2.3 Conservation laws in the 3+1 formalism

As we saw in Section 2.1, the evolution of a fluid in general relativity is dictated by the local conservation laws of stress-energy and baryon number given in Eqs. (2.1.13) and (2.1.14), respectively. In this section we follow Laguna et al. (1993) and Siegler & Riffert (2000) for splitting these two equations using the 3+1 formalism and recasting them in a way suitable for a Lagrangian description (i.e. in terms of total time derivatives).

In this section we shall use some physical properties of the fluid as described by a LEO. In particular, it is convenient to introduce at this point the baryon number density

$N$ , the mass-energy density  $\epsilon$ , the three-momentum  $S^i$ , and the spatial stress tensor  $\sigma^{ij}$ . These quantities are defined as (Arnowitt et al., 1959)

$$N = -N^\mu (n U_\mu) = \Gamma n, \quad (2.3.1)$$

$$\epsilon = N^\mu N^\nu T_{\mu\nu} = n \omega \Gamma^2 - P, \quad (2.3.2)$$

$$S^i = -N^\mu \gamma^{\nu i} T_{\mu\nu} / N = \omega \Gamma V^i, \quad (2.3.3)$$

$$\sigma^{ij} = \gamma^{\mu i} \gamma^{\nu j} T_{\mu\nu} = n \omega \Gamma^2 V^i V^j + P \gamma^{ij}. \quad (2.3.4)$$

where  $\gamma^{\mu\nu}$  is the projection tensor defined in Eq. (2.2.20).

### 2.3.1 Continuity equation

Let us consider first the continuity equation as given in Eq. (2.1.14). Using the well-known expression for the divergence of a four-vector (Landau & Lifshitz, 1975)

$$(A^\mu)_{;\mu} = \frac{1}{\sqrt{-g}} \frac{\partial}{\partial x^\mu} (\sqrt{-g} A^\mu), \quad (2.3.5)$$

together with Eqs. (2.2.5), (2.2.18) and (2.3.1), we can split Eq. (2.1.14) as

$$\frac{\partial}{\partial x^\mu} (\alpha \sqrt{\gamma} n U^\mu) = \frac{\partial(\sqrt{\gamma} N)}{\partial t} + \frac{\partial(\sqrt{\gamma} N v^i)}{\partial x^i} = 0. \quad (2.3.6)$$

Moreover, if we use the total time derivative

$$\frac{d}{dt} = \frac{\partial}{\partial t} + \frac{dx^i}{dt} \frac{\partial}{\partial x^i}, \quad (2.3.7)$$

we can recast Eq. (2.3.6) as

$$\frac{dN}{dt} = -N \frac{\partial v^i}{\partial x^i} - \frac{N}{\sqrt{\gamma}} \frac{d\sqrt{\gamma}}{dt}. \quad (2.3.8)$$

The first term on the right hand side of this equation tells us that the baryon number density associated with a volume element  $dV$  will change as a result of the total flux of baryons entering or leaving  $dV$ , while the second term tells us that the variation might also be due to the expansion or contraction of the volume element. Note that, if instead of  $N$ , we use the quantity

$$N^* = \sqrt{\gamma} N, \quad (2.3.9)$$

we can forget about this geometric factor and write

$$\frac{dN^*}{dt} = -N^* \frac{\partial v^i}{\partial x^i}. \quad (2.3.10)$$

We need to stress that, in general,  $N^*$  does not necessarily have units of inverse volume (as does  $N$ ) since the dimensions of  $\gamma$  will depend on the particular definition of the spatial coordinates ( $x^i$ ). Nevertheless, we shall assume that ( $x^i$ ) can be rescaled in such a way that each component has units of length. Doing so,  $dV = dx^3$  will have units of volume, while  $\gamma$  will be a dimensionless factor.

### 2.3.2 Spatial part of the stress-energy equation

We consider now the spatial part of the local conservation law for the stress-energy tensor  $T^{\mu\nu}$  as given in Eq. (2.1.13). For a symmetric tensor such as  $T^{\mu\nu}$ , we can use the following identity for calculating its four-divergence and rewrite Eq. (2.1.13) as (Landau & Lifshitz, 1975)

$$T^{\mu}_{\nu;\mu} = \frac{1}{\sqrt{-g}} \frac{\partial(\sqrt{-g} T^{\mu}_{\nu})}{\partial x^{\mu}} - \frac{1}{2} \frac{\partial g_{\mu\sigma}}{\partial x^{\nu}} T^{\mu\sigma} = 0 \quad (2.3.11)$$

In order to split the spatial part of Eq. (2.3.11) in terms of 3+1 quantities, we need the mixed components

$$T^0_i = \frac{n\omega\Gamma^2 V_i}{\alpha} = \frac{NS_i}{\alpha}, \quad (2.3.12)$$

$$T^j_i = \frac{n\omega\Gamma^2 V_i v^j}{\alpha} + P\delta^j_i = \frac{NS_i v^j}{\alpha} + P\delta^j_i. \quad (2.3.13)$$

Taking the spatial part of Eq. (2.3.11) and using Eqs. (2.3.12) and (2.3.13), results in

$$\frac{\partial(\alpha\sqrt{\gamma}T^{\mu}_i)}{\partial x^{\mu}} = \frac{\partial(N^*S_i)}{\partial t} + \frac{\partial(N^*S_i v^j)}{\partial x^j} + \frac{\partial(\alpha\sqrt{\gamma}P\delta^j_i)}{\partial x^j} = \frac{\alpha\sqrt{\gamma}}{2} \frac{\partial g_{\mu\sigma}}{\partial x^i} T^{\mu\sigma}. \quad (2.3.14)$$

Using Eqs. (2.3.7) and (2.3.10), we can rewrite Eq. (2.3.14) as

$$\frac{dS_i}{dt} = -\frac{1}{N^*} \frac{\partial(\alpha\sqrt{\gamma}P)}{\partial x^i} + \frac{\alpha\sqrt{\gamma}}{2N^*} \frac{\partial g_{\mu\sigma}}{\partial x^i} T^{\mu\sigma}, \quad (2.3.15)$$

where we still need to expand the second term on the right hand side in terms of 3+1 quantities. To this end, let us note that the 3+1 decomposition of  $T^{\mu\nu}$  is given by

$$T^{00} = \frac{n\omega\Gamma^2 - P}{\alpha^2} = \frac{\epsilon}{\alpha^2}, \quad (2.3.16)$$

$$T^{0i} = \frac{n\omega\Gamma^2}{\alpha^2} (\alpha V^i - \beta^i) + \frac{P\beta^i}{\alpha^2} = \frac{NS^i}{\alpha} - \frac{\epsilon\beta^i}{\alpha^2}, \quad (2.3.17)$$

$$\begin{aligned} T^{ij} &= \frac{n\omega\Gamma^2}{\alpha^2} (\alpha V^i - \beta^i)(\alpha V^j - \beta^j) - \frac{P\beta^i\beta^j}{\alpha^2} + P\gamma^{ij} \\ &= \frac{\epsilon\beta^i\beta^j}{\alpha^2} - \frac{N(S^i\beta^j + S^j\beta^i)}{\alpha} + \sigma^{ij}. \end{aligned} \quad (2.3.18)$$

With the aid of Eqs. (2.3.16)-(2.3.18), the second term on the right hand side of Eq. (2.3.15) can be rewritten as

$$\frac{\alpha\sqrt{\gamma}}{2N^*} \frac{\partial g_{\mu\sigma}}{\partial x^i} T^{\mu\sigma} = -\frac{\sqrt{\gamma}\epsilon}{N^*} \frac{\partial\alpha}{\partial x^i} + S_j \frac{\partial\beta^j}{\partial x^i} + \frac{\alpha\sqrt{\gamma}\sigma^{jk}}{2N^*} \frac{\partial\gamma_{jk}}{\partial x^i}. \quad (2.3.19)$$

By substituting this result back into Eq. (2.3.15), we finally get

$$\frac{dS_i}{dt} = -\frac{1}{N^*} \frac{\partial(\alpha\sqrt{\gamma}P)}{\partial x^i} - \frac{\sqrt{\gamma}\epsilon}{N^*} \frac{\partial\alpha}{\partial x^i} + S_j \frac{\partial\beta^j}{\partial x^i} + \frac{\alpha\sqrt{\gamma}\sigma^{jk}}{2N^*} \frac{\partial\gamma_{jk}}{\partial x^i}. \quad (2.3.20)$$

### 2.3.3 Temporal part of the stress-energy equation

Finally we consider the 3+1 decomposition of the time component of Eq. (2.3.11). In this case we need the mixed components

$$T_0^0 = -\frac{n\omega\Gamma^2}{\alpha}(\alpha - \vec{V} \cdot \vec{\beta}) + P = -\frac{Ne}{\alpha} \quad (2.3.21)$$

$$T_0^j = -\frac{n\omega\Gamma^2}{\alpha}(\alpha - \vec{V} \cdot \vec{\beta})v^j = -\frac{Ne v^j}{\alpha} - P v^j, \quad (2.3.22)$$

where

$$e = \omega\Gamma(\alpha - \vec{V} \cdot \vec{\beta}) - \frac{\alpha P}{N} = \vec{S} \cdot \vec{v} + \frac{\alpha(1+u)}{\Gamma} \quad (2.3.23)$$

is the canonical energy associated with the three momentum  $\vec{S}$ , as we shall show in Section 2.4.3. Using Eqs. (2.3.21) and (2.3.22), we can rewrite the time component of Eq. (2.3.11) as

$$\frac{\partial(\alpha\sqrt{\gamma}T_0^\mu)}{\partial x^\mu} = -\frac{\partial(N^*e)}{\partial t} - \frac{\partial(N^*e v^j)}{\partial x^j} - \frac{\partial(\alpha\sqrt{\gamma}P v^j)}{\partial x^j} = \frac{\alpha\sqrt{\gamma}}{2} \frac{\partial g_{\mu\sigma}}{\partial t} T^{\mu\sigma}. \quad (2.3.24)$$

Using Eqs. (2.3.7), (2.3.10) and (2.3.19), this last equation transforms as

$$\frac{de}{dt} = -\frac{1}{N^*} \frac{\partial(\alpha\sqrt{\gamma}P v^j)}{\partial x^j} + \frac{\sqrt{\gamma}\epsilon}{N^*} \frac{\partial\alpha}{\partial t} - S_j \frac{\partial\beta^j}{\partial t} - \frac{\alpha\sqrt{\gamma}\sigma^{jk}}{2N^*} \frac{\partial\gamma_{jk}}{\partial t}. \quad (2.3.25)$$

### 2.3.4 Non-relativistic limit

It is clear that for a flat spacetime and in the non-relativistic limit, the hydrodynamic equations discussed in the previous section should reduce to the equivalent Newtonian expressions. Using ordinary Cartesian coordinates  $(t, x, y, z)$  we have that in this limit  $\alpha = 1$ ,  $\vec{\beta} = 0$ , and  $\gamma_{ij} = \delta_{ij}$ . Restoring standard units, in the non-relativistic limit we have that  $v^2/c^2 \equiv \|\vec{v}\|^2/c^2 \ll 1$ ,  $u \ll c^2$  and  $P \ll \rho c^2$ . Then, from the definitions in Eqs. (2.2.17), (2.3.3), (2.3.9), and (2.3.23), we obtain the following expressions for the fluid variables:

$$\Gamma = \sqrt{1 - v^2/c^2} \rightarrow 1 + v^2/(2c^2), \quad (2.3.26)$$

$$\omega = c^2 + u + P/\rho, \quad (2.3.27)$$

$$m_0 N^* = \Gamma \rho \rightarrow \rho, \quad (2.3.28)$$

$$\vec{S} = (\omega/c^2)\Gamma \vec{v} \rightarrow \vec{v}, \quad (2.3.29)$$

$$e = \Gamma\omega - P/\rho \rightarrow c^2 + \hat{e}, \quad (2.3.30)$$

where  $\hat{e} = u + v^2/2$  is the specific thermokinetic energy. The corresponding evolution equations, as follow from Eqs. (2.3.9), (2.3.20) and (2.3.25), are given by

$$\frac{d\rho}{dt} = -\rho \frac{\partial v^i}{\partial x^i} \quad (2.3.31)$$

$$\frac{dv_i}{dt} = -\frac{1}{\rho} \frac{\partial P}{\partial x^i}, \quad (2.3.32)$$

$$\frac{d\hat{e}}{dt} = -\frac{1}{\rho} \frac{\partial (P v^i)}{\partial x^i}. \quad (2.3.33)$$

Here we see that Eqs. (2.3.31) and (2.3.32) are the well-known continuity equation and Euler equations of non-relativistic hydrodynamics, respectively. We note that in the Newtonian context, it is more common to use the variable  $u$  rather than  $\hat{e}$  for expressing the energy equation. Using Eqs. (2.3.31)-(2.3.33) it is simple to obtain the following evolution equation for  $u$

$$\frac{du}{dt} = -\frac{P}{\rho} \frac{\partial v^i}{\partial x^i} = \frac{P}{\rho^2} \frac{d\rho}{dt}, \quad (2.3.34)$$

which is the first law of thermodynamics for adiabatic flows derived previously in Eq. (2.1.17).

## 2.4 SPHINCS

In this section we introduce a formalism for applying the SPH method to solve the general relativistic hydrodynamic equations. For the present discussion we shall assume that a fixed spacetime metric is given as a known function of the coordinates. As we mention in Chapter 1, there exist in the literature several implementations of the SPH method in general relativity (e.g. Kheifets et al., 1990; Laguna et al., 1993; Siegler & Riffert, 2000; Taylor, 2008) in which the evolution equations in Eqs. (2.3.20) and (2.3.25) are approximated by using SPH interpolation. However, in these kinds of approach the symmetry properties of the evolution equations, which are crucial to enforce conservation, are in a way introduced ‘by hand’ and, moreover, they do not account self-consistently for an adaptive resolution.<sup>(4)</sup> For this reason, we follow here the recent formulation by Rosswog (2010b) which is derived from a variational principle from a relativistic Lagrangian and accounts for the corrective terms coming from a varying smoothing length.

The evolution equations in this formulation are derived from three basic ingredients: an interpolation formula for calculating the baryon number density, the Lagrangian for a perfect fluid, and the first law of thermodynamics. The next step in this strategy is to discretise the Lagrangian in a way suitable for SPH and then to use the Euler-Lagrange equations as a guides for defining a canonical momentum and a canonical energy which are used as numerical variables. Due to the symmetries of this Lagrangian, the resulting evolution equations in the special relativistic case (flat spacetime) feature exact conservation of linear momentum, angular momentum, and energy. However, for an arbitrary

<sup>(4)</sup>In Taylor (2008) a different approach was used in which the terms related with the spacetime curvature were translated as an effective Newtonian force, and then it was used a non-relativistic Lagrangian formulation of SPH.

spacetime and in the absence of dissipative processes, the total energy will be conserved only if the metric is time-independent, while the necessary condition for the total angular momentum to be conserved is that the metric should be axisymmetric. Linear momentum will not be conserved unless the field equations are solved simultaneously with the hydrodynamic equations.

### 2.4.1 SPH interpolation and density estimate

We introduce here a suitable definition of the SPH estimate for the baryon number density. As discussed in Section 2.3.1, the quantity  $N^*$  defined in Eq. (2.3.9) is a convenient numerical variable for doing this since the continuity equation written in terms of it acquires a simple form without the source term that appeared in Eq. (2.3.8).

In the SPH method, the density and other fluid properties are calculated by interpolation over a set of SPH particles. As mentioned in Section 1.4, this is done via a weighted sum over the SPH particles in the vicinity of the point of interest. This procedure is referred to as smoothing and is achieved by introducing a window or kernel function  $W(\|\vec{r} - \vec{r}'\|, h)$ , that weights the relative contribution of each neighbouring particle located at  $\vec{r}' = (x'^i)$  to the target point at  $\vec{r} = (x^i)$  as a function of the distance between them  $\|\vec{r} - \vec{r}'\|$ . The parameter  $h$  is called the smoothing length and it characterises the, typically compact, spatial support of the kernel function. The value of a quantity calculated via the smoothing procedure is called its SPH interpolation value or kernel estimate. The error associated with this procedure will in general depend on the particular kernel function that is being used, but also on the relative degree of order of the SPH particles. Further discussion about how to determine the degree of accuracy associated with a particular choice of kernel estimate can be found in, e.g. Monaghan (2005).

Various approaches have been proposed for introducing a kernel estimate in the relativistic context (see e.g. Laguna et al., 1993; Kheifets et al., 1990). However, the specific way in which this is done in practice has turned out to be a crucial factor that limited the performance and stability of previous relativistic implementations of SPH (see e.g. Siegler & Riffert, 2000; Rosswog, 2009, for a discussion). Here we follow Siegler & Riffert (2000); Monaghan & Price (2001); Rosswog (2010b) and introduce a ‘computing’ frame which is taken to be locally flat; this frame is then used to compute all of the kernel estimates involved in the SPH method. There are several advantages of defining the smoothing procedure in this way: it simplifies some of the calculations; it allows for the use of any kernel that is used in non-relativistic SPH; but, more importantly, it enables one to avoid previous pitfalls that had limited earlier implementations in which only mildly relativistic shocks could be treated without the appearance of numerical instabilities. For instance, using this prescription in the ultra-relativistic wall shock test presented by Rosswog (2010a), a strong shock with a Lorentz factor as high as  $\Gamma = 50000$  was correctly captured. Nevertheless, this choice comes at the price that the quantities estimated using the computing frame do not correspond to the physical quantities which, as we shall see in the following, are required in the evaluation of the equations of motion. This means that in practice, after every time step, an additional procedure is needed for

recovering the physical variables in terms of the numerical variables. In Section 2.4.4 below we introduce a scheme for such a recovery strategy in the general relativistic case.

With this choice for calculating kernel estimates in a locally flat reference frame, we can then define the interpolated value of a fluid quantity  $f$  as

$$f(\vec{r}^*) = \int f(\vec{r}) W(\|\vec{r} - \vec{r}'\|_f, h) dV' + O(h^2), \quad (2.4.1)$$

where

$$\|\vec{r} - \vec{r}'\|_f = \sqrt{\delta_{ij}(x^i - x'^i)(x^j - x'^j)} \quad (2.4.2)$$

is the coordinate distance in a flat spacetime. We have denoted this explicitly with the suffix ‘f’ to distinguish it from the physical distance calculated using the spatial metric  $\gamma_{ij}$  as defined in Eq. (2.2.2). A kernel function suitable for the SPH method should satisfy the following conditions

- It should be spherically symmetric (already implicit in Eq. (2.4.1), where we wrote it as depending only on the absolute value of the distance  $\|\vec{r} - \vec{r}'\|_f$ ). This is a key factor in guaranteeing the conservative features of the final set of evolution equations.
- It should be differentiable at least once and its derivative should be continuous.
- It should be normalised as

$$\int W(\|\vec{r} - \vec{r}'\|_f, h) dV' = 1. \quad (2.4.3)$$

- In the limit of a vanishing smoothing length,  $W$  should reduce to the delta function, i.e.

$$\lim_{h \rightarrow 0} W(\|\vec{r} - \vec{r}'\|_f, h) = \delta(\|\vec{r} - \vec{r}'\|_f). \quad (2.4.4)$$

Several different kernels have been implemented in the non-relativistic SPH method. They differ from each other in the accuracy of the interpolated values as well as in their robustness against known pathological effects such as the so-called tensile instability which leads to the pairing of SPH particles in the presence of shocks (see e.g. Price, 2004). As mentioned before, due to our choice of calculating the kernel interpolation in a locally flat reference frame (computing frame), we can use here any suitable kernel used in non-relativistic SPH. For a discussion of the performance of different kernels in standard SPH see, e.g. Cabezón et al. (2008), while a detailed comparison of the use of various kernels for special relativistic tests can be found in Rosswog (2010a).

The next step in the SPH method is to substitute the integration in Eq. (2.4.1) by a finite summation over the interpolation points. For this, we note that in standard SPH each particle carries a fixed mass  $m$ , but given that here we are using specific quantities, we shall take each SPH particle to represent a fixed number of baryons  $\nu$ . Denoting by  $m_0$  the average baryonic rest mass, we have that these two quantities are simply related

by  $m = m_0 \nu$ . It is clear that the total number of baryons enclosed within a differential volume element  $dV$  is an invariant quantity given by

$$\nu = N^* dV = \Gamma n \sqrt{\gamma} dV. \quad (2.4.5)$$

We can use this expression to estimate a finite volume element as  $\Delta V \simeq \nu/N^*$  and then discretise Eq. (2.4.1) as

$$f_a = f(\vec{r}_a) \simeq \sum_b \frac{\nu_b f_b}{N_b^*} W(r_{ab}, h_a), \quad (2.4.6)$$

where we have used the short-hand notation  $r_{ab} = \|\vec{r}_a - \vec{r}_b\|_f$  and the summation extends over all of the SPH particles contained within the compact support of  $W$ .

From Eq. (2.4.6) we see that, in particular, the baryon number density in the computing frame can be calculated as

$$N_a^* = \sum_b \nu_b W(r_{ab}, h_a). \quad (2.4.7)$$

Note that calculating the baryon number density in this way together with Eq. (2.4.3) automatically ensures that the total number of baryons is conserved since

$$\int N^*(\vec{r}) dV = \sum_b \nu_b = \text{const.} \quad (2.4.8)$$

In other words, just as in standard SPH, there is no need to evolve the continuity equation to recover the density value. However, in order to get full adaptivity, the smoothing length  $h_a$  in Eq. (2.4.7) should vary in such a way that the number of neighbours of each particle remains approximately constant, i.e. the resolution of the method should adapt to the local baryon number density. There have been many different implementations for adapting  $h_a$  but here we follow Gingold & Monaghan (1982) and adapt  $h_a$  according to

$$h_a = \eta \left( \frac{\nu_a}{N_a^*} \right)^{1/3}, \quad (2.4.9)$$

where  $\eta$  is a dimensionless parameter which specifies the extent of the compact support of the kernel as a function of the average particle spacing. For simulations in 3D, it is typically taken in the range  $\eta \in (1.2, 1.5)$  (see e.g. Price, 2012). Note that the present scheme for varying the smoothing length requires an iteration between Eqs. (2.4.7) and (2.4.9) in order to reach consistency, since  $N_a^*$  and  $h_a$  are mutually dependent quantities. As discussed by Price & Monaghan (2007), these equations can be solved self-consistently by using a root-finding algorithm such as the Newton-Raphson method.

It is useful for us at this point to calculate appropriate expressions for the spatial gradient and the time derivative of  $N^*$  as given by Eq. (2.4.7) since they are used several

times in the following sections. In order to do so, first we need to compute  $dr_{ab}/dt$  and  $\partial r_{ab}/\partial x_c^i$ . From Eq. (2.4.2) we have

$$\begin{aligned}\frac{dr_{ab}}{dt} &= \frac{1}{2r_{ab}} \frac{d(\delta_{ij} x_{ab}^i x_{ab}^j)}{dt} \\ &= \frac{\delta_{ij} x_{ab}^i}{r_{ab}} \left( \frac{dx_a^j}{dt} - \frac{dx_b^j}{dt} \right) \\ &= (\hat{r}_j)_{ab} v_{ab}^j\end{aligned}\tag{2.4.10}$$

where  $v_{ab}^i = v_a^i - v_b^i$  and  $\hat{r}_{ab}^i = x_{ab}^i/r_{ab}$  is a unit vector in the direction joining the particles  $a$  and  $b$ . On the other hand, its gradient is calculated as

$$\begin{aligned}\frac{\partial r_{ab}}{\partial x_c^i} &= \frac{\delta_{jk} x_{ab}^j}{r_{ab}} \left( \frac{\partial x_a^k}{\partial x_c^i} - \frac{\partial x_b^k}{\partial x_c^i} \right) \\ &= (\hat{r}_k)_{ab} (\delta_i^k \delta_{ac} - \delta_i^k \delta_{bc}) \\ &= (\hat{r}_i)_{ab} (\delta_{ac} - \delta_{bc}).\end{aligned}\tag{2.4.11}$$

Adopting the short-hand notation  $W_{ab} = W(r_{ab}, h_a)$ , from Eq. (2.4.11) we get the following expression for the gradient of  $W_{ab}$

$$\frac{\partial W_{ab}}{\partial x_c^i} = \frac{\partial W_{ab}}{\partial r_{ab}} \frac{\partial r_{ab}}{\partial x_c^i} = \frac{\partial W_{ab}}{\partial r_{ab}} (\hat{r}_i)_{ab} (\delta_{ac} - \delta_{bc}),\tag{2.4.12}$$

from where we get the important identity

$$\frac{\partial W_{ab}}{\partial x_a^i} = -\frac{\partial W_{ab}}{\partial x_b^i},\tag{2.4.13}$$

which guarantees a symmetric interaction between pairs of SPH particles.

Using Eqs. (2.4.7) and (2.4.12), we calculate the gradient of  $N_a^*$  as

$$\frac{\partial N_a^*}{\partial x_c^i} = \sum_b \nu_b \frac{\partial W_{ab}}{\partial r_{ab}} (\hat{r}_i)_{ab} (\delta_{ac} - \delta_{bc}),\tag{2.4.14}$$

while from Eq. (2.4.10) its time derivative is given by

$$\begin{aligned}\frac{dN_a^*}{dt} &= \sum_b \nu_b \left[ \frac{\partial W_{ab}(h_a)}{\partial r_{ab}} \frac{dr_{ab}}{dt} + \frac{\partial W_{ab}(h_a)}{\partial h_a} \frac{dh_a}{dt} \right] \\ &= \sum_b \nu_b v_{ab}^j (\hat{r}_j)_{ab} \frac{\partial W_{ab}}{\partial r_{ab}} + \sum_b \nu_b \frac{\partial W_{ab}(h_a)}{\partial h_a} \frac{\partial h_a}{\partial N_a^*} \frac{dN_a^*}{dt} \\ &= \sum_b \nu_b v_{ab}^j (\hat{r}_j)_{ab} \frac{\partial W_{ab}}{\partial r_{ab}} + \frac{\partial h_a}{\partial N_a^*} \frac{dN_a^*}{dt} \sum_b \nu_b \frac{\partial W_{ab}(h_a)}{\partial h_a}.\end{aligned}\tag{2.4.15}$$

Collecting the terms with  $dN_a^*/dt$  we get

$$\frac{dN_a^*}{dt} = \frac{1}{\Omega_a} \sum_b \nu_b v_{ab}^j (\hat{r}_j)_{ab} \frac{\partial W_{ab}}{\partial r_{ab}},\tag{2.4.16}$$

where

$$\Omega_a = 1 - \frac{\partial h_a}{\partial N_a^*} \sum_b \nu_b \frac{\partial W_{ab}(h_a)}{\partial h_a}, \quad (2.4.17)$$

is the so-called ‘grad- $h$ ’ term that accounts, in a self-consistent way, for a varying smoothing length.

The next step in the strategy followed by Rosswog (2010b) is to introduce a suitable Lagrangian and use it as a guide for defining the numerical three-momentum and energy that are going to be dynamically evolved. In the next section we start by considering the former.

### 2.4.2 Canonical momentum

A convenient Lagrangian of a perfect fluid in general relativity is given by (e.g. Fock, 1964)

$$\begin{aligned} L &= - \int T^{\mu\nu} U_\mu U_\nu \sqrt{-g} dV \\ &= - \int \alpha n (1 + u) \sqrt{\gamma} dV, \end{aligned} \quad (2.4.18)$$

where we have used Eq. (2.2.5) and the definition of  $T^{\mu\nu}$  for a perfect fluid given in Eq. (2.1.12). If we now use Eq. (2.4.5) to estimate a differential volume element as  $dV \simeq \nu / (\sqrt{\gamma} \Gamma n)$  we can approximate the Lagrangian in Eq. (2.4.18) by the following discrete sum

$$L = - \int \alpha n (1 + u) \sqrt{\gamma} dV \simeq - \sum_b \left[ \frac{\alpha \nu}{\Gamma} (1 + u) \right]_b. \quad (2.4.19)$$

As is well-known, the result of varying the action associated with  $L$ , while keeping the spacetime metric fixed, is the Euler-Lagrange equations given by

$$\frac{d}{dt} \left( \frac{\partial L}{\partial v^i} \right) - \frac{\partial L}{\partial x^i} = 0. \quad (2.4.20)$$

The canonical momentum  $(p_i)_a$  of a particle  $a$  is defined in terms of the Lagrangian as

$$(p_i)_a \equiv \frac{\partial L}{\partial v_a^i}. \quad (2.4.21)$$

Substituting the discretised Lagrangian in Eq. (2.4.19) into Eq. (2.4.21) we get

$$(p_i)_a = \frac{\partial L}{\partial v_a^i} = - \sum_b \alpha_b \nu_b \left[ - \frac{1 + u_b}{\Gamma_b^2} \frac{\partial \Gamma_b}{\partial v_a^i} + \frac{1}{\Gamma_b} \frac{\partial u_b}{\partial v_a^i} \right]. \quad (2.4.22)$$

From the definition of  $\Gamma$  in Eq. (2.2.17), we calculate the partial derivative in the first

term of Eq. (2.4.22) as

$$\begin{aligned}
\frac{\partial \Gamma_b}{\partial v_a^i} &= \left( \frac{\Gamma^3 \gamma_{jk}}{2} \right)_b \frac{\partial (V_b^j V_b^k)}{\partial v_a^i} \\
&= \left( \frac{\Gamma^3 \gamma_{jk}}{2} \right)_b \left[ 2 V_b^j \frac{\partial}{\partial v_a^i} \left( \frac{v^k + \beta^k}{\alpha} \right)_b \right] \\
&= \left( \frac{\Gamma^3 \gamma_{jk} V^j}{\alpha} \right)_b \frac{\partial v_b^k}{\partial v_a^i} = \left( \frac{\Gamma^3 V_k}{\alpha} \right)_b \delta_i^k \delta_{ab} \\
&= \left( \frac{\Gamma^3 V_i}{\alpha} \right)_b \delta_{ab},
\end{aligned} \tag{2.4.23}$$

while, using the first law of thermodynamics for a perfect fluid as given in Eq. (2.1.13), we can calculate the partial derivative of  $u_b$  as

$$\begin{aligned}
\frac{\partial u_b}{\partial v_a^i} &= \frac{\partial u_b}{\partial n_b} \Big|_s \frac{\partial n_b}{\partial v_a^i} = \frac{P_b}{n_b^2} \frac{\partial n_b}{\partial v_a^i} = \frac{P_b}{n_b^2} \frac{\partial}{\partial v_a^i} \left( \frac{N^*}{\sqrt{\gamma} \Gamma} \right)_b \\
&= \left( \frac{P N^*}{\sqrt{\gamma} n^2} \right)_b \frac{\partial (1/\Gamma_b)}{\partial v_a^i} = - \left( \frac{P \Gamma^2 V_i}{\alpha n} \right)_b \delta_{ab},
\end{aligned} \tag{2.4.24}$$

where we have used the relation between baryon number densities given in Eq. (2.3.9). Bringing together the results in Eqs. (2.4.22)-(2.4.24), we get

$$\begin{aligned}
(p_i)_a &= - \sum_b \nu_b \left\{ - [(1+u)\Gamma V_i]_b - \left( \frac{P \Gamma V_i}{n} \right)_b \right\} \delta_{ab} \\
&= [\nu(1+u+P/n)\Gamma V_i]_a = (\nu \omega \Gamma V_i)_a,
\end{aligned} \tag{2.4.25}$$

where we have used the Kronecker delta symbol to get rid of the summation over nearest neighbours. Note that the canonical momentum per baryon given as

$$\vec{S}_a = (\vec{p}/\nu)_a = (\omega \Gamma \vec{V})_a, \tag{2.4.26}$$

had already been introduced in Eq. (2.3.3), where we defined it as the three-momentum measured in the LEO reference frame.

Since in the present formulation the baryon number is a fixed quantity, it is convenient for us to use  $\vec{S}_a$  as numerical variable. According to the Euler-Lagrange equations in Eq. (2.4.20), the time evolution of  $\vec{S}_a$  is given by

$$\frac{d(S_i)_a}{dt} = \frac{1}{\nu_a} \frac{\partial L}{\partial x_a^i} = - \sum_b \frac{\nu_b}{\nu_a} \left[ \frac{1+u_b}{\Gamma_b} \frac{\partial \alpha_b}{\partial x_a^i} \delta_{ab} - \frac{\alpha_b (1+u_b)}{\Gamma_b^2} \frac{\partial \Gamma_b}{\partial x_a^i} + \frac{\alpha_b}{\Gamma_b} \frac{\partial u_b}{\partial x_a^i} \right]. \tag{2.4.27}$$

From the definition of  $\Gamma$  in Eq. (2.2.17), we calculate its gradient as

$$\begin{aligned}
\frac{\partial \Gamma_b}{\partial x_a^i} &= \frac{\Gamma_b^3}{2} \frac{\partial (\gamma_{jk} V^j V^k)_b}{\partial x_a^i} \\
&= \frac{\Gamma_b^3}{2} \left[ 2 (\gamma_{jk} V^j)_b \frac{\partial}{\partial x_a^i} \left( \frac{v^k + \beta^k}{\alpha} \right)_b + V_b^j V_b^k \frac{\partial (\gamma_{jk})_b}{\partial x_a^i} \delta_{ab} \right] \\
&= \Gamma_b^3 \left[ - \left( \frac{V_j V^j}{\alpha} \right)_b \frac{\partial \alpha_b}{\partial x_a^i} + \left( \frac{V_j}{\alpha} \right)_b \frac{\partial \beta_b^j}{\partial x_a^i} + \frac{V_b^j V_b^k}{2} \frac{\partial (\gamma_{jk})_b}{\partial x_a^i} \right] \delta_{ab}.
\end{aligned} \tag{2.4.28}$$

On the other hand, using once again the first law of thermodynamics in Eq. (2.1.13), we calculate the gradient of the specific internal energy as

$$\begin{aligned} \frac{\partial u_b}{\partial x_a^i} &= \frac{\partial u_b}{\partial n_b} \bigg|_s \frac{\partial n_b}{\partial x_a^i} = \frac{P_b}{n_b^2} \frac{\partial}{\partial x_a^i} \left( \frac{N^*}{\sqrt{\gamma} \Gamma} \right)_b \\ &= \frac{P_b}{n_b^2} \left[ \frac{1}{\sqrt{\gamma_b} \Gamma_b} \frac{\partial N_b^*}{\partial x_a^i} - \frac{N_b^*}{\sqrt{\gamma_b} \Gamma_b^2} \frac{\partial \Gamma_b}{\partial x_a^i} - \frac{N_b^*}{2 \gamma_b^{3/2} \Gamma_b} \frac{\partial \gamma_b}{\partial x_a^i} \right]. \end{aligned} \quad (2.4.29)$$

We have already calculated the gradients of  $N_b^*$  and  $\Gamma_b$  in Eqs. (2.4.14) and (2.4.28), respectively, while by using Eq. (2.2.6) we can calculate the gradient of  $\gamma_b$  as

$$\frac{\partial \gamma_b}{\partial x_a^i} = (\gamma \gamma^{jk})_b \frac{\partial (\gamma_{jk})_b}{\partial x_a^i} \delta_{ab}. \quad (2.4.30)$$

Substituting Eqs. (2.4.14) and (2.4.28)-(2.4.30) into Eq. (2.4.27) results in

$$\begin{aligned} \frac{d(S_i)_a}{dt} &= - \sum_b \frac{\nu_b}{\nu_a} \left[ \left( \frac{\alpha P}{\sqrt{\gamma} \Gamma^2 n^2} \right)_b \frac{\partial N_b^*}{\partial x_a^i} + \alpha_b \left( 1 + u + \frac{P}{n} \right)_b \frac{\partial (1/\Gamma_b)}{\partial x_a^i} \right. \\ &\quad \left. + \frac{1 + u_b}{\Gamma_b} \frac{\partial \alpha_b}{\partial x_a^i} \delta_{ab} - \left( \frac{\alpha P \gamma^{jk}}{2 \Gamma n} \right)_b \frac{\partial (\gamma_{jk})_b}{\partial x_a^i} \delta_{ab} \right] \\ &= - \sum_b \frac{\nu_b}{\nu_a} \left[ \left( \frac{\alpha \sqrt{\gamma} P}{\Omega N^{*2}} \right)_b \sum_c \frac{\nu_c}{\Omega_b} \frac{\partial W_{bc}(h_b)}{\partial x_b^i} (\delta_{ba} - \delta_{ca}) \right] \\ &\quad + \sum_b \frac{\nu_b}{\nu_a} \left\{ \omega_b \Gamma_b \left[ -(V_j V^j)_b \frac{\partial \alpha_b}{\partial x_a^k} + (V_j)_b \frac{\partial \beta_b^j}{\partial x_a^k} + \frac{\alpha_b V_b^i V_b^j}{2} \frac{\partial (\gamma_{ij})_b}{\partial x_a^k} \right] + \right. \\ &\quad \left. - \frac{1 + u_b}{\Gamma_b} \frac{\partial \alpha_b}{\partial x_a^i} + \left( \frac{\alpha P \gamma^{jk}}{2 \Gamma n} \right)_b \frac{\partial (\gamma_{jk})_b}{\partial x_a^i} \right\} \delta_{ab} \\ &= - \sum_b \nu_b \left[ \left( \frac{\alpha \sqrt{\gamma} P}{\Omega N^{*2}} \right)_a \frac{\partial W_{ab}(h_a)}{\partial x_a^i} + \left( \frac{\alpha \sqrt{\gamma} P}{\Omega N^{*2}} \right)_b \frac{\partial W_{ab}(h_b)}{\partial x_a^i} \right] \\ &\quad - \left[ \left( \Gamma \omega - \frac{\sqrt{\gamma} P}{N^*} \right) \frac{\partial \alpha}{\partial x^i} - \omega \Gamma V_j \frac{\partial \beta^j}{\partial x^i} \right. \\ &\quad \left. - \frac{\alpha}{2} \left( \omega \Gamma V^i V^j + \frac{\sqrt{\gamma} P \gamma^{jk}}{N^*} \right) \frac{\partial (\gamma_{jk})}{\partial x^i} \right]_a, \end{aligned} \quad (2.4.31)$$

where in the last step we have used the Kronecker delta symbols to get rid of one summation over nearest neighbours, then we have relabelled dummy indices ( $c \rightarrow b$ ), and finally used

$$\begin{aligned} \frac{\partial W_{ab}}{\partial x_b^i} &= - \frac{\partial W_{ab}}{\partial x_a^i}, \\ 1 + u &= \omega - P/n, \\ V_j V^j &= 1 - 1/\Gamma^2. \end{aligned}$$

Using the definitions in Eqs. (2.3.1)-(2.3.4) we can rewrite Eq. (2.4.31) as

$$\begin{aligned} \frac{d(S_i)_a}{dt} &= - \sum_b \nu_b \left[ \left( \frac{\alpha\sqrt{\gamma}P}{\Omega N^{*2}} \right)_a \frac{\partial W_{ab}(h_a)}{\partial x_a^i} + \left( \frac{\alpha\sqrt{\gamma}P}{\Omega N^{*2}} \right)_b \frac{\partial W_{ab}(h_b)}{\partial x_a^i} \right] \\ &\quad - \left[ \frac{\sqrt{\gamma}\epsilon}{N^*} \frac{\partial \alpha}{\partial x^i} - S_j \frac{\partial \beta^j}{\partial x^i} - \frac{\alpha\sqrt{\gamma}\sigma^{jk}}{2N^*} \frac{\partial \gamma_{jk}}{\partial x^i} \right]_a \\ &\equiv \left[ \frac{d(S_i)_a}{dt} \right]_h + \left[ \frac{d(S_i)_a}{dt} \right]_g, \end{aligned} \quad (2.4.32)$$

where we have split  $dS_i/dt$  in two parts: a first one, that we shall refer to as the h-term (or ‘hydro’ term), that involves an SPH kernel estimate and that dictates how the neighbours of the target particle  $a$  contribute to the total force acting over it; and a second one, that we shall refer to as the g-term (or ‘gravity’ term), that depends only on the position of the target particle  $a$ , and that can be interpreted as an effective contribution from the curvature of the spacetime to the total force acting on the particle  $a$ .

Let us now compare the result in Eq. (2.4.32) with the equation of motion for  $\vec{S}$  that was obtained before from the conservation of the stress-energy tensor in Eq. (2.3.20). The g-term in Eq. (2.4.32) is exactly the same as the last three terms on the right hand side of Eq. (2.3.20). Additionally, it is apparent that the h-term represents the SPH estimate of the gradient of the pressure that appears in the first term on the right hand side of Eq. (2.3.20). In order to see this, let us forget for the moment about the varying smoothing length (i.e. considering temporarily the case of  $h = \text{const.}$ ,  $\Omega = 1$ ), and use the following standard result of SPH for estimating the gradient of a scalar  $f$  as (see e.g. Monaghan, 2005)

$$\frac{\partial f_a}{\partial x_a^i} = \sum_b \frac{\nu_b f_b}{N_b^*} \frac{\partial W_{ab}}{\partial x_a^i}, \quad (2.4.33)$$

in such a way that

$$\begin{aligned} \left[ \frac{d(S_i)_a}{dt} \right]_h &= - \left( \frac{\alpha\sqrt{\gamma}P}{N^{*2}} \right)_a \sum_b \nu_b \frac{\partial W_{ab}}{\partial x_a^i} - \sum_b \nu_b \left[ \left( \frac{\alpha\sqrt{\gamma}P}{N^{*2}} \right)_b \frac{\partial W_{ab}}{\partial x_a^i} \right] \\ &= - \left[ \frac{\alpha\sqrt{\gamma}P}{N^{*2}} \frac{\partial N^*}{\partial x^i} + \frac{\partial}{\partial x^i} \left( \frac{\alpha\sqrt{\gamma}P}{N^*} \right) \right]_a = - \left[ \frac{1}{N^*} \frac{\partial(\alpha\sqrt{\gamma}P)}{\partial x^i} \right]_a, \end{aligned} \quad (2.4.34)$$

which exactly recapitulates the first term on the right hand side of Eq. (2.3.20). We also note that the result in Eq. (2.4.32) is exactly the same as the one given by Rosswog (2010b) with the only difference that here  $dS/dt$  is written in terms of the 3+1 formalism.

### 2.4.3 Canonical energy

Since the discretised Lagrangian given in Eq. (2.4.19) does not depend explicitly on the coordinate time  $t$ , we know that the associated total canonical energy  $E$  is a conserved

quantity, i.e.

$$\begin{aligned} E &= \sum_b \frac{\partial L}{\partial v_b^i} v_b^i - L \\ &= \sum_b \nu_b \left[ S_i v^i + \frac{\alpha(1+u)}{\Gamma} \right]_b = \sum_b \nu_b e_b, \end{aligned} \quad (2.4.35)$$

where  $e = S_i v^i + \alpha(1+u)/\Gamma$  is the canonical energy per baryon carried by each SPH particle. This quantity had been introduced before in Eq. (2.3.23), when we discussed the time component of the stress-energy conservation equation. Following Rosswog (2010b), we take  $e$  as a numerical variable. Its evolution equation is given by

$$\frac{de_a}{dt} = \left[ v^i \frac{dS_i}{dt} + S_i \frac{dv^i}{dt} + \frac{1+u}{\Gamma} \frac{d\alpha}{dt} + \frac{\alpha}{\Gamma} \frac{du}{dt} - \frac{\alpha(1+u)}{\Gamma^2} \frac{d\Gamma}{dt} \right]_a. \quad (2.4.36)$$

Using again the first law of thermodynamics in Eq. (2.1.13), the time derivative of the specific internal energy  $u_a$  is given by

$$\begin{aligned} \frac{du_a}{dt} &= \frac{P_a}{n_a^2} \frac{d}{dt} \left( \frac{N^*}{\sqrt{\gamma}\Gamma} \right)_a \\ &= \frac{P_a}{n_a^2} \left[ \frac{1}{\sqrt{\gamma}\Gamma} \frac{dN^*}{dt} - \frac{N^*}{\sqrt{\gamma}\Gamma^2} \frac{d\Gamma}{dt} - \frac{N^*}{2\gamma^{3/2}\Gamma} \frac{d\gamma}{dt} \right]_a, \end{aligned} \quad (2.4.37)$$

and substituting this result back into Eq. (2.4.36) leads to

$$\begin{aligned} \frac{de_a}{dt} &= \left[ v^i \frac{dS_i}{dt} + S_i \frac{dv^i}{dt} + \frac{1+u}{\Gamma} \frac{d\alpha}{dt} \right. \\ &\quad \left. + \frac{\alpha\sqrt{\gamma}P}{N^{*2}} \frac{dN^*}{dt} - \frac{\alpha\omega}{\Gamma^2} \frac{d\Gamma}{dt} - \frac{\alpha P}{2\sqrt{\gamma}N^*} \frac{d\gamma}{dt} \right]_a. \end{aligned} \quad (2.4.38)$$

If we use the expression for  $dS_i/dt$  found in Eq. (2.4.32), we can rewrite Eq. (2.4.38) as

$$\begin{aligned} \frac{de_a}{dt} &= \left[ v^i \left( \frac{dS_i}{dt} \right)_h + \frac{\alpha\sqrt{\gamma}P}{N^{*2}} \frac{dN^*}{dt} \right]_a \\ &\quad + \left[ v^i \left( \frac{dS_i}{dt} \right)_g + S_i \frac{dv^i}{dt} + \frac{1+u}{\Gamma} \frac{d\alpha}{dt} - \frac{\alpha\omega}{\Gamma^2} \frac{d\Gamma}{dt} - \frac{\alpha P}{2\sqrt{\gamma}N^*} \frac{d\gamma}{dt} \right]_a \\ &\equiv \left( \frac{de_a}{dt} \right)_h + \left( \frac{de_a}{dt} \right)_g, \end{aligned} \quad (2.4.39)$$

where, similarly as in the canonical momentum case, we have split  $de/dt$  into an h-term that involves an SPH interpolation, and a g-term that depends only on the position of the target particle. Now we consider each term separately. Substituting  $dN^*/dt$  from

Eq. (2.4.16) we get that the h-term is given by

$$\begin{aligned}
\left(\frac{de_a}{dt}\right)_h &= \left[ v^i \left(\frac{dS_i}{dt}\right)_h + \frac{\alpha\sqrt{\gamma}P}{N^{*2}} \frac{dN^*}{dt} \right]_a \\
&= - \sum_b \nu_b \left[ \left(\frac{\alpha\sqrt{\gamma}P}{\Omega N^{*2}}\right)_a \frac{\partial W_{ab}(h_a)}{\partial x_a^i} + \left(\frac{\alpha\sqrt{\gamma}P}{\Omega N^{*2}}\right)_b \frac{\partial W_{ab}(h_b)}{\partial x_a^i} \right] v_a^i \\
&\quad + \left(\frac{\alpha\sqrt{\gamma}P}{\Omega N^{*2}}\right)_a \sum_b \frac{\nu_b}{\Omega_b} (v_a^i - v_b^i) \frac{\partial W_{ab}(h_b)}{\partial x_a^i} \\
&= - \sum_b \nu_b \left[ \left(\frac{\alpha\sqrt{\gamma}P}{\Omega N^{*2}}\right)_a v_b^i \frac{\partial W_{ab}(h_a)}{\partial x_a^i} + \left(\frac{\alpha\sqrt{\gamma}P}{\Omega N^{*2}}\right)_b v_a^i \frac{\partial W_{ab}(h_b)}{\partial x_a^i} \right].
\end{aligned} \tag{2.4.40}$$

On the other hand, for calculating the g-term we need the derivatives  $d\Gamma/dt$  and  $d\gamma/dt$ . From the definition of the Lorentz factor in Eq. (2.2.17), we calculate its time derivative as

$$\frac{d\Gamma_a}{dt} = \Gamma_a^3 \left[ -\frac{V_j V^j}{\alpha} \frac{d\alpha}{dt} + \frac{V_j}{\alpha} \left( \frac{dv^j}{dt} + \frac{d\beta^j}{dt} \right) + \frac{V^j V^k}{2} \frac{d\gamma_{jk}}{dt} \right]_a, \tag{2.4.41}$$

while we use Eq. (2.2.6) for calculating the time derivative of the determinant  $\gamma$  as

$$\frac{d\gamma_a}{dt} = (\gamma \gamma^{jk})_a \frac{d(\gamma_{jk})_a}{dt}. \tag{2.4.42}$$

Substituting Eqs. (2.4.41) and (2.4.42) back into Eq. (2.4.39), the g-term transforms as

$$\begin{aligned}
\left(\frac{de_a}{dt}\right)_g &= \left[ v^i \left(\frac{dS_i}{dt}\right)_g + S_i \frac{dv^i}{dt} + \frac{1+u}{\Gamma} \frac{d\alpha}{dt} - \frac{\alpha\omega}{\Gamma^2} \frac{d\Gamma}{dt} - \frac{\alpha P}{2\sqrt{\gamma}N^*} \frac{d\gamma}{dt} \right]_a \\
&= \left[ - \left( \Gamma\omega - \frac{\sqrt{\gamma}P}{N^*} \right) \frac{\partial\alpha}{\partial x^i} v_a^i + \omega \Gamma V_j \frac{\partial\beta^j}{\partial x^i} v_a^i \right. \\
&\quad + \frac{\alpha}{2} \left( \omega \Gamma V^j V^k + \frac{\sqrt{\gamma}P\gamma^{jk}}{N^*} \right) \frac{\partial\gamma_{jk}}{\partial x^i} v_a^i + S_i \frac{dv^i}{dt} + \frac{1+u}{\Gamma} \frac{d\alpha}{dt} \\
&\quad - \omega \Gamma \left( -V_j V^j \frac{d\alpha}{dt} + V_j \frac{dv^j}{dt} + V_j \frac{d\beta^j}{dt} + \frac{\alpha V^j V^k}{2} \frac{d\gamma_{jk}}{dt} \right) \\
&\quad \left. - \frac{\alpha\sqrt{\gamma}P\gamma^{jk}}{2N^*} \frac{d\gamma_{jk}}{dt} \right]_a \\
&= \left[ \left( \Gamma\omega - \frac{\sqrt{\gamma}P}{N^*} \right) \left( \frac{d\alpha}{dt} - v_a^i \frac{\partial\alpha}{\partial x^i} \right) - \omega \Gamma V_j \left( \frac{d\beta^j}{dt} - v_a^i \frac{\partial\beta^j}{\partial x^i} \right) \right. \\
&\quad \left. - \frac{\alpha}{2} \left( \omega \Gamma V^j V^k + \frac{\sqrt{\gamma}P\gamma^{jk}}{N^*} \right) \left( \frac{d\gamma_{jk}}{dt} - v_a^i \frac{\partial\gamma_{jk}}{\partial x^i} \right) \right]_a \\
&= \left[ \frac{\sqrt{\gamma}\epsilon}{N^*} \frac{\partial\alpha}{\partial t} - S_j \frac{\partial\beta^j}{\partial t} - \frac{\alpha\sqrt{\gamma}\sigma^{jk}}{2N^*} \frac{\partial\gamma_{jk}}{\partial t} \right]_a,
\end{aligned} \tag{2.4.43}$$

where for the last step we have used Eqs. (2.3.1)-(2.3.4) and (2.3.7). Bringing together the results from Eqs. (2.4.40) and (2.4.43), we finally get

$$\begin{aligned} \frac{de_a}{dt} = & - \sum_b \nu_b \left[ \left( \frac{\alpha\sqrt{\gamma}P}{\Omega N^{*2}} \right)_a v_b^i \frac{\partial W_{ab}(h_a)}{\partial x_a^i} + \left( \frac{\alpha\sqrt{\gamma}P}{\Omega N^{*2}} \right)_b v_a^i \frac{\partial W_{ab}(h_b)}{\partial x_a^i} \right] \\ & + \left[ \frac{\sqrt{\gamma}\epsilon}{N^*} \frac{\partial \alpha}{\partial t} - S_j \frac{\partial \beta^j}{\partial t} - \frac{\alpha\sqrt{\gamma}\sigma^{jk}}{2N^*} \frac{\partial \gamma_{jk}}{\partial t} \right]_a. \end{aligned} \quad (2.4.44)$$

This expressions is the same as that given in Rosswog (2010b) but rewritten in terms of 3+1 quantities. Finally, we can compare this result with Eq. (2.3.25), the evolution equation for  $de/dt$  that we had found before. Here we see that the last three terms on the right hand side of the two equations coincide. Regarding the first term: ignoring the ‘grad- $h$ ’ correction terms, we can use the following expression for estimating the divergence of a vector in standard SPH (see e.g Monaghan, 2005):

$$\frac{\partial f_a^i}{\partial x_a^i} = \sum_b \frac{\nu_b}{N_b^*} f_b^i \frac{\partial W_{ab}}{\partial x_a^i}, \quad (2.4.45)$$

and see that

$$\begin{aligned} \left( \frac{de_a}{dt} \right)_h &= - \sum_b \nu_b \left[ \left( \frac{\alpha\sqrt{\gamma}P}{N^{*2}} \right)_a v_b^i \frac{\partial W_{ab}}{\partial x_a^i} + \left( \frac{\alpha\sqrt{\gamma}P}{N^{*2}} \right)_b v_a^i \frac{\partial W_{ab}}{\partial x_a^i} \right] \\ &= - \left( \frac{\alpha\sqrt{\gamma}P}{N^{*2}} \right)_a \sum_b \nu_b v_b^i \frac{\partial W_{ab}}{\partial x_a^i} - v_a^i \sum_b \nu_b \left[ \left( \frac{\alpha\sqrt{\gamma}P}{N^{*2}} \right)_b \frac{\partial W_{ab}}{\partial x_a^i} \right] \\ &= - \left( \frac{\alpha\sqrt{\gamma}P}{N^{*2}} \right)_a \frac{\partial(N^*v^i)_a}{\partial x_a^i} - v_a^i \frac{\partial}{\partial x_a^i} \left( \frac{\alpha\sqrt{\gamma}P}{N^*} \right)_a \\ &= - \left[ \frac{1}{N^*} \frac{\partial(\alpha\sqrt{\gamma}P v^i)}{\partial x^i} \right]_a \end{aligned} \quad (2.4.46)$$

indeed corresponds to the first term on the right hand side of Eq. (2.3.25).

#### 2.4.4 Recovery of primitive variables

The SPHINCS formulation consists of five equations (one SPH interpolation and four differential equations) for evolving a set of five numerical variables ( $e$ ,  $N^*$ ,  $\vec{S}$ ) in time. However, the right hand side of the evolution equations (see Eqs. 2.4.32 and 2.4.44) involves explicitly the primitive variables ( $n$ ,  $u$ ,  $P$ ,  $\vec{v}$ ). We are then faced with the necessity of recovering the primitive variables after every time step as a function of the updated values of the numerical variables. What this means in practice is that we need

to invert the following non-linear system of equations:

$$N^* = \sqrt{\gamma} \Gamma n, \quad (2.4.47)$$

$$\vec{S} = \Gamma \omega \frac{\vec{v} + \vec{\beta}}{\alpha} = \Gamma \omega \vec{V}, \quad (2.4.48)$$

$$e = \vec{S} \cdot \vec{v} + \frac{\alpha(1+u)}{\Gamma}, \quad (2.4.49)$$

$$\Gamma = \left(1 - \vec{V} \cdot \vec{V}\right)^{-1/2}. \quad (2.4.50)$$

This can be done by using the following recovery scheme:

- i)** Use the EoS  $f(n, u, P) = 0$  to solve for the enthalpy as

$$\omega = \omega(n, P), \quad (2.4.51)$$

- ii)** Express  $n$ ,  $P$  and  $\vec{v}$  as functions of  $\omega$  and the updated numerical variables. This is easily done by using Eqs. (2.3.23) and (2.4.47)-(2.4.49), the result is

$$n(\omega) = \frac{N^*}{\sqrt{\gamma} \Gamma(\omega)} \quad (2.4.52)$$

$$P(\omega) = \frac{N^*}{\alpha \sqrt{\gamma}} \left[ \omega \Gamma(\omega) - e - \vec{S} \cdot \vec{\beta} \right], \quad (2.4.53)$$

$$\vec{v}(\omega) = \frac{\alpha \vec{S}}{\omega \Gamma(\omega)} - \vec{\beta}, \quad (2.4.54)$$

where  $\Gamma(\omega)$  can be calculated by taking the square of Eq. (2.4.48) which results in

$$\Gamma(\omega) = \sqrt{1 + \vec{S} \cdot \vec{S} / \omega^2}. \quad (2.4.55)$$

- iii)** Choose a trial value for the enthalpy  $\omega'$ . This value could be, for instance, the value of  $\omega$  at the previous time step.

- iv)** Update the values of  $n'$  and  $P'$  according to Eqs. (2.4.52) and (2.4.53).

**v)** The updated values for  $n'$  and  $P'$  will, in general, fail to satisfy the EoS in Eq. (2.4.51), i.e.  $\omega' - \omega(n', P') \neq 0$ . From this last condition, a better trial value for  $\omega'$  should be produced (e.g. using a standard root-finding algorithm) with which one repeats the procedure until a given convergence criterion is satisfied.

### 2.4.5 Geodesic motion limit

In the preceding sections, we have derived equations for the evolution of a set of SPH quantities in a general curved spacetime. In this section we consider the limit of vanishing hydrodynamic forces, i.e. the limit in which the matter content of the spacetime is composed of non-interacting particles. It is clear that in this limit the SPHINCS equations should reduce to the geodesic equations. We can effectively zero the hydrodynamic interaction between SPH particles by taking an EoS for which  $u = P = 0$ . Substituting these values into Eqs. (2.4.32) and (2.4.44) we get that the evolution equations are given by

$$\frac{dS_i}{dt} = -\frac{\sqrt{\gamma}\epsilon}{N^*} \frac{\partial\alpha}{\partial x^i} + S_j \frac{\partial\beta^j}{\partial x^i} + \frac{\alpha\sqrt{\gamma}\sigma^{jk}}{2N^*} \frac{\partial\gamma_{jk}}{\partial x^i} = \frac{\alpha\sqrt{\gamma}}{2N^*} \frac{\partial g_{\mu\nu}}{\partial x^i} T^{\mu\nu}, \quad (2.4.56)$$

$$\frac{de}{dt} = \frac{\sqrt{\gamma}\epsilon}{N^*} \frac{\partial\alpha}{\partial t} - S_j \frac{\partial\beta^j}{\partial t} - \frac{\alpha\sqrt{\gamma}\sigma^{jk}}{2N^*} \frac{\partial\gamma_{jk}}{\partial t} = -\frac{\alpha\sqrt{\gamma}}{2N^*} \frac{\partial g_{\mu\nu}}{\partial t} T^{\mu\nu}, \quad (2.4.57)$$

where we have dropped the now unnecessary particle label and used Eqs. (2.3.19) and (2.3.25). Also note that in this case the numerical variables are simply

$$S_i = \Gamma V_i = U_i, \quad (2.4.58)$$

$$e = S_i v^i + \alpha/\Gamma = \Gamma(\alpha - V_i \beta^i) = -U_0, \quad (2.4.59)$$

while

$$T^{\mu\nu} = n U^\mu U^\nu. \quad (2.4.60)$$

With the aid of Eqs. (2.4.58)-(2.4.60) we can combine Eqs. (2.4.56) and (2.4.57) into a single equation, i.e.

$$\frac{dU_\lambda}{dt} = \frac{\alpha\sqrt{\gamma}n}{2N^*} \frac{\partial g_{\mu\nu}}{\partial x^\lambda} U^\mu U^\nu = \frac{\alpha}{2\Gamma} \frac{\partial g_{\mu\nu}}{\partial x^\lambda} U^\mu U^\nu. \quad (2.4.61)$$

Using the identity  $dt = (dt/d\tau)d\tau = (\Gamma/\alpha)d\tau$ , we can rewrite Eq. (2.4.61) as

$$\frac{d(g_{\lambda\mu}U^\mu)}{d\tau} = g_{\lambda\mu} \frac{dU^\mu}{d\tau} + U^\mu \frac{dg_{\lambda\mu}}{d\tau} = \frac{1}{2} \frac{\partial g_{\mu\nu}}{\partial x^\lambda} U^\mu U^\nu. \quad (2.4.62)$$

On the other hand, using the identity  $d/d\tau = U^\mu \partial/\partial x^\mu$  and relabelling dummy indices, we have

$$U^\mu \frac{dg_{\lambda\mu}}{d\tau} = U^\mu U^\nu \frac{\partial g_{\lambda\mu}}{\partial x^\nu} = \frac{1}{2} \left( \frac{\partial g_{\lambda\mu}}{\partial x^\nu} + \frac{\partial g_{\lambda\nu}}{\partial x^\mu} \right) U^\mu U^\nu. \quad (2.4.63)$$

Using this result allows us to rewrite Eq. (2.4.62) as

$$g_{\lambda\mu} \frac{dU^\mu}{d\tau} = -\frac{1}{2} \left( \frac{\partial g_{\lambda\mu}}{\partial x^\nu} + \frac{\partial g_{\lambda\nu}}{\partial x^\mu} - \frac{\partial g_{\mu\nu}}{\partial x^\lambda} \right) U^\mu U^\nu. \quad (2.4.64)$$

Finally, using Eq. (2.1.6) and multiplying both sides of Eq. (2.4.64) by the inverse  $g^{\sigma\lambda}$  results in

$$\frac{dU^\sigma}{d\tau} = -\frac{g^{\sigma\lambda}}{2} \left( \frac{\partial g_{\lambda\sigma}}{\partial x^\nu} + \frac{\partial g_{\lambda\nu}}{\partial x^\sigma} - \frac{\partial g_{\mu\nu}}{\partial x^\lambda} \right) U^\mu U^\nu = -\Gamma_{\mu\nu}^\sigma U^\mu U^\nu, \quad (2.4.65)$$

which is indeed the geodesic equation as given in Eq. (2.1.7).

### 2.4.6 Special relativistic limit

We consider now the special relativistic limit in which the background metric is simply given by that for flat spacetime, i.e.  $g_{\mu\nu} = \text{diag}(-1, 1, 1, 1)$ . It is clear that in this case  $\alpha = 1$ ,  $\vec{\beta} = 0$  and  $\gamma_{ij} = \delta_{ij}$ , while the numerical variables are now given by

$$N^* = N = \Gamma n, \quad (2.4.66)$$

$$\vec{S} = \Gamma \omega \vec{v}, \quad (2.4.67)$$

$$e = \vec{S} \cdot \vec{v} + \frac{1+u}{\Gamma} = \Gamma \omega - \frac{P}{N}, \quad (2.4.68)$$

where  $\Gamma = (1 - \vec{v} \cdot \vec{v})^{-1/2}$ . Additionally, the evolution equations in this case simplify as

$$\frac{d(S_i)_a}{dt} = - \sum_b \nu_b \left[ \left( \frac{P}{\Omega N^2} \right)_a \frac{\partial W_{ab}(h_a)}{\partial x_a^i} + \left( \frac{P}{\Omega N^2} \right)_b \frac{\partial W_{ab}(h_b)}{\partial x_a^i} \right], \quad (2.4.69)$$

$$\frac{de_a}{dt} = - \sum_b \nu_b \left[ \left( \frac{P}{\Omega N^2} \right)_a v_b^i \frac{\partial W_{ab}(h_a)}{\partial x_a^i} + \left( \frac{P}{\Omega N^2} \right)_b v_a^i \frac{\partial W_{ab}(h_b)}{\partial x_a^i} \right], \quad (2.4.70)$$

and the

$$\Omega_a = 1 - \frac{\partial h_a}{\partial N_a} \sum_b \nu_b \frac{\partial W_{ab}(h_a)}{\partial h_a}, \quad (2.4.71)$$

This set of equations (without the ‘grad- $h$ ’ terms) was first derived by Monaghan & Price (2001), while the corrective terms were included in Rosswog (2010a) together with an artificial viscosity prescription to handle relativistic shocks. The numerical code introduced in Rosswog (2010a) was presented along with an extensive suite of benchmark tests, including: supersonic advection, one and two-dimensional relativistic shock tubes, ultra-relativistic wall shock, and the relativistic simple wave. We use this special relativistic code as the starting point for numerically implementing the SPHINCS equations.

### 2.4.7 Non-relativistic limit

Finally, in this section we consider the non-relativistic limit of the SPHINCS formulation. It is clear that in this limit the usual variables and associated equations of motion of standard SPH should be recovered. Just as in Section 2.4.6, here the components of the metric are clearly given as  $g_{\mu\nu} = \text{diag}(-1, 1, 1, 1)$ , while  $N^* = N$ . Additionally, restoring standard units and using the results given in Eqs. (2.3.28)-(2.3.30), we have that, within this limit, the numerical variables reduce as

$$N \rightarrow n = \varrho/m_0, \quad (2.4.72)$$

$$\vec{S} \rightarrow \vec{v}, \quad (2.4.73)$$

$$e \rightarrow c^2 + \hat{e} \quad (2.4.74)$$

where  $m_0$  is the average baryonic mass and  $\hat{e} = v^2/2 + u$  is the specific thermokinetic energy. As in Section 2.4.1, we here call  $m_b = m_0 \nu_b$  the fixed mass carried by a general particle  $b$ . Using Eq. (2.4.7) we have that the mass density at the position of a target particle  $a$  can be calculated as

$$\varrho_a = \sum_b m_b W(r_{ab}, h_a), \quad (2.4.75)$$

which is the usual way of computing the kernel estimate of the density  $\varrho$  in non-relativistic SPH. On the other hand, using Eqs. (2.4.69)-(2.4.70), it is straightforward to obtain the following expressions for the evolution equations of  $\vec{v}$  and  $\hat{e}$ :

$$\frac{d(v_i)_a}{dt} = - \sum_b m_b \left[ \left( \frac{P}{\Omega \varrho^2} \right)_a \frac{\partial W_{ab}(h_a)}{\partial x_a^i} + \left( \frac{P}{\Omega \varrho^2} \right)_b \frac{\partial W_{ab}(h_b)}{\partial x_a^i} \right], \quad (2.4.76)$$

$$\frac{d\hat{e}_a}{dt} = - \sum_b m_b \left[ \left( \frac{P}{\Omega \varrho^2} \right)_a v_b^i \frac{\partial W_{ab}(h_a)}{\partial x_a^i} + \left( \frac{P}{\Omega \varrho^2} \right)_b v_a^i \frac{\partial W_{ab}(h_b)}{\partial x_a^i} \right], \quad (2.4.77)$$

while the ‘grad- $h$ ’ term transforms as

$$\Omega_a = 1 - \frac{\partial h_a}{\partial \varrho_a} \sum_b m_b \frac{\partial W_{ab}(h_a)}{\partial h_a}. \quad (2.4.78)$$

As an alternative to the specific thermokinetic energy, we can give an evolution equation for the specific internal energy  $u$  by using the definition of  $\hat{e}$  together with Eqs. (2.4.76) and (2.4.77). After some algebra, we get

$$\frac{du_a}{dt} = \left( \frac{P}{\Omega \varrho^2} \right)_a \sum_b m_b (v_a^i - v_b^i) \frac{\partial W_{ab}(h_a)}{\partial x_a^i}. \quad (2.4.79)$$

Similarly to what was done in Sections 2.4.2 and 2.4.3, by using the expressions for the SPH estimate of the gradient of a scalar in Eq. (2.4.33) and for the divergence of a vector in Eq. (2.4.45), it is simple to check that Eqs. (2.4.76), (2.4.77) and (2.4.79) are nothing more than the SPH discretisation of the Newtonian hydrodynamic equations as given in Eqs. (2.3.32)-(2.3.34).

## 2.5 Summary

In this chapter we have given a review of the basic elements of general relativistic hydrodynamics using the language of the 3+1 formalism. Based on these tools, we have discussed an extension of the SPH method to a general relativistic context in which a perfect fluid is evolved numerically within a given curved spacetime. This particular formulation, for which we have adopted the acronym SPHINCS, was derived by Rosswog (2010b) from the Lagrangian of a perfect fluid accounting, in a self-consistent way, for the corrective terms that arise when a varying smoothing length is used. The numerical

variables in SPHINCS are the baryon number density in the computing frame  $N^*$ , the canonical three-momentum per baryon  $\vec{S}$ , and the canonical energy per baryon  $e$  which were defined in Eqs. (2.3.9), (2.4.26) and (2.4.35) in terms of the primitive variables  $n$ ,  $u$ ,  $P$  and  $\vec{v}$  as

$$N^* = \sqrt{\gamma} \Gamma n, \quad (2.5.80)$$

$$\vec{S} = \Gamma \omega \vec{V}, \quad (2.5.81)$$

$$e = \vec{S} \cdot \vec{v} + \frac{\alpha(1+u)}{\Gamma}, \quad (2.5.82)$$

where  $\vec{V} = (\vec{v} + \vec{\beta})/\alpha$  is the physical three-velocity as measured by a LEO and  $\Gamma = (1 - \vec{V} \cdot \vec{V})^{-1/2}$  is the associated Lorentz factor. Using an SPH interpolation,  $N^*$  was calculated in Eq. (2.4.7) as

$$N_a^* = \sum_b \nu_b W(r_{ab}, h_a), \quad (2.5.83)$$

where  $W$  can be any kernel for a flat spacetime used in standard non-relativistic SPH. On the other hand, the evolution equations for  $\vec{S}$  and  $e$  were given in Eqs. (2.4.32) and (2.4.44) as

$$\begin{aligned} \frac{d(S_i)_a}{dt} = & - \sum_b \nu_b \left[ \left( \frac{\alpha \sqrt{\gamma} P}{\Omega N^{*2}} \right)_a \frac{\partial W_{ab}(h_a)}{\partial x_a^i} + \left( \frac{\alpha \sqrt{\gamma} P}{\Omega N^{*2}} \right)_b \frac{\partial W_{ab}(h_b)}{\partial x_a^i} \right] \\ & - \left[ \frac{\sqrt{\gamma} \epsilon}{N^*} \frac{\partial \alpha}{\partial x^i} - S_j \frac{\partial \beta^j}{\partial x^i} - \frac{\alpha \sqrt{\gamma} \sigma^{jk}}{2 N^*} \frac{\partial \gamma_{jk}}{\partial x^i} \right]_a, \end{aligned} \quad (2.5.84)$$

and

$$\begin{aligned} \frac{de_a}{dt} = & - \sum_b \nu_b \left[ \left( \frac{\alpha \sqrt{\gamma} P}{\Omega N^{*2}} \right)_a v_b^i \frac{\partial W_{ab}(h_a)}{\partial x_a^i} + \left( \frac{\alpha \sqrt{\gamma} P}{\Omega N^{*2}} \right)_b v_a^i \frac{\partial W_{ab}(h_b)}{\partial x_a^i} \right] \\ & + \left[ \frac{\sqrt{\gamma} \epsilon}{N^*} \frac{\partial \alpha}{\partial t} - S_j \frac{\partial \beta^j}{\partial t} - \frac{\alpha \sqrt{\gamma} \sigma^{jk}}{2 N^*} \frac{\partial \gamma_{jk}}{\partial t} \right]_a, \end{aligned} \quad (2.5.85)$$

where  $\epsilon$  and  $\sigma^{jk}$  are part of the 3+1 decomposition of the stress-energy tensor as defined in Eqs. (2.3.2) and (2.3.4), respectively, and

$$\Omega_a = 1 - \frac{\partial h_a}{\partial N_a^*} \sum_b \nu_b \frac{\partial W_{ab}(h_a)}{\partial h_a}, \quad (2.5.86)$$

is the relativistic ‘grad- $h$ ’ term.

Our original contribution here has been to recast the evolution equations of SPHINCS into the 3+1 formalism, to introduce a simple strategy for recovering the primitive variables from the numerically evolved ones, and to show that geodesic motion is recovered from the SPHINCS equations in the limit of vanishing hydrodynamic forces. In our opinion, adopting the 3+1 formalism allows for a more transparent notation in which

---

there is a clear distinction between four and three-dimensional objects. Moreover, using the 3+1 formalism in the SPHINCS equations is also advantageous if at a future stage we want to couple SPHINCS with a metric solver, since most of those are written in terms of this formalism. Nevertheless, it is clear that a fixed, time-independent metric is the obvious choice for a first implementation of the SPHINCS equations. If, in addition, this metric is a known analytic solution of general relativity, we can benchmark the actual numerical implementation against well-studied scenarios, as discussed in Section 1.4. In the next chapter we give appropriate expressions for the implementation of SPHINCS in a rotating BH spacetime.



## Chapter 3

# SPHINCS implementation for Kerr spacetime

In the previous chapter we gave a general formulation of the SPHINCS equations and mentioned that a first obvious implementation of them would be for a time-independent and analytically known metric. Moreover, since our main motivation for developing a numerical tool like SPHINCS is to study accretion flows onto BHs, it is clear that a BH spacetime would be a good first candidate. As we discussed in Section 1.2, for astrophysical applications in which the mass-energy of the fluid has a negligible effect on the spacetime curvature, the exterior metric around a physical BH should be well approximated by the Kerr solution.

An important point that we need to consider before the actual implementation of the SPHINCS equations is that several procedures inherent to the SPH method (e.g. neighbour search, tree walk, force calculation, etc.), are easier to do if one adopts a set of Cartesian coordinates. In addition, the starting point of the SPHINCS code is the special relativistic SPH code developed by Rosswog (2010a), which is written in terms of Cartesian coordinates (as is the case, as far as we know, for all of the other existing multi-dimensional SPH codes, both Newtonian and relativistic). Since we want to modify this code only where strictly necessary, it is clear that it would be advantageous if we provided a formulation of the SPHINCS equations using a Cartesian coordinate system. However, for an arbitrary curved spacetime, it is not possible to define global Cartesian coordinates in the classical sense. Nonetheless, we can instead introduce a system of coordinates that locally is as close as possible to a Cartesian one. In other words, we want to define a reference system for which local volume elements look like unit cubes, i.e. for which the determinant of the metric is simply  $g = -1$ . Moreover, for asymptotically flat spacetimes (such as the Kerr spacetime), it is always possible to define a set of coordinates that, asymptotically far away from the central mass, converges to the usual set of Cartesian coordinates. In the following, we call such a system a ‘Cartesian-like’ coordinate system. Finally, we note that adopting this set of coordinates automatically guarantees that the numerical variable  $N^*$  (defined in Eq. 2.3.9) has appropriate units of a baryon number density (units of inverse volume).

In this chapter we discuss the SPHINCS implementation for a Kerr spacetime. We start by giving a general review of the Kerr metric based on Chandrasekhar (1983); Frolov & Novikov (1998); Wiltshire et al. (2009). Along the way we introduce two systems of coordinates, the Boyer-Lindquist and Kerr-Schild coordinates, and discuss the advantages and disadvantages associated with each of them. We introduce the Cartesian-like form of each of these coordinate systems, as well as showing their relation with the 3+1 formalism, for which we introduce the associated families of local Eulerian observers (LEOs). In the final part of this chapter we give appropriate expressions for the gravity terms in the SPHINCS equations of motion for the Kerr and Schwarzschild spacetimes.

### 3.1 Boyer-Lindquist coordinates $(t, r, \theta, \phi)$

The Boyer-Lindquist (BL) system of coordinates was introduced by Boyer & Lindquist (1967) for studying the Kerr metric, and it is one of the most commonly used in the literature. These coordinates are particularly convenient for describing the spacetime far away from the central BH since the BL coordinate time approaches asymptotically that of a family of observers situated at rest at infinity. However, they are ill-behaved in the vicinity of the BH (coordinate singularity), and, for this reason, they are not the best suited for implementing the SPHINCS equations. Nevertheless, in what follows we give a brief review of these coordinates in order to facilitate future reference to other works. Using BL coordinates, the Kerr metric line element has the following form (Misner et al., 1973)

$$\begin{aligned} ds^2 &= g_{\mu\nu} dx^\mu dx^\nu \\ &= - \left( 1 - \frac{2Mr}{\rho^2} \right) dt^2 - \frac{4aMr \sin^2 \theta}{\rho^2} dt d\phi \\ &\quad + \frac{\rho^2}{\Delta} dr^2 + \rho^2 d\theta^2 + \frac{\Sigma \sin^2 \theta}{\rho^2} d\phi^2, \end{aligned} \quad (3.1.1)$$

where

$$\rho^2 = r^2 + a^2 \cos^2 \theta, \quad (3.1.2)$$

$$\Delta = r^2 - 2Mr + a^2, \quad (3.1.3)$$

$$\Sigma = (r^2 + a^2)^2 - a^2 \Delta \sin^2 \theta. \quad (3.1.4)$$

The components of the inverse metric  $g^{\mu\nu}$  are easily calculated from Eq. (3.1.1) as

$$\begin{aligned} g^{tt} &= -\frac{\Sigma}{\Delta \rho^2}, & g^{t\phi} &= -\frac{2aMr}{\Delta \rho^2}, \\ g^{rr} &= \frac{\Delta}{\rho^2}, & g^{\theta\theta} &= \frac{1}{\rho^2}, & g^{\phi\phi} &= \frac{\Delta - a^2 \sin^2 \theta}{\Delta \rho^2 \sin^2 \theta}, \end{aligned} \quad (3.1.5)$$

while the determinant of the metric in these coordinates is given by  $g = -\rho^4 \sin^2 \theta$ .

In Kerr spacetime, we must distinguish some special values for the radial coordinate: the outer and inner ergosurfaces  $r_{s\pm}$ , and the outer and inner event horizons  $r_{\pm}$ .<sup>(1)</sup> The first two correspond to the roots of the quadratic equation obtained by setting the metric coefficient  $g_{tt} = 0$ , i.e.

$$r_{s\pm} = M \pm \sqrt{M^2 - a^2 \cos^2 \theta}. \quad (3.1.6)$$

The outer ergosurface is also known as the static limit and it determines the boundary within which all physical reference frames are compelled to co-rotate with the central object. The phenomenon of local inertial frames being pulled round by a rotating object is known as the frame-dragging or Lense-Thirring effect (Lense & Thirring, 1918). On the other hand, the two event horizons are defined as the roots of the equation  $\Delta = 0$ , i.e.

$$r_{\pm} = M \pm \sqrt{M^2 - a^2}. \quad (3.1.7)$$

The two event horizons act as one-way membranes in the sense that null and time-like trajectories can cross them just in one direction. From the metric expression in Eq. (3.1.1), it follows that the  $g_{rr}$  metric component diverges at these two locations. This behaviour is just a coordinate singularity related with the choice of reference frame in which Eq. (3.1.1) has been written and may not be present for a different choice, as is for instance the case of Kerr-Schild coordinates as we shall show later on. Nevertheless, a true spacetime singularity is hidden within the two event horizons and it is given by  $\rho = 0$ , i.e.

$$r = 0 \quad \text{and} \quad \theta = \pi/2. \quad (3.1.8)$$

This singularity is not a single point of the Kerr spacetime but rather a one-dimensional object which is often referred to as a ring singularity. It is best seen using the Cartesian-like form of the spatial BL coordinates  $(x, y, z)$ , defined as

$$\begin{aligned} x &= \sqrt{r^2 + a^2} \sin \theta \cos \phi, \\ y &= \sqrt{r^2 + a^2} \sin \theta \sin \phi, \\ z &= r \cos \theta, \end{aligned} \quad (3.1.9)$$

and the associated cylindrical radius given by

$$R = \sqrt{x^2 + y^2} = \sqrt{r^2 + a^2} \sin \theta. \quad (3.1.10)$$

In terms of these coordinates, the ring singularity is located at

$$R = a, \quad z = 0. \quad (3.1.11)$$

In Figure 3.1 we show the intersection of the four surfaces  $r_{\pm}, r_{s\pm}$  with the  $R$ - $z$  plane of a Kerr spacetime with  $a = 0.98 M$ . Note that  $r_+ < r_{s+}$  and  $r_- > r_{s-}$  everywhere except at the poles ( $\theta = 0, \pi$ ), where they coincide. Also note that the surface  $r_{s-}$  has a cusp at the ring singularity.

---

<sup>(1)</sup>Note, however, that only the outer horizon and outer ergosurface come within the region to which the uniqueness theorems apply; it is unclear whether the parts of the Kerr solution inside the outer event horizon have any physical relevance.

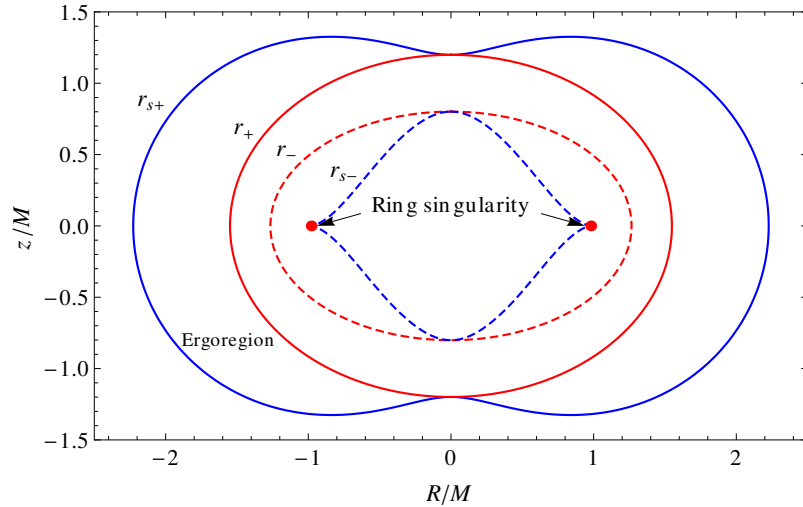


**Figure 3.1:** Location of the ergosurfaces, horizons and ring singularity of Kerr spacetime projected onto the  $R$ - $z$  plane. In this particular example we have taken  $a = 0.98 M$ . The ergoregion is the region of spacetime delimited between the outer ergosurface and the outer event horizon.

Using the cylindrical coordinates, we can see that the condition  $r = \text{const.}$  defines the two-dimensional surface

$$\frac{R^2}{r^2 + a^2} + \frac{z^2}{r^2} = 1, \quad (3.1.12)$$

which corresponds to an ellipsoid of revolution with its rotation axis coinciding with the polar axis of the BH. On the other hand, the condition  $\theta = \text{const.}$  defines the surface

$$\frac{R^2}{a^2 \sin^2 \theta} - \frac{z^2}{a^2 \cos^2 \theta} = 1, \quad (3.1.13)$$

which corresponds to a hyperboloid of revolution with the same rotation axis as the ellipsoid  $r = \text{const.}$  The foci of both surfaces coincide and are located on the  $R$ - $z$  plane at  $(a, 0)$  and  $(-a, 0)$ .

In Figure 3.2 we plot the constant- $r$  and constant- $\theta$  coordinate surfaces as projected onto the  $R$ - $z$  plane. From Eq. (3.1.12) we see that varying the constant radius  $r$  as a continuous parameter defines a family of co-focal ellipses, while doing the same with the polar angle  $\theta$  in Eq. (3.1.13) defines a family of co-focal hyperbolae. In the first case, the ellipsoid corresponding to  $r = 0$  degenerates as the circular section of the equatorial plane interior to the ring singularity. On the other hand, the hyperbola corresponding to  $\theta = \pi/2$  also degenerates into the equatorial plane but now for the section exterior to the ring singularity. Note that there is also a degeneracy for  $\theta = 0, \pi$ , but that it corresponds instead to the polar axis.

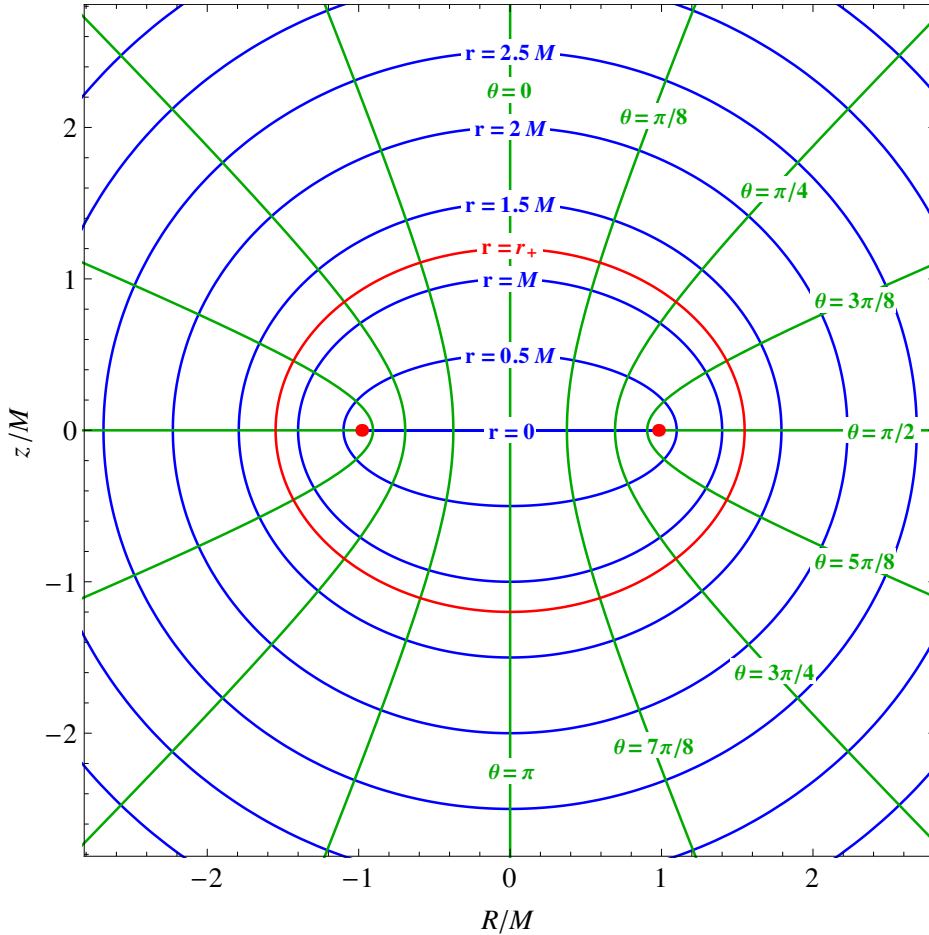


**Figure 3.2:** This figure shows a spatial projection of the coordinate surfaces  $r = \text{const.}$  and  $\theta = \text{const.}$  onto the  $R$ - $z$  plane of a Kerr spacetime with  $a = 0.98 M$ . In this projection, the lines  $r = \text{const.}$  represent a family of co-focal ellipses (blue lines) while the lines  $\theta = \text{const.}$  constitute a family of co-focal hyperbolae (green lines). For both families, the foci (red points) coincide with the intersections of the ring singularity with the  $R$ - $z$  plane, i.e.  $(a, 0)$ ,  $(-a, 0)$ . The ellipse corresponding to  $r = r_+$  is highlighted with a red line.

### 3.2 Locally non-rotating frames

Here we use the machinery developed in Section 2.2.1 to define local Eulerian observers (LEOs). We start by noting that, in BL coordinates, the hypersurfaces defined by the condition  $t = \text{const.}$  are spacelike for all  $r > r_+$ . For this reason, we can use the BL coordinates as a particular 3+1 decomposition of the Kerr metric but only for the section of spacetime exterior to the BH horizon. In order to do so, we start by rewriting Eq. (3.1.1) as

$$ds^2 = - \left( \frac{\Delta}{\Sigma} \right) \rho^2 dt^2 + \frac{\rho^2}{\Delta} dr^2 + \rho^2 d\theta^2 + \frac{\Sigma \sin^2 \theta}{\rho^2} (d\phi - \omega dt)^2, \quad (3.2.1)$$

where  $\omega = 2aMr/\Sigma$ . By comparing this expression with Eq. (2.2.1), we can immediately see that the lapse  $\alpha$ , the shift  $\beta^i$  and the spatial metric  $\gamma_{ij}$  corresponding to the 3+1 decomposition of BL coordinates, are given by

$$\alpha = \sqrt{\frac{\Delta}{\Sigma}} \rho, \quad (3.2.2)$$

$$(\beta^i) = (0, 0, -\omega), \quad (3.2.3)$$

$$(\gamma_{ij}) = \text{diag} \left( \frac{\rho^2}{\Delta}, \rho^2, \frac{\Sigma \sin^2 \theta}{\rho^2} \right). \quad (3.2.4)$$

Using these expressions, we can introduce the LEOs associated with the BL coordinates as described in Section 2.2.1. Note that in the context of Kerr spacetime, members of this family of observers are more commonly referred to as zero angular momentum observers (ZAMOs). For this reason, in the present work we reserve the name ZAMO to refer to the Eulerian observers associated with the BL coordinates.

From Eq. (3.2.4) we see that the spatial metric in this case is diagonal; it follows then that the basis vectors carried along by each ZAMO are orthogonal to each other and can, in principle, be normalised to be of unit length (and the same for the associated base for the covariant components of a vector). Such a family of orthonormal tetrads was introduced by Bardeen et al. (1972) with the name of locally non-rotating frames (LNRFs). They are given this name because they rotate with the spacetime geometry in such a way that, locally, they actually determine to be non-rotating.

Following the notation that was introduced in Section 2.2.1, we here call  $\{\mathbf{e}_{(\mu)}\}$  and  $\{\mathbf{e}^{(\mu)}\}$  the bases for vectors associated with a BL observer; while we call  $\{\bar{\mathbf{e}}_{(\mu)}\}$  and  $\{\bar{\mathbf{e}}^{(\mu)}\}$  the corresponding (normalised) bases for vectors associated with the ZAMO. By substituting Eqs. (3.2.2)-(3.2.4) into Eqs. (2.2.9), it follows that these sets of bases are related through

$$\begin{aligned}
\bar{\mathbf{e}}_{(t)} &= \sqrt{\frac{\Sigma}{\Delta}} \frac{1}{\rho} (\mathbf{e}_{(t)} + \omega \mathbf{e}_{(\phi)}), & \bar{\mathbf{e}}^{(t)} &= \sqrt{\frac{\Delta}{\Sigma}} \rho \mathbf{e}^{(t)}, \\
\bar{\mathbf{e}}_{(r)} &= \frac{\sqrt{\Delta}}{\rho} \mathbf{e}_{(r)}, & \bar{\mathbf{e}}^{(r)} &= \frac{\rho}{\sqrt{\Delta}} \mathbf{e}^{(r)}, \\
\bar{\mathbf{e}}_{(\theta)} &= \frac{1}{\rho} \mathbf{e}_{(\theta)}, & \bar{\mathbf{e}}^{(\theta)} &= \rho \mathbf{e}^{(\theta)}, \\
\bar{\mathbf{e}}_{(\phi)} &= \frac{\rho}{\sqrt{\Sigma} \sin \theta} \mathbf{e}_{(\phi)}, & \bar{\mathbf{e}}^{\phi} &= \frac{\sqrt{\Sigma} \sin \theta}{\rho} (\mathbf{e}^{(\phi)} - \omega \mathbf{e}^{(t)}).
\end{aligned} \tag{3.2.5}$$

From Eq. (3.2.5), it is immediate to read off the components of the Jacobian tensors which dictate the transformation of tensors between the LNRF and the BL frame. For instance, we can check that the metric tensor in the LNRF is simply given by  $\bar{g}_{\mu\nu} = \text{diag}(-1, 1, 1, 1)$  (as one would have expected, given that the LNRF is a local orthonormal reference frame).

### 3.3 Kerr-Schild coordinates $(T, r, \theta, \psi)$

We consider now the Kerr-Schild (KS) coordinate system for which the metric is regular all the way through the two event horizons. This system of coordinates was the original one used by Kerr (1963) when he first presented the Kerr metric. In this reference system, the radial and polar coordinates ( $r$  and  $\theta$ ) coincide with the BL ones while the temporal coordinate  $T$  and the azimuthal angle  $\psi$  are defined in terms of  $t$ ,  $r$  and  $\phi$  according to the following transformation rules

$$\begin{aligned}
dT &= dt + \frac{2Mr}{\Delta} dr, \\
d\psi &= d\phi + \frac{a}{\Delta} dr.
\end{aligned} \tag{3.3.1}$$

Using a tilde to denote general KS coordinates, i.e.  $(\tilde{x}^\mu) = (T, r, \theta, \psi)$ , from Eq. (3.3.1) it is straightforward to get the components of the Jacobian matrices of the direct and inverse transformations (i.e.  $\partial\tilde{x}^\mu/\partial x^\nu$  and  $\partial x^\mu/\partial\tilde{x}^\nu$ , respectively). Using these two matrices, we can transform any vector or tensor back and forth between the BL and KS reference frames. For instance, from the transformation of the metric tensor, we get that the differential line element in KS coordinates is given by

$$\begin{aligned}
ds^2 &= - \left(1 - \frac{2Mr}{\rho^2}\right) dT^2 + \left(1 + \frac{2Mr}{\rho^2}\right) dr^2 + \frac{4Mr}{\rho^2} dr dT - \frac{4Mar}{\rho^2} \sin^2 \theta d\psi dT \\
&\quad - 2a \left(1 + \frac{2Mr}{\rho^2}\right) \sin^2 \theta dr d\psi + \rho^2 d\theta^2 + \frac{\Sigma \sin^2 \theta}{\rho^2} d\psi^2,
\end{aligned} \tag{3.3.2}$$

while the non-vanishing components of the inverse metric are given by

$$\begin{aligned} g^{TT} &= -\left(1 + \frac{2Mr}{\rho^2}\right), & g^{Tr} &= \frac{2Mr}{\rho^2}, & g^{r\psi} &= \frac{a}{\rho^2}, \\ g^{rr} &= \frac{\Delta}{\rho^2}, & g^{\theta\theta} &= \frac{1}{\rho^2}, & g^{\psi\psi} &= \frac{1}{\rho^2 \sin^2 \theta}. \end{aligned} \quad (3.3.3)$$

For the determinant of the metric in KS coordinates, given that the  $r$  and  $\theta$  coordinates remained untouched, it is found that the result given for the BL case applies also for KS, i.e.  $\tilde{g} = g = -\rho^4 \sin^2 \theta$ . From Eq. (3.3.2) we also note that the components of the metric in KS coordinates are regular everywhere except at the ring singularity (where  $\rho = 0$ ).

We consider now the 3+1 decomposition of Kerr spacetime using KS coordinates. In this case, the hypersurfaces of constant  $T$  are spacelike for every  $r > 0$  and can be extended past the horizons and down to the ring singularity. Appropriate definitions for the lapse  $\alpha$ , shift  $\beta^i$  and spatial metric  $\gamma_{ij}$  in this case, are given by

$$\alpha = \frac{\rho}{\sqrt{\rho^2 + 2Mr}}, \quad (3.3.4)$$

$$(\beta^i) = \left( \frac{2Mr}{\rho^2 + 2Mr}, 0, 0 \right), \quad (3.3.5)$$

$$(\gamma_{ij}) = \begin{pmatrix} 1 + \frac{2Mr}{\rho^2} & 0 & -a \sin^2 \theta \left(1 + \frac{2Mr}{\rho^2}\right) \\ 0 & \rho^2 & 0 \\ -a \sin^2 \theta \left(1 + \frac{2Mr}{\rho^2}\right) & 0 & \frac{\Sigma \sin^2 \theta}{\rho^2} \end{pmatrix}. \quad (3.3.6)$$

From this we see that the frames carried by the LEOs associated with this particular 3+1 splitting of Kerr spacetime are not orthonormal tetrads as in the BL case. Expressions for the set of vector bases in this case follow immediately from substituting Eqs. (3.3.4)-(3.3.6) into Eq. (2.2.9).

At this point we could wonder about the practical issue of which coordinate system should be used to tackle a given problem in Kerr spacetime using the SPHINCS method. It is clear that the KS system is more suitable than the BL one for describing physical processes nearby the BH horizon or even past it. On the other hand, the description made in terms of BL coordinates has the advantage of corresponding to that made by physical observers located at infinity with respect to the BH (essentially our location with respect to any astrophysical BH).

As we have already discussed, the transformation of vectors and tensors between the BL and the KS systems is a trivial operation mediated by the Jacobian matrices. However, before applying this transformation to the components of any given tensor, we need to know the coordinates of the point at which the tensor is located in both reference systems.

For instance, let us assume that we know explicitly the time evolution of a given SPH particle in KS coordinates, i.e. its world line  $(\tilde{x}^\mu) = (T, \tilde{x}^i(T))$  is known. At every point along this we will have recorded several different scalar and tensorial quantities ( $P$ ,  $\tilde{T}^{\mu\nu}$ ,  $\tilde{U}^\mu$ ,  $\tilde{V}^i$  etc.) but, before being able to transform any of these from the KS to the BL system, we need to know the description of the particle's world line in terms of BL coordinates.<sup>(2)</sup> This can be done by picking up a reference or 'synchronisation' point  $(\tilde{x}_0^\mu) = (T_0, r_0, \theta_0, \psi_0)$  on the particle's world line, for which the corresponding BL coordinates  $(x_0^\mu) = (t_0, r_0, \theta_0, \phi_0)$  are also known. This point can be taken, for instance, at the initial-condition hypersurface  $T = T_0$ . Once the reference point has been defined, we can directly integrate the transformation rules in Eq. (3.3.1) and get

$$\begin{aligned} t - t_0 &= T - T_0 + \frac{M}{\sqrt{M^2 - a^2}} \left[ r_+ \ln \left( \frac{r - r_+}{r_0 - r_+} \right) - r_- \ln \left( \frac{r - r_-}{r_0 - r_-} \right) \right], \\ \phi - \phi_0 &= \psi - \psi_0 + \frac{1}{2} \frac{a}{\sqrt{M^2 - a^2}} \ln \left( \frac{r - r_+}{r - r_-} \frac{r_0 - r_-}{r_0 - r_+} \right). \end{aligned} \quad (3.3.7)$$

From this we can then express the world line of the given particle in BL coordinates as  $(x^\mu) = (t, x^i(t))$ . Therefore, it does not matter which coordinates we choose for solving a given problem, since we can always transform the results back and forth between these two coordinate systems. For this reason, given that the KS coordinates are well-behaved in the proximity of the BH horizon, they seem to be the better choice for implementing the SPHINCS equations.

### 3.4 Cartesian-like form of the KS coordinates $(T, \tilde{x}, \tilde{y}, \tilde{z})$

The set of Cartesian-like coordinates  $(\tilde{x}, \tilde{y}, \tilde{z})$  associated to the spatial KS coordinates  $(r, \theta, \psi)$  is defined as

$$\begin{aligned} \tilde{x} &= \sin \theta (r \cos \psi - a \sin \psi), \\ \tilde{y} &= \sin \theta (a \cos \psi + r \sin \psi), \\ \tilde{z} &= r \cos \theta, \end{aligned} \quad (3.4.1)$$

while the time coordinate  $T$  is taken to be the same in both systems. From Eqs. (3.1.9) and (3.4.1), it is clear that  $\tilde{z} = z$ , while the cylindrical radius is also the same as in the BL case, i.e.

$$\tilde{R} = \sqrt{\tilde{x}^2 + \tilde{y}^2} = \sqrt{r^2 + a^2} \sin \theta = R. \quad (3.4.2)$$

In order to ease the notation, whenever it is unambiguous that we are referring only to Cartesian-like KS coordinates, we will drop the tilde. From Eq. (3.4.1) we get that the

---

<sup>(2)</sup>Clearly, for scalar quantities such as  $P$ , no further transformation is needed once we know the coordinates of a given point in the two coordinate systems.

Jacobian corresponding to this transformation is given by

$$\left( \frac{\partial \check{x}^\mu}{\partial x^\nu} \right) = \begin{pmatrix} 1 & 0 & 0 & 0 \\ 0 & \sin \theta \cos \psi & \cos \theta (r \cos \psi - a \sin \psi) & -\sin \theta (a \cos \psi + r \sin \psi) \\ 0 & \sin \theta \sin \psi & \cos \theta (a \cos \psi + r \sin \psi) & \sin \theta (r \cos \psi - a \sin \psi) \\ 0 & \cos \theta & -r \sin \theta & 0 \end{pmatrix}, \quad (3.4.3)$$

where  $(\check{x}^\mu) = (T, x, y, z)$  and  $(x^\mu) = (T, r, \theta, \psi)$ . On the other hand, it is simple to invert Eq. (3.4.1) and get the following expressions for the inverse transformation

$$\begin{aligned} r &= \sqrt{\frac{1}{2}(x^2 + y^2 + z^2 - a^2) + \frac{1}{2}\sqrt{(x^2 + y^2 + z^2 - a^2)^2 + 4a^2z^2}}, \\ \theta &= \cos^{-1}\left(\frac{z}{r}\right), \\ \psi &= \tan^{-1}\left(\frac{ry - ax}{rx + ay}\right), \end{aligned} \quad (3.4.4)$$

from which we get the following Jacobian for the inverse transformation:

$$\left( \frac{\partial x^\mu}{\partial \check{x}^\nu} \right) = \begin{pmatrix} 1 & 0 & 0 & 0 \\ 0 & \frac{rx}{\rho^2} & \frac{ry}{\rho^2} & \frac{z(r^2+a^2)}{r\rho^2} \\ 0 & \frac{xz}{r\rho^2} \sqrt{\frac{r^2+a^2}{x^2+y^2}} & \frac{yz}{r\rho^2} \sqrt{\frac{r^2+a^2}{x^2+y^2}} & \frac{z^2-r^2}{r\rho^2} \sqrt{\frac{r^2+a^2}{x^2+y^2}} \\ 0 & \frac{arx}{\rho^2(r^2+a^2)} - \frac{y}{x^2+y^2} & \frac{ary}{\rho^2(r^2+a^2)} + \frac{x}{x^2+y^2} & \frac{az}{r\rho^2} \\ 0 & -\frac{yr^2\rho^2+arx(r^2-\rho^2)}{r^2\rho^2(x^2+y^2)} & \frac{xr^2\rho^2-ary(r^2-\rho^2)}{r^2\rho^2(x^2+y^2)} & \frac{az}{r\rho^2} \end{pmatrix}, \quad (3.4.5)$$

where  $r$  and  $\rho$  should be considered as implicit functions of  $(x, y, z)$  that satisfy

$$r^4 - r^2(x^2 + y^2 + z^2 - a^2) - a^2z^2 = 0, \quad (3.4.6)$$

$$\rho^2 = r^2 + \frac{a^2z^2}{r^2} = \sqrt{(x^2 + y^2 + z^2 - a^2)^2 + 4a^2z^2}. \quad (3.4.7)$$

In terms of these coordinates, the differential line element is

$$\begin{aligned} ds^2 &= -dT^2 + dx^2 + dy^2 + dz^2 \\ &+ \frac{2Mr}{\rho^2} \left[ \frac{r(x dx + y dy) - a(x dy - y dx)}{r^2 + a^2} + \frac{z dz}{r} + dT \right]^2, \end{aligned} \quad (3.4.8)$$

or, in terms of the metric components

$$\begin{aligned}
g_{TT} &= -1 + \frac{2Mr}{\rho^2}, & g_{xx} &= 1 + \frac{2Mr}{\rho^2} \left( \frac{rx + ay}{r^2 + a^2} \right)^2, \\
g_{yy} &= 1 + \frac{2Mr}{\rho^2} \left( \frac{ry - ax}{r^2 + a^2} \right)^2, & g_{zz} &= 1 + \frac{2Mz^2}{r\rho^2}, \\
g_{Tx} &= \frac{2Mr}{\rho^2} \left( \frac{rx + ay}{r^2 + a^2} \right), & g_{Ty} &= \frac{2Mr}{\rho^2} \left( \frac{ry - ax}{r^2 + a^2} \right), & g_{Tz} &= \frac{2Mz}{\rho^2}, \\
g_{xz} &= \frac{2Mz}{\rho^2} \left( \frac{rx + ay}{r^2 + a^2} \right), & g_{yz} &= \frac{2Mz}{\rho^2} \left( \frac{ry - ax}{r^2 + a^2} \right), \\
g_{xy} &= \frac{2Mr}{\rho^2} \frac{(rx + ay)(ry - ax)}{(r^2 + a^2)^2}.
\end{aligned} \tag{3.4.9}$$

The inverse metric components are given by

$$\begin{aligned}
g^{TT} &= -1 - \frac{2Mr}{\rho^2}, & g^{xx} &= 1 - \frac{2Mr}{\rho^2} \left( \frac{rx + ay}{r^2 + a^2} \right)^2, \\
g^{yy} &= 1 - \frac{2Mr}{\rho^2} \left( \frac{ry - ax}{r^2 + a^2} \right)^2, & g^{zz} &= 1 - \frac{2Mz^2}{r\rho^2}, \\
g^{Tx} &= \frac{2Mr}{\rho^2} \left( \frac{rx + ay}{r^2 + a^2} \right), & g^{Ty} &= \frac{2Mr}{\rho^2} \left( \frac{ry - ax}{r^2 + a^2} \right), & g^{Tz} &= \frac{2Mz}{\rho^2}, \\
g^{xz} &= -\frac{2Mz}{\rho^2} \left( \frac{rx + ay}{r^2 + a^2} \right), & g^{yz} &= -\frac{2Mz}{\rho^2} \left( \frac{ry - ax}{r^2 + a^2} \right), \\
g^{xy} &= -\frac{2Mr}{\rho^2} \frac{(rx + ay)(ry - ax)}{(r^2 + a^2)^2}.
\end{aligned} \tag{3.4.10}$$

Note that in Eq. (3.4.8) we have explicitly split the Kerr metric into a flat spacetime in Cartesian coordinates (flat spacetime metric) plus a term that, for  $r \gg M$ , asymptotically vanishes as  $\mathcal{O}(M/r)$ .

The corresponding 3+1 decomposition is given by

$$\alpha = \frac{\rho}{\sqrt{\rho^2 + 2Mr}}, \tag{3.4.11}$$

$$(\beta^i) = \frac{2Mr}{\rho^2 + 2Mr} \left( \frac{rx + ay}{r^2 + a^2}, \frac{ry - ax}{r^2 + a^2}, \frac{z}{r} \right), \tag{3.4.12}$$

$$(\beta_i) = \frac{2Mr}{\rho^2} \left( \frac{rx + ay}{r^2 + a^2}, \frac{ry - ax}{r^2 + a^2}, \frac{z}{r} \right), \tag{3.4.13}$$

$$\gamma_{ij} = \delta_{ij} + \frac{\rho^2}{2Mr} \beta_i \beta_j \tag{3.4.14}$$

$$\gamma^{ij} = \delta^{ij} - \frac{\rho^2 + 2Mr}{2Mr} \beta^i \beta^j. \tag{3.4.15}$$

where  $\delta_{ij}$  is the Kronecker delta and  $\beta_i = \gamma_{ij} \beta^j = \beta^i / \alpha^2$ . In this case the shift satisfies  $\|\vec{\beta}\|^2 = \beta_i \beta^i = \alpha^2 (2Mr / \rho^2)^2$ .

### 3.5 SPHINCS in Kerr spacetime

In Chapter 2 we derived, for an arbitrary spacetime, the SPHINCS evolution equations for the canonical momentum  $\vec{S}$  and the canonical energy  $e$  as given in Eqs. (2.5.84) and (2.5.85), respectively. As we have already discussed, these two equations can be split as

$$\frac{d\vec{S}_a}{dT} = \left( \frac{d\vec{S}_a}{dT} \right)_h + \left( \frac{d\vec{S}_a}{dT} \right)_g, \quad (3.5.1)$$

$$\frac{de_a}{dT} = \left( \frac{de_a}{dT} \right)_h + \left( \frac{de_a}{dT} \right)_g, \quad (3.5.2)$$

where a term with the label h represents the ‘hydrodynamic’ contribution to the force acting on a given SPH particle, while a term with the label g represents the ‘gravity’ contribution. The h-terms involve smoothed averages over the closest neighbours of the particle  $a$  and, due to our choice of a kernel  $W$  defined in flat spacetime, their only dependence on the metric tensor comes through the geometric factor  $\sqrt{-g} = \alpha\sqrt{\gamma}$ . However, since we have adopted Cartesian-like coordinates, we have that  $\sqrt{-g} = 1$ , and so we only need to consider the g-terms. In the following we give explicit expressions for these in the particular case of Kerr spacetime using Cartesian-like KS coordinates.

According to Eqs. (2.5.84) and (2.5.85), the g-terms are given by

$$\left( \frac{d(S_i)_a}{dT} \right)_g = - \left[ \frac{\sqrt{\gamma} \epsilon}{N^*} \frac{\partial \alpha}{\partial x^i} - S_j \frac{\partial \beta^j}{\partial x^i} - \frac{\alpha \sqrt{\gamma} \sigma^{jk}}{2 N^*} \frac{\partial \gamma_{jk}}{\partial x^i} \right]_a, \quad (3.5.3)$$

$$\left( \frac{de_a}{dT} \right)_g = \left[ \frac{\sqrt{\gamma} \epsilon}{N^*} \frac{\partial \alpha}{\partial T} - S_j \frac{\partial \beta^j}{\partial T} - \frac{\alpha \sqrt{\gamma} \sigma^{jk}}{2 N^*} \frac{\partial \gamma_{jk}}{\partial T} \right]_a, \quad (3.5.4)$$

where  $\epsilon$  and  $\sigma^{jk}$  were defined in Eqs. (2.3.2) and (2.3.4), respectively. From Eqs. (3.5.3) and (3.5.4) we see that they depend only on the position of the target particle ( $x_a^i$ ) and on the value of the derivatives of the metric components at that position. In other words, the g-terms are independent of any kernel estimate and can be viewed as giving an effective ‘gravitational acceleration’.

Also note that for the present choice of coordinates, the components of the metric tensor are independent of the time coordinate, and so it follows from Eq. (3.5.4) that  $(de/dT)_g = 0$ . Therefore, we only need to provide expressions for the  $(dS_i/dT)_g$  terms. Using the Cartesian-like form of the KS coordinates, and after some algebra, it is found

that the g-terms in Eq. (3.5.3) are given by

$$\begin{aligned} \left(\frac{dS_x}{dT}\right)_g &= \frac{\omega M \Gamma^2 (\rho^2 + 2Mr)}{r \rho^8 N^* (r^2 + a^2)^3} [(r^2 + a^2) (r + z v^z) + r v^x (a y + r x) + r v^y (r y - a x)] \\ &\quad \left\{ x (r^2 + a^2)^2 [r (3\rho^2 - 4r^2) + z v^z (\rho^2 - 4r^2)] + \right. \\ &\quad \quad x a r (x v^y - y v^x) [\rho^2 (r^2 - 3a^2) + 4r^2 (r^2 + a^2)] + \\ &\quad \quad x r^2 (x v^x + y v^y) [\rho^2 (r^2 + 5a^2) - 4r^2 (r^2 + a^2)] + \\ &\quad \quad \left. 2r\rho^4 (r v^x - a v^y) (r^2 + a^2) \right\}, \end{aligned} \tag{3.5.5}$$

$$\begin{aligned} \left(\frac{dS_y}{dT}\right)_g &= \frac{\omega M \Gamma^2 (\rho^2 + 2Mr)}{r \rho^8 N^* (r^2 + a^2)^3} [(r^2 + a^2) (r + z v^z) + r v^x (a y + r x) + r v^y (r y - a x)] \\ &\quad \left\{ y (r^2 + a^2)^2 [r (3\rho^2 - 4r^2) + z v^z (\rho^2 - 4r^2)] + \right. \\ &\quad \quad y a r (x v^y - y v^x) [\rho^2 (r^2 - 3a^2) + 4r^2 (r^2 + a^2)] + \\ &\quad \quad y r^2 (x v^x + y v^y) [\rho^2 (r^2 + 5a^2) - 4r^2 (r^2 + a^2)] + \\ &\quad \quad \left. 2r\rho^4 (r v^y + a v^x) (r^2 + a^2) \right\}, \end{aligned} \tag{3.5.6}$$

$$\begin{aligned} \left(\frac{dS_z}{dT}\right)_g &= \frac{\omega M \Gamma^2 (\rho^2 + 2Mr)}{r^3 \rho^8 N^* (r^2 + a^2)^2} [(r^2 + a^2) (r + z v^z) + r v^x (a y + r x) + r v^y (r y - a x)] \\ &\quad \left\{ z r (r^2 + a^2) [2r^2 \rho^2 - (r^2 + a^2) (4r^2 - \rho^2)] + \right. \\ &\quad \quad v^z (r^2 + a^2) [r^2 \rho^2 (z^2 + 2\rho^2) - a^2 z^2 (4r^2 + \rho^2) - 4r^4 z^2] + \\ &\quad \quad z a r (x v^y - y v^x) [\rho^2 (r^2 - a^2) + 4r^2 (r^2 + a^2)] + \\ &\quad \quad \left. z r^2 (x v^x + y v^y) [\rho^2 (r^2 + 3a^2) - 4r^2 (r^2 + a^2)] \right\}. \end{aligned} \tag{3.5.7}$$

### 3.6 SPHINCS in Schwarzschild spacetime

It is clear that appropriate expressions for the SPHINCS implementation in a Schwarzschild spacetime should follow immediately after substituting  $a = 0$  into the results derived in the previous section. Nevertheless, the results obtained from that procedure correspond to the so-called Eddington-Finkelstein coordinate system which is not the most commonly-used one in the context of the Schwarzschild metric. In what follows, we give the expressions corresponding to the Cartesian-like form of the usual Schwarzschild coordinates  $(t, r, \theta, \phi)$ . These coordinates are defined as

$$\begin{aligned} x &= r \sin \theta \cos \phi, \\ y &= r \sin \theta \sin \phi, \\ z &= r \cos \theta, \end{aligned} \tag{3.6.1}$$

while the inverse transformation is simply given by

$$\begin{aligned} r &= \sqrt{x^2 + y^2 + z^2}, \\ \theta &= \arctan \frac{\sqrt{x^2 + y^2}}{z}, \\ \phi &= \arctan \frac{y}{x}. \end{aligned} \tag{3.6.2}$$

On the other hand, using the transformation law in Eq. (3.6.1), one finds that the differential line element takes the form

$$\begin{aligned} ds^2 &= -dt^2 + dx^2 + dy^2 + dz^2 \\ &+ \frac{2M}{r^2(r-2M)} \left[ r(r-2M)dt^2 + (x dx + y dy + z dz)^2 \right], \end{aligned} \tag{3.6.3}$$

from where we can obtain the metric coefficients  $g_{\mu\nu}$  and also calculate the components of the inverse metric as being

$$\begin{aligned} g^{tt} &= - \left( 1 - \frac{2M}{r} \right)^{-1}, \\ g^{xx} &= 1 - \frac{2Mx^2}{r^3}, \quad g^{yy} = 1 - \frac{2My^2}{r^3}, \quad g^{zz} = 1 - \frac{2Mz^2}{r^3}, \\ g^{xy} &= -\frac{2Mxy}{r^3}, \quad g^{yz} = -\frac{2Myz}{r^3}, \quad g^{xz} = -\frac{2Mxz}{r^3}. \end{aligned} \tag{3.6.4}$$

Using these coordinates the gravity terms in Eq. (3.5.1) are then given by

$$\begin{aligned} \left( \frac{dS_i}{dt} \right)_g &= \frac{\omega M \Gamma^2}{r^3 N^* (r-2M)^3} \left[ 2 v^i r^2 (r-2M) (x v^x + y v^y + z v^z) \right. \\ &\quad \left. - x^i r (r-2M)^2 - x^i (3r-4M) (x v^x + y v^y + z v^z)^2 \right] \end{aligned} \tag{3.6.5}$$

where  $(x^i) = (x, y, z)$ .

### 3.7 Summary

In this chapter we have discussed several aspects concerning the implementation of SPHINCS in Kerr spacetime. We started by giving a brief review of some general characteristics of the Kerr metric using both the BL and KS systems of coordinates. We have presented the Cartesian-like coordinates associated to each of them, as well as rewritten them in terms of the 3+1 formalism. We have also shown the relation between the BL and KS coordinates as well as appropriate expressions for transforming in practice any given vectorial or tensorial quantity back and forth between these two systems. Given that the KS coordinates are well-behaved in the vicinity of the BH and regular across the horizon, we have argued that they are the best suited for a practical implementation of SPHINCS.

---

We have seen that using a Cartesian-like set of coordinates represents several advantages for our present purpose. First, their adoption facilitates the direct use of previous Newtonian and special relativistic codes as seeds for the new code. And second, the fact that the determinant of the metric in this coordinates is identically equal to (minus) one has the important consequence that the h-terms in the equations of motion formally reduce to the form that they had in the special relativistic case. This should further simplify the code development. We have also seen that for stationary metrics, such as the Kerr one, the g-terms entering the energy equation identically vanish. We have then calculated and given explicit expressions for the g-terms that are needed in the momentum equation using the Cartesian-like form of the KS coordinates for the Kerr metric. Additionally, for the non-rotating case we have given alternative expressions for these terms using the Cartesian-like form of the usual Schwarzschild coordinates.



## Chapter 4

# Timelike geodesics in Kerr spacetime

In this chapter we give a general review of the geodesic motion of test particles in Kerr spacetime based on the extensive literature on this subject (e.g. Wilkins, 1972; Bardeen, 1973; Sharp, 1979; Chandrasekhar, 1983; Dymnikova, 1986). The study of geodesics constitutes a fundamental tool for exploring and gaining intuition concerning the geometric and dynamic properties of a given spacetime. Moreover, based on the material introduced in this chapter, we have compiled a catalogue of representative timelike geodesics which is intended to be used as test suite for benchmarking the ability of the SPHINCS code to recover geodesic motion in the limit in which hydrodynamic forces are zeroed. Additionally, the tools presented here are used in the next chapter to construct an analytic toy model for relativistic accretion, that constitutes a more compelling test solution.

We start this chapter by showing how the isometries intrinsic to the Kerr metric lead to the existence of four first integrals of motion that allow us to recast the geodesic equations as a quadrature problem. We give special emphasis to the discussion of circular orbits in the equatorial plane as well as to the study of radial and latitudinal motion for general trajectories (see e.g. de Felice & Calvani, 1972; Bičák & Stuchlík, 1976a, for an in-depth analysis on these kind of motions). Introducing the concepts of radial and polar effective potentials, we provide a broad classification of the different types of orbit. See Bardeen (1973) for a classification of trajectories in the equatorial plane in terms of the physical three-velocity measured by the ZAMOs and Levin & Perez-Giz (2008); Grossman et al. (2012) for a thorough classification of bound orbits based on geometric considerations. The presentation given here is accompanied by examples of actual numerical integrations of test particle trajectories which are given in the Appendix A (orbit catalogue).

### 4.1 Constants of motion

Consider a test particle freely-falling in a Kerr spacetime with four-velocity  $\mathbf{U}$  and rest mass  $m_0$ . Its four-momentum is defined as  $\mathbf{p} = m_0 \mathbf{U}$ . In general, for a test particle moving in a given spacetime, one has that  $m_0$  is a trivially conserved quantity directly connected with the invariance of the modulus of the four-momentum, i.e.  $\mathbf{p} \cdot \mathbf{p} = -m_0^2$ . On the other hand, the stationarity and axisymmetry of Kerr spacetime lead to two further conserved quantities along the trajectory of the particle, namely, the total energy  $E$ , as measured by an observer at spatial infinity, and the component of the angular momentum along the rotation axis of the BH  $L_z$ . These two symmetries of Kerr spacetime are connected with the existence of two linearly independent solutions of the Killing equation  $\xi_{(\mu;\nu)} = 0$ , where a semicolon represents the covariant derivative and round parentheses indicate symmetrisation over the enclosed indices. Any vector  $\xi$  satisfying this is called a Killing vector. For a stationary and axisymmetric spacetime, it is customary to single out two of these vectors,  $\xi_{(t)}$  and  $\xi_{(\phi)}$ , by taking them to be orthogonal to each other and by requiring that, at spatial infinity, the former is timelike while the latter is spacelike, i.e.

$$\begin{aligned}\xi_{(t)} \cdot \xi_{(\phi)} &= 0, \\ \xi_{(t)} \cdot \xi_{(t)} \Big|_{r \rightarrow \infty} &= -1, \\ \xi_{(\phi)} \cdot \xi_{(\phi)} \Big|_{r \rightarrow \infty} &= 1.\end{aligned}\tag{4.1.1}$$

Using BL coordinates, the components of the two Killing vectors are simply given by

$$\xi_{(t)}^\mu = \delta_t^\mu, \quad \xi_{(\phi)}^\mu = \delta_\phi^\mu.\tag{4.1.2}$$

An extra fourth integral of motion  $Q$ , was originally obtained by Carter (1968) by considering the separability of the Hamilton-Jacobi equations associated with the geodesic motion. It was shown by Walker & Penrose (1970); Hughston et al. (1972) that this extra integral of motion is associated with the existence of a quadratic Killing tensor satisfying the equation  $\xi_{(\mu\nu;\lambda)} = 0$ . In BL coordinates this Killing tensor is given by (Stewart & Walker, 1973)

$$\xi_{\mu\nu} = 2\rho^2 n_{(\mu} l_{\nu)} + r^2 g_{\mu\nu}\tag{4.1.3}$$

where  $l_\mu$  and  $n_\mu$ , together with  $m_\mu$ , constitute the repeated principal null vectors of Kerr spacetime given by

$$\begin{aligned}(l^\mu) &= \frac{1}{2\rho^2} (r^2 + a^2, \Delta, 0, a), \\ (n^\mu) &= \frac{1}{\Delta} (r^2 + a^2, -\Delta, 0, a), \\ (m^\mu) &= \frac{1}{\sqrt{2}\rho} (i a \sin \theta, 0, 1, i \csc \theta).\end{aligned}\tag{4.1.4}$$

These vectors are connected with the metric tensor in the following way

$$g_{\mu\nu} = -2n_{(\mu}l_{\nu)} + 2m_{(\mu}m_{\nu)}^*, \quad (4.1.5)$$

where an asterisk denotes a complex conjugate. Exploiting this identity, we can rewrite  $\xi_{\mu\nu}$  as

$$\xi_{\mu\nu} = 2\rho^2 m_{(\mu} m_{\nu)}^* - a^2 \cos^2 \theta g_{\mu\nu}. \quad (4.1.6)$$

For convenience, in the following we shall employ only the specific values of the conserved quantities, defined as:

$$\mathcal{E} = E/m_0, \quad \ell_z = L_z/m_0, \quad \mathcal{Q} = Q/m_0^2.$$

Note that in geometric units,  $\mathcal{E}$  is a dimensionless quantity while  $\ell_z$  and  $\mathcal{Q}$  have units of length and length squared, respectively.

The contraction of the four-momentum of the test particle with each Killing vector and the Killing tensor leads to a conserved quantity along its trajectory. Using BL coordinates, we have

$$\mathcal{E} = -\xi_{\mu(t)} U^\mu = \left(1 - \frac{2Mr}{\rho^2}\right) \dot{t} + \frac{2aMr \sin^2 \theta}{\rho^2} \dot{\phi}, \quad (4.1.7)$$

$$\ell_z = \xi_{\mu(\phi)} U^\mu = -\frac{2aMr \sin^2 \theta}{\rho^2} \dot{t} + \frac{\Sigma \sin^2 \theta}{\rho^2} \dot{\phi}, \quad (4.1.8)$$

$$\begin{aligned} \ell^2 = \xi_{\mu\nu} U^\mu U^\nu &= \rho^4 \dot{\theta}^2 + \left[ (r^2 + a^2) \dot{\phi} - a \dot{t} \right]^2 \sin^2 \theta + a^2 \cos^2 \theta \\ &= -\frac{\rho^4}{\Delta} \dot{r}^2 + \Delta (\dot{t} - a \sin^2 \theta \dot{\phi})^2 - r^2, \end{aligned} \quad (4.1.9)$$

while in KS coordinates, using the transformation rule in Eq. (3.3.1), the expressions for these quantities are

$$\mathcal{E} = \left(1 - \frac{2Mr}{\rho^2}\right) \dot{T} + \frac{2aMr \sin^2 \theta}{\rho^2} \dot{\psi} - \frac{2Mr}{\rho^2} \dot{r}, \quad (4.1.10)$$

$$\ell_z = -\frac{2aMr \sin^2 \theta}{\rho^2} \dot{T} + \frac{\Sigma \sin^2 \theta}{\rho^2} \dot{\psi} - a \left(1 + \frac{2Mr}{\rho^2}\right) \sin^2 \theta \dot{r}, \quad (4.1.11)$$

$$\begin{aligned} \ell^2 &= \rho^4 \dot{\theta}^2 + \left[ (r^2 + a^2) \dot{\psi} - a (\dot{T} + \dot{r}) \right]^2 \sin^2 \theta + a^2 \cos^2 \theta \\ &= -\frac{\rho^4}{\Delta} \dot{r}^2 + \Delta \left[ \dot{T} - a \sin^2 \theta \dot{\psi} + \left( \frac{a^2 \sin^2 \theta - 2Mr}{\Delta} \right) \dot{r} \right]^2 - r^2. \end{aligned} \quad (4.1.12)$$

The constants of motion  $\mathcal{E}$ ,  $\ell_z$  and  $\ell^2$  are connected with the Carter constant  $\mathcal{Q}$  through the following identity<sup>(1)</sup>

$$\mathcal{Q} = \ell^2 - (\ell_z - a \mathcal{E})^2. \quad (4.1.13)$$

---

<sup>(1)</sup>The quantity  $\xi_{\mu\nu} U^\mu U^\nu$  is usually denoted as  $K$  in the literature. We have called it  $\ell^2$  here instead because, although an unconventional choice, it helps us to ease subsequent notation.

Substituting Eqs. (4.1.7)-(4.1.9) into Eq. (4.1.13) gives an alternative way of calculating  $\mathcal{Q}$ , i.e.

$$\mathcal{Q} = \rho^4 \dot{\theta}^2 + \ell_z^2 \cot^2 \theta - \varepsilon a^2 \cos^2 \theta, \quad (4.1.14)$$

where we have used the shorthand notation  $\varepsilon = \mathcal{E}^2 - 1$ . From Eq. (4.1.9) we see that  $\ell^2$  is a positive quantity by definition, while the constants  $\varepsilon$ ,  $\ell_z$  and  $\mathcal{Q}$  can have either sign. Now, if we consider the non-rotating limit, and substitute  $a = 0$  into Eq. (4.1.9), we get

$$\ell^2 = \mathcal{Q} + \ell_z^2 = r^4 (\dot{\theta}^2 + \sin^2 \theta \dot{\phi}^2), \quad (4.1.15)$$

which is just the square of the total magnitude of the angular momentum of a test particle in Schwarzschild spacetime. Nevertheless, in the general case  $a \neq 0$ , the interpretation of  $\ell^2$  is not as straightforward since its definition includes terms that couple, in a non-trivial way, the energy of the test particle and the spin of the BH (see de Felice & Preti, 1999, for a discussion about the physical interpretation of  $\ell^2$ ).

## 4.2 Equations of motion

As we saw in Section 2.1, the evolution with respect to the proper time of the coordinates of a given test particle freely falling in a general spacetime is determined by the geodesic equations (2.1.7). These equations constitute a system of second order, coupled ordinary differential equations. Nevertheless, the four first integrals of motion introduced in the previous section allow us to partially decouple them and to reduce them to a set of first-order ordinary differential equations. Using BL coordinates, the inversion of the system of Eqs. (4.1.7)-(4.1.10) leads to

$$\rho^2 \frac{dr}{d\tau} = \pm \sqrt{\mathcal{R}(r)}, \quad (4.2.1)$$

$$\rho^2 \frac{d\theta}{d\tau} = \pm \sqrt{\Theta(\theta)}, \quad (4.2.2)$$

$$\rho^2 \frac{d\phi}{d\tau} = \frac{\mathcal{A}(\theta)}{\sin^2 \theta} + \frac{a}{\Delta} \mathcal{B}(r), \quad (4.2.3)$$

$$\rho^2 \frac{dt}{d\tau} = a \mathcal{A}(\theta) + \frac{r^2 + a^2}{\Delta} \mathcal{B}(r), \quad (4.2.4)$$

with

$$\mathcal{R}(r) = \mathcal{B}^2(r) - (r^2 + \ell^2) \Delta, \quad (4.2.5)$$

$$\Theta(\theta) = \mathcal{Q} + \varepsilon a^2 \cos^2 \theta - \ell_z^2 \cot^2 \theta, \quad (4.2.6)$$

$$\mathcal{A}(\theta) = \ell_z - a \mathcal{E} \sin^2 \theta, \quad (4.2.7)$$

$$\mathcal{B}(r) = (r^2 + a^2) \mathcal{E} - a \ell_z. \quad (4.2.8)$$

Adopting KS coordinates instead, Eqs. (4.2.3) and (4.2.4) need to be changed to

$$\rho^2 \frac{d\psi}{d\tau} = \frac{\mathcal{A}(\theta)}{\sin^2 \theta} + \frac{a}{\Delta} \mathcal{B}(r) \pm \frac{2Mr}{\Delta} \sqrt{\mathcal{R}}, \quad (4.2.9)$$

$$\rho^2 \frac{dT}{d\tau} = a \mathcal{A}(\theta) + \frac{r^2 + a^2}{\Delta} \mathcal{B}(r) \pm \frac{a}{\Delta} \sqrt{\mathcal{R}}. \quad (4.2.10)$$

The signs in Eqs. (4.2.1) and (4.2.2) are independent of each other and change whenever the test particle reaches a radial or a polar turning point, respectively, in its trajectory. The sign in each of the last terms of Eqs. (4.2.9) and (4.2.10) should change in the same way as that of Eq. (4.2.1).

It is clear that the trajectory followed by a test particle is completely determined once a set of initial conditions

$$(x_0^\mu) = (t_0, r_0, \theta_0, \phi_0), \quad (\dot{x}_0^\mu) = (\dot{t}_0, \dot{r}_0, \dot{\theta}_0, \dot{\phi}_0) \quad (4.2.11)$$

is given. Note that the stationarity and axisymmetry of the Kerr metric allow us to take  $t_0 = 0$  and  $\phi_0 = 0$  without loss of generality while, by using the normalisation condition  $U^\mu U_\mu = -1$ , we can express  $\dot{t}_0$  as a function of the other three initial velocities. In this way we are left with five degrees of freedom for specifying an individual trajectory. Finally note that we can also characterise an individual timelike geodesic by giving the initial position in terms of  $r_0$  and  $\theta_0$ , and then fixing three of the constants of motion  $\mathcal{E}$ ,  $\ell_z$ ,  $\ell$  and  $\mathcal{Q}$  (these constants are related through Eq. (4.1.13)). The initial velocities then follow by substituting these values into Eqs. (4.2.1)-(4.2.4).

As mentioned in Section 3.3, when solving the geodesic equation for a particular case, one can choose to work either with BL or KS coordinates and, if necessary, relate back the results through Eq. (3.3.3). The actual choice is irrelevant as long as the test particle under consideration does not plunge into the black hole horizon. If it does do that, one should use the KS description since that coordinate system is well-behaved at the horizons as we discussed in Section 3.3.

Before proceeding with a more detailed analysis of the system of differential equations in Eqs. (4.2.1)-(4.2.4), we note here that they can be easily recast as the following system of integral equations (Chandrasekhar, 1983)

$$\int_{r_0}^r \frac{dr'}{\sqrt{\mathcal{R}(r')}} = \pm \int_{\theta_0}^\theta \frac{d\theta'}{\sqrt{\Theta(\theta')}}, \quad (4.2.12)$$

$$\phi = \int_{r_0}^r \frac{\ell_z r'^2 + 2Mr'(a\mathcal{E} - \ell_z)}{\Delta \sqrt{\mathcal{R}(r')}} dr' + \int_{\theta_0}^\theta \frac{\ell_z \cot^2 \theta'}{\sqrt{\Theta(\theta')}} d\theta', \quad (4.2.13)$$

$$t = \int_{r_0}^r \frac{r'^2(r'^2 + a^2)\mathcal{E} + 2aMr'(a\mathcal{E} - \ell_z)}{\Delta \sqrt{\mathcal{R}(r')}} dr' + \int_{\theta_0}^\theta \frac{\mathcal{E} a^2 \cos^2 \theta'}{\sqrt{\Theta(\theta')}} d\theta', \quad (4.2.14)$$

$$\tau = \int_{r_0}^r \frac{r'^2}{\sqrt{\mathcal{R}(r')}} dr' + \int_{\theta_0}^\theta \frac{a^2 \cos^2 \theta'}{\sqrt{\Theta(\theta')}} d\theta'. \quad (4.2.15)$$

As discussed by Chandrasekhar (1983), each of these integrals is solvable in terms of Jacobi elliptic functions. In particular, in Chapter 5 we show in detail how to solve the two integrals in Eq. (4.2.12), since the resulting analytic expression will be used as the basic building block for the toy model which we intend to use as a benchmark for the SPHINCS code. The solutions for the rest of the integrals can be found in, e.g. Kraniotis (2004); Fujita & Hikida (2009).

### 4.3 Circular orbits in the equatorial plane

Before studying in general the different possible trajectories of test particles, here we briefly review some results concerning circular orbits in the equatorial plane that will be useful for the subsequent sections. We follow here the exposition given in Bardeen et al. (1972). This kind of motion also plays a prominent role in the context of thin accretion discs, where the fluid in the disc moves, to a first approximation, along circular orbits with a slow secular inspiralling motion driven by viscous stresses acting on time scales that are typically much longer than the orbital period (see e.g. Shakura & Sunyaev, 1973; Pringle, 1981).

A necessary condition for the motion of a test particle to be restricted to the equatorial plane comes from substituting  $\theta = \pi/2$  and  $\dot{\theta} = 0$  into Eq. (4.1.14), which results in  $\mathcal{Q} = 0$ . This condition, together with Eq. (4.1.13), implies that  $\ell^2 = (\ell_z - a\mathcal{E})^2$ . However, in order to have circular motion we must also require that both  $\dot{r}$  and  $\ddot{r}$  are identically zero. From Eq. (4.2.1), these two conditions translate as

$$\mathcal{R}(r) = 0, \quad \frac{\partial \mathcal{R}(r)}{\partial r} = 0, \quad (4.3.1)$$

giving a coupled system of quadratic expressions involving  $\mathcal{E}$  and  $\ell_z$ . After some algebra, the solution to this system is found to be

$$\mathcal{E} = \frac{r^{3/2} - 2Mr^{1/2} + aM^{1/2}}{r^{3/4}(r^{3/2} - 3Mr^{1/2} + 2aM^{1/2})^{1/2}}, \quad (4.3.2)$$

$$\ell_z = \frac{M^{1/2}(r^2 - 2aM^{1/2}r^{1/2} + a^2)}{r^{3/4}(r^{3/2} - 3Mr^{1/2} + 2aM^{1/2})^{1/2}}. \quad (4.3.3)$$

In these expressions we have assumed that  $\ell_z > 0$ . Whether the particle is in co-rotation or counter-rotation with the spin of the BH is then determined by the sign of  $a$ , i.e.  $a > 0$  for a co-rotating orbit and  $a < 0$  for counter-rotating one.

In Figure 4.1 we plot  $\mathcal{E}$  and  $\ell_z$  as functions of  $r$  for  $a = 0$  and  $\pm 0.98$ . From Eqs. (4.3.2) and (4.3.3), it is clear that the spin of the BH in a Kerr spacetime plays an important role through a non-trivial coupling with the energy and angular momentum of the test particle. Indeed, for  $a \neq 0$  one has that, in order to remain in a circular orbit at a constant radius  $r$ , a co-rotating particle needs less angular momentum than the corresponding counter-rotating one, whereas the former particle is more tightly bound than the latter at the same radius. Note that in the non-rotating case (i.e. Schwarzschild spacetime) it is irrelevant to make any distinction between co-rotating and counter-rotating motion.

The fact that co-rotating circular orbits around a rotating BH are more tightly bound has important implications for the study of accretion discs. This opens the possibility of extracting more binding energy for conversion into thermal or neutrino emission before the fluid particles ultimately disappear inside the BH horizon (see e.g. Novikov & Thorne, 1973). Moreover, co-rotating orbits are expected to occur more frequently in astrophysical systems in which the accreting matter and the central BH share a common origin (e.g. the outer layers of a star falling onto a collapsing stellar core Woosley, 1993).

Now, going back to Eqs. (4.3.2) and (4.3.3), we note that the common denominator becomes singular when

$$r^{3/2} - 3Mr^{1/2} + 2aM^{1/2} = 0. \quad (4.3.4)$$

This cubic polynomial in  $r^{1/2}$  has only one real root which is given by

$$\frac{r_{\text{ph}}}{2M} = 1 + \cos \left[ \frac{2}{3} \cos^{-1} \left( \frac{-a}{M} \right) \right]. \quad (4.3.5)$$

The circular orbit corresponding to this radius is characterised by infinite energy and angular momentum, which means that it can only be reached by particles moving at the speed of light. In other words,  $r_{\text{ph}}$  corresponds to the radial location of a photon moving along this circular orbit. We can also see that the denominator in Eqs. (4.3.2) and (4.3.3) is real only for  $r > r_{\text{ph}}$ , i.e. circular orbits can only exist for radii larger than  $r_{\text{ph}}$ .

Now we need to note that, contrary to the Newtonian case, not all of the circular orbits in Kerr (or Schwarzschild) spacetime are necessarily stable. Stability requires that, in addition to Eq. (4.3.1), the condition

$$\frac{\partial^2 \mathcal{R}(r)}{\partial r^2} < 0 \quad (4.3.6)$$

should also be satisfied. Eq. (4.3.6) translates into

$$r^2 - 6Mr + 8a(Mr)^{1/2} - 3a^2 \geq 0. \quad (4.3.7)$$

The equality in this expression defines the location of a marginally stable (ms) circular orbit (also known as innermost stable circular orbit). This equation can be viewed as a fourth order polynomial in  $r^{1/2}$  whose only root larger than  $r_+$  is given by

$$\begin{aligned} r_{\text{ms}} &= 3M + Z_2 - \text{Sign}(a)[(3M - Z_1)(3M + Z_1 + 2Z_2)]^{1/2}, \\ Z_1 &= M + (M^2 - a^2)^{1/3} \left[ (M + a)^{1/3} + (M - a)^{1/3} \right], \\ Z_2 &= (3a^2 + Z_1^2)^{1/2}. \end{aligned} \quad (4.3.8)$$

We can then conclude that stable circular motion occurs for  $r > r_{\text{ms}}$ . For a radius  $r$  between  $r_{\text{ph}}$  and  $r_{\text{ms}}$  we find circular orbits which are unstable since any small perturbation of a test particle at that position, will lead it to either fall into the BH horizon or

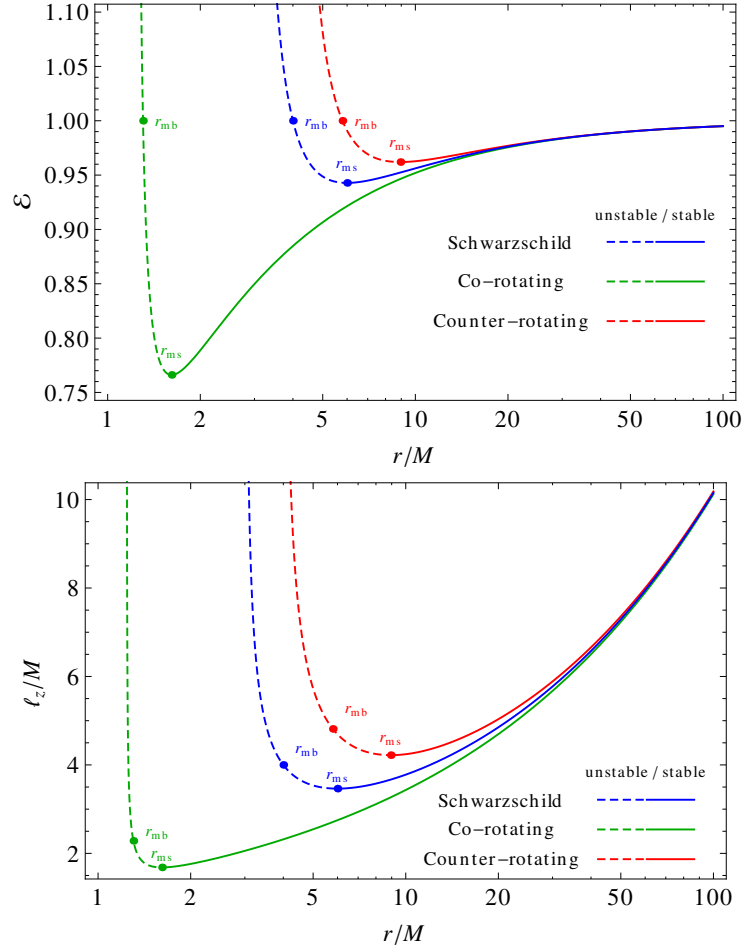


**Figure 4.1:** The energy  $\mathcal{E}$  and the axial component of the angular momentum  $\ell_z$  are plotted as functions of the radius of circular orbits for  $a = 0$  and  $\pm 0.98$ . Note how the curves for both energy and angular momentum split into two branches for  $a \neq 0$  as a result of the spin-orbit coupling effect described in Eqs. (4.3.2) and (4.3.3). Given a fixed radius, the values of  $\mathcal{E}$  and  $\ell_z$  are smaller for a co-rotating particle with  $a \neq 0$  than the corresponding values in the  $a = 0$  case, while the opposite happens for a counter-rotating particle. Also note that co-rotating circular orbits can extend to smaller radii than the counter-rotating ones.

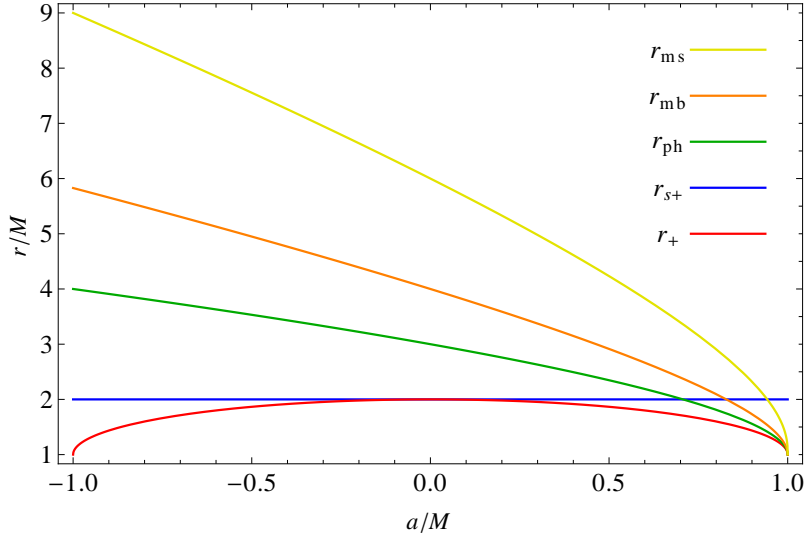


**Figure 4.2:** The radii of various circular orbits in the equatorial plane of a Kerr spacetime are plotted as functions of the spin parameter  $a$ . Cases with  $a > 0$  correspond to orbits co-rotating with the BH, while counter-rotating orbits correspond to  $a < 0$ . The locations of the outer event horizon  $r_+$  and of the static limit  $r_{s+}$  are also indicated. Note that all of the radii  $r_+$ ,  $r_{ph}$ ,  $r_{mb}$  and  $r_{ms}$  converge into  $r = M$  for  $a = M$ . This is a misleading effect related to the fact that the BL  $r$  coordinate is not well-behaved for this extreme value of  $a$ . All these radii are, in fact, seen to be distinct when measurements are made in terms of proper radial distance.

escape to infinity. Note that this second possibility is only possible for orbits with  $\mathcal{E} > 1$ , since unstable circular orbits with  $\mathcal{E} < 1$  are inevitably bound to fall into the BH. For this reason, the unstable circular orbit corresponding to  $\mathcal{E} = 1$  is called the marginally bound (mb) circular orbit. Solving for  $r$  in Eq. (4.3.2), the position of this orbit is given by

$$r_{mb} = 2M - a + 2M^{1/2}(M - a)^{1/2}. \quad (4.3.9)$$

In Figure 4.2 we plot the radii of all of the circular orbits discussed in this section as a function of the spin parameter  $a$ . As already noted, unstable and unbound circular orbits are found for  $r_{ph} < r < r_{mb}$ , unstable and bound circular orbits correspond to  $r_{mb} < r < r_{ms}$ , while stable circular orbits exist only for  $r > r_{ms}$ .

## 4.4 Radial motion

We study here the radial motion as determined by Eq. (4.2.1), i.e.

$$\rho^2 \frac{dr}{d\tau} = \pm \sqrt{\mathcal{R}(r)}. \quad (4.4.1)$$

From the definition of  $\mathcal{R}(r)$  in Eq. (4.2.5), we can expand it as the following fourth order polynomial in  $r$

$$\mathcal{R}(r) = \varepsilon r^4 + 2Mr^3 + (\varepsilon a^2 - \ell_z^2 - \mathcal{Q}) r^2 + 2M\ell^2 r - a^2 \mathcal{Q}. \quad (4.4.2)$$

From Eq. (4.4.1), it is clear that the radial coordinate is constrained to vary within an interval in which the condition  $\mathcal{R}(r) \geq 0$  is fulfilled. It follows then that, whenever the roots of  $\mathcal{R}(r)$  are real and greater than  $r_+$ , they constitute turning points at which  $\dot{r}$  vanishes and the radial motion reverses direction. Moreover, a simple consequence that can be drawn from the coefficient accompanying the leading power of  $r$  in Eq. (4.4.2) is that a necessary condition for a trajectory to extend to infinity is  $\varepsilon \geq 0$  ( $\mathcal{E} \geq 1$ ). Hence, bound orbits can exist only for  $\varepsilon < 0$  ( $\mathcal{E} < 1$ ). By inspecting the rest of the coefficients in Eq. (4.4.2), it is possible to show (see e.g. Dymnikova, 1986) that, whenever  $\varepsilon > 0$ , there can exist at most two turning points (i.e. there are only two roots larger than  $r_+$ ). Instead for a particle with  $\varepsilon < 0$ , there cannot be more than three turning points.

In order to study in further detail the different types of radial motion, it is convenient to introduce a pair of radial effective potentials  $\mathcal{V}_\pm(r)$ . This approach is very common in the context of Newtonian gravity as well as for the Schwarzschild spacetime. Different implementations of radial effective potentials for the Kerr spacetime exist (see e.g. Krivenko et al., 1976; Frolov & Novikov, 1998), although they have been of limited use. This is in part due to their definition not being unique but, more importantly, also because  $\mathcal{R}$  involves both quadratic and linear terms in  $\mathcal{E}$ , which means that in Kerr spacetime two radial effective potentials are needed rather than a single one as in the Newtonian and Schwarzschild cases.

Just as in Newtonian mechanics, a radial effective potential should involve the source of the gravitational field (in this case both  $M$  and  $a$ ) and the angular momentum of the test particle, but should be independent of  $\mathcal{E}$ . The technical issue that arises for the Kerr spacetime is that we have three quantities related to the angular momentum of the particle ( $\mathcal{Q}$ ,  $\ell$ ,  $\ell_z$ ) which, at the same time, are coupled in a non-trivial way with  $a$  and  $\mathcal{E}$  (see Eq. 4.1.13). Moreover, out of these three quantities, just two can be chosen independently, and different combinations of them lead to different definitions of  $\mathcal{V}_\pm(r)$ . For example, Krivenko et al. (1976) defined a pair of radial effective potentials in terms of  $\ell_z$  and  $\ell$ , while Frolov & Novikov (1998) defined another pair in terms of  $\ell_z$  and  $\mathcal{Q}$ . Instead, we have found that defining them in terms of  $\ell$  and  $\mathcal{Q}$  gives the following relatively simple expression

$$\mathcal{V}_\pm(r) = \frac{a\sqrt{\ell^2 - \mathcal{Q}} \pm \sqrt{(\ell^2 + r^2)\Delta}}{r^2}. \quad (4.4.3)$$

As far as we know, this particular definition has not been used in the literature before. We can now rewrite  $\mathcal{R}(r)$  in terms of  $\mathcal{V}_\pm(r)$  as

$$\begin{aligned} \mathcal{R}(r) &= \left( r^2 \mathcal{E} - a\sqrt{\ell^2 - \mathcal{Q}} \right)^2 - (\ell^2 + r^2)\Delta \\ &= r^4 [\mathcal{E} - \mathcal{V}_+(r)] [\mathcal{E} - \mathcal{V}_-(r)], \end{aligned} \quad (4.4.4)$$

with which Eq. (4.4.4) then becomes

$$\left(\frac{\rho}{r}\right)^2 \frac{dr}{d\tau} = \pm \sqrt{[\mathcal{E} - \mathcal{V}_+(r)][\mathcal{E} - \mathcal{V}_-(r)]}. \quad (4.4.5)$$

Note that in the non-rotating case ( $a = 0$ ), we have that  $\mathcal{V}_- = -\mathcal{V}_+$  and so Eq. (4.4.5) reduces to

$$\frac{dr}{d\tau} = \pm \sqrt{\mathcal{E}^2 - \mathcal{V}_s(r)}. \quad (4.4.6)$$

where  $\mathcal{V}_s(r) = \mathcal{V}_+^2 = \mathcal{V}_-^2$  is the radial effective potential for Schwarzschild spacetime given by

$$\mathcal{V}_s(r) = 1 - \frac{2M}{r} + \frac{\ell^2}{r^2} - \frac{2M\ell^2}{r^3}. \quad (4.4.7)$$

The following are some relevant properties of  $\mathcal{V}_\pm(r)$

$$\mathcal{V}_+(r) > \mathcal{V}_-(r), \quad (\text{for } r > r_+) \quad (4.4.8)$$

$$\mathcal{V}_+(r_+) = \mathcal{V}_-(r_+), \quad (4.4.9)$$

$$\frac{\partial \mathcal{V}_+}{\partial r}(r_+) = \frac{\partial \mathcal{V}_-}{\partial r}(r_+) = \infty, \quad (4.4.10)$$

$$\lim_{r \rightarrow \infty} \mathcal{V}_+(r) = 1, \quad (4.4.11)$$

$$\lim_{r \rightarrow \infty} \mathcal{V}_-(r) = -1. \quad (4.4.12)$$

From Eqs.(4.4.5) and (4.4.8) it follows that the radial motion is restricted by

$$\mathcal{E} \geq \mathcal{V}_+(r) \quad \text{or} \quad \mathcal{E} \leq \mathcal{V}_-(r). \quad (4.4.13)$$

In Figure 4.3 we plot the radial effective potentials as functions of  $r$  for typical values of the parameters  $\mathcal{Q}$  and  $\ell$  that lead to generic, non-equatorial orbits. In this figure we see that each potential has two extreme points: a global maximum and a local minimum (these extremes are highlighted in the figure using red and green points, respectively). The former corresponds to an unstable constant-radius trajectory while the latter corresponds to a stable constant-radius trajectory. When  $\mathcal{Q} = 0$ , these two trajectories reduce to the stable and unstable circular orbits discussed in Section 4.3. In the general case of non-equatorial motion, these trajectories are not restricted to move in a circle but rather on the surface of a sphere between two fixed latitudes. For this reason, stable constant-radius trajectories are usually referred to as ‘spherical’ trajectories. This kind of motion is due to the fact that in a Kerr spacetime, in addition to the pericentre precession, the frame-dragging effect forces the orbital plane to precess latitudinally as well. See Figures A.14 and A.18 for examples of these two types of trajectory.

We can also see in this figure that most of the energy levels that satisfy  $\mathcal{E} \leq \mathcal{V}_-(r)$  are negative, while the few which are positive correspond to short-lived trajectories that are always trapped inside the BH horizon. The study of this type of trajectory is relevant in the context of energy extraction from a rotating BH by the mechanism known as Penrose process (Penrose, 1969). But besides this phenomenon, trajectories associated

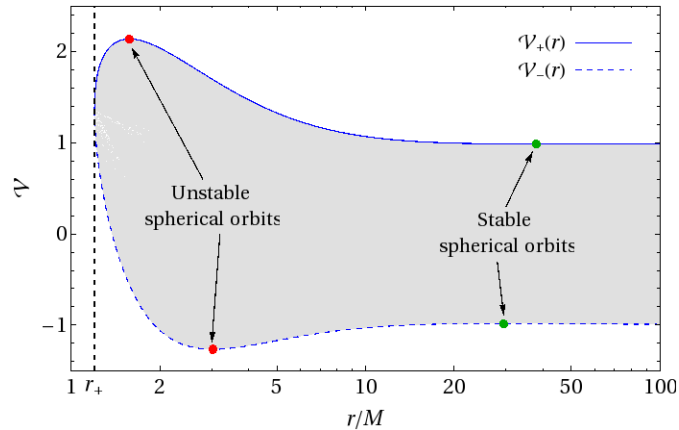


**Figure 4.3:** The two radial effective potentials  $\mathcal{V}_{\pm}(r)$  are plotted for a Kerr spacetime with spin parameter  $a = 0.98 M$  and for fixed values of the constants of motion  $\ell = 6 M$  and  $\mathcal{Q} = M$ . The shaded region represents the forbidden set of trajectories for which  $\mathcal{R}(r) < 0$ . The red and green dots indicate the location of unstable and stable spherical orbits, respectively.

with  $\mathcal{V}_-(r)$  have limited importance for observations made far away from the BH. For this reason, in the present work we further consider only energy levels satisfying  $\mathcal{E} \geq \mathcal{V}_+(r)$ .

In Figure 4.4 we show the behaviour of  $\mathcal{V}_+(r)$  as the parameter  $\ell$  is decreased from  $\ell = 3 M$  to  $\ell = M$  while holding fixed the ratio  $\mathcal{Q}/\ell^2 = 0.8$ . Here we again take  $a = 0.98 M$ . From this figure we see that, for a large enough value of  $\ell$ , the curve  $\mathcal{V}_+(r)$  presents the two extreme points described in the previous paragraph. In the case with the largest  $\ell$  depicted in this figure, we have that the unstable spherical orbit is energetically unbound ( $\mathcal{E} > 1$ ), while the stable one is energetically bound ( $\mathcal{E} < 1$ ). As the value of  $\ell$  is decreased, the two extreme points start approaching each other. Eventually, a first critical value  $\ell = \ell_{\text{mb}}$  is reached when the unstable spherical orbit becomes marginally bound ( $\mathcal{E} = 1$ ). The trajectory located at this radius  $r_{\text{mb}}$ , represents the generalisation of the marginally bound circular orbit discussed in Section 4.3. As we keep decreasing the value of  $\ell$ , a second critical value  $\ell = \ell_{\text{ms}}$  is reached when the two extreme points merge into a single saddle point. This kind of trajectory, located at  $r_{\text{ms}}$ , generalises the marginally stable circular orbit discussed in Section 4.3. For values of  $\ell < \ell_{\text{ms}}$ ,  $\mathcal{V}_+(r)$  has no extremum at all, becoming a monotonically increasing function of  $r$ .

Let us now go back to the differential equation in Eq. (4.4.5). This equation can be identified as a dynamical system which is almost autonomous in  $r$  since the only dependence on  $\theta$  comes through the term  $\rho^2$  on the left hand side of the equation, while all of the important information about the qualitative behaviour of  $\dot{r}$  is encoded on the right hand side. Following Krivenko et al. (1976), we consider the mapping of the original phase-space  $r-\dot{r}$  into the equivalent dynamical system  $r-(\rho/r)^2\dot{r}$ . Since the

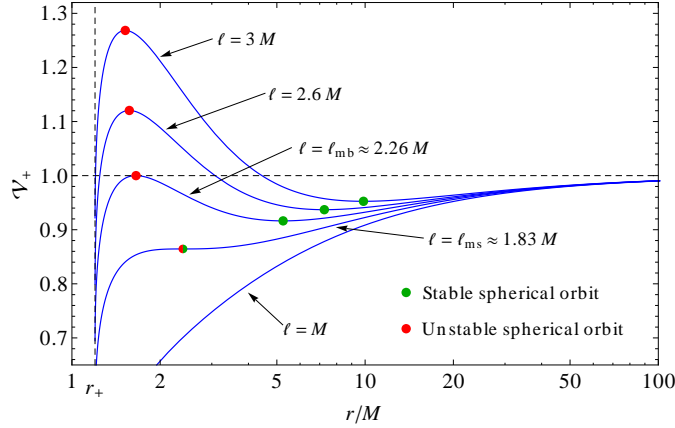


**Figure 4.4:** The radial effective potential  $\mathcal{V}_+(r)$  in a Kerr spacetime with  $a = 0.98 M$  is plotted for different decreasing values of  $\ell$  while the ratio  $\mathcal{Q}/\ell^2 = 0.8$  is kept fixed.

factor  $(\rho/r)^2 \approx 1$ , we see that this is a trivial mapping which is unique, continuous, and non-singular for  $r > 0$ .

In Figure 4.5 we show some representative examples of non-equatorial trajectories with  $\ell = 3 M$  and  $\mathcal{Q} = 8.5 M^2$  in a Kerr spacetime with  $a = 0.98 M$ . In the top panel of the figure, we plot the radial effective potential for these parameter values and highlight six  $\mathcal{E} = \text{const.}$  levels. In the bottom panel we show the corresponding trajectories as seen in the equivalent phase-space  $r - (\rho/r)^2 \dot{r}$ . The results of the numerical integration of these trajectories are presented in Section A.3.

As is clear from Figure 4.5, an energy level that does not intersect the curve  $\mathcal{V}_+(r)$  corresponds to a trajectory that plunges inside  $r_+$ . On the other hand, for every level  $\mathcal{E} = \text{const.}$  that intersects  $\mathcal{V}_+(r)$ , there are two possible trajectories: one above  $r_{\text{mb}}$  and the other below it. Trajectories of the latter type are restricted to a narrow radial domain and, eventually, end up trapped inside the BH horizon. As mentioned before, the physical relevance of this type of trajectory is rather limited and, for this reason, in the following we shall only consider trajectories that can extend to  $r > r_{\text{mb}}$ . In general, the trajectories of this type can be classified as:

**Stable spherical trajectories** (see purple trajectory in Figure 4.5 and Figure A.14). As already mentioned, this type of trajectory is characterised by a constant radius. On the other hand, as we discuss in the next section, the polar motion in this case is restricted between two fixed latitudes which are symmetric with respect to the equatorial plane.

**Elliptic-like trajectories** (see blue trajectory in Figure 4.5 and Figure A.15). In this case we have that the radial coordinate oscillates periodically between the turning

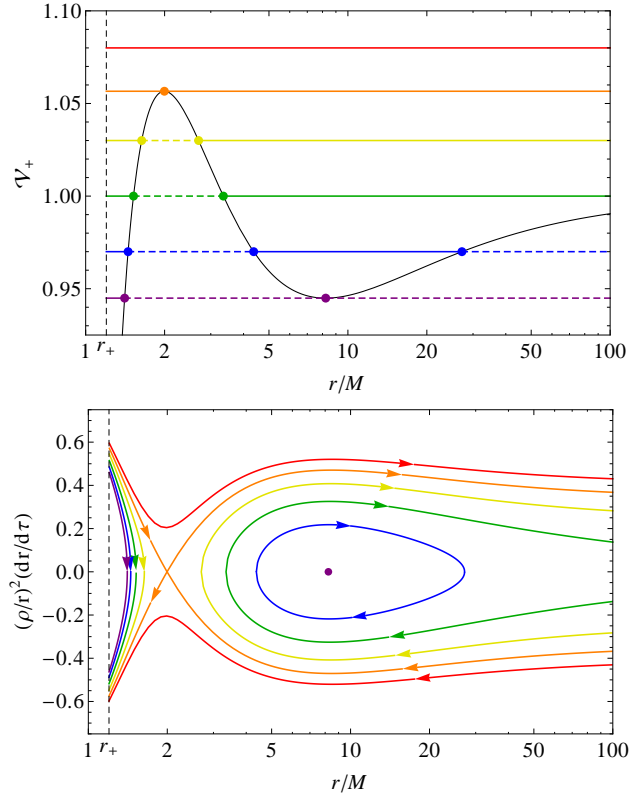


**Figure 4.5:** This figure shows the radial component of a set of representative off-equatorial orbits in a Kerr spacetime with  $a = 0.98 M$ . Fixed values for the specific angular momentum parameters are taken as  $\ell = 3 M$  and  $\mathcal{Q} = 8.5 M^2$ . The top panel shows the radial effective potential  $\mathcal{V}_+(r)$  with the highlighted energy levels plotted as  $\mathcal{E} = \text{const.}$  lines. Radial turning points are also highlighted, while the dashed segment on each of the energy levels represents points which are physically inaccessible since for them  $\mathcal{R}(r) < 0$ . The bottom panel shows the trajectories as seen in the phase-space of the equivalent dynamical system  $r - (\rho/r)^2 \dot{r}$ .

points. The actual period of  $r(\tau)$  is a non-trivial combination of the radial and polar epicyclic frequencies (see e.g. Mino, 2003; Drasco & Hughes, 2004; Schmidt, 2002).

**Parabolic-like trajectories** (see green trajectory in Figure 4.5 and Figure A.16). This type of trajectory is the degenerate case of an elliptic-like trajectory in which the apocentre (turning point farthest from the centre) diverges to infinity. In this case we have that the test particle asymptotically approaches spatial infinity with a vanishing radial velocity, i.e.  $\dot{r}_\infty = 0$ .

**Hyperbolic-like trajectories** (see yellow trajectory in Figure 4.5 and Figure A.17). Similarly to parabolic-like trajectory, here there is no upper bound to the radial motion but in this case the asymptotic value of  $\dot{r}_\infty$  is a finite quantity.

**Unstable spherical trajectories** (see orange trajectory in Figure 4.5 and Figure A.18). As already discussed, this kind of trajectory represents an example of unstable motion. Note that the necessary initial conditions leading to one of these trajectories need to be very finely-tuned. For this reason, these trajectories are actually part of a set of measure zero.

**Plunging trajectories** (see red trajectory in Figure 4.5 and Figure A.19). A test particle on this type of trajectory never encounters the centrifugal barrier of the effective potential (no lower turning points) and, if it is initially moving inwards, it will end up plunging into the BH horizon.

## 4.5 Polar motion

We study now the polar motion as determined by Eq. (4.2.2), i.e.

$$\rho^2 \frac{d\theta}{d\tau} = \pm \sqrt{\Theta(\theta)}, \quad (4.5.1)$$

with  $\Theta(\theta)$  as given in Eq. (4.2.6). In order to analyse the different possible types of polar motion, we introduce a polar effective potential  $\mathcal{H}(\theta)$  defined by

$$\mathcal{H}(\theta) = \ell_z^2 \cot^2 \theta - \varepsilon a^2 \cos^2 \theta, \quad (4.5.2)$$

and then recast Eq. (4.5.1) in terms of  $\mathcal{H}(\theta)$  as

$$\rho^2 \frac{d\theta}{d\tau} = \pm \sqrt{\mathcal{Q} - \mathcal{H}(\theta)}. \quad (4.5.3)$$

As in the radial case, we can identify this equation as a dynamical system which is almost decoupled from the radial coordinate. Indeed, all of the relevant qualitative features of  $\dot{\theta}$  are determined by the right hand side of Eq. (4.5.3) which depends just on  $\theta$ .

Note that a trivial solution for Eq. (4.5.3) arises when  $\mathcal{Q} = \ell_z = \varepsilon = 0$ , since then  $\dot{\theta} \equiv 0$ . In this case, the polar angle  $\theta$  can take any constant value. This special set of trajectories is discussed in detail in Bičák & Stuchlík (1976b).

From Eq. (4.5.3), we see that the constant of motion  $\mathcal{Q}$  now plays the role that  $\mathcal{E}$  played for the radial effective potential, i.e. given a constant value of  $\mathcal{Q}$ , the polar angle  $\theta$  is allowed to vary within a range such that

$$\mathcal{Q} \geq \mathcal{H}(\theta). \quad (4.5.4)$$

For each root of the equation  $\mathcal{H}(\theta) = \mathcal{Q}$  one has that  $\dot{\theta} = 0$  and so these values of  $\theta$  represent turning points in the polar motion. It then follows that the polar solution is

bracketed between two consecutive real roots of the equation  $\mathcal{H}(\theta) = \mathcal{Q}$  (to be found within the natural domain of  $\theta$ , i.e.  $\theta \in [0, \pi]$ ). Another simple consequence that can be drawn from Eq. (4.5.2), is that the real roots of  $\mathcal{H}(\theta) = \mathcal{Q}$  come in pairs which are symmetric with respect to  $\theta = \pi/2$ . In other words, if  $\theta_a$  is a root of  $\mathcal{H}(\theta) = \mathcal{Q}$ , then  $\theta_{a'} = \pi - \theta_a$  will also be a root. Provided that  $\varepsilon \neq 0$ , the equation  $\mathcal{H}(\theta) = \mathcal{Q}$  can be further simplified to the following quadratic expression in  $Y = \sin^2 \theta$

$$Y^2 - 2BY + C = 0, \quad (4.5.5)$$

with

$$B = \frac{\mathcal{Q} + \ell_z^2 + \varepsilon a^2}{2\varepsilon a^2} \quad \text{and} \quad C = \frac{\ell_z^2}{\varepsilon a^2}.$$

From Eq. (4.5.5), explicit expressions for the roots follow immediately as

$$\begin{aligned} \theta_{a,b} &= \sin^{-1} \left[ B \mp \text{Sign}(\varepsilon) \sqrt{B^2 - C} \right]^{1/2}, \\ \theta_{a',b'} &= \pi - \theta_{a,b}. \end{aligned} \quad (4.5.6)$$

On the other hand, if  $\varepsilon = 0$  then there are only two real roots of the equation  $\mathcal{H}(\theta) = \mathcal{Q}$  given by

$$\theta_{a,a'} = \tan^{-1} \left( \pm \frac{\ell_z}{\sqrt{\mathcal{Q}}} \right). \quad (4.5.7)$$

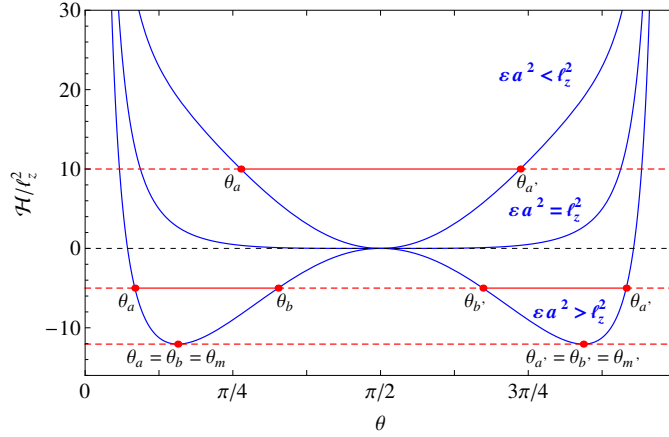


**Figure 4.6:** The polar effective potential  $\mathcal{H}(\theta)$  is plotted for different combinations of the ratio  $\varepsilon a^2/\ell_z^2$ . From top to bottom, the blue curves correspond to  $\varepsilon a^2/\ell_z^2 = -20, 1, 20$ , while the horizontal red lines correspond to  $\mathcal{Q} = \text{const.}$  levels. A dashed segment in these levels indicates a set of forbidden orbits since for them  $\Theta(\theta) < 0$ . Turning points of the polar motion are indicated by red dots.

In order to proceed with the study of the qualitative features of the polar motion, we consider first the case when  $\ell_z \neq 0$ . In Figure 4.6 we show  $\mathcal{H}(\theta)$  for representative

values of the constants of motion in this case. As is clear from Eq. (4.5.3), here the polar effective potential diverges as  $\theta$  approaches either 0 or  $\pi$ . In other words, a test particle with  $\ell_z \neq 0$  cannot cross the polar axis. Moreover, it also follows from Eq. (4.5.3) that the ratio  $\varepsilon a^2/\ell_z^2$  is the key parameter combination determining the overall shape of  $\mathcal{H}(\theta)$ . Let us examine the following cases:

- i)  $\varepsilon a^2 \leq \ell_z^2$ . Here we have that  $\mathcal{H}(\theta)$  is characterised by a single global minimum located at  $\theta = \pi/2$ . In this case, Eq. (4.5.6) leads to only two real roots ( $\theta_a$  and  $\theta_{a'}$ ). If, in addition,  $\mathcal{Q} = 0$ , then these two roots merge as  $\theta_a = \theta_{a'} = \pi/2$  and the solution is simply  $\theta \equiv \pi/2$ . This case represents an equilibrium solution for the polar motion. Instead, for  $\mathcal{Q} > 0$  the multiplicity is broken and we get trajectories off the equatorial plane that oscillate symmetrically about it ( $\theta \in [\theta_a, \theta_{a'}]$ ).
- ii)  $\varepsilon a^2 > \ell_z^2$ . Clearly this kind of motion is accessible just for test particles with  $\varepsilon > 0$ , i.e. for unbound energy levels. In this case we have that the point  $\theta = \pi/2$  becomes a local maximum (the motion in the equatorial plane is no longer stable) and that two minima appear located symmetrically on either side of the equator at

$$\theta_m = \sin^{-1} \sqrt{\frac{|\ell_z/a|}{\sqrt{\varepsilon}}} \quad \text{and} \quad \theta_{m'} = \pi - \theta_m. \quad (4.5.8)$$

For  $\mathcal{Q} > 0$ , Eq. (4.5.6) leads again to only two real roots ( $\theta_a$  and  $\theta_{a'}$ ). Instead, for  $\mathcal{Q} \leq 0$ , the four roots in Eq. (4.5.6) are real and ordered as  $\theta_a < \theta_b \leq \pi/2 \leq \theta_{b'} < \theta_{a'}$ . In this last case we have that the motion is confined to a single hemisphere and  $\theta \in [\theta_a, \theta_b]$  (or  $\theta \in [\theta_{b'}, \theta_{a'}]$ ). Note that when  $\mathcal{Q} = 0$  there is a degeneracy of the roots since  $\theta_b = \theta_{b'} = \pi/2$ . On the other hand, when  $\mathcal{Q}$  reaches its minimum possible value, i.e.  $\mathcal{Q} = \mathcal{H}(\theta_m) = -(\ell_z - a\sqrt{\varepsilon})^2$ , we have  $\theta_a = \theta_b = \theta_m$  and  $\theta_{a'} = \theta_{b'} = \theta_{m'}$ . In this last case the polar solution is simply  $\theta \equiv \theta_m$ .

In Figure 4.7 we show some representative polar orbits for different combinations of the parameters  $\varepsilon$ ,  $\ell_z$  and  $\mathcal{Q}$ . First, we locate these orbits as  $\mathcal{Q} = \text{const.}$  levels on a plot of  $\mathcal{H}(\theta)$ , and then show the corresponding trajectories on the trivial mapping of the phase-space  $\theta - \dot{\theta} \mapsto \theta - \rho^2 \dot{\theta}$ . In Sections A.4 and A.5, we show examples of the numerical integration of some of these trajectories.

For the sake of completeness, we consider now the case  $\ell_z = 0$ . In Figure 4.8 we show generic forms of  $\mathcal{H}(\theta)$  in this case as well as some representative trajectories in the phase-space of the equivalent dynamical system  $\theta - \rho^2 \dot{\theta}$ . A special characteristic of this case, is that now there are trajectories that can cross the polar axis where the polar coordinate is singular. From Eq. (4.5.6) it follows that

$$\begin{aligned} \theta_a &= 0, & \theta_{a'} &= \pi, \\ \theta_{b, b'} &= \cos^{-1} \left( \pm \sqrt{\frac{-\mathcal{Q}}{\varepsilon a^2}} \right). \end{aligned} \quad (4.5.9)$$

Note that, even though  $\theta_a$  and  $\theta_{a'}$  are not roots of Eq. (4.5.5), they do constitute formal turning points since, at these angles, the polar coordinate reverses direction and  $\dot{\theta}$

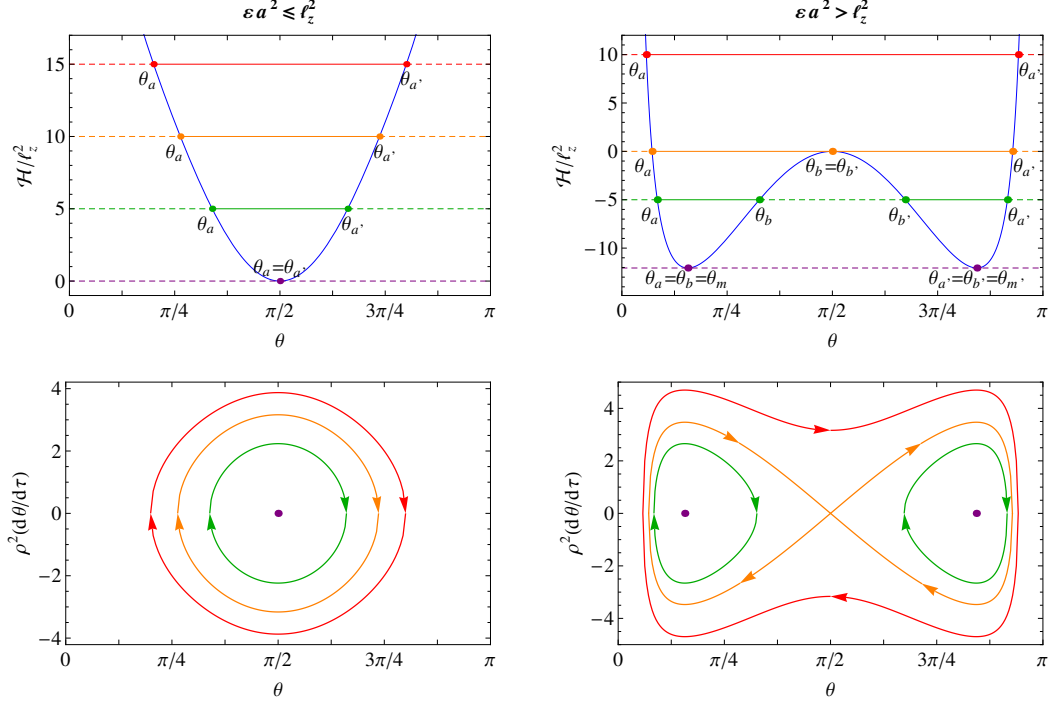


**Figure 4.7:** The figure shows the polar component of a set of representative orbits in a Kerr spacetime with  $a = 0.98 M$ . Fixed values for the specific angular momentum parameters are taken as  $\ell = 4 M$  and  $\ell_z = M$ . The top panel shows the polar effective potential  $\mathcal{H}(\theta)$  with highlighted  $\mathcal{Q} = \text{const.}$  levels. Polar turning points are also highlighted, while the dashed segment on each of the  $\mathcal{Q} = \text{const.}$  levels represents points which are physically inaccessible since for them  $\Theta(\theta) < 0$ . The bottom panel shows a phase-space of the equivalent dynamical system  $\theta - \rho^2\dot{\theta}$ .

changes sign discontinuously. This effect is clearly seen in the phase-space diagrams in the bottom panels of Figure 4.8.

From Eq. (4.5.9) we see that, a sufficient condition for  $\theta_b$  to be real is that, if  $\varepsilon > 0$  then  $\mathcal{Q} < 0$ , or if  $\varepsilon \leq 0$  then  $\mathcal{Q} \leq |\varepsilon|a^2$ . In any other case there will be no real roots for the equation  $\Theta(\theta) = 0$  which implies that the polar coordinate can in principle sweep across the whole polar domain and repeatedly cross the polar axis.

## 4.6 Summary

In this chapter we have given a general review of timelike geodesics in a Kerr spacetime. We have shown how the symmetries of the Kerr metric lead to the existence of four first integrals of motion that effectively reduce the geodesic equations to a system of first-order ordinary differential equations. This system can be further recast as a problem of quadratures. Moreover, we have also seen that the differential equations determining

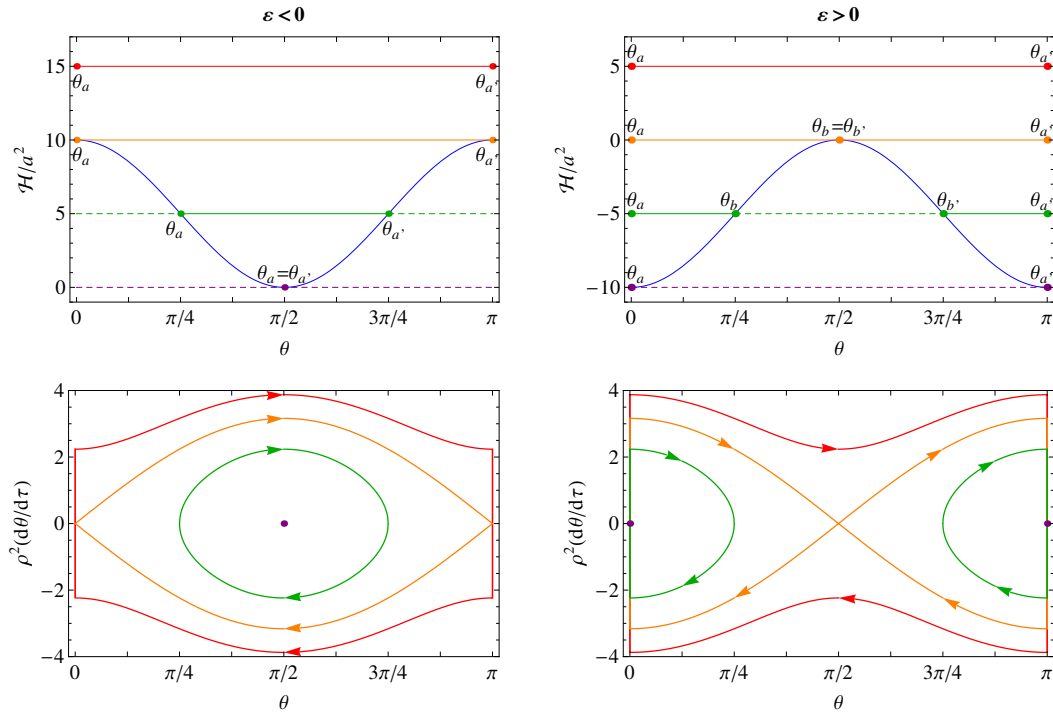


**Figure 4.8:** The same as Figure 4.7 but now for the case  $\ell_z = 0$ . The panels on the left hand side correspond to  $\varepsilon = -10$  while those on the right hand side correspond to  $\varepsilon = 10$ . Note that in this case the test particle can reach the polar axis and every time that it does so,  $\theta$  changes sign discontinuously.

the radial and latitudinal motion are almost completely decoupled. This allowed us to analyse each of these components of the motion as quasi-autonomous dynamical systems. As part of these analyses, we introduced a pair of effective potentials, in terms of which we were able to classify the different possible types of trajectory that are relevant for physical processes taking place outside the BH horizon. This chapter is accompanied with several examples of numerically integrated trajectories in Appendix A. In the following we summarise some results concerning the constants of motion which have been demonstrated in this chapter:

- $\mathcal{Q} = 0$  is a necessary condition for a test particle to stay in the equatorial plane.
- $\mathcal{Q} > 0$  is a necessary condition for a test particle to cross the equatorial plane.
- $\mathcal{Q} < 0$  confines the motion of a test particle to a single hemisphere.
- $\ell_z = 0$  is a necessary condition for a test particle to cross the polar axis.
- $\mathcal{E} \geq 1$  is a necessary condition for a test particle to be radially unbound.



## Chapter 5

# Toy model for relativistic accretion

In this chapter we construct a toy model for the accretion of a rotating gas cloud of non-interacting particles infalling towards a Kerr BH. This model was introduced in Tejeda et al. (2012b) (referred to in the following as Paper III), and it represents a generalisation of the models introduced in Mendoza et al. (2009) and Tejeda et al. (2012a) (that we shall refer to as Paper I and II, respectively). In Paper I the toy model was introduced within a Newtonian framework. The model was then extended to a general relativistic context in Paper II, in which the central accretor was a Schwarzschild BH. The aim in this series of papers has been to construct a toy model for the infall feeding an accretion disc around a massive object based solely on the two leading ingredients determining the fluid bulk motion: gravity and rotation.

The present toy model is based on the assumptions of stationarity, axisymmetry and ballistic motion, that is, we assume that the gas particles follow geodesic lines and neglect any deviation from their free-falling trajectories due to pressure gradients, magnetic fields, self-gravity, radiative processes, etc. It is clear that these assumptions constitute an oversimplification of a real situation, but they allow us to give a useful analytic description of the streamlines and velocity field of the resulting flow. In addition, this permits us to highlight signatures of pure relativistic effects on the accretion dynamics either due to the strong gravitational field regime or to the frame dragging effect that might be otherwise masked in a full-hydrodynamic treatment.

The present solution is based on the results introduced in the previous chapter in which we gave a general review of the extensive body of work on geodesic motion that exists in the literature. Here we construct an analytic description of the streamlines of the toy model in terms of Jacobi elliptic functions. By using some standard identities for these functions, we provide a novel approach for describing the projection onto the  $r$ - $\theta$  plane of all possible trajectories of test particles in a Kerr spacetime by means of a single analytic expression. Moreover, we also discuss the simple numerical scheme introduced in Paper II for calculating the density field.

For the derivation of the expressions describing the accretion flow we adopt BL

coordinates while a local description of the velocity field is also given in terms of the ZAMO reference frame. However, note that, given the symmetries of the problem, only the radial and polar coordinates have non-trivial solutions and, therefore, the final results are equally useful for describing the flow in the KS coordinate system.

One of the main motivations for extending the toy model to a Kerr spacetime is to use it as a test solution for benchmarking general relativistic numerical hydrodynamics codes and, in particular, the future SPHINCS code. We demonstrate the use of the model as a benchmark by comparing it against a series of numerical simulations made with two different SPH codes that use pseudo-Newtonian potentials for mimicking general relativistic effects. First, we show the results presented in Paper II for the comparisons of the analytic toy model with a roughly equivalent 2D SPH simulation from Lee & Ramírez-Ruiz (2006) (referred to as LR in the following). Next we show the results of the comparisons presented in Paper III against a series of 3D simulations performed using a version of the SPH code Gadget-2 (Springel, 2005) modified by Taylor, Miller & Podsiadlowski (2011) (referred to as TMP in the following). In LR and TMP, the authors explored numerically the infall of rotating gas towards a newborn BH, with the aim of gaining insight into the formation of progenitors for long GRBs by means of collapse of the interior regions of massive rotating stars. LR neglected rotational effects of the BH itself, approximating its gravitational field by means of the pseudo-Newtonian potential introduced by Paczyński & Wiita (1980), whereas TMP also included rotational effects of the BH, as found in the Kerr metric, by using the second-order expansion pseudo-Newtonian potential developed by Mukhopadhyay & Misra (2003). Note that, among the several different pseudo-Newtonian potentials that exist for mimicking effects of Kerr spacetime, the choice of the one used by TMP was meant to minimise the errors in the approximation of various dynamic properties such as location of the inner most stable circular orbit, epicyclic frequencies and radial acceleration.

The simulations presented at the end of this chapter are specifically designed to show the usefulness of the toy model as a simple, practical test for numerical codes which include dynamical effects of general relativity. With this, we are able to make a detailed comparison by gradually implementing the different aspects of the code that we are interested in testing. At a first stage, the simulations are performed for a ballistic flow (with zero pressure) and then for a hydrodynamical one where we measure the effects of pressure gradients on the infall, thus exploring the extent of applicability of the ballistic approximation.

## 5.1 Model description and boundary conditions

We are interested here in modelling a rotating gas cloud falling towards a central BH with mass  $M$  and specific angular momentum  $a$ , whose exterior gravitational field is described by the Kerr metric. We assume that the flow has reached a stationary state characterised by a constant accretion rate  $\dot{M}$ . Moreover, we restrict our analysis to axisymmetric distributions of the gas where the rotation axis of the cloud is parallel to the spin of the BH (either aligned or anti-aligned with it). For describing the dynamics

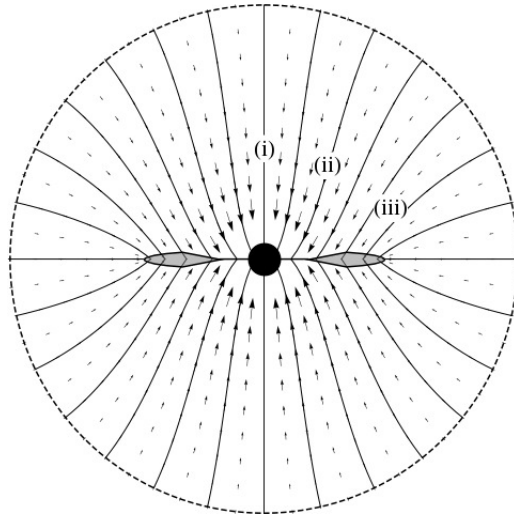


**Figure 5.1:** Schematic illustration of the toy model. Boundary conditions are fixed at a shell with radius  $r_0$  and fluid elements then move along ballistic trajectories. For this figure we take the distribution of angular momentum on the initial shell to be increasing monotonically in magnitude towards the equator. The streamlines can be divided into three groups: (i) ones with low angular momentum that accrete directly into the BH; (ii) ones with intermediate angular momentum which arrive at the equator but do not find a circularisation radius; (iii) ones with large enough angular momentum to be incorporated into an equatorial Keplerian-type accretion disc.

of the infall, we assume that the gravitational field of the BH plays the dominant role, and therefore neglect the effects of fluid self gravity, pressure gradients, fluid viscosity, radiation pressure, neutrino emission, etc. This in practice means that we are performing a ballistic treatment of the accretion flow and, therefore, that flow streamlines correspond to timelike geodesics of the Kerr spacetime. Furthermore, we assume that infalling gas particles end up being either incorporated into an infinitesimally thin equatorial disc or directly accreted inside the BH horizon. The analytic description of the infall does not include the disc itself where clearly a ballistic treatment is no longer valid; we shall just consider both disc and BH as passive sinks of particles and energy. Figure 5.1 shows a schematic diagram of the accretion scenario.

Under the ballistic approximation, it is convenient to describe the whole gas cloud as a collection of equal mass test particles which we shall refer to as fluid elements. As in the previous chapters, we call  $\varrho$  the matter density and  $n$  the baryon number density, both measured in a comoving reference frame. We also introduce the average baryonic rest mass  $m_0$ , such that  $\varrho = m_0 n$ . For the boundary conditions of the model, we assume that gas particles are continuously injected from a shell at  $r = r_0$  where the particle

properties are given by specified distribution functions:

$$n_0 = n(r_0, \theta_0), \quad (5.1.1)$$

$$\dot{r}_0 = \dot{r}(r_0, \theta_0), \quad (5.1.2)$$

$$\dot{\theta}_0 = \dot{\theta}(r_0, \theta_0), \quad (5.1.3)$$

$$\dot{\phi}_0 = \dot{\phi}(r_0, \theta_0). \quad (5.1.4)$$

We require these four distribution functions to be differentiable and symmetric with respect to the equatorial plane. Additionally, in order to avoid streamlines intersecting before they reach the equatorial plane, two further conditions need to be fulfilled. First, we require that the test particles do not have turning points in their polar or radial motion as they descend towards the equatorial plane. Second, we require that

$$\left( \frac{\partial \theta}{\partial \theta_0} \right) \Big|_r > 0. \quad (5.1.5)$$

These conditions allow us to use the initial polar angle  $\theta_0$  as a label of the individual streamlines and, moreover, to use the streamlines as a mapping  $\theta_0 \mapsto \theta$  (for every given  $r$ ). The condition in Eq. (5.1.5) assures us that the mapping will be non-singular.

Since for the present model each streamline corresponds to a timelike geodesic, according to the results discussed in Section 4.1, we have that the integrals of motion  $\mathcal{E}$ ,  $\ell_z$ ,  $\ell$ , and  $\mathcal{Q}$  are conserved quantities along individual streamlines. Clearly, their actual values will depend on the initial polar angle  $\theta_0$  and, hence, will vary from streamline to streamline. Once the boundary conditions in Eqs. (5.1.1)-(5.1.4) have been fixed, we can substitute them into Eqs. (4.1.7)-(4.1.9) and (4.1.14) so as to obtain the values of the conserved quantities on each streamline:

$$\mathcal{E}(\theta_0) = \left( 1 - \frac{2Mr_0}{\rho_0^2} \right) \dot{t}_0 + \frac{2aMr_0 \sin^2 \theta_0}{\rho_0^2} \dot{\phi}_0, \quad (5.1.6)$$

$$\ell_z(\theta_0) = -\frac{2aMr_0 \sin^2 \theta_0}{\rho_0^2} \dot{t}_0 + \frac{\Sigma_0 \sin^2 \theta_0}{\rho_0^2} \dot{\phi}_0, \quad (5.1.7)$$

$$\ell^2(\theta_0) = \rho_0^4 \dot{\theta}_0^2 + \left[ (r_0^2 + a^2) \dot{\phi}_0 - a \dot{t}_0 \right]^2 \sin^2 \theta_0 + a^2 \cos^2 \theta_0, \quad (5.1.8)$$

$$\mathcal{Q}(\theta_0) = \rho_0^4 \dot{\theta}_0^2 + \ell_z^2(\theta_0) \cot^2 \theta_0 - \varepsilon(\theta_0) a^2 \cos^2 \theta_0, \quad (5.1.9)$$

where  $\varepsilon = \mathcal{E}^2 - 1$  and  $\dot{t}_0$  is an implicit function of  $\dot{r}_0$ ,  $\dot{\theta}_0$ ,  $\dot{\phi}_0$  which can be directly calculated from the normalisation of the four-velocity, i.e.  $U^\mu U_\mu = -1$ .

As we saw in Section 4.4, test particles freely falling in a Kerr spacetime can be captured by the central BH even for a non-vanishing angular momentum. This general relativistic feature led LR to classify the streamlines into three groups depending on the value of their specific angular momentum (see Figure 5.1): (i) streamlines with low angular momentum, which cross the BH horizon before reaching the equatorial plane; (ii) streamlines with intermediate angular momentum, which form a small disc within which accretion proceeds on a free-fall time scale; (iii) streamlines with larger

angular momentum, which have sufficient centrifugal support on their arrival at the equator so that subsequent accretion would occur on a viscous time scale in a Keplerian-type accretion disc. The streamlines of type (ii) correspond to the accretion regime discussed by Beloborodov & Illarionov (2001) for a Schwarzschild BH and by Zalamea & Beloborodov (2009) for a Kerr BH. In the former work, the authors introduced the concept of a ‘small-scale inviscid disc’ in which the mechanism driving accretion is a purely relativistic one related to the existence of an innermost stable circular orbit.

Note that when streamlines of type (ii) and (iii) reach the equatorial plane, they encounter there a mirror symmetric streamline coming from  $\pi - \theta_0$ . In a real physical situation one expects that if these two streamlines were to collide supersonically then two shock fronts would appear above and below the equatorial plane, with the fluid being incorporated into a disc-like structure. Provided that there is an efficient dissipation mechanism, the shock fronts will remain pinned down to the equator and the disc will remain thin. It is clear that the study of the disc dynamics requires a full hydrodynamical treatment, in which redistribution of angular momentum and energy losses are self consistently taken into account, but such an analysis lies beyond the scope of the present toy model. Instead, we assume here that an efficient mechanism dissipates all of the kinetic energy associated with the vertical component of the velocity, in such a way that an infinitesimally thin disc forms in the equatorial plane which is then taken to act as a passive energy sink. In Section 5.6 we show some idealised collapsar-like simulations made with the TMP code in which first this zero-pressure (ballistic) flow is simulated, as well as a non-zero temperature hydrodynamic flow (with a simple cooling mechanism), in which this behaviour is observed. Also see López-Cámara et al. (2009) for a full hydrodynamical simulation of a collapsar in which they show that an isothermal disc does indeed remain thin.

In principle one could relax the condition of symmetry with respect the equatorial plane. However, in that case we would not have the symmetric collision of streamlines described above. This would lead to the formation of a warped disc, making the situation much more complicated (see e.g. Bardeen & Petterson, 1975).

Now consider the situation in which two neighbouring streamlines start approaching each other in such a way that they would intersect. This type of encounter is qualitatively different from the head-on collision described above since, with a full hydrodynamical treatment, the two approaching streamlines would here be prevented from intersecting by the smooth action of pressure forces. It is clear, however, that this cannot be handled within the ballistic approximation and this is why we have restricted our analysis to distribution functions for which streamlines do not have crossings before reaching the equator.

## 5.2 Velocity field

As already discussed, due to the ballistic approximation, the streamlines of the toy model correspond to timelike geodesics of Kerr spacetime. In Section 4.2 we saw that the symmetries of this spacetime allow us to write the four-velocity components of a

test particle as a function of its position and of the constants of motion as given by Eqs. (5.1.6)-(5.1.9). According to Eqs. (4.2.1)-(4.2.4), the BL components of the velocity field are

$$U^r = -\frac{\sqrt{\mathcal{R}}}{\rho^2}, \quad (5.2.1)$$

$$U^\theta = \pm \frac{\sqrt{\Theta}}{\rho^2}, \quad (5.2.2)$$

$$U^\phi = \frac{\mathcal{A} + a\mathcal{B} \sin^2 \theta}{\rho^2 \sin^2 \theta}, \quad (5.2.3)$$

$$U^t = \frac{a\mathcal{A} + \mathcal{B}(r^2 + a^2)}{\rho^2}. \quad (5.2.4)$$

where  $\mathcal{R}$ ,  $\Theta$ ,  $\mathcal{A}$  and  $\mathcal{B}$  were defined in Eqs. (4.2.5)-(4.2.8). In Eq. (5.2.1) we take the minus sign because, for the present scenario, the radial coordinate decreases monotonically as the particle approaches the equator. On the other hand, in Eq. (5.2.2) the upper sign corresponds to a particle starting to fall-in from the northern hemisphere while the lower one corresponds to a particle starting off from the southern hemisphere since, in either case, the polar coordinate should go from  $\theta_0$  to  $\pi/2$ .

We can also give a local description of the velocity field in terms of the ZAMOs introduced in Section 3.2. The physical three-velocity field as described by local ZAMOs is given by

$$\bar{V}^r = -\frac{\sqrt{\mathcal{R}/\Delta}}{\Gamma \rho}, \quad (5.2.5)$$

$$\bar{V}^\theta = \pm \frac{\sqrt{\Theta}}{\Gamma \rho}, \quad (5.2.6)$$

$$\bar{V}^\phi = \frac{\rho \ell_z}{\Gamma \sqrt{\Sigma} \sin \theta}, \quad (5.2.7)$$

where  $\Gamma$  is the Lorentz factor between the local ZAMO and the test particle passing by, and is given by

$$\Gamma = \sqrt{1 + \frac{\mathcal{R}}{\Delta \rho^2} + \frac{\Theta}{\rho^2} + \frac{\rho^2 h_z^2}{\Sigma \sin^2 \theta}}. \quad (5.2.8)$$

Note that the expressions for the velocity field (both Eqs. 5.2.1 - 5.2.4 and Eqs. 5.2.5 - 5.2.7) are functions of position  $(r, \theta)$  but also of the conserved quantities along each streamline, and hence of  $(r_0, \theta_0)$ . Therefore, to use them in practice we need to provide an explicit mapping  $(r_0, \theta_0) \mapsto (r, \theta)$ . Such a mapping is given in the next section in terms of an analytic expression for the streamlines.

### 5.3 Streamlines

In this section we give an analytic expression for the streamlines of the toy model. Given the assumptions of stationarity and axisymmetry, all that is needed for this description

is to consider the solutions for the radial and latitudinal motion of a test particle freely falling in Kerr spacetime, i.e. the projection of an arbitrary timelike geodesic onto the  $r$ - $\theta$  plane. For doing this, it is sufficient to consider Eq. (4.2.12), i.e.

$$\int_{r_0}^r \frac{dr'}{\sqrt{\mathcal{R}(r')}} = \mp \int_{\theta_0}^{\theta} \frac{d\theta'}{\sqrt{\Theta(\theta')}} \quad (5.3.1)$$

where the upper sign corresponds to a particle in the northern hemisphere and the lower sign corresponds to a particle in the southern hemisphere. We now introduce the following definitions

$$\Phi(r) \equiv \int_{r_a}^r \frac{dr'}{\sqrt{\mathcal{R}(r')}} \quad (5.3.2)$$

$$\Psi(\theta) \equiv \int_{\theta_a}^{\theta} \frac{d\theta'}{\sqrt{\Theta(\theta')}} \quad (5.3.3)$$

where  $r_a$  and  $\theta_a$  are as yet unspecified reference points in the particle trajectory. With these definitions we can rewrite Eq. (5.3.1) as

$$\Phi(r) - \Phi(r_0) = \mp [\Psi(\theta) - \Psi(\theta_0)] \quad (5.3.4)$$

In the following subsections we show how to solve Eqs. (5.3.2) and (5.3.3) in terms of elliptic integrals. Based on the extensive literature on elliptic integrals and Jacobi elliptic functions (e.g. Hancock, 1917; Byrd & Friedman, 1954; Cayley, 1961), we provide explicit analytic expressions for  $\Phi(r)$  and  $\Psi(\theta)$ . In Appendix B we give a brief review of these integrals, discuss their connection with Jacobi elliptic functions and list some of their properties which will be relevant for the present discussion.

Elliptic integrals have been used extensively in the literature in the context of geodesic motion in Kerr spacetime (see e.g. Chandrasekhar, 1983; Kraniotis, 2004; Fujita & Hikida, 2009). It has been customary to split the solution into different analytical expressions corresponding to different types of trajectory (bound orbits, unbound orbits, trapped orbits, etc.). Instead, we follow a different strategy and, by integrating directly Eqs. (5.3.2) and (5.3.3), we show that all of these different expressions can be reduced to a single one. Based on this proof, in the present work we are able to describe the projection onto the  $r$ - $\theta$  plane of all of the different types of trajectory by means of a single analytical formula.

### 5.3.1 Radial solution

Consider first Eq. (5.3.2). From the theory of elliptic functions we know that, given that  $\mathcal{R}(r)$  is a fourth order polynomial in  $r$ , the solution for the radial integral can be given in terms of elliptic integrals. The actual functional form of the solution depends on the nature of the roots of  $\mathcal{R}(r)$ . The physical interpretation of these roots was given in Section 4.4, where we saw that, whenever they are real and greater than  $r_+$ , they constitute radial turning points at which  $\dot{r}$  changes sign and thus, the direction

of integration for the radial integral should reverse. It is clear that the roots of  $\mathcal{R}(r)$  should satisfy one of the following possibilities: all four roots are real; two are real while the other two form a complex conjugate pair; there are two pairs of complex conjugates. The first two cases include the possibility of multiplicity of the real roots. Although one can express the roots analytically in terms of the parameters of the orbit ( $\mathcal{E}$ ,  $\ell_z$  and  $\ell$ ) (see e.g. Abramowitz & Stegun, 1970), we do not give the final expressions coming from this here because we do not find them particularly useful in practice. Instead, we assume that we have already found the four roots, either analytically or by means of a root finding algorithm, and write  $\mathcal{R}(r)$  as

$$\mathcal{R}(r) = \varepsilon(r - r_a)(r - r_b)(r - r_c)(r - r_d). \quad (5.3.5)$$

Let us now consider these cases one at a time.

**Case I:** Four real roots.

As was discussed in Section 4.4, from the different possibilities of sign alternation of the coefficients of  $\mathcal{R}(r)$ , it is found that, whenever  $\varepsilon > 0$ , there cannot exist more than two roots greater than  $r_+$ , while for  $\varepsilon < 0$ , there cannot be more than three roots greater than  $r_+$ . Then, we have that in order to satisfy the condition  $\mathcal{R}(r) > 0$ , there are two possibilities: either  $r$  is bracketed in between two non-negative consecutive roots of  $\mathcal{R}(r)$  or  $r$  is unbounded above. The elliptic-like type of trajectory that we discussed in Section 4.4, represents an example of the former case. On the other hand, the latter case represents an unbound trajectory (hyperbolic-like type) with the largest positive root being the only turning point. In the first case, we call the roots bracketing  $r$ ,  $r_a$  and  $r_b$  (with  $r_a < r_b$ ). Instead, in the second case, we again take  $r_a$  as the lower bound for  $r$  and let  $r_b$  be the negative root with the largest absolute value. In both cases the two remaining roots are denoted as  $r_c$  and  $r_d$  (with  $|r_c| < |r_d|$ ). From these definitions it follows that, either

$$r_a \leq r_b \leq r_c < |r_d| \quad \text{or} \quad r_c \leq r_d \leq r_a < |r_b|. \quad (5.3.6)$$

Having labelled the roots in the above described fashion, we can now write the solution to Eq. (5.3.2) as (Byrd & Friedman, 1954)

$$\Phi(r) = \frac{2}{\sqrt{\varepsilon(r_a - r_c)(r_d - r_b)}} \text{cn}^{-1} \left[ \sqrt{\frac{(r_d - r_a)(r_b - r)}{(r_b - r_a)(r_d - r)}}, k_r \right], \quad (5.3.7)$$

where  $\text{cn}^{-1}(x, k_r)$  is the inverse of the elliptic function  $\text{cn}(u, k_r)$  as defined in Eq. (B.8). The constant  $k_r$  is called the modulus and it is given by

$$k_r^2 = \frac{(r_b - r_a)(r_d - r_c)}{(r_d - r_b)(r_c - r_a)}. \quad (5.3.8)$$

The relations in Eq. (5.3.6) ensure that the product  $\varepsilon(r_a - r_c)(r_d - r_b)$  is always positive and that  $0 < k_r < 1$ .

**Case II:** Two real roots and a complex conjugate pair.

This case corresponds to various different types of plunging trajectories. Here we take  $r_a$  and  $r_d$  (with  $|r_a| < |r_d|$ ) to be the real roots while  $r_b$  and  $r_c$  form the complex conjugate pair. With this choice, the solution for  $\Phi(r)$  given in Eq. (5.3.7) can be used without any further modification, and we obtain a real quantity as the final result. Nevertheless, intermediate steps in the evaluation involve the use of complex quantities. In what follows we show how to rewrite  $\Phi(r)$  as an explicitly real function of  $r$  by using standard identities for Jacobi elliptic functions.

We start by combining the four roots into the following real constants:

$$\alpha = \text{Sign}(\varepsilon) \sqrt{(r_d - r_b)(r_d - r_c)}, \quad (5.3.9)$$

$$\beta = \sqrt{(r_a - r_b)(r_a - r_c)}, \quad (5.3.10)$$

$$\tilde{k}_r^2 = \frac{(\alpha + \beta)^2 - (r_d - r_a)^2}{4\alpha\beta}. \quad (5.3.11)$$

From the definition of  $k_r$  in Eq. (5.3.7), it is easy to check that  $\tilde{k}_r$  and  $k_r$  are related by

$$\tilde{k}_r^2 = \frac{(1 + k_r)^2}{4k_r}. \quad (5.3.12)$$

We now invoke the identities for Jacobi elliptic functions given in Eqs. (B.32) and (B.42), and combine them into

$$\text{cn} \left( 2\sqrt{k} u, \frac{1+k}{2\sqrt{k}} \right) = \frac{1 - k \text{sn}^2(u, k)}{1 + k \text{sn}^2(u, k)}, \quad (5.3.13)$$

where  $\text{sn}(u, k)$  is the elliptic function defined in Eq. (B.6). Calling  $x = \text{cn}(u, k)$  and inverting Eq. (5.3.13) results in

$$\text{cn}^{-1}(x, k) = \frac{1}{2\sqrt{k}} \text{cn}^{-1} \left[ \frac{1 - k(1 - x^2)}{1 + k(1 - x^2)}, \frac{1+k}{2\sqrt{k}} \right]. \quad (5.3.14)$$

Then, we substitute in this expression

$$x = \sqrt{\frac{(r_d - r_a)(r_b - r)}{(r_b - r_a)(r_d - r)}}, \quad \text{and} \quad k = k_r$$

and, after some simple manipulation, we are now able to rewrite  $\Phi(r)$  as

$$\Phi(r) = \frac{1}{\sqrt{\varepsilon\alpha\beta}} \text{cn}^{-1} \left[ \frac{\beta r_d - \alpha r_a + (\alpha - \beta)r}{\beta r_d + \alpha r_a - (\alpha + \beta)r}, \tilde{k}_r \right]. \quad (5.3.15)$$

Note that this alternative expression for  $\Phi(r)$  involves just explicitly real quantities. This same result also follows from direct integration of Eq. (5.3.2) as in Byrd & Friedman (1954).

**Case III:** Two complex conjugate pairs

This case also represents a particular type of plunging trajectory and is a possibility for Kerr spacetime that is not present for Schwarzschild spacetime, for which one of the roots of  $\mathcal{R}(r)$  is always zero and, therefore, there is at least one other real root. Now we take  $r_a = r_d^*$  and  $r_b = r_c^*$ , with  $\text{Re}(r_a) < \text{Re}(r_b)$ . Note that in this case, the function  $\Phi(r)$ , as defined in Eq. (5.3.2), is a complex function of  $r$  since it is defined in terms of an integral with  $r_a$  as its lower limit. Nevertheless, the combination  $\Phi(r) - \Phi(r_0)$  is a real function of  $r$  and still represents a formal solution to the radial integral on the right hand side of Eq. (5.3.1).

In order to prove this, we start by noting that  $\alpha$  and  $\beta$ , as defined in Eqs. (5.3.9) and (5.3.10), now form a complex conjugate pair, i.e.  $\alpha = \beta^*$ . We then introduce the following real constants:

$$\begin{aligned} \mu &= \frac{r_a + r_d}{2}, & \nu &= \frac{r_a - r_d}{2i}, \\ \zeta &= \frac{\alpha + \beta}{2}, & \eta &= \frac{\alpha - \beta}{2i}. \end{aligned} \quad (5.3.16)$$

Using these definitions, it is simple to check that  $\tilde{k}_r$ , as defined in Eq. (5.3.11), can also be expressed as

$$\tilde{k}_r^2 = \frac{\zeta^2 + \nu^2}{\zeta^2 + \eta^2}, \quad (5.3.17)$$

from which it is clear that  $\tilde{k}_r$  is still a real quantity. On the other hand, from Eq. (5.3.15) and the definitions in Eq. (5.3.16), it is simple to check that

$$\frac{\beta r_d - \alpha r_a + (\alpha - \beta)r}{\beta r_d + \alpha r_a - (\alpha + \beta)r} = i \frac{\zeta \nu - \eta(r - \mu)}{\eta \nu + \zeta(r - \mu)}. \quad (5.3.18)$$

In other words, the argument of the function  $\text{cn}^{-1}(x, \tilde{k}_r)$  in Eq. (5.3.15) is a purely imaginary number. Moreover, from Eqs. (5.3.16) and (5.3.17), it is simple to check that

$$\sqrt{\varepsilon \alpha \beta \tilde{k}_r} = \sqrt{\varepsilon (\zeta^2 + \nu^2)}. \quad (5.3.19)$$

We now consider the identities for Jacobi elliptic functions given in Eqs. (B.46) and (B.47). Taking their quotient, substituting appropriate values from Eqs. (B.18) and (B.28)-(B.30), and finally using Eq. (B.33), results in

$$\text{cn}(u, k) = i \text{cs} \left[ k u + i K \left( 1 + \frac{1}{k} \right), \frac{1}{k} \right], \quad (5.3.20)$$

where  $\text{cs}(u, k) = \text{cn}(u, k)/\text{sn}(u, k)$  and  $K$  is the complete elliptic integral of the first kind as defined in Eq. (B.4). Once again, we invert this identity by defining  $x = \text{cn}(u, k)$  and solving for  $u$ , which results in

$$\text{cn}^{-1}(x, k) = \frac{1}{k} \left[ \text{cs}^{-1} \left( -i x, \frac{1}{k} \right) - i K \left( 1 + \frac{1}{k} \right) \right]. \quad (5.3.21)$$

Finally, substituting

$$x = \frac{\beta r_d - \alpha r_a + (\alpha - \beta)r}{\beta r_d + \alpha r_a - (\alpha + \beta)r} \quad \text{and} \quad k = \tilde{k}_r,$$

into Eq. (5.3.21), together with Eqs. (5.3.18) and (5.3.19), allows us to split  $\Phi(r)$  into a real function of  $r$  and an imaginary constant, i.e.

$$\Phi(r) = \tilde{\Phi}(r) - \frac{iK \left(1 + \frac{1}{k_r}\right)}{\sqrt{\varepsilon(\zeta^2 + \nu^2)}}, \quad (5.3.22)$$

where

$$\tilde{\Phi}(r) = \frac{1}{\sqrt{\varepsilon(\zeta^2 + \nu^2)}} \text{cs}^{-1} \left[ \frac{\zeta \nu - \eta(r - \mu)}{\eta \nu + \zeta(r - \mu)}, \frac{1}{\tilde{k}_r} \right]. \quad (5.3.23)$$

From Eq. (5.3.22), it follows that

$$\Phi(r) - \Phi(r_0) = \tilde{\Phi}(r) - \tilde{\Phi}(r_0) \quad (5.3.24)$$

is a real function of  $r$ .

**Case IV:**  $\varepsilon = 0$

In this case, we have that one of the roots of  $\mathcal{R}(r)$  diverges to infinity, so that it reduces to a third order polynomial. For this reason, there are now two possibilities for the roots: either the three of them are all real, or one is real and the other two form a complex conjugate pair. Appropriate expressions for each case are straightforward to obtain from Eqs. (5.3.7) and (5.3.15) after taking the appropriate limit.

### 5.3.2 Polar angle solution

We next consider the polar integral in Eq. (5.3.3). In Section 4.5 we saw that the latitudinal motion is restricted to values of  $\theta$  such that  $\Theta(\theta) \geq 0$ , and so, in general,  $\theta$  is bracketed between two consecutive real roots of the equation  $\Theta(\theta) = 0$ . These roots correspond to turning points of the polar motion and explicit expressions for them were given in Eq. (4.5.5). Just as in Section 4.5, we denote as  $\theta_a$  the turning point of the polar motion which is closest to the polar axis. Since we have assumed symmetry with respect to the equatorial plane, we can consider, without loss of generality, that the streamline on which we are focusing starts from, say, the northern hemisphere, i.e.  $\theta_a \leq \theta_0 \leq \pi/2$ . For  $\ell_z \neq 0$ ,  $\theta_a$  corresponds to the smallest positive root of the equation  $\Theta(\theta) = 0$ , and in this case we can use Eq. (5.1.9) to rewrite  $\mathcal{Q}$  in terms of  $\theta_a$  as

$$\mathcal{Q} = \ell_z^2 \cot^2 \theta_a - \varepsilon a^2 \cos^2 \theta_a. \quad (5.3.25)$$

As was discussed in Section 4.5, we know that the polar equation  $\Theta(\theta) = 0$  can have zero, two or four real roots in the interval  $\theta \in [0, \pi]$ . The first case arises when  $\ell_z = 0$

and  $\mathcal{Q} > -\varepsilon a^2$ , corresponding to a test particle that can sweep the whole polar domain and repeatedly cross the polar axis.<sup>(1)</sup> The second case corresponds to bounded polar motion, with  $\theta \in [\theta_a, \pi - \theta_a]$ , where the test particle repeatedly crosses the equatorial plane. The third case corresponds to a test particle restricted to move within a single hemisphere (in this case the northern one) as  $\theta \in [\theta_a, \theta_b]$ , where  $\theta_b \leq \pi/2$  is the second turning point of the polar motion.

If we return to the polar integral in Eq. (5.3.3) and consider the change of variable  $\xi = \cos \theta / \cos \theta_a$ , the integral transforms as

$$\Psi(\theta) = \int_{\theta_a}^{\theta} \frac{d\theta'}{\sqrt{\Theta(\theta')}} = \cos \theta_a \int_{\xi}^1 \frac{d\xi'}{\sqrt{\mathcal{P}(\xi')}}, \quad (5.3.26)$$

where

$$\mathcal{P}(\xi) = \mathcal{Q}(1 - \xi^2)(1 - k_{\theta}^2 \xi^2), \quad (5.3.27)$$

$$k_{\theta}^2 = -(\varepsilon a^2 / \mathcal{Q}) \cos^4 \theta_a. \quad (5.3.28)$$

Note that, when real, the angles  $\theta_a$  and  $\theta_b$  satisfy

$$\cos \theta_a = k_{\theta} \cos \theta_b. \quad (5.3.29)$$

It is clear that  $\mathcal{P}(\xi)$  is a fourth order polynomial in  $\xi$  and, as such, the solution to Eq. (5.3.26) can be given in terms of an elliptic integral. We now proceed with the integration of Eq. (5.3.26) by considering the following cases:

#### Case I: $\varepsilon \leq 0$

In this case, we have that  $\mathcal{Q} \geq 0$  and that  $k_{\theta}$  is a real number. We can then write the solution to Eq. (5.3.26) as (Byrd & Friedman, 1954)

$$\Psi(\theta) = \frac{\cos \theta_a}{\sqrt{\mathcal{Q}}} \operatorname{cd}^{-1} \left( \frac{\cos \theta}{\cos \theta_a}, k_{\theta} \right), \quad (5.3.30)$$

where  $\operatorname{cd}^{-1}(x, k_r)$  is the inverse of the elliptic function  $\operatorname{cd}(u, k_r) = \operatorname{cn}(u, k_r) / \operatorname{dn}(u, k_r)$  as defined in Eq. (B.17). Note that  $\Psi(\theta_a) = 0$ , while for  $\theta = \pi/2$

$$\Psi(\pi/2) = \frac{\cos \theta_a}{\sqrt{\mathcal{Q}}} K(k_{\theta}). \quad (5.3.31)$$

Also note that when  $\varepsilon = 0$ , one gets  $k_{\theta} = 0$  from Eq. (5.3.28). According to Eq. (B.13), for a null value of the modulus, one has that  $\operatorname{cd}(u, 0) = \cos(u)$ , and so Eq. (5.3.30) can be simplified as

$$\Psi(\theta) = \frac{\cos \theta_a}{\sqrt{\mathcal{Q}}} \cos^{-1} \left( \frac{\cos \theta}{\cos \theta_a} \right). \quad (5.3.32)$$

This same result also follows in the non-rotating BH case ( $a = 0$ ), that is, Eq. (5.3.32) is the expression to use in Schwarzschild spacetime.

<sup>(1)</sup>Even though in this case the angles  $\theta = 0, \pi$  do not satisfy  $\Theta(\theta) = 0$ , they still represent turning points since at those locations the polar velocity changes sign discontinuously, as discussed in Section 4.5. When this happens, we take  $\theta_a = 0$ .

**Case II:**  $\varepsilon > 0$  and  $\mathcal{Q} > 0$

Here one has that  $k_\theta$  is a purely imaginary number. Nevertheless, we can still use the solution given in Eq. (5.3.30) and get a resulting real quantity. Just as in the radial case, it is possible to rewrite  $\Psi(\theta)$  as an explicitly real function of  $\theta$ . In order to do so, we invoke the identity for Jacobi elliptic functions in Eq. (B.29), and invert it as

$$\text{cd}^{-1}(\xi, k) = \sqrt{1 - k^2} \text{cn}^{-1} \left( \xi, \sqrt{\frac{-k^2}{1 - k^2}} \right). \quad (5.3.33)$$

By substituting  $\xi = \cos \theta / \cos \theta_a$  and  $k = k_\theta$  into the previous result together with Eq. (5.3.30), we get

$$\Psi(\theta) = \frac{\cos \theta_a}{\sqrt{\mathcal{Q} + \varepsilon a^2 \cos^4 \theta_a}} \text{cn}^{-1} \left( \frac{\cos \theta}{\cos \theta_a}, \tilde{k}_\theta \right), \quad (5.3.34)$$

with

$$\tilde{k}_\theta = \sqrt{\frac{-k_\theta^2}{1 - k_\theta^2}} = \sqrt{\frac{\varepsilon a^2 \cos^4 \theta_a}{\mathcal{Q} + \varepsilon a^2 \cos^4 \theta_a}}, \quad (5.3.35)$$

which is now a real number.

**Case III:**  $\varepsilon > 0$  and  $\mathcal{Q} \leq 0$

Here, again, we have that the expression for  $\Psi(\theta)$  given in Eq. (5.3.30) can be used without any further modification, even though some intermediate steps involve the use of complex quantities. An alternative, explicitly real expression for  $\Psi(\theta)$  in this case follows from using the identity in Eq. (B.32). If we invert this identity, we get

$$\text{cn}^{-1}(\xi, k) = \frac{1}{k} \text{dn}^{-1} \left( \xi, \frac{1}{k} \right). \quad (5.3.36)$$

Substituting  $\xi = \cos \theta / \cos \theta_a$  and  $k = \tilde{k}_\theta$  into this result, we get that  $\Psi(\theta)$  can be rewritten as

$$\Psi(\theta) = \frac{1}{\sqrt{\varepsilon} a \cos \theta_a} \text{dn}^{-1} \left( \frac{\cos \theta}{\cos \theta_a}, \frac{1}{\tilde{k}_\theta} \right). \quad (5.3.37)$$

Note that when  $\mathcal{Q} = 0$  then  $\tilde{k}_\theta = 1$  and, since  $\text{dn}(u, 1) = \text{sech}(u)$ , Eq. (5.3.37) can be simplified as

$$\Psi(\theta) = \frac{1}{\sqrt{\varepsilon} a \cos \theta_a} \text{sech}^{-1} \left( \frac{\cos \theta}{\cos \theta_a} \right). \quad (5.3.38)$$

**Case IV:**  $l_z = 0$

In this case, the expressions in Eqs. (5.3.30), (5.3.34) and (5.3.37) can be used without further modification, but note that here one has the possibility of reaching the polar axis where the polar coordinate is singular. As was discussed in Section 5.3.2, this happens when  $l_z = 0$  and  $\mathcal{Q} > -\varepsilon a^2$ , and in this case one should take  $\theta_a = 0$  which, although it is not a formal root of the equation  $\Theta(\theta) = 0$ , does constitute a turning point of the polar motion since here one has that the polar velocity changes sign discontinuously every time that the particle crosses the polar axis. In the following equation we collect all of the alternative expressions for the different possible combinations of  $\varepsilon$  and  $\mathcal{Q}$  in this case:

$$\Psi(\theta) = \begin{cases} \frac{1}{\sqrt{\mathcal{Q}}} \operatorname{cd}^{-1} \left( \cos \theta, \sqrt{\frac{-\varepsilon a^2}{\mathcal{Q}}} \right) & \text{for } \varepsilon < 0, \mathcal{Q} > -\varepsilon a^2, \theta \in [0, \pi] \\ \frac{1}{\sqrt{-\varepsilon a}} \operatorname{cd}^{-1} \left( \sqrt{\frac{-\varepsilon a^2}{\mathcal{Q}}} \cos \theta, \sqrt{\frac{\mathcal{Q}}{-\varepsilon a^2}} \right) & \text{for } \varepsilon < 0, \mathcal{Q} < -\varepsilon a^2, \theta \in [\theta_a, \theta_a'] \\ \frac{1}{\sqrt{\varepsilon a^2 + \mathcal{Q}}} \operatorname{cn}^{-1} \left( \cos \theta, \sqrt{\frac{\varepsilon a^2}{\varepsilon a^2 + \mathcal{Q}}} \right) & \text{for } \varepsilon > 0, \mathcal{Q} > 0, \theta \in [0, \pi] \\ \frac{1}{\sqrt{\varepsilon a}} \operatorname{dn}^{-1} \left( \cos \theta, \sqrt{\frac{\varepsilon a^2 + \mathcal{Q}}{\varepsilon a^2}} \right) & \text{for } \varepsilon > 0, \mathcal{Q} < 0, \theta \in [0, \theta_b]. \end{cases}$$

### 5.3.3 Timelike geodesics in the $r$ - $\theta$ plane

Let us summarise the results obtained up to now for the radial and latitudinal motion for general timelike geodesics in a Kerr spacetime. In Section 5.3.1 we showed that the radial integral on the left hand side of Eq. (5.3.1) has as its solution

$$\int_{r_0}^r \frac{dr'}{\sqrt{\mathcal{R}(r')}} = \Phi(r) - \Phi(r_0),$$

$$\Phi(r) = \frac{2}{\sqrt{\varepsilon(r_a - r_c)(r_d - r_b)}} \operatorname{cn}^{-1} \left[ \sqrt{\frac{(r_d - r_a)(r_b - r)}{(r_b - r_a)(r_d - r)}}, k_r \right]. \quad (5.3.39)$$

On the other hand, in Section 5.3.2 we proved that the polar integral on the right hand side of Eq. (5.3.1) has as its solution

$$\int_{\theta_0}^{\theta} \frac{d\theta'}{\sqrt{\Theta(\theta')}} = \Psi(\theta) - \Psi(\theta_0),$$

$$\Psi(\theta) = \frac{\cos \theta_a}{\sqrt{\mathcal{Q}}} \operatorname{cd}^{-1} \left( \frac{\cos \theta}{\cos \theta_a}, k_\theta \right). \quad (5.3.40)$$

Combining Eqs. (5.3.39) and (5.3.40) we can express  $r$  as function of  $\theta$  as

$$r(\theta) = \frac{r_b(r_d - r_a) - r_d(r_b - r_a) \operatorname{cn}^2(u(\theta), k_r)}{r_d - r_a - (r_b - r_a) \operatorname{cn}^2(u(\theta), k_r)},$$

$$u(\theta) = \frac{\sqrt{\varepsilon(r_a - r_c)(r_d - r_b)}}{2} [\Phi(r_0) + \Psi(\theta_0) - \Psi(\theta)], \quad (5.3.41)$$

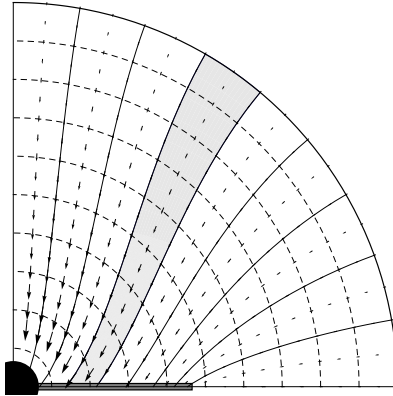


**Figure 5.2:** Schematic illustration of the construction of a regular grid in  $(r, \theta_0)$  for calculating the density field. The highlighted region constitutes one of the streamline tubes involved in the derivation of Eq. (5.4.5).

or, conversely,  $\theta$  as function of  $r$  as

$$\begin{aligned}\theta(r) &= \cos^{-1} [\cos \theta_a \text{cd}(v(r), k_\theta)], \\ v(r) &= \frac{\sqrt{\mathcal{Q}}}{\cos \theta_a} [\Psi(\theta_0) + \Phi(r_0) - \Phi(r)].\end{aligned}\quad (5.3.42)$$

Both Eqs. (5.3.41) and (5.3.42) constitute general expressions for the streamlines of the present accretion model.

## 5.4 Density field

In this section we derive a numerical scheme for calculating the density field based on the continuity equation:

$$\nabla \cdot (n\mathbf{U}) = (nU^\mu)_{;\mu} = 0. \quad (5.4.1)$$

We integrate the above expression over a four-volume element  $\mathcal{S}$ , consisting of a streamline tube extending for an infinitesimal interval of coordinate time  $dt$ . We take the spatial cross-section of this streamline tube to be the collection of all of the streamlines starting to fall-in from a differential area element  $dx^2|_{r_0}$  at the initial shell and ending up at a second sphere with arbitrary radius  $r < r_0$ . In Figure 5.2 we illustrate the projection of such a streamline tube onto the  $R$ - $z$  plane. Denoting by  $\partial\mathcal{S}$  the hypersurface delimiting the integrating volume and invoking the Gauss theorem, we have that

$$\int_{\mathcal{S}} (nU^\mu)_{;\mu} \sqrt{-g} d^4x = \oint_{\partial\mathcal{S}} nU^\mu N_\mu \sqrt{|\gamma|} d^3x = 0, \quad (5.4.2)$$

where  $N_\mu$  is a unit vector normal to  $\partial\mathcal{S}$  and  $\gamma$  is the determinant of the induced metric on this hypersurface. Since we have assumed stationarity, it is clear that the net particle flux

through any closed spatial hypersurface at a given time  $t$  equals zero. Moreover, for the remaining mixed time-space parts of  $\partial\mathcal{S}$ , the contraction  $U^\mu N_\mu$  will be, by construction, different from zero just for a hypersurface oriented perpendicularly to the radial direction. Hence, we have that Eq. (5.4.2) reduces to

$$n U^\mu N_\mu^{(r)} \sqrt{|\gamma^{(r)}|} dt d\theta d\phi \Big|_r^{r_0} = 0. \quad (5.4.3)$$

Substituting into this equation that  $N_\mu^{(r)} = \delta_\mu^r / \sqrt{g^{rr}}$  where  $g^{rr} = \Delta/\rho^2$ , together with  $\gamma^{(r)} = \Delta\rho^2 \sin^2\theta$ , we arrive at

$$n U^r \rho^2 \sin\theta dt d\theta d\phi \Big|_r^{r_0} = 0. \quad (5.4.4)$$

Invoking once again the stationarity and axisymmetry conditions, it follows that

$$dt_0 d\phi_0 = dt d\phi.$$

Using this result in Eq. (5.4.4) allows us to solve for  $n$ , getting

$$n = \frac{n_0 U_0^r \rho_0^2 \sin\theta_0}{U^r \rho^2 \sin\theta} \left( \frac{\partial\theta}{\partial\theta_0} \right)^{-1}. \quad (5.4.5)$$

Evaluating analytically the partial derivative which appears here would require a complicated calculation involving derivatives of an elliptic integral with respect its argument, modulus and integration limit. However, it is straightforward to evaluate it numerically and so it does not seem worth searching further for a full analytic expression.

We construct a suitable grid for calculating  $\partial\theta/\partial\theta_0$  in the following way: we start with a homogeneous partition of the initial polar angle  $\theta_0$ , and then follow the fluid lines down to the equator in regular radial steps. At every grid point  $(r, \theta_0)$ , we store the values of  $\theta$  and  $U^r$ , and then approximate  $\partial\theta/\partial\theta_0$  by means of standard finite differences. Figure 5.2 illustrates the construction of such a grid.

We recall here that in Section 5.1 we limited the boundary conditions to distributions of the velocity field that prevented the existence of radial turning points before the equatorial plane had been reached, i.e.  $U^r \neq 0$  for the whole radial domain of interest. Moreover, we also required the mapping  $\theta \mapsto \theta_0$  to be non-singular. For these two reasons, we can conclude that the expression for the density field given in Eq. (5.4.5) is a well-defined function.

Finally, note that the expressions for the velocity field and the streamlines given in Sections 5.2 and 5.3 are independent of the value of the density at the boundary and hence the scale for the density ( $n_0$ ) can be set arbitrarily.

## 5.5 Applications of the analytic model

We now illustrate our analytic model by applying it to an example scenario with boundary conditions consisting of matter in uniform rotation on a uniform shell, i.e.:

$$n_0 = \text{const.}, \quad (5.5.1)$$

$$\dot{r}_0 = \text{const.}, \quad (5.5.2)$$

$$\dot{\phi}_0 = \text{const.}, \quad (5.5.3)$$

$$\dot{\theta}_0 = 0. \quad (5.5.4)$$

The condition in Eq. (5.5.4) implies that, for every streamline,  $\theta_a = \theta_0$ .

Figure 5.3 shows six panels with the streamlines, velocity field and density contours for six different combinations of the flow parameters. The panels consist of spatial projections onto the  $R$ - $z$  plane, where  $R$  and  $z$  (together with  $\theta$ ) are the cylindrical coordinates defined in Eq. (3.1.10). For specifying the set of model parameters in each case, we have used  $a$ ,  $r_0$ ,  $\bar{V}_e^r$  and  $\bar{V}_e^\phi$ , where the subscript  $e$  indicates that the corresponding quantity is being evaluated at the equator of the shell. Note that, for the present boundary conditions, the set of parameters  $(a, r_0, \bar{V}_e^r, \bar{V}_e^\phi)$  has a one-to-one correspondence with  $(a, r_0, \dot{r}_0, \dot{\phi}_0)$  given by the inversion of the system of Eqs. (5.2.5)-(5.2.7). Also note that fixing this set of parameters specifies a family of models rather than a single one, since both length and density scales can still be arbitrarily and independently chosen.

The radius of the outer edge of the disc formed as matter reaches the equatorial plane,  $r_D$ , can be calculated from Eq. (5.3.40), taking first  $\theta = \pi/2$  and then  $\theta_0 = \pi/2$ , giving

$$\xi_D = \frac{\sqrt{\varepsilon(r_a - r_c)(r_d - r_b)}}{2} \left[ \Phi(r_0) - \frac{\pi}{2\sqrt{\ell_e^2 - \varepsilon a^2}} \right], \quad (5.5.5)$$

and then substituting the result into Eq. (5.3.41).

In Figure 5.4, we have plotted  $r_D$ , first as a function of the BH spin  $a$  and then as a function of the specific angular momentum at the equator of the shell  $\ell_e = \ell_z(\pi/2)$ . Here we have assumed  $\bar{V}_e^\phi > 0$ , and so a negative value of  $a$  implies a counter-rotating disc. From this figure we can clearly see how the BH spin couples with the angular momentum of the disc (through the frame-dragging effect), giving rise to a larger  $r_D$  for a co-rotating disc and a smaller  $r_D$  for a counter-rotating one. It is also clear that, as intuitively expected,  $r_D$  is a monotonically increasing function of both  $\bar{V}_e^\phi$  and  $\bar{V}_e^r$ .

Working with the LNRF velocities  $\bar{V}_e^r$  and  $\bar{V}_e^\phi$ , makes the exploration of the parameter space easier since, being physical velocities, they are naturally bounded as  $\bar{V}_e^r \in (-1, 0]$  and  $\bar{V}_e^\phi \in [0, 1)$ . Furthermore, for fixed values of  $r_0$  and  $a$ , a pair of velocities in the  $\bar{V}_e^r$ - $\bar{V}_e^\phi$  plane is also restricted by the condition that the resulting  $r_D$  should satisfy  $r_D \in (r_+, r_0)$ . In Figure 5.5 we have plotted the regions on the velocity space which lead to an outer radius of the disc satisfying this criterion. The plot has been constructed for a fixed value of  $r_0 = 10M$  and three different values of  $a$ . From this figure we observe that the domain of values in the velocity space leading to physically relevant accretion

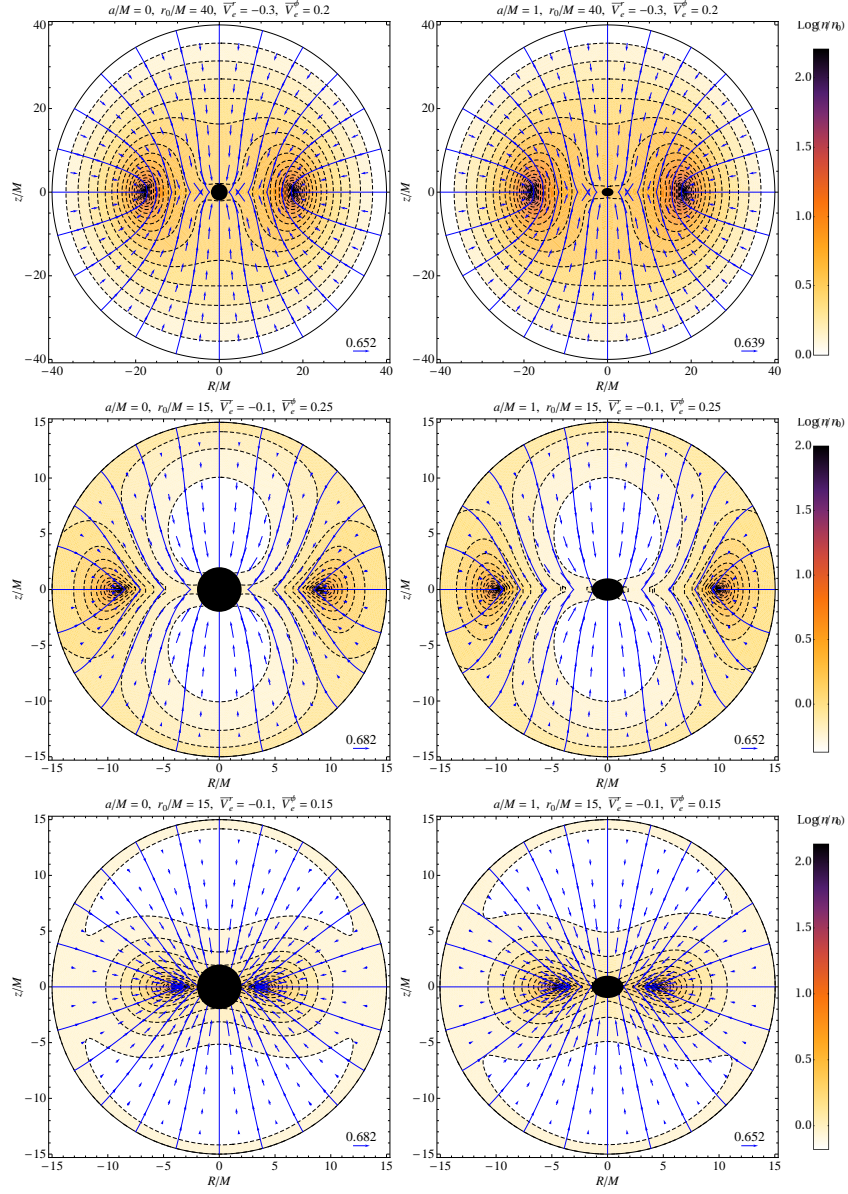


**Figure 5.3:** Streamlines, velocity field and density contours for six different combinations of the flow parameters. The values of the parameters used in each case are indicated above each panel. Each panel shows the spatial projection onto the  $R$ - $z$  plane and the colour coding corresponds to the value of the logarithm of the particle number density  $\text{Log}(n/n_0)$ , with the scale being indicated by the colour-coding bar at the left of each row. The arrows correspond to the  $\bar{V}^r$  and  $\bar{V}^\theta$  components of the velocity field. The magnitude of the largest arrow is indicated at the bottom right of each panel.

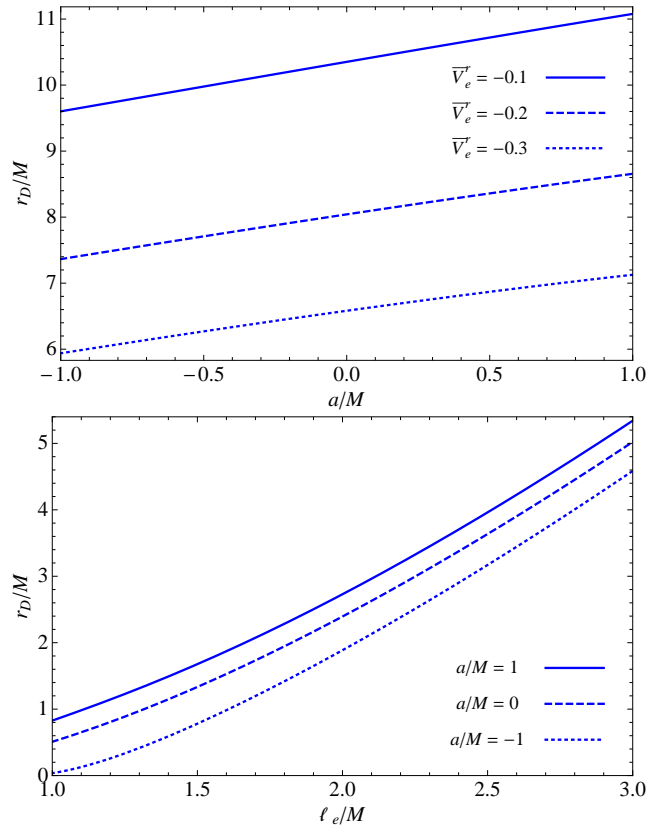


**Figure 5.4:** This figure shows  $r_D$  plotted against  $a$  (top panel) and  $\ell_e$  (bottom panel). In the top panel, fixed values are taken for  $r_0(= 20 M)$  and  $\bar{V}_e^\phi(= 0.2)$  while in the bottom panel, fixed values are taken for  $r_0(= 60 M)$  and  $\bar{V}_e^r(= -0.2)$ . Note how the BH spin couples with the angular momentum of the infalling matter and leads to a larger  $r_D$  for a co-rotating flow and to a smaller  $r_D$  for a counter-rotating one.

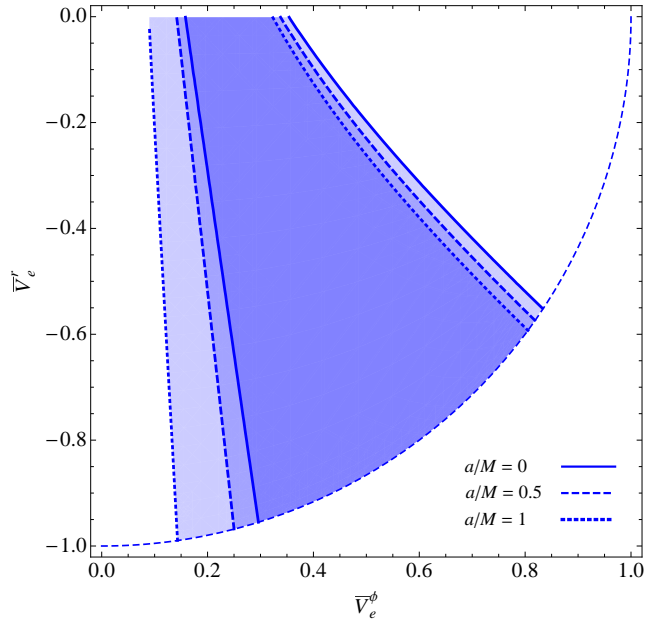


**Figure 5.5:** The pairs of velocity values  $\bar{V}_e^r$ - $\bar{V}_e^\phi$  leading to a disc radius such that  $r_D \in [r_+, r_0]$  are plotted for a fixed value of  $r_0 = 10M$  and for  $a/M = 0, 0.5, 1$ . The upper boundary for each value of  $a$  represents the points  $(\bar{V}_e^r, \bar{V}_e^\phi)$  such that  $r_D = r_0$ , while the lower one represents those such that  $r_D = r_+$ . Note how the domain of values in the velocity space leading to physically relevant accretion models shifts to smaller values of  $\bar{V}_e^\phi$  as  $a$  increases because of the frame-dragging effect.

models shifts to smaller values of  $\bar{V}_e^\phi$  as  $a$  increases. This behaviour is a consequence of the frame-dragging effect: for a given test particle with fixed azimuthal velocity  $\bar{V}_e^\phi$ , its associated angular momentum is an increasing function of  $a$ , and hence points in the  $\bar{V}_e^r$ - $\bar{V}_e^\phi$  plane which, in the low- $a$  case, did not have large enough angular momentum to keep the outer edge of the disc outside the event horizon are able to do so for a larger value of  $a$ . Conversely, low- $a$  models with an angular momentum only just small enough to form any disc inside their initial shell would have discs entirely outside of their initial shell when  $a$  is increased (thus becoming excluded from the parameter domain). Also note that this parameter-space effect is greater on the lower boundary of  $\bar{V}_e^\phi$  than on the upper one, which is simply due to the fact that the frame-dragging increases as  $r \rightarrow r_+$ .

## 5.6 Comparison with numerical simulations

In this section we compare the analytic solution derived above against one of the simulations in LR and a series of simulations performed with the modified version of the code Gadget 2 (Springel, 2005) presented and used by TMP. The first comparison was presented in Paper II, while the second one forms part of Paper III.

In both LR and TMP, the authors studied numerically the production of the progeni-

tors for long-duration GRBs as the aftermath of the collapse of a massive star. In LR, the authors investigated the formation of a small-scale accretion disc around a Schwarzschild BH by using 2D SPH simulations starting off from idealised initial conditions. They included an analytic approximation for neutrino cooling and considered an equation of state (EoS) with contributions from radiation,  $e^\pm$  pairs,  $\alpha$  particles and free nucleons. In their work relativistic gravitational effects are mimicked with the pseudo-Newtonian potential defined by Paczyński & Wiita (1980) (PW):

$$\Phi_{\text{PW}}(r) = -\frac{M}{r - 2M}. \quad (5.6.1)$$

TMP, instead, presented 3D simulations for a rotating BH starting off from realistic initial conditions (a pre-supernova model coming from stellar evolution codes), using tabulated values for neutrino cooling (by plasma processes, pair annihilation and non-degenerate bremsstrahlung scattering) and including a rough treatment of general relativistic effects in the Kerr metric by using the modification to the Newtonian radial acceleration given by Mukhopadhyay & Misra (2003) (MM):

$$a_{\text{MM}}(r) = -\frac{M}{r^2} \left[ 1 - \left( \frac{r_{\text{ms}}}{r} \right) + \left( \frac{r_{\text{ms}}}{r} \right)^2 \right], \quad (5.6.2)$$

where  $r_{\text{ms}}$  is the radius of the marginally stable circular orbit defined in Eq. (4.3.8). MM called the associated pseudo-Newtonian potential the ‘second-order expansion potential’. From direct integration of Eq. (5.6.2), the gravitational potential corresponding to this is given by

$$\Phi_{\text{MM}}(r) = -\frac{M}{r} + \frac{Mr_{\text{ms}}}{2r^2} - \frac{Mr_{\text{ms}}^2}{3r^3}. \quad (5.6.3)$$

In addition to these two pseudo-Newtonian potentials, in this section we also compare our ballistic toy model with results obtained using the classical Newtonian potential

$$\Phi_{\text{N}}(r) = -\frac{M}{r}. \quad (5.6.4)$$

We should stress that the two pseudo-Newtonian potentials used in the simulations presented in this section have been previously designed for capturing relevant relativistic features of importance for accretion discs, including getting correct locations for the marginally stable circular orbit in Schwarzschild and Kerr spacetimes. This does not at all guarantee that they would be good for other purposes such as the infall calculations being discussed here (and particularly for motion away from the equatorial plane). However, they have been widely used in more general contexts and simulations and so it is relevant for us to test them against the toy model.

It is clear that in a full hydrodynamic simulation, the final accretion flow is determined by a combination of all of the physical processes that have been included: gravitational field of the central object, self gravity of the fluid, hydrodynamic forces, and microphysical processes such as neutrino cooling and physical viscosity. Since in the

final outcome of the simulation, all of these effects are mixed together, it is not completely straightforward to know how to interpret the results of a comparison with the toy model. Therefore, the aim of this study is to start by analysing what we consider to be two dominant effects on the flow, those of hydrodynamics and gravitation. In order to perform a systematic analysis to distinguish between these, we have used the TMP code to consider two kinds of simulation (with the physical conditions chosen to be those of a possible model GRB):

(i) Ballistic free-fall, with the SPH particles being automatically removed when they reach either the equatorial plane or the BH horizon. Here we consider an EoS for which the fluid pressure  $P = 0$ , effectively ‘turning off’ the hydrodynamical forces. The aim of this kind of simulation is to highlight the differences in the flow dynamics coming from both the use of different gravity descriptions (full general relativity, Newtonian gravity, and the MM and PW pseudo-Newtonian potentials) and the different numerical implementations of the equations of motion for the particles.

(ii) Full-hydrodynamical simulations, including back reaction from a growing equatorial disc and cooling in regions where the gas gets very hot ( $\geq 10^9\text{K}$ ). Here we do not remove SPH particles when they reach the equatorial plane but rather let them settle down by themselves into a disc structure. In this case we employ a polytropic EoS of the form  $P = (\gamma - 1)nu$ , where  $n$  is the baryon number density,  $u$  the internal energy per baryon and  $\gamma$  is the adiabatic index.<sup>(2)</sup> We take  $\gamma = 4/3$ , and the value of the internal energy (taken to be constant in the initial shell) is set at an arbitrary but non-negligible value of one tenth of the sum of kinetic energy and absolute value of the Newtonian potential energy of an SPH particle at the equator of the shell, i.e.  $u = 0.1 \left( \dot{r}_0^2/2 + r_0^2 \dot{\phi}_0^2/2 + M/r_0 \right)$ .

For both types of simulation, we take stationary boundary conditions with SPH particles being continuously injected with constant density and velocity distributions from a fixed injection radius  $r_0$ . We treat the BH horizon as an inner boundary at which particles are extracted from the simulation. For a fair comparison with the toy model, we report here late-time snapshots of the simulations in which the system has evolved to a quasi-stationary situation (at least in the region away from the disc). As mentioned above, the number of particles being used in these simulations was continuously changing but was consistently around  $2.5 \times 10^5$  at the time shown. Moreover, in order to reduce the noise level (and exploiting the axisymmetry of the system), the results presented in the following were obtained after averaging over 24 cross-sectional  $\phi = \text{const.}$  slices of the 3D simulations.

---

<sup>(2)</sup>We note that the adiabatic index  $\gamma$  is only used in this section and should not be confused with the determinant of the three-metric that we have denoted with the same symbol.

### 5.6.1 Schwarzschild case

First, we consider a set of boundary conditions corresponding to infall of a rotating gas cloud onto a non-rotating black hole, similar to those used by LR in their numerical calculations. We have made comparisons for several of their models, finding a qualitative good agreement in all cases. For illustration, we show the results for the simulation in LR with the following set of parameter values

$$a = 0, \quad (5.6.5)$$

$$M = 4 M_{\odot}, \quad (5.6.6)$$

$$\dot{M} = 0.01 M_{\odot}/s, \quad (5.6.7)$$

$$r_0 = 100 M, \quad (5.6.8)$$

$$\dot{r}_0 = -1/\sqrt{50}, \quad (5.6.9)$$

$$r_0 \dot{\phi}_0 = 0.038, \quad (5.6.10)$$

$$\dot{\theta}_0 = 0. \quad (5.6.11)$$

Note that, for convenience, we have used standard (non-geometrized) units to express the total accretion rate in Eq. (5.6.7).

Using the results from Section 4.3, it is simple to check that for  $a = 0$ , the minimum necessary angular momentum that a test particle must possess in order to be in a stable circular orbit is  $\ell_{\text{ms}} = 4M$ . However, for the present boundary conditions, the fluid particle with the largest angular momentum (i.e. one that starts from the equator of the initial shell) has  $\ell = 3.8M$ . Therefore, in this case one expects that none of the matter arriving at the equatorial plane would possess enough angular momentum to maintain a stable orbit around the central BH and, hence, that all of the infalling material should be accreted into the BH on a dynamical time-scale. This kind of accretion corresponds to the ‘small-scale inviscid disc’ regime discussed by Beloborodov & Illarionov (2001) and, indeed, is what we observe in the LR simulation.

The top left panel in Figure 5.6 shows the accretion flow as calculated from the analytic model, while the top right panel shows a late-time snapshot of the LR simulation, taken when a quasi-stationary state had been reached. There is an overall good agreement between them, even though it is not completely clear how to differentiate pure hydrodynamic effects from the ones related to the different descriptions of gravity. The other four panels present a detailed comparison of the spatial components of the velocity and the density at four spherical cuts. Here, we see a good agreement between the analytical and numerical results for  $U^{\theta}$  and  $U^{\phi}$ . For  $U^r$  and  $\varrho$ , there is quite good qualitative agreement, although the numerical results for  $\varrho$  suffer from numerical noise inherent in the interpolation scheme at low particle number densities, and the numerical results for  $U^r$  show larger radial infall velocities. This last discrepancy can be attributed to the use of the PW pseudo-Newtonian potential there, which artificially enhances the radial acceleration.

In order to analyse this in more detail and to disentangle hydrodynamic effects from free-fall motion, we consider here a series of ballistic simulations performed with the

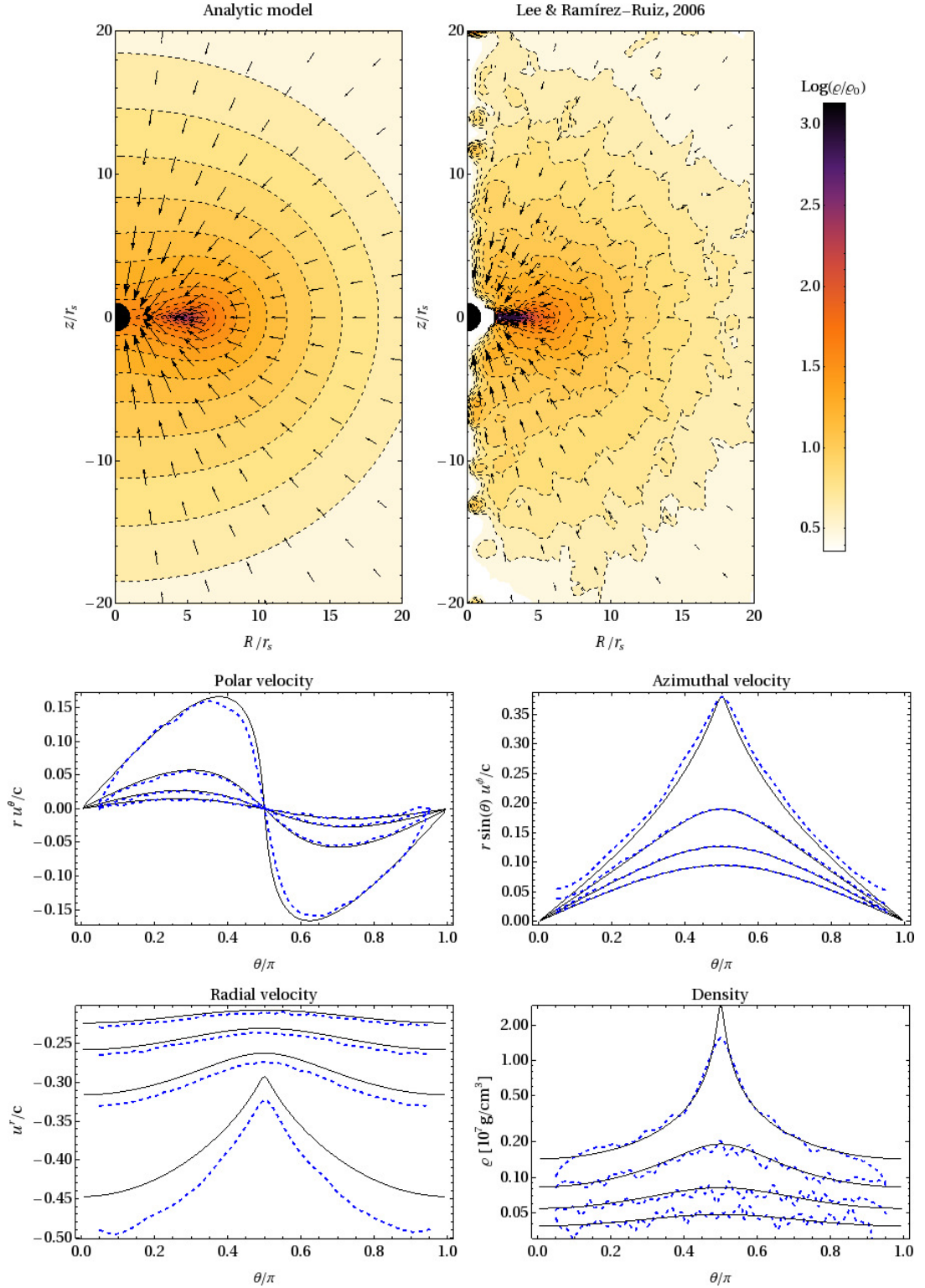


**Figure 5.6:** Comparison between the analytic model and one of the LR simulations. The plots are for an accretion flow towards a Schwarzschild BH with mass  $M = 4M_{\odot}$ , starting from a spherical shell at  $r_0 = 100M$ . The rest of the boundary conditions are given in Eqs. (5.6.7)-(5.6.11). The top panels show a projection of the accretion flow onto the  $R$ - $z$  plane, together with isodensity contours, for the analytic solution (left) and the LR numerical simulation (right). The remaining four panels show the velocity components and the density at the radial cuts  $r/M = 40, 30, 20, 10$  with the analytic and numerical results being represented by solid and dashed lines respectively.

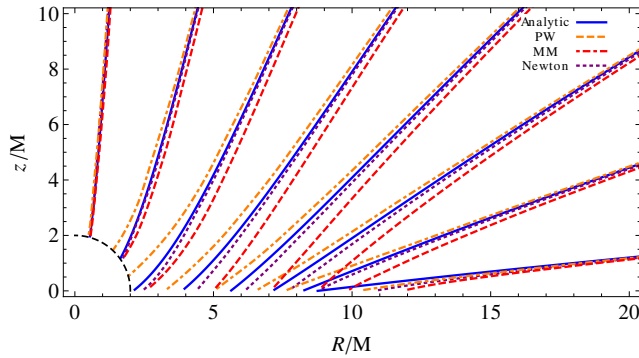


**Figure 5.7:** Streamlines corresponding to the analytic solution and to the three ballistic SPH simulations for a non-rotating BH ( $a = 0$ ) with the remaining boundary conditions being as in Eqs. (5.6.6)-(5.6.11). The figure shows a zoom-in of the first quadrant of the  $R$ - $z$  plane. The BH horizon (located at  $r_+$  and which represents the inner boundary) is indicated with the dashed-line quarter-circle.

TMP code for the same boundary conditions. Moreover, to clarify the role played by the PW potential in approximating general relativistic features, we consider simulations using three different potentials: the usual Newtonian one, and the PW and MM pseudo-Newtonian potentials (this last one with  $a = 0$ ). In Figure 5.7 we compare the streamlines coming from each of these simulations against the streamlines from the toy model. Since hydrodynamical effects are absent in these ballistic simulations, the differences between the numerical simulations and the toy model can reasonably be attributed mainly to the different descriptions of gravity (although, some very small differences may be attributed to the finite stepping of the discrete method, etc.). In this figure we observe that the different streamlines start to deviate importantly from each other just for  $r \lesssim 20M$  and that far away from the central BH the differences between the different descriptions of gravity become negligible (bear in mind that the streamlines originate from  $r = 100M$ ). In the vicinity of the equatorial plane, the streamlines obtained with the Newtonian potential are closer to the general relativity solution than those obtained with the pseudo-Newtonian potentials. In this figure we can also see that the PW streamlines arrive at the equatorial plane at smaller radii than the analytic relativistic ones, while the Newtonian and MM ones arrive at larger radii. This suggests that equivalent hydrodynamical simulations implementing the PW potential would underestimate the extension of any resulting disc while those implementing the Newtonian and MM potentials would overestimate it.

We now investigate the inclusion of hydrodynamic properties of the flow by considering polytropic simulations made with the three potentials employed in the previous ballistic runs. In Figure 5.8 we show the comparison of the ballistic streamlines in Figure 5.7 with the fluid streamlines for each of the three potentials. When comparing these two sets of streamlines, it is important to bear in mind that in the polytropic simulations, unlike in the ballistic one, SPH particles are not removed from the simulation

at the equatorial plane and, therefore, the build-up of a disc can take place. From this figure we can see that an important feature characterising the polytropic simulations is the existence of a shock front around the disc, marking the boundary between two different flow regimes. In the pre-shock region, a clear stationary regime is rapidly reached where the flow moves supersonically and is highly laminar. In this region, which we shall refer to as the infall region, we find that the polytropic simulations produce quite similar results to the ballistic ones, and hence also to the toy model. On the other hand, in the post-shock region the hydrodynamic effects become dominant, causing the flow to decelerate and deviating the streamlines away from the ballistic paths towards the equatorial plane. In this way, the action of pressure gradients prevent the streamlines from having a ‘head-on’ collision with their symmetric counterparts coming from the opposite hemisphere. Clearly, the full hydrodynamical evolution in this region depends on the particular EoS being used as well as on the particular mechanism driving the accretion (e.g. viscosity, dynamical instabilities, etc.) and also on the cooling prescription, but again, the details of this post-shock region are outside the scope of the present study.

From Figure 5.8 we also note a crucial difference in terms of the long term evolution of the disc resulting from the use of different potentials. In this figure we see that only the simulation using the PW potential (top panel of Figure 5.8) captures correctly the ‘small-scale inviscid disc’ regime that is expected for the present boundary conditions. For the other two potentials (middle and bottom panels of Figure 5.8), we observe a growing ring of matter with enough angular momentum to avoid direct accretion onto the BH. As a consequence, the resulting disc in each of these cases evolves on a viscous time-scale rather than the much shorter dynamical time-scale that characterises the ‘small-scale inviscid disc’ regime.

From these comparisons we can conclude that, even though the ballistic streamlines for the Newtonian potential appear to give the best match to those of the analytic relativistic solution in Figure 5.7, as far as the hydrodynamic long-term evolution of the resulting disc is concerned, among the the three potentials studied here, only the PW potential leads to the expected ‘small-scale inviscid disc’ regime which is an important relativistic feature of this system.

### 5.6.2 Kerr case

Here we consider the same boundary conditions as in Eqs. (5.6.6)-(5.6.11) but now for a rotating BH with spin parameter  $a = 0.5 M$ . Since the MM potential is the only one specifically devised to approximate relativistic effects for a rotating BH, in what follows here we only consider simulations that implement the MM potential.

For this set of boundary conditions, we present in Figure 5.9 the analytic solution alongside the results of both the ballistic and polytropic simulations. The figure shows a spatial projection onto the  $R$ - $z$  plane of isodensity contours, streamlines and velocity fields for each case. Let us focus first on the ballistic simulation result (middle panel), which rapidly reached a stationary state. In this figure we see an overall satisfactory agreement with the analytic solution, although a closer inspection of the streamlines reveals some quantitative differences. As in Figure 5.6, here we also note that the

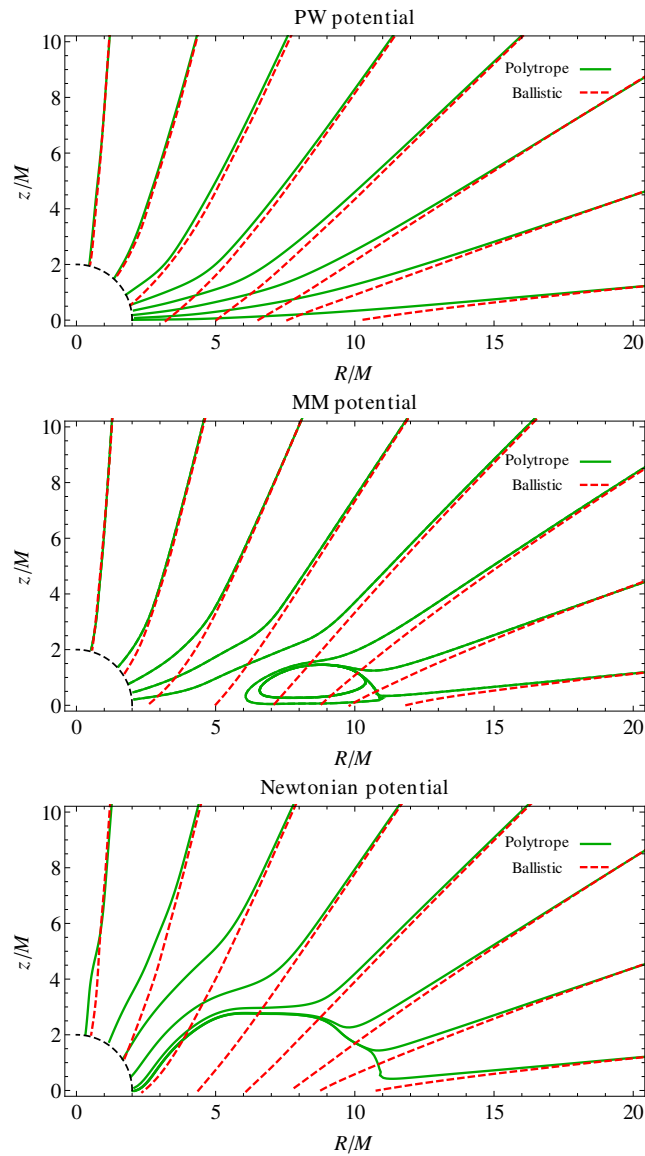


**Figure 5.8:** This figure compares the streamlines from simulations performed with the TMP code for ballistic motion against those for a polytropic fluid. Note that only for the run using the PW potential does the resulting flow correspond to a ‘small-scale inviscid disc’. In the other two cases, the infalling matter keeps accumulating in a ring around the BH. This effect is more evident in the case with the Newtonian potential.

simulation isodensity contours are somewhat ‘noisy’ compared with the analytic results. Nevertheless, this level of fluctuation is consistent with the effects of discretisation and interpolation within SPH simulations.

Figure 5.10 shows a closer comparison of the streamlines of the analytic solution with the ones of the ballistic simulation. Similarly as in Figure 5.7, here we see that the ballistic streamlines deviate significantly from the analytic ones only for  $r \lesssim 10 M$  and that far away from the central BH the differences between them become negligible.

Once more we analyse the role of pressure gradients on the infall by comparing the polytropic SPH simulation shown in the bottom panel of Figure 5.9 with the corresponding ballistic flow shown in the middle one. In the polytropic simulation we observe the formation of a disc that keeps growing in mass and expanding horizontally. The material in this disc corresponds to the fraction of the infalling matter which possesses enough angular momentum to remain in a stable orbit around the BH. Since it is not within the scope of the present work to study the evolution of such a disc, we show here a snapshot at a time at which any kind of initial transient related to the initial conditions has faded away, but, at the same time, neither the mass nor the extension of the disc have grown importantly (additionally, the presence of cooling in the simulation aids in limiting the disc height). In Figure 5.11 we present a direct comparison of the streamlines for these two cases. In this figure we see a quite good match between the two sets of streamlines in the infall region while the effects of the pressure gradients become significant only in the high density region near to the equatorial plane. Again, in this region we observe that a shock front develops around the disc where the incoming streamlines decelerate and deviate from the corresponding ballistic trajectories. From Figure 5.9 we also note that the isodensity contours of the polytropic simulation in the infall region are less noisy than those of the ballistic simulation. This is due to the action of pressure forces that smooth out the particle distribution and so reduce discretisation fluctuations.

Note that, in comparing Figures 5.10 and 5.11, the departure of the ballistic streamlines from the analytic solution occurs earlier and for a larger fraction of the simulation domain than the differences between the ballistic and polytropic streamlines. In other words we see that here, adopting an improved description for the gravitational field of the BH has a greater effect on the infall part of the simulation than including pressure.

Finally we note that, with respect to the  $a = 0$  case discussed in Section 5.6.1, the change in the spin parameter of the BH does not lead to significant qualitative differences in either the velocity field or the density field of the accretion flow in the infall region.

## 5.7 Summary and discussion

In this chapter we have presented an analytic toy model for the relativistic accretion of non-interacting particles onto a Kerr BH. Taking the assumptions of stationarity, axisymmetry and ballistic motion, we have given analytic expressions for the streamlines and the velocity fields as well as a simple numerical scheme for calculating the density field. This model is a generalisation of the one presented in Paper II for Schwarzschild spacetime, and it has been demonstrated how the earlier results are easily recovered

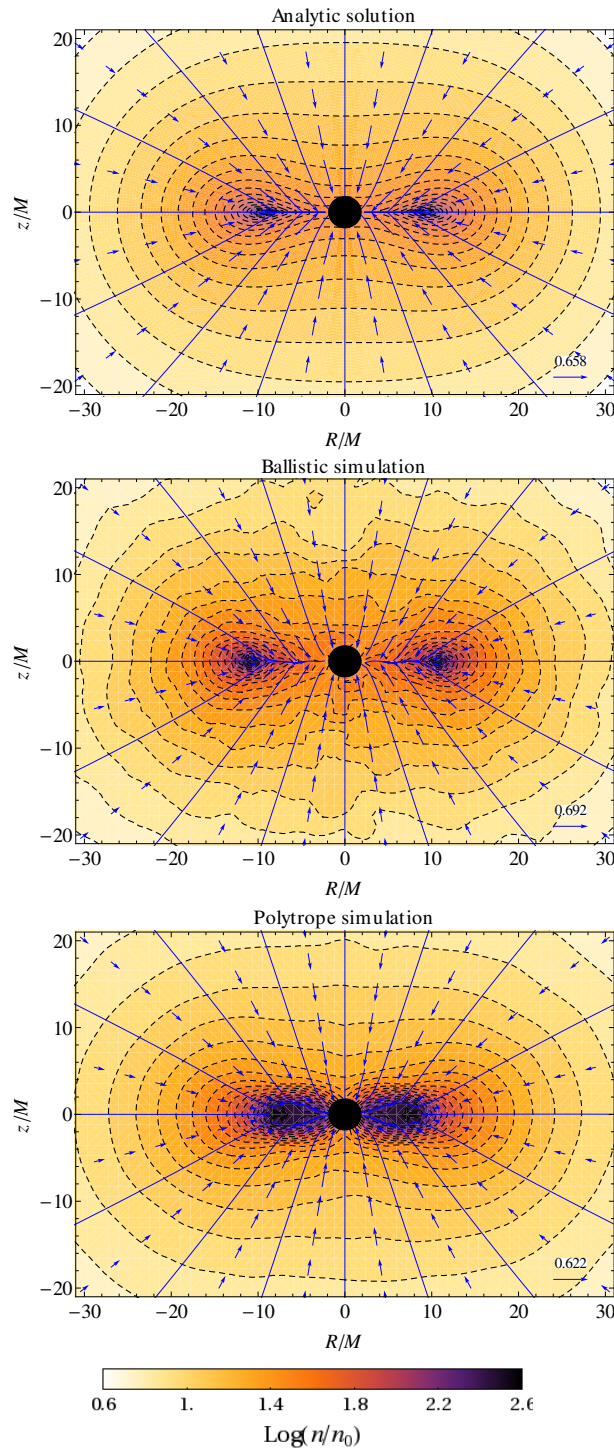


**Figure 5.9:** This figure shows isodensity contours, streamlines and velocity fields for the analytic solution and for the ballistic and polytropic SPH simulations, for an accretion flow onto a rotating BH with  $a = 0.5 M$ . The other model parameters are as given in Eqs. (5.6.6)-(5.6.11). The common scale for the density colour coding is shown at the bottom of the figure. The velocity field in each panel is represented by the two-vectors  $(\bar{V}^R, \bar{V}^z)$ ; the length scale for these vectors is given at the bottom right corner of each panel. The SPH simulations used a varying total particle number, but typically this was around  $2.5 \times 10^5$  at the times shown (mass per SPH particle  $\approx 3.6 \times 10^{-10} M_\odot$ ).

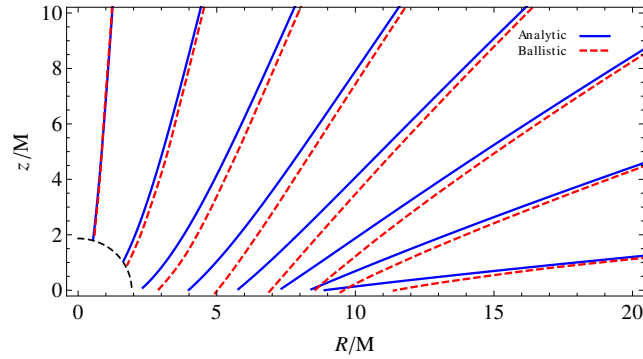


**Figure 5.10:** Streamlines corresponding to the analytic solution and to the ballistic SPH simulation presented in the top and middle panels of Figure 5.9. The figure shows the first quadrant of the  $R$ - $z$  plane with the BH horizon (located at  $r_+$ ) indicated with a black dashed-line quarter-circle.

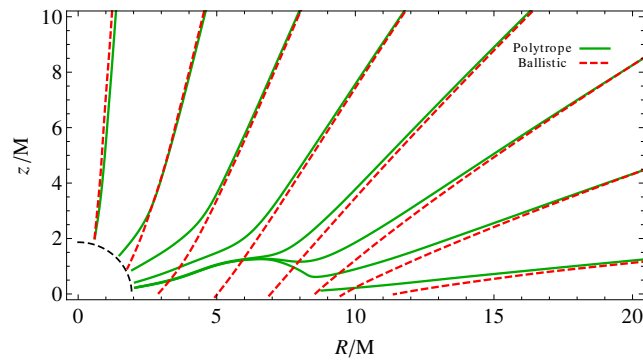


**Figure 5.11:** Streamlines corresponding to the ballistic and polytropic SPH simulations presented in the middle and bottom panels of Figure 5.9. The figure shows a zoom-in of the first quadrant of the  $R$ - $z$  plane. The BH horizon (located at  $r_+$ ) is indicated with the dashed-line quarter-circle.

from the present solution in the non-rotating limit.

Using a single analytic expression for describing the streamlines constitutes a novel way of expressing the solution to the latitudinal and radial motion of timelike geodesics in Kerr spacetime. The generality of this expression has been shown by using standard identities of the Jacobi elliptic functions.

We have explored the effect of frame-dragging on the resulting accretion flow and found that an effective coupling occurs between the BH spin and the angular momentum of the infall, leading to more extended discs if the flow is co-rotating with the BH and smaller discs in the counter-rotating case.

Given the analytic nature of the present model, it provides a very practical tool for use in benchmarking general relativistic hydrodynamics codes as we have demonstrated here by comparing it against several SPH simulations (both with  $P = 0$  and for a polytropic EoS). Also, this toy model allows simple and direct comparisons between approximate methods for including general relativistic effects in simulations on a case-by-case basis. We have used it here to test the performance of SPH simulations implementing two pseudo-Newtonian potentials (MM and PW) and found an overall good qualitative agreement between the toy model and the simulations, although we have also seen that apparently small quantitative discrepancies in the flows can eventually lead to rather different long-term evolutions (see e.g. Figure 5.8). In the purely ballistic comparisons, we found a good agreement between the trajectories coming from different gravity descriptions in the regions far away from the BH. However, as the test particles approach the inner region, the different trajectories start to deviate significantly from each other (see e.g. Figure 5.7). How important these discrepancies are in practice will certainly depend on the particular application; nonetheless, from the present results we can conclude that neither of the two pseudo-Newtonian potentials considered here is particularly well-suited for reproducing off-equatorial motion of test particles.

Besides the utility of the toy model as a test solution, its flexibility for setting a fairly wide range of boundary conditions makes it an ideal tool for exploring the effect of different flow parameters (accretion rates, angular momentum and density distributions, etc.) in applications where the approximations of steady-state and axisymmetry are reasonable ones. These assumptions are often met in some interesting astrophysical scenarios such as under-luminous accretion towards supermassive BHs, wind-fed X-ray binaries and collapsars in which the accretion disc remains thin either due to efficient cooling or because it evolves within the ‘small-scale inviscid’ regime. In this chapter we have shown a series of comparisons between the toy model and full-hydrodynamic, numerical simulations for a collapsar-like setup. Rather good agreement was obtained between the simulations and the toy model, under circumstances where one might expect to have agreement. The main discrepancies between the resulting accretion flows in the infall region have been shown to be related more to the different treatments of the gravitational field produced by the BH rather than to the ballistic description of the infall. Indeed, we observed that the effects of pressure gradients tend to become important just in the immediate proximity of the disc, where a shock front develops and decelerates the incoming flow. A new kind of exploratory simulation can be envisaged in

which simple but general boundary conditions are set far away from the central object and then, by using the toy model, the flow is transported down to the region in which pressure gradients become dominant where a proper hydrodynamical study can then be performed. This kind of approach would greatly reduce the spatial domain of the simulation, allowing greater resolution and reducing the computing time.

## Chapter 6

# Final remarks and conclusions

The work presented in this thesis is framed within a collaborative project concerning the development of the new SPHINCS code, which is intended for studying astrophysical phenomena involving the accretion flow of fluids towards a rotating BH. In the applications we want to investigate, special and general relativistic effects coming from a strong gravitational field with frame-dragging are key factors for determining the fluid motion.

SPHINCS is conceived as a natural extension of the special relativistic code introduced and successfully tested by Rosswog (2010a), and will also benefit from the new density-balanced binary tree developed by Gafton & Rosswog (2011) which allows an efficient and accurate neighbour search and (Newtonian) gravitational force calculation. The mathematical framework on which SPHINCS is based consists of a recent general relativistic formulation of SPH (Monaghan & Price, 2001; as extended by Rosswog, 2010b), which is derived self-consistently from a perfect-fluid Lagrangian and includes corrective terms that account for time-varying adaptivity. We feel that SPHINCS should constitute a substantial advance with respect to previous implementations of the SPH method in the context of general relativity.

In Chapter 2 of this thesis, we have rederived the evolution equations used in SPHINCS in terms of the 3+1 formalism. The adoption of this formalism has proven to be very useful for handling the three reference systems involved in this set of equations: the comoving reference frame in which the physical properties of the fluid are defined, the reference frame of the Eulerian observers in which the numerical variables are defined, and the locally flat computing frame in which the SPH interpolation is carried out. This formalism has also allowed us to introduce a simple scheme for recovering the physical variables from the numerical ones. Additionally, we have demonstrated that in a flat spacetime, SPHINCS reduces to the special relativistic formulation of Rosswog (2010a), that the geodesic equations are recovered in the limit of vanishing hydrodynamical forces, and that the usual expressions of standard SPH are recovered in the non-relativistic limit.

The first step in our development programme is to implement the SPHINCS equations in Kerr spacetime. Several aspects concerning this were discussed in Chapter 3. There, we have given a general review of the Kerr metric in terms of the two most com-

monly used coordinate systems: Boyer-Lindquist (BL) and Kerr-Schild (KS). The first of these corresponds to observers located at infinity and, for this reason, these coordinates are relevant for making connections to observations. However, given that these coordinates become singular at the horizon, they are not the most convenient choice for describing processes in the vicinity of the BH. The KS coordinates, on the other hand, are regular everywhere except at the ring singularity, and because of this they are well suited for the implementation of our numerical code. In Chapter 3 we have also discussed the transformation of vectorial and tensorial quantities back and forth between these two coordinate systems, as well as expressing them in terms of the 3+1 formalism. Finally, using the Cartesian-like form of the KS coordinates, we have provided explicit expressions for the acceleration terms due to the spacetime curvature that enter into the SPHINCS evolution equations. A key feature of this discussion is that, due to our choice of coordinates and kernel estimate, the acceleration terms in the evolution equations formally reduce to those in the special relativistic set of equations.

An important aspect in the development of any numerical code is the process of calibration and testing. In this thesis we have introduced a number of tools which are intended to be used for testing the features of SPHINCS which are directly related to its implementation in a curved spacetime. Based on the detailed analysis of the time-like geodesics of Kerr spacetime given in Chapter 4, we have prepared a catalogue of representative test particle trajectories that will be used for benchmarking the ability of the new code in recovering geodesic motion. A more complex test was presented in Chapter 5 consisting of a toy model for the relativistic accretion of a rotating gas cloud towards a Kerr BH. In Section 5.6 we demonstrated the use of the toy model as a test solution by comparing it with two distinct SPH codes that implement pseudo-Newtonian potentials for mimicking general relativistic effects of Schwarzschild and Kerr spacetimes. From these results we saw that, even though the outcome of two simulations might be qualitatively similar, small discrepancies between the streamlines in the vicinity of the BH might lead to drastically different long-term evolutions. We also concluded that neither of the two potentials considered in that section correctly reproduced off-equatorial motion. This is not surprising if we consider that these potentials were not designed to reproduce this kind of motion, however they are frequently used in applications in which correctly reproducing these types of trajectory might be of crucial importance (e.g. successive passages of a star orbiting a BH before becoming tidally disrupted). Moreover, there are many other important dynamical features of the Kerr spacetime that should be taken into account (e.g. correct location of the innermost stable circular orbit, radial acceleration, epicyclic frequencies), and no pseudo-Newtonian potential can accurately approximate all of these simultaneously. This is one of the reasons why we consider that having a numerical tool such as SPHINCS, which by construction should reproduce all of these effects exactly, will represent important progress with respect to previous studies using different pseudo-Newtonian potentials to mimic general relativistic effects.

In addition to geodesic motion, there are other relevant general relativistic effects that the new code should reproduce. Further test solutions that we will consider are: the extension of the Bondi model for spherical accretion onto a Schwarzschild BH given by

Michel (1972); the Bondi-Hoyle model for wind accretion onto a Kerr BH, as considered in Font et al. (1999); the pressure-balanced fat-disc model of Jaroszyński et al. (1980).

Once we have considered all of these tests and are confident that the new code is correctly calibrated, we will have arrived at a working implementation of SPHINCS in Kerr spacetime with a Newtonian treatment of the fluid self-gravity. This research tool will then be used for studying several interesting astrophysical phenomena in which the main contribution to the spacetime curvature is given by the central BH, such as:

- The early stages of long GRB progenitors, in the model where these arise from the collapse of a rather rapidly rotating core of a massive star to form a black hole plus an encircling disc of high density matter. In the simulations presented by Taylor et al. (2011), the authors found a dynamical instability in the disc leading to the formation of spiral arms that drastically increased the accretion rate of matter flowing onto the central BH. Key features determining the onset of this instability were modelled in that work by means of a pseudo-Newtonian potential. It would be interesting to know if the same result holds with a more accurate description of the gravitational field of the BH.
- The interaction of the BH spin with the inner parts of an accretion disc around it. Various mechanisms can exert a torque on the accreting matter in the disc leading to the formation of a warp (see e.g. Bardeen & Petterson, 1975). The dynamics of a warped disc can strongly affect the spin history of a BH, and, conversely, the frame-dragging due to a rapidly rotating BH can enhance or suppress the formation and propagation of warps. SPHINCS can be useful for revisiting a number of previous investigations of these systems (see e.g. Lodato & Pringle, 2006; Perego et al., 2009; Lodato & Price, 2010).
- The tidal disruption of a star by a central BH. These systems are considered to be the engine behind some X-ray flares (see e.g. Burrows et al., 2011). In recent work, using a pseudo-Newtonian potential, Rosswog et al. (2009) suggested that the tidal disruption of a white dwarf by an intermediate mass BH may be observed as a particular type of thermonuclear supernova. It would be worth exploring this same system with an accurate modelling of the strong gravity and frame-dragging effects induced by the BH.

Future developments of the code may also involve a post-Kerr approximation in which self-gravity is modelled as a small perturbation of the background metric and then treated as an effective force in the evolution equations. However, for applications in which the self gravity of the fluid cannot be considered as giving only a small perturbation to the spacetime, SPHINCS could be made fully general-relativistic by coupling it with a metric solver (e.g. Löffler et al., 2012). Since metric solvers are usually written in terms of the 3+1 formalism, having rewritten the SPHINCS evolution equations in a 3+1 form will be advantageous for this.



# Appendix A

## Catalogue of test particle orbits

In this appendix we present a catalogue of representative timelike geodesics in Kerr spacetime. The results are reported for both the Boyer-Lindquist (BL) coordinates  $(t, r, \theta, \phi)$  and the Kerr-Schild (KS) coordinates  $(T, r, \theta, \psi)$  as introduced in Chapter 3. The results presented here were obtained by direct numerical integration of the system of differential equations in Eqs. (4.2.1), (4.2.2), (4.2.9) and (4.2.10), that describe the proper time evolution of the particle coordinates in the KS system. As discussed in Sections 3.3, the use of KS coordinates allows us to follow trajectories that plunge into the event horizon, without encountering a coordinate singularity. We map the resulting trajectories into BL coordinates by using the transformation rules in Eq. (3.3.1).

The purpose of the present orbit catalogue is two-fold. First, it contributes with practical examples to the general discussion of timelike geodesics given in Chapter 4. And second, it provides a basic test suite for benchmarking the ability of the SPHINCS code at recovering geodesic motion in the limit in which hydrodynamic forces are zeroed.

In what follows we report results for the motion of some representative examples of test particles freely falling in a Kerr spacetime. We also show spatial projections of the resulting trajectories. We consider first the case of trajectories in the equatorial plane for co-rotating and counter-rotating motion, and then the more general case of trajectories off the equatorial plane.

### A.1 Orbits in the equatorial plane I: co-rotating case

Here we consider a family of trajectories in the equatorial plane ( $\dot{\theta} = 0$  and  $\mathcal{Q} = 0$ ) characterised by a common value of  $\ell = 3.7 M$ . For the spin parameter of the BH we take  $a = 0.5 M$ . The radial effective potential  $\mathcal{V}_+(r)$  corresponding to these parameters is plotted as a function of  $r$  in Figure A.1. In this case  $\mathcal{V}_+(r)$  has two stationary points at

$$r_{\text{uc}} \approx 2.77 M \quad \text{and} \quad r_{\text{sc}} \approx 10.84 M.$$

The first value corresponds to the radius of an unstable circular orbit (maximum of  $\mathcal{V}_+$ ), while the second value corresponds to the radius of a stable circular orbit (local

minimum of  $\mathcal{V}_+$ ). In Figure A.1 we have highlighted six energy levels that correspond to six qualitatively different types of trajectory. The energy levels are

- $\mathcal{E}_1 = \mathcal{V}_+(r_{sc}) \approx 0.957$ , stable circular trajectory,
- $\mathcal{E}_2 = 0.98$ , elliptical-like trajectory,
- $\mathcal{E}_3 = 1.0$ , parabolic-like trajectory,
- $\mathcal{E}_4 = 1.03$ , hyperbolic-like trajectory,
- $\mathcal{E}_5 = \mathcal{V}_+(r_{uc}) \approx 1.054$ , unstable circular trajectory,
- $\mathcal{E}_6 = 1.07$ , plunging trajectory.

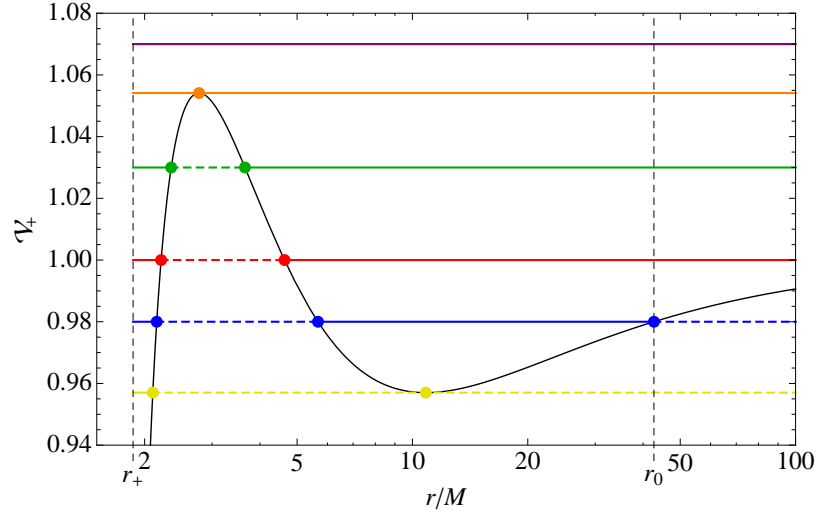


**Figure A.1:** The radial effective potential  $\mathcal{V}_+(r)$  is plotted for  $a = 0.5 M$ ,  $\ell = 3.7 M$  and  $Q = 0$ . The energy levels of the six representative trajectories considered in this section are highlighted with coloured lines while the starting points for the numerical integration are indicated by the intersections with the vertical line  $r_0 \approx 42.69$ .

The intersections between the energy levels and the vertical line  $r_0 \approx 42.69$  in Figure A.1 indicate the starting point of each of the six trajectories considered here. The test particle in the stable circular orbit describes a trajectory with constant radius  $r_{sc}$ . For the other five orbits, we take a common initial radius of  $r_0 \approx 42.69 M$  which was chosen to coincide with the apocentre (radius of maximum distance from the origin) of the elliptical-like orbit. In the last four cases, we have considered a negative value for the initial radial velocity  $\dot{r}_0$ . The initial values for  $\dot{r}_0$  and  $\dot{\psi}_0$  were obtained from Eqs. (4.2.1) and (4.2.10) after substituting  $r = r_0$  and the conserved quantities  $\mathcal{E}$ ,  $\ell$  and  $Q$  in each case. Concerning the transformation from KS to BL coordinates: in each case

we take the initial point of the trajectory as the synchronisation point, i.e.  $T_0 = t_0 = 0$  and  $\psi_0 = \phi_0 = 0$ .

Figures A.2, A.3 and A.4 show, respectively, the results of the numerical integration of the elliptical-like, parabolic-like, and hyperbolic-like trajectories considered in this case. In the first panel of each of these figures we plot  $r$  as a function of  $\tau$ . The second row of the figures is divided into two panels, in the panel on the right hand side we plot  $\phi(\tau)$  and  $\psi(\tau)$ , while in the panel on the left hand side we plot the difference between these two azimuthal angles. From this panel we see that  $\phi(\tau)$  and  $\psi(\tau)$  increase at a faster pace (steeper slope) at the pericentre and at a slower pace as the particle recedes from the BH. We also see that the difference  $\phi(\tau) - \psi(\tau)$  vanishes at  $r_0$  (since we use this as the synchronisation radius) and that becomes maximum at the pericentre. The third row is again divided into two panels. On the left we plot  $t(\tau)$  and  $T(\tau)$ , and on the right we plot the difference  $t(\tau) - T(\tau)$ . Just as for the azimuthal coordinate, here we see that the pace of growth of  $t(\tau)$  and  $T(\tau)$ , as well as of the difference  $t(\tau) - T(\tau)$  is maximum at the pericentre. In the last panel we show the spatial projection of the trajectory on the  $x$ - $y$  plane.

The results for the unstable circular trajectory are shown in Figure A.5. This figure is organised in panels in the same way as Figure A.2. From this figure we note that due to round-off error, the actual energy level in this case was slightly below the real  $\mathcal{V}_+(r_{uc})$  value. As a consequence of this, after one or two nearly circular orbits the test particle finally reaches a turning point and then goes away again towards infinity.

The results for the plunging trajectory are shown in Figure A.6. Here we have that the energy level of the trajectory is above the centrifugal barrier of the radial effective potential, i.e.  $\mathcal{E}_6 > \mathcal{V}_+(r_{uc})$ , and therefore the test particle ends up plunging into the BH. In the first three panels of Figure A.6, we show the proper time evolution of the particle's radial, azimuthal and time coordinates, respectively. The bottom row of the figure consists of two panels with the spatial projection of the trajectory onto the  $x$ - $y$  plane. The panel on the left hand side shows the resulting trajectory in the KS description, while the panel on the right hand side shows the same trajectory in the BL description. As discussed in Section 3.1, the  $t$  and  $\phi$  BL coordinates diverge as  $r \rightarrow r_+$  and, as a result, the trajectory in this description actually never crosses the outer event horizon. On the other hand, in the KS description the test particle reaches the ring singularity after a finite amount of both proper time  $\tau$  and KS coordinate time  $T$ .

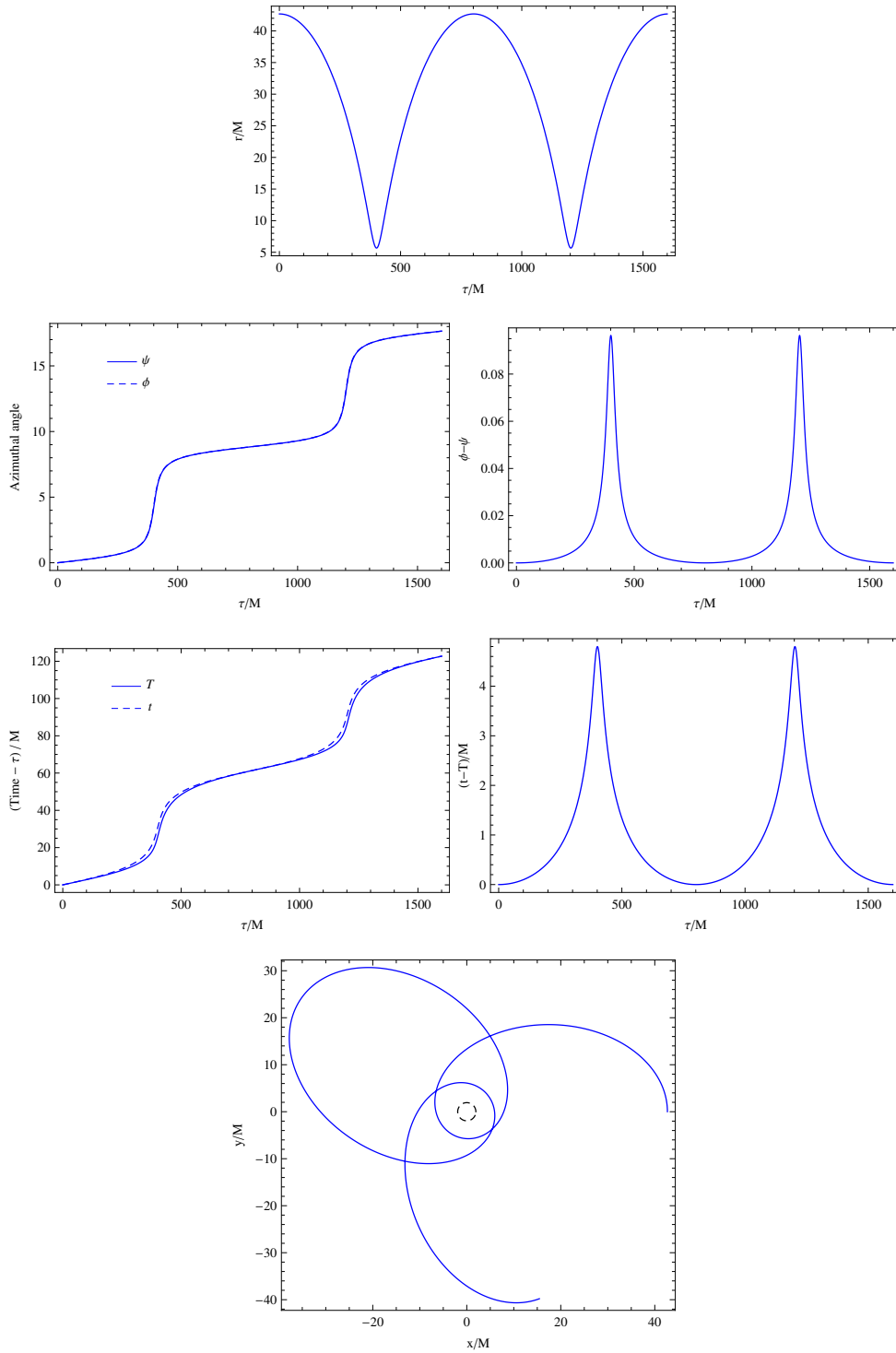


**Figure A.2:** Elliptical-like trajectory for the parameter values  $a = 0.5 M$ ,  $\mathcal{E}_2 = 0.98$ ,  $\ell = 3.7 M$  and  $\mathcal{Q} = 0$ . The first five panels show the proper time evolution of  $r(\tau)$ ,  $\psi(\tau)$ ,  $\phi(\tau)$ ,  $t(\tau)$  and  $T(\tau)$ , as well as the differences  $\phi(\tau) - \psi(\tau)$  and  $t(\tau) - T(\tau)$ . The last panel shows the spatial projection of the trajectory in the  $x$ - $y$  plane. In this last panel (and in all of the following plots with spatial projections) the outer event horizon  $r_+$ , is indicated with a dashed black line.

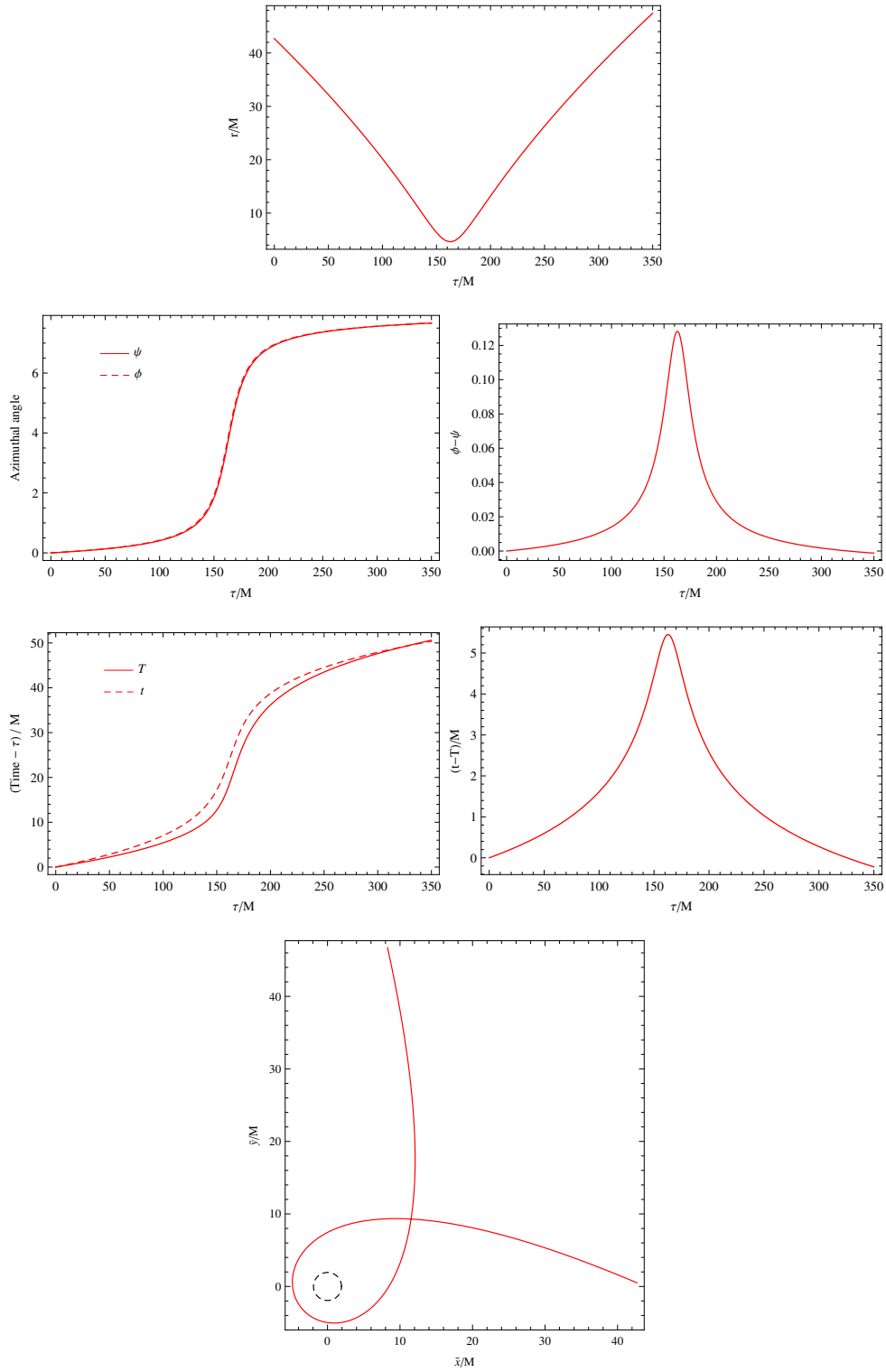


**Figure A.3:** Parabolic-like trajectory for the parameter values  $a = 0.5 M$ ,  $\mathcal{E}_3 = 1$ ,  $\ell = 3.7 M$  and  $Q = 0$ . The panels in the figure follow the same structure as in Figure A.2.

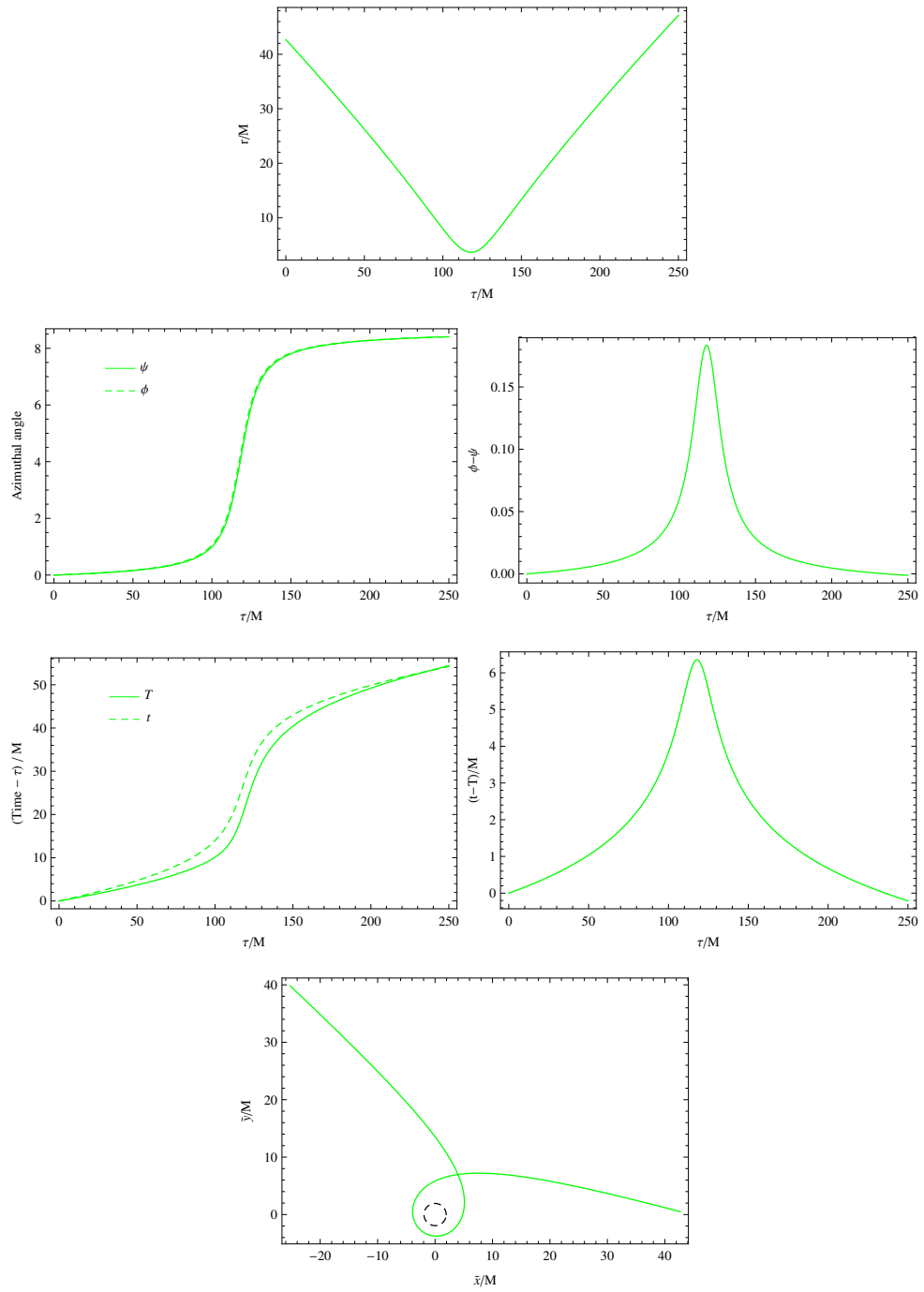


**Figure A.4:** Hyperbolic-like trajectory with parameter values  $a = 0.5 M$ ,  $\mathcal{E}_4 = 1.03$ ,  $\ell = 3.7 M$  and  $Q = 0$ . The panels in the figure follow the same structure as in Figure A.2.

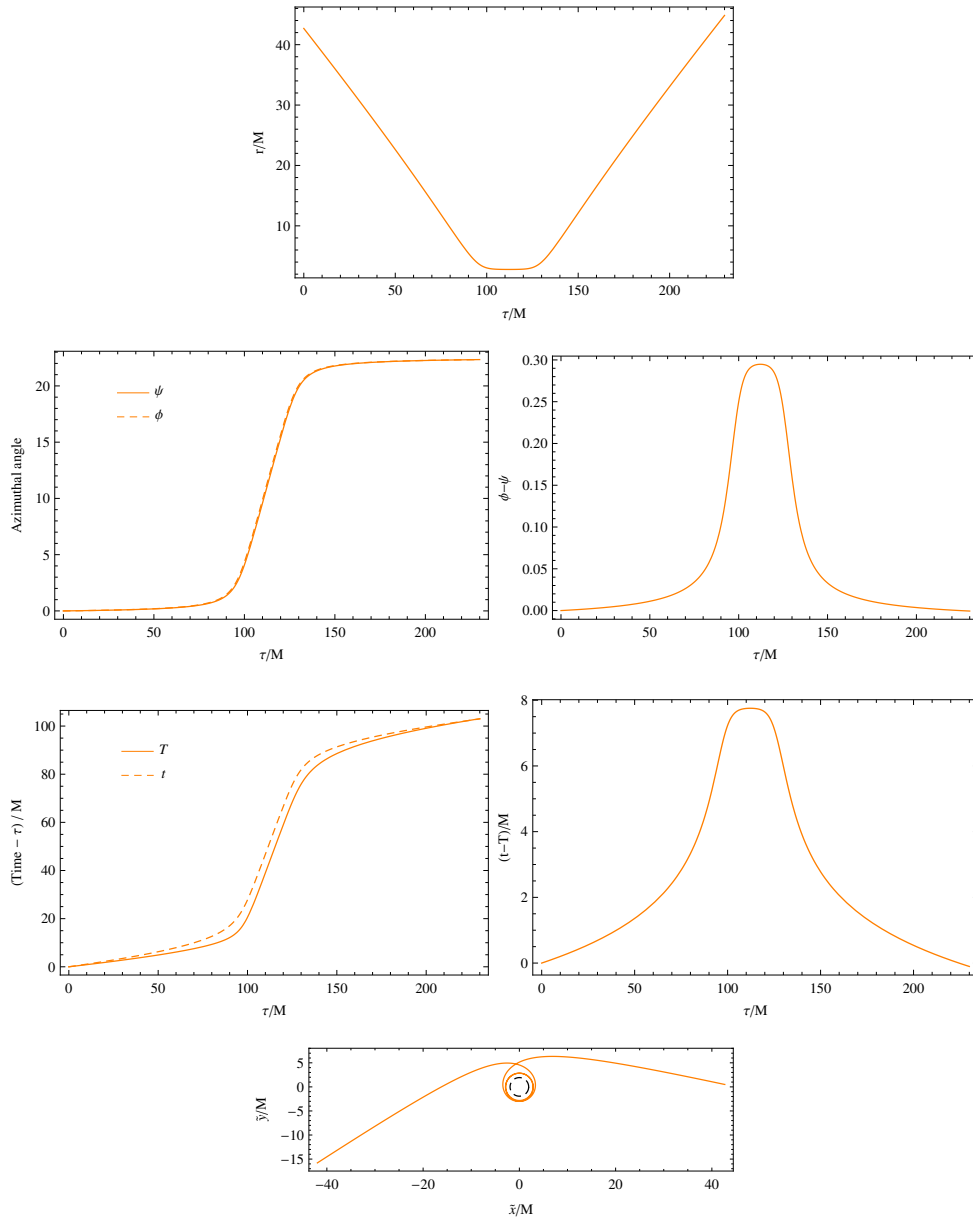


**Figure A.5:** Unstable circular trajectory with parameter values  $a = 0.5 M$ ,  $\mathcal{E}_5 = \mathcal{V}_+(r_{\text{uc}}) \approx 1.054$ ,  $\ell = 3.7 M$  and  $\mathcal{Q} = 0$ . The panels in the figure follow the same structure as in Figure A.2.

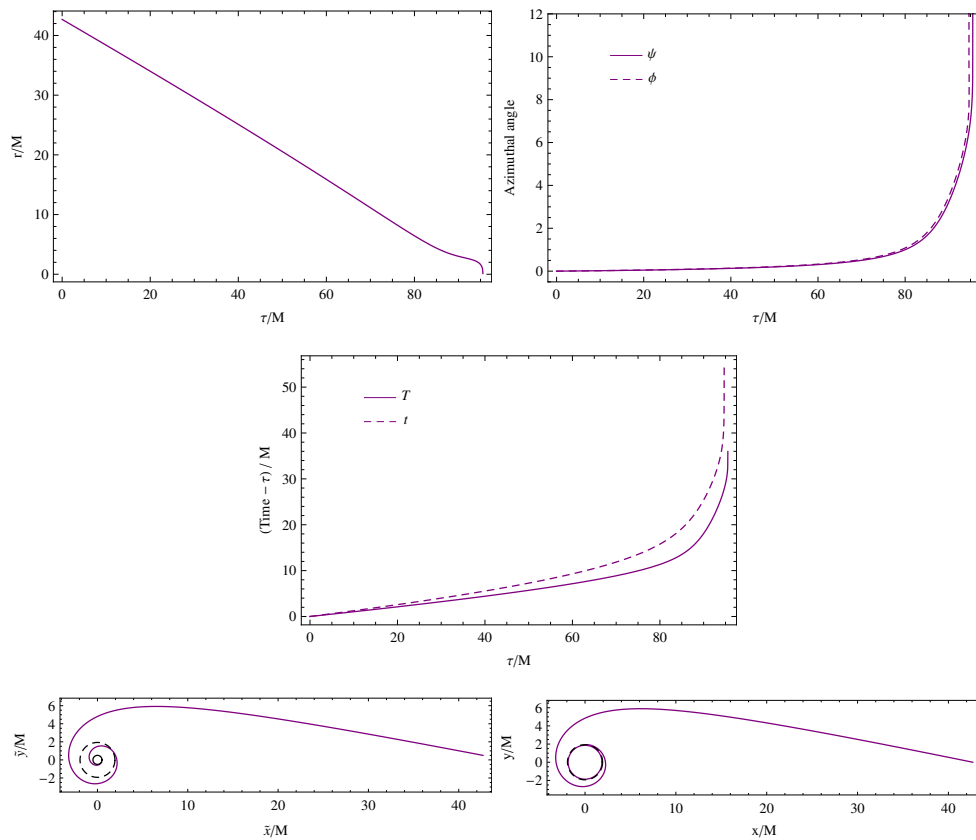


**Figure A.6:** Plunging trajectory with parameter values  $a = 0.5 M$ ,  $\mathcal{E}_6 = 1.07$ ,  $\ell = 3.7 M$  and  $Q = 0$ . The first three panels show the proper time evolution of the radial, azimuthal and time coordinates, respectively. The panel at the bottom left shows the trajectory in the KS description projected onto the  $x$ - $y$  plane. The bottom right panel shows the same projection but for the BL description.

## A.2 Orbits in the equatorial plane II: counter-rotating case

We consider now a family of trajectories in the equatorial plane with a common value of  $\ell = 4.7M$ . In this case the trajectories counter-rotate around a BH with spin parameter  $a = -0.5M$ . The radial effective potential in this case has been plotted in Figure A.7. The radial effective potential  $\mathcal{V}_+(r)$  has two stationary points at

$$r_{\text{uc}} \approx 4.69M \quad \text{and} \quad r_{\text{sc}} \approx 17.49M,$$

that correspond to unstable and stable circular orbits, respectively. The energy levels (highlighted in Figure A.7) for the test particle trajectories considered in this case are

- $\mathcal{E}_1 = \mathcal{V}_+(r_{\text{sc}}) \approx 0.97$ , stable circular trajectory,
- $\mathcal{E}_2 = 0.98$ , elliptical-like trajectory,
- $\mathcal{E}_3 = 1.0$ , parabolic-like trajectory,
- $\mathcal{E}_4 = 1.01$ , hyperbolic-like trajectory,
- $\mathcal{E}_5 = \mathcal{V}_+(r_{\text{uc}}) \approx 1.025$ , unstable circular trajectory,
- $\mathcal{E}_6 = 1.03$ , plunging trajectory.

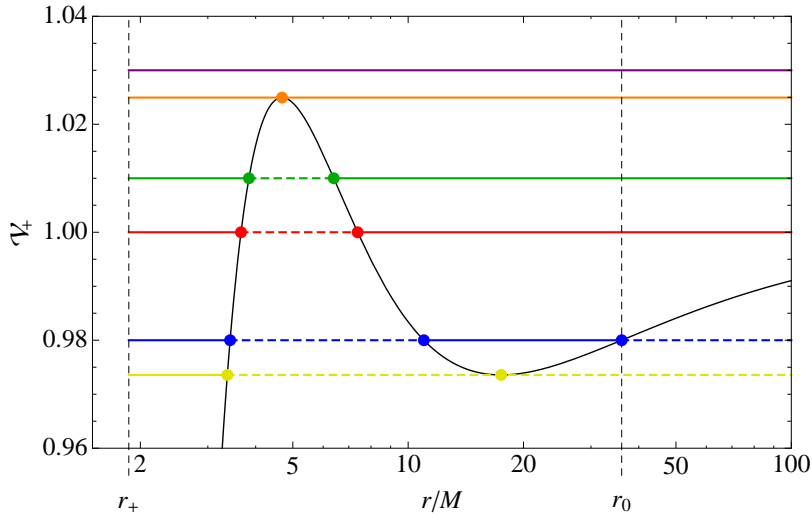


**Figure A.7:** The effective potential  $\mathcal{V}_+(r)$  is plotted for  $a = -0.5M$ ,  $\ell = 4.7M$  and  $Q = 0$ . Six different energy levels are indicated by coloured lines while the intersections with the vertical line  $r_0 \approx 36.1$  represent the starting points for the numerical integration of the trajectories considered in this section.

Except for the stable circular orbit, the starting radius of all the other trajectories is taken to be at the apocentre of the elliptical-like orbit,  $r_0 \approx 36.1M$ . The rest of

the initial conditions are taken as in Section A.1. Figures A.8, A.9 and A.10 show, respectively, the results of the numerical integration of the elliptical-like, parabolic-like, and hyperbolic-like trajectories considered in this case. These figures are organised in panels in the same way as Figure A.2.

The results for the unstable circular trajectory are shown in Figure A.11. This figure is organised in panels as in Figure A.6. In this case the rounded-off energy level was slightly above the real  $\mathcal{V}_+(r_{uc})$  value and so, after performing a succession of nearly circular orbits, the test particle finally plunges into the BH and ends up at the ring singularity after a finite amount of proper time  $\tau$ , and KS coordinate time  $T$ . In contrast, the BL coordinates  $t$  and  $\phi$  diverge at  $r = r_+$ . Therefore, in the BL description, the particle never crosses the outer event horizon. We also note in this figure that, due to the frame dragging effect, the BL azimuthal coordinate  $\phi$  ceases to be monotonically increasing in the vicinity of  $r_+$ .

The results for the plunging trajectory are shown in Figure A.12 that is again organised in the same way as Figure A.6. Just as in the previous case, in this figure we notice how the trajectory in the BL description is trapped in an infinite loop around the outer event horizon and is forced to co-rotate with the black hole in the vicinity of  $r_+$ .

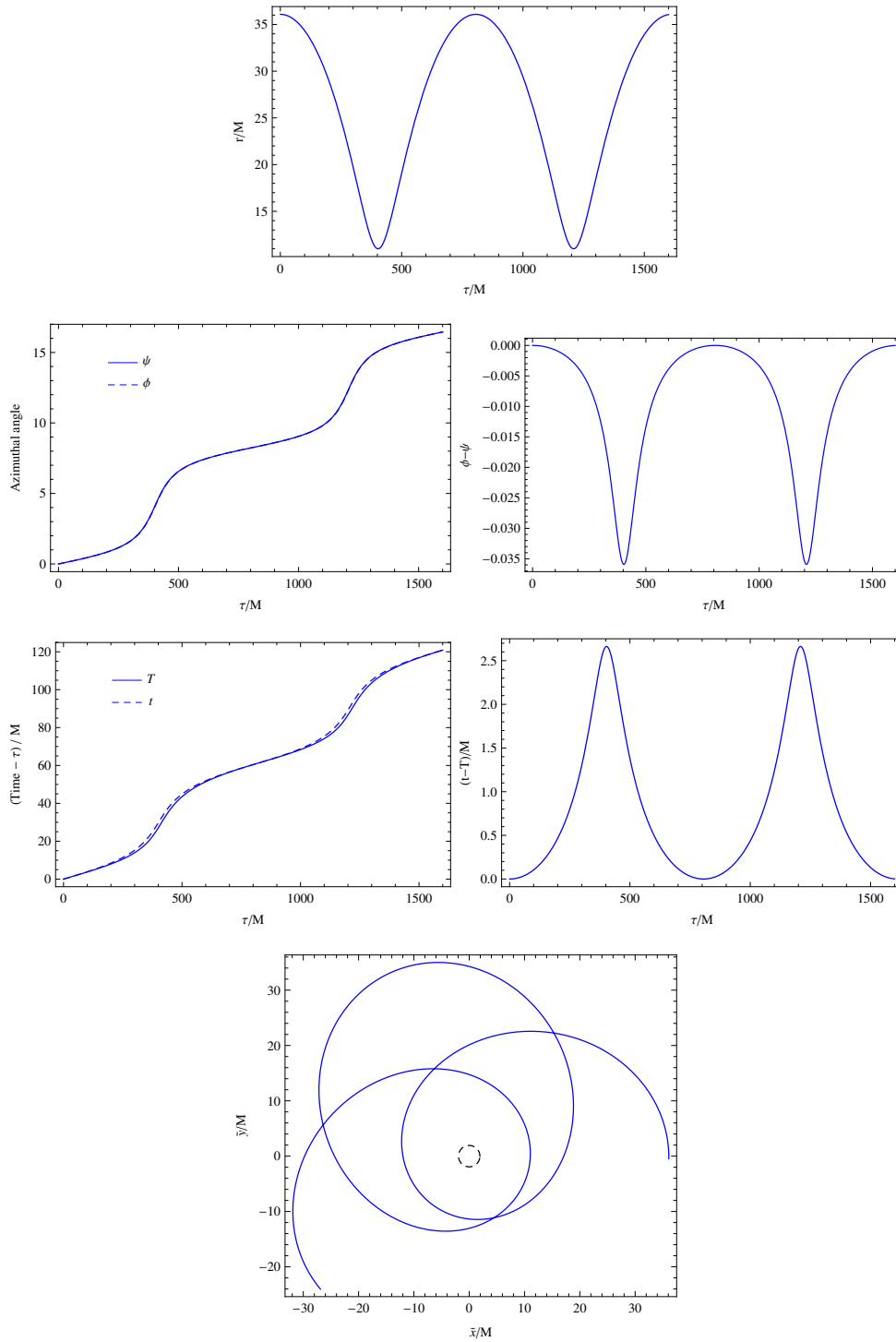


**Figure A.8:** Elliptical-like trajectory with parameter values  $a = -0.5 M$ ,  $\mathcal{E} = 0.98$ ,  $\ell = 4.7 M$  and  $Q = 0$ .

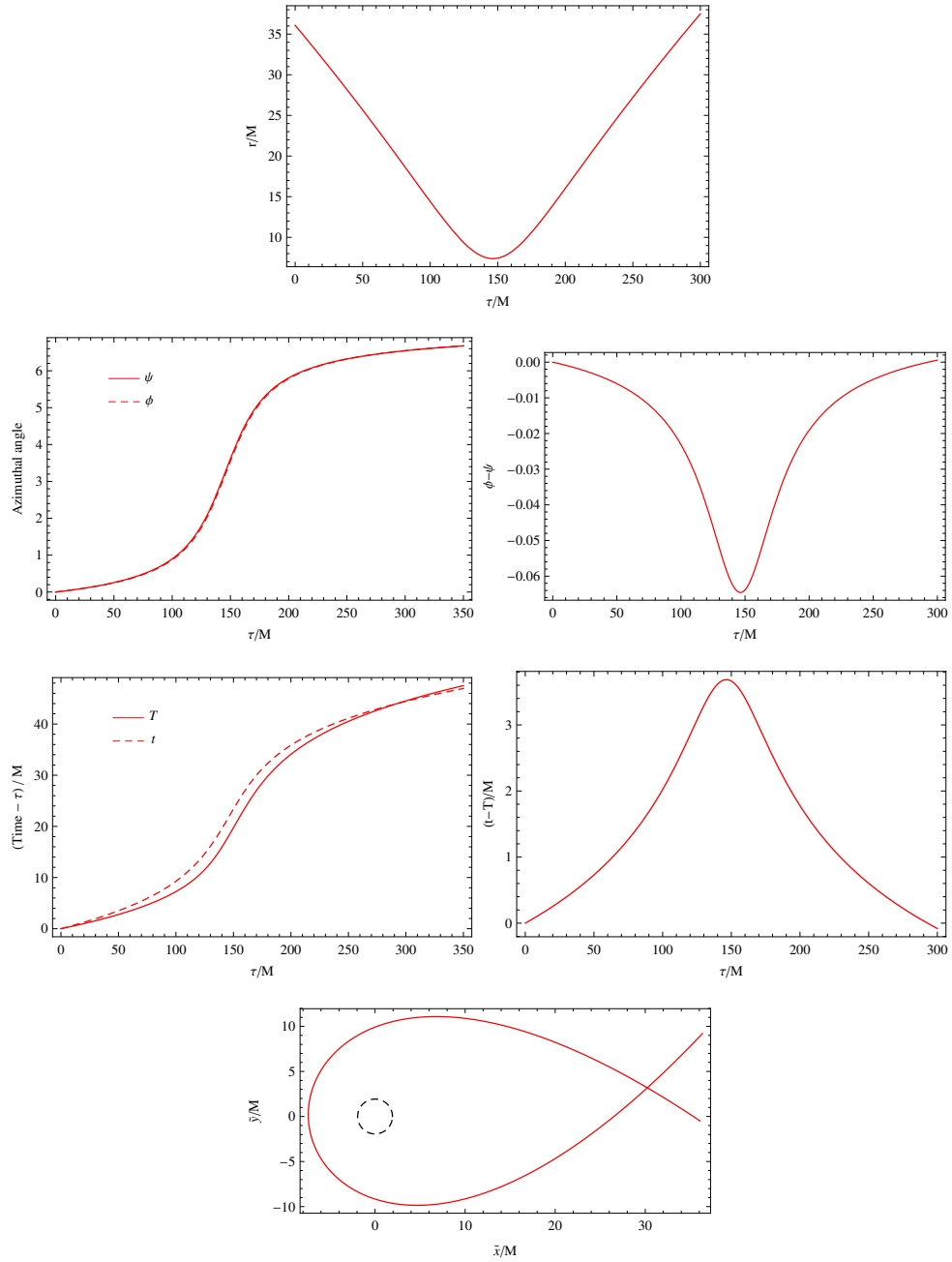


**Figure A.9:** Parabolic-like trajectory with parameter values  $a = -0.5M$ ,  $\mathcal{E} = 1$ ,  $\ell = 4.7M$  and  $Q = 0$ .

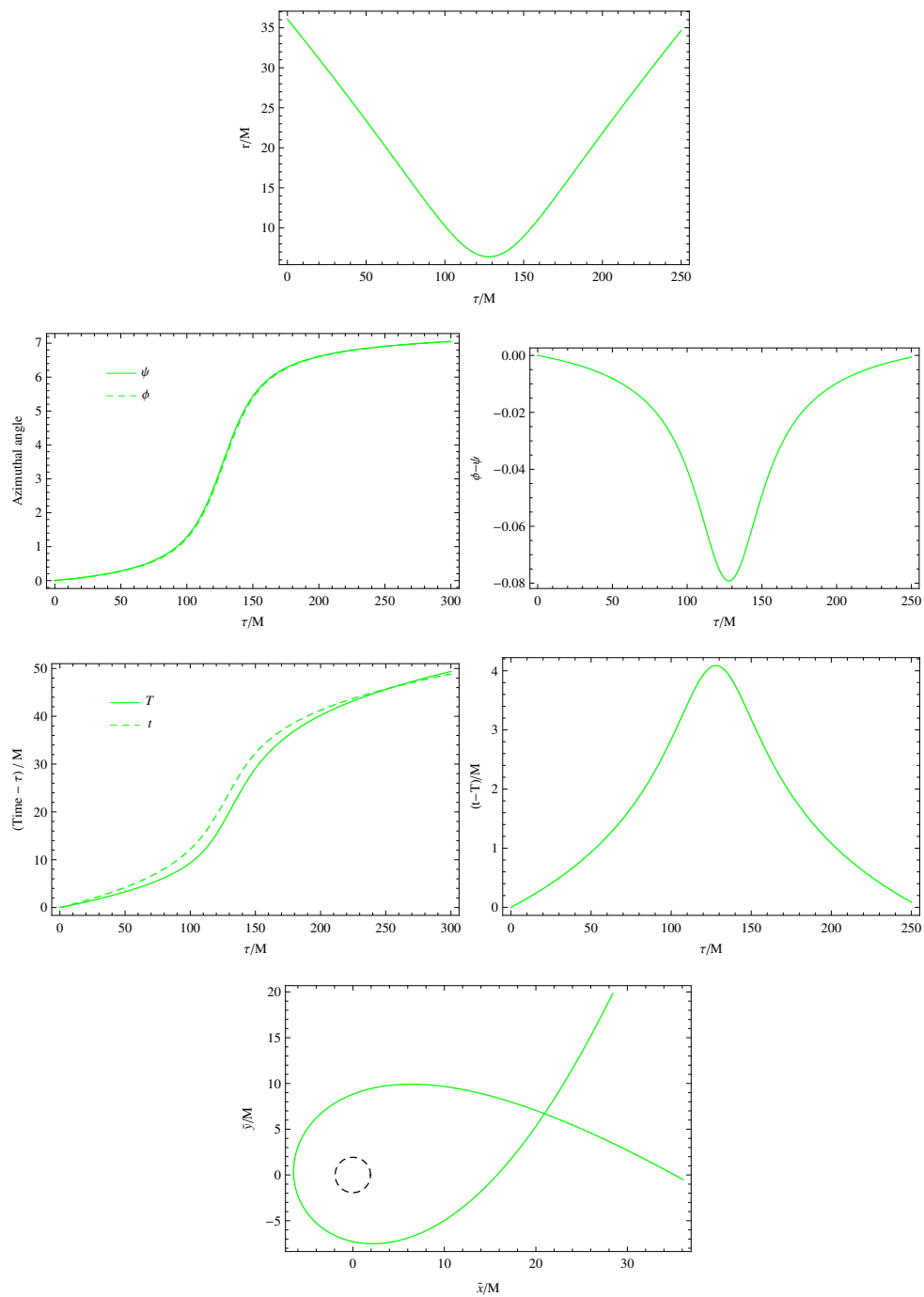


**Figure A.10:** Hyperbolic-like trajectory with parameter values  $a = -0.5 M$ ,  $\mathcal{E} = 1.01$ ,  $\ell = 4.7 M$  and  $Q = 0$ .

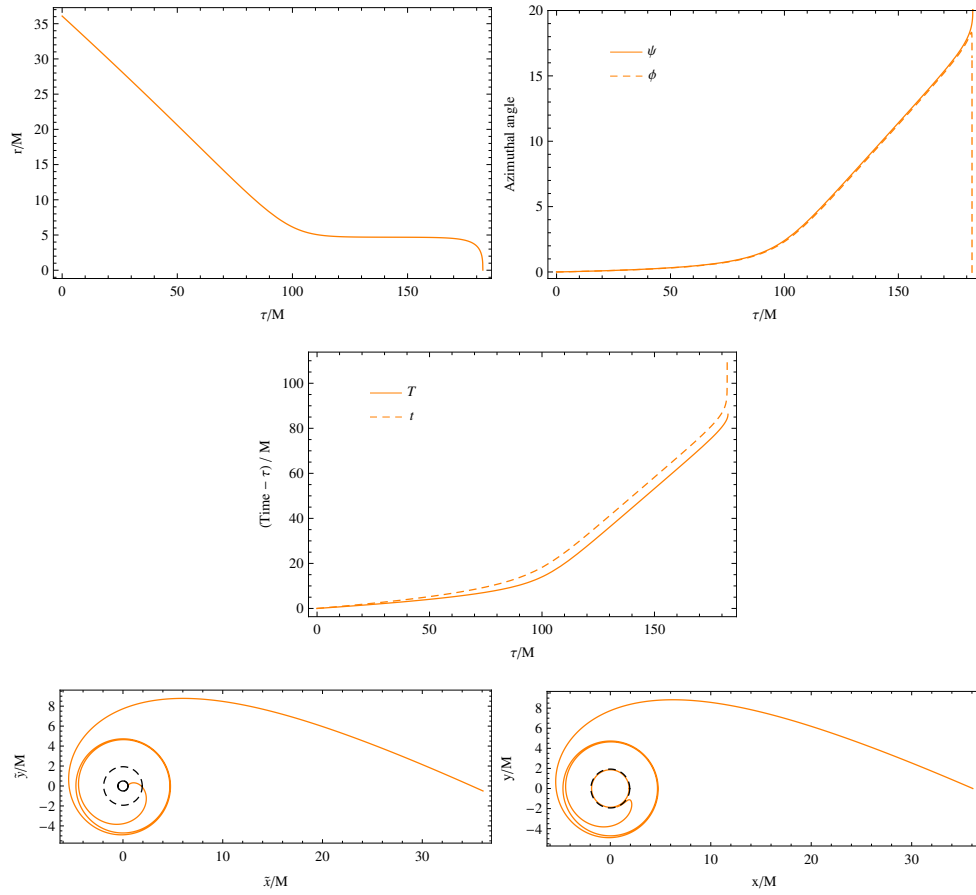


**Figure A.11:** Unstable circular trajectory with parameter values  $a = -0.5 M$ ,  $\mathcal{E} = \mathcal{V}_+(r_{\text{uc}}) \approx 1.025$ ,  $\ell = 4.7 M$  and  $\mathcal{Q} = 0$ .

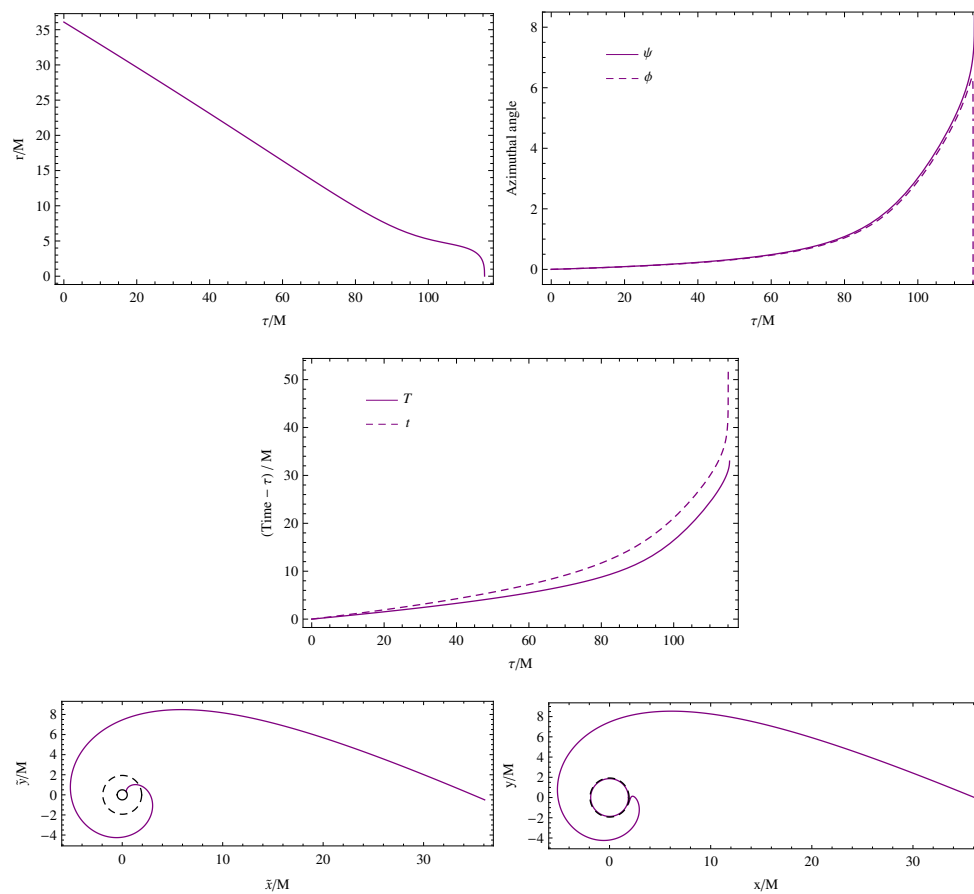


**Figure A.12:** Plunging trajectory with parameter values  $a = -0.5 M$ ,  $\mathcal{E} = 1.03$ ,  $\ell = 4.7 M$  and  $Q = 0$ .

### A.3 Orbits off the equatorial plane I

In this section we examine the six representative trajectories associated with the energy levels highlighted in Figure A.13, where the radial effective potential  $\mathcal{V}_+(r)$  has been plotted for  $a = 0.98 M$ ,  $\ell = 3 M$  and  $Q = 8.5 M^2$ . In this case the two stationary points of  $\mathcal{V}_+(r)$  are at

$$r_{\text{uc}} \approx 1.99 M, \quad \text{and} \quad r_{\text{sc}} \approx 8.23 M.$$

The highlighted energy levels in Figure A.13 correspond to

- $\mathcal{E}_1 = \mathcal{V}_+(r_{\text{sc}}) \approx 0.94$ , stable spherical trajectory,
- $\mathcal{E}_2 = 0.97$ , elliptical-like trajectory,
- $\mathcal{E}_3 = 1.0$ , parabolic-like trajectory,
- $\mathcal{E}_4 = 1.03$ , hyperbolic-like trajectory,
- $\mathcal{E}_5 = \mathcal{V}_+(r_{\text{uc}}) \approx 1.05$ , unstable spherical trajectory,
- $\mathcal{E}_6 = 1.08$ , plunging trajectory.

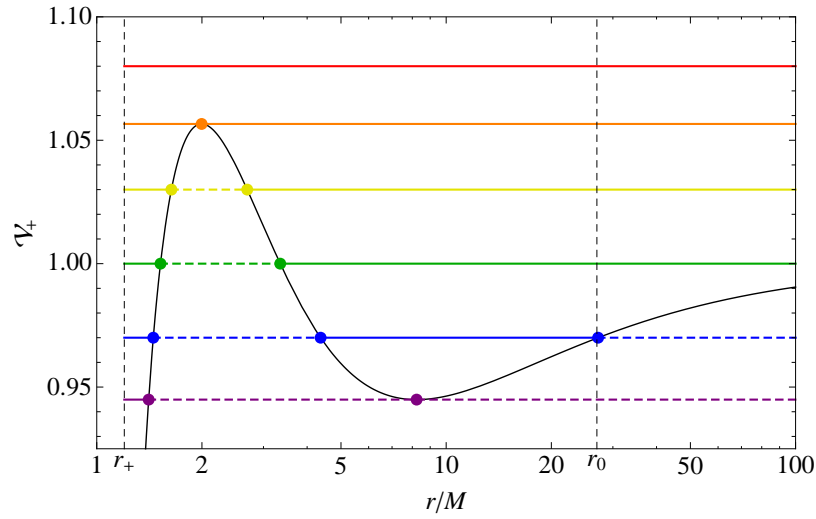


**Figure A.13:** The effective potential  $\mathcal{V}_+(r)$  is plotted for  $a = 0.98 M$ ,  $\ell = 3 M$  and  $Q = 8.5 M^2$ .

All of the trajectories considered in this section start from a common polar angle  $\theta_0 = \pi/3$ , with a negative value of  $\dot{\theta}_0$ , and co-rotate with the black hole ( $\dot{\psi}_0 > 0$ ). Besides the stable spherical orbit, the initial common radius for all of the other trajectories corresponds to the apocentre of the elliptical-like orbit,  $r_0 \approx 27.2 M$ . As in the previous sections, we have considered in the last four cases a negative value for the initial radial

velocity  $\dot{r}_0$ , while the initial values for  $\dot{r}_0$ ,  $\dot{\theta}_0$  and  $\dot{\psi}_0$  were obtained from Eqs. (4.2.1), (4.2.2) and (4.2.10), respectively. We have also taken the initial point of each trajectory (intersections with the dashed vertical line in Figure A.13) as the synchronisation point for the transformation from KS to BL coordinates.

Figure A.14 shows the results of the numerical integration of the stable spherical orbit. The first four panels in this figure show the proper time evolution of the coordinates of the particle, while the other three panels show a three-dimensional plot of the trajectory and two spatial projections of it on the  $R$ - $z$  and  $\tilde{x}$ - $\tilde{y}$  planes. It is interesting to notice that in this case, as opposed to that for an equatorial stable circular orbit, the azimuthal coordinate is not a linear function of the proper time and present slight undulations, being steeper when the particle is closer to a turning point in its polar motion. Also note that in this case, given that  $r = \text{const.}$ , from Eq. (3.3.1) it follows that  $T(\tau) = t(\tau)$  and  $\psi(\tau) = \phi(\tau)$ .

Figures A.15, A.16, A.17 and A.18 show, respectively, the results for the elliptical-like, parabolic-like, hyperbolic-like and unstable spherical trajectories. The first row of each of these figures shows two panels with  $r(\tau)$  and  $\theta(\tau)$ . The second row shows  $\phi(\tau)$ ,  $\psi(\tau)$  and  $\phi(\tau) - \psi(\tau)$ , while the third row shows  $t(\tau)$ ,  $T(\tau)$  and  $t(\tau) - T(\tau)$ . The last three panels of each of these figures show the same spatial projections as in Figure A.14.

The results for the plunging trajectory are shown in Figure A.19. As in Figure A.14, the first four panels of this figure show the proper time evolution of the coordinates of the particle. The remaining panels show three spatial projections of the trajectory on the  $R$ - $z$ ,  $x$ - $y$  and  $\tilde{x}$ - $\tilde{y}$  planes. We note in this case the interesting effect that, in general, an off-equatorial orbit with an energy high enough to plunge into the event horizon does not necessarily end up at the singularity as it is in Schwarzschild spacetime or for trajectories in the equatorial plane in Kerr spacetime. In the present case, the trajectory reaches a turning point in its radial motion for a radius  $0 < r < r_+$ , but, since the  $r$  coordinate becomes timelike inside the event horizon it cannot become non-monotonic, and the particle is trapped on a circular orbit slightly outside the ring singularity. Finally note that this effect is only visible in the KS representation, while, as before, in the BL representation the particle apparently never crosses the outer event horizon.

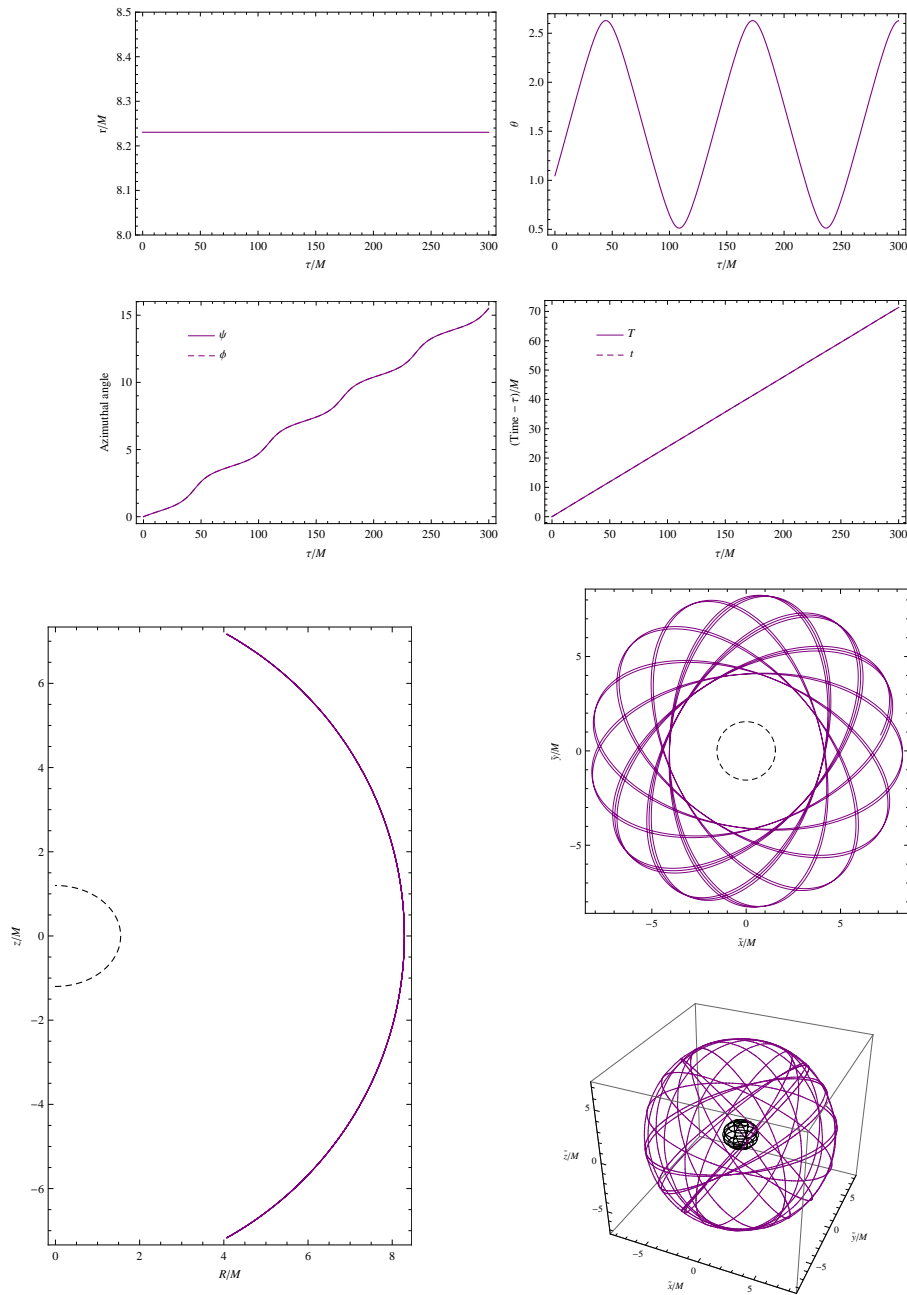


**Figure A.14:** Stable spherical orbit for the parameters  $a = 0.98 M$ ,  $\mathcal{E} = \mathcal{V}_+(r_{\text{sc}}) \approx 0.94$ ,  $\ell = 3 M$  and  $\mathcal{Q} = 8.5 M^2$ . The black spheroid in the three-dimensional plot corresponds to the outer event horizon  $r_+$ .

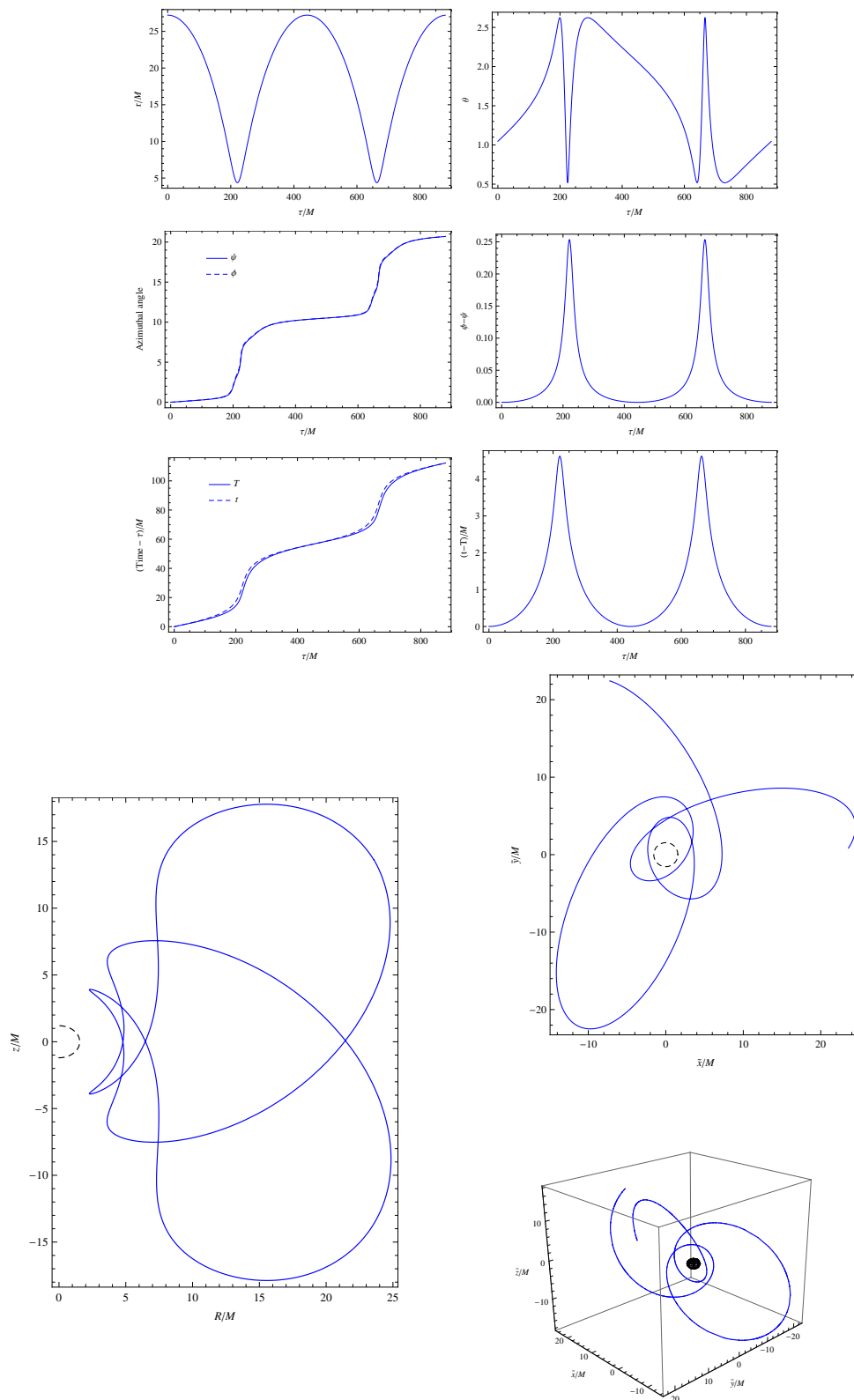


**Figure A.15:** Elliptical-like trajectory for the parameter values  $a = 0.98 M$ ,  $\mathcal{E} = 0.97$ ,  $\ell = 3 M$  and  $Q = 8.5 M^2$ .

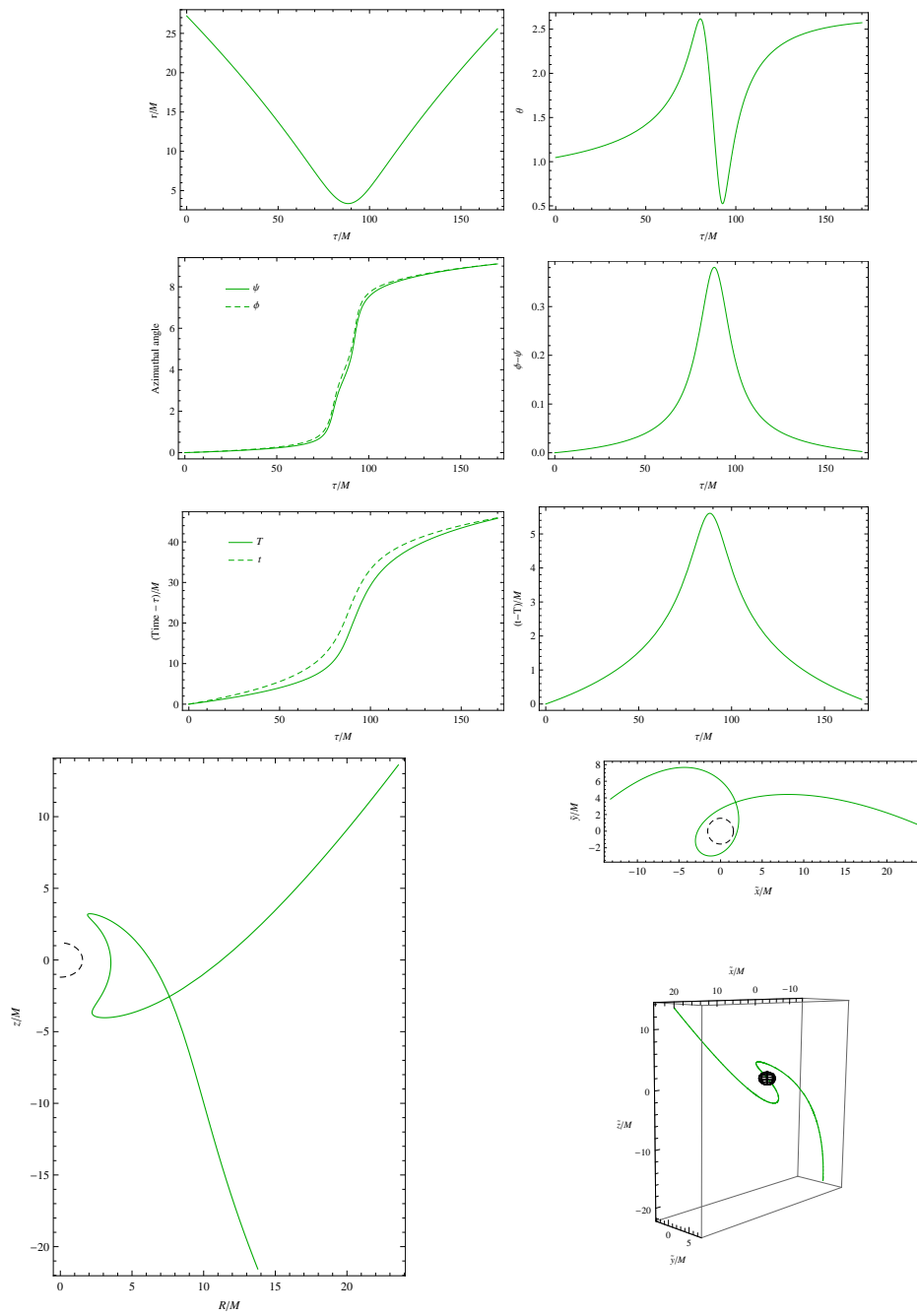


**Figure A.16:** Parabolic-like trajectory for the parameter values  $a = 0.98 M$ ,  $\mathcal{E} = 1$ ,  $l = 3 M$  and  $Q = 8.5 M^2$ .

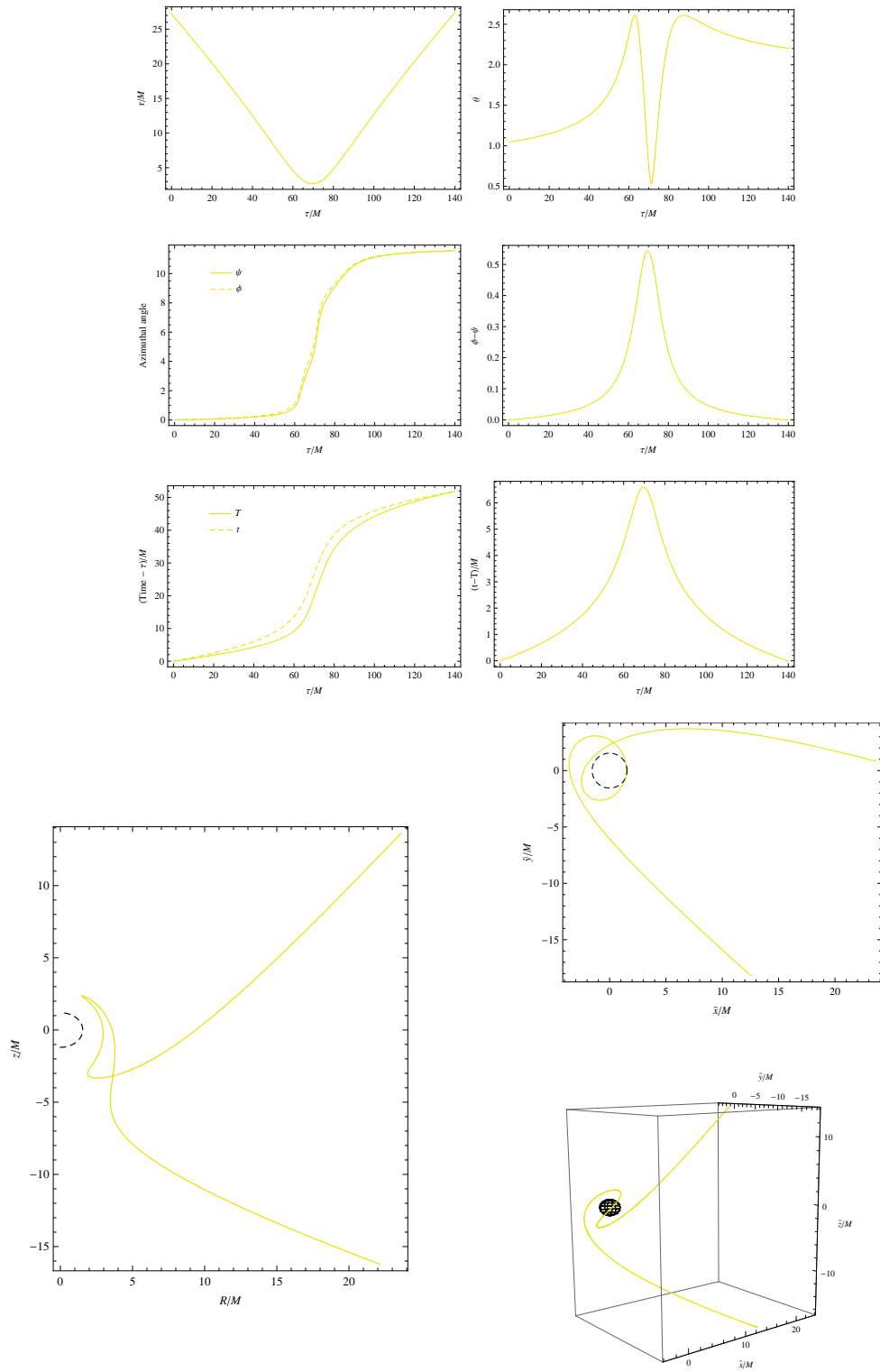


**Figure A.17:** Hyperbolic-like trajectory for the parameter values  $a = 0.98 M$ ,  $\mathcal{E} = 1.03$ ,  $\ell = 3 M$  and  $Q = 8.5 M^2$ .

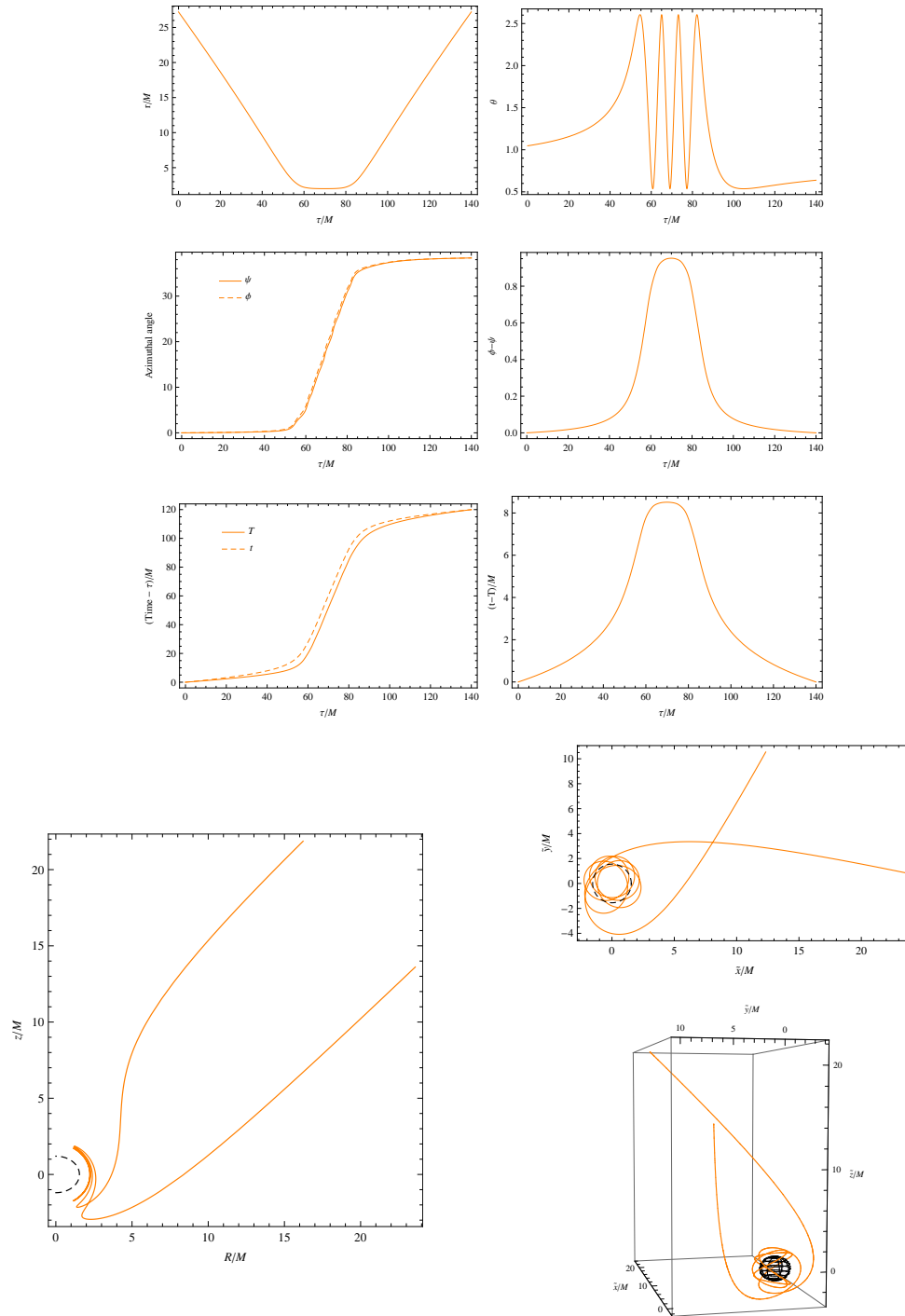


**Figure A.18:** Unstable spherical orbit for the parameter values  $a = 0.98 M$ ,  $\mathcal{E} = \mathcal{V}_+(r_{\text{uc}}) \approx 1.05$ ,  $\ell = 3 M$  and  $Q = 8.5 M^2$ .

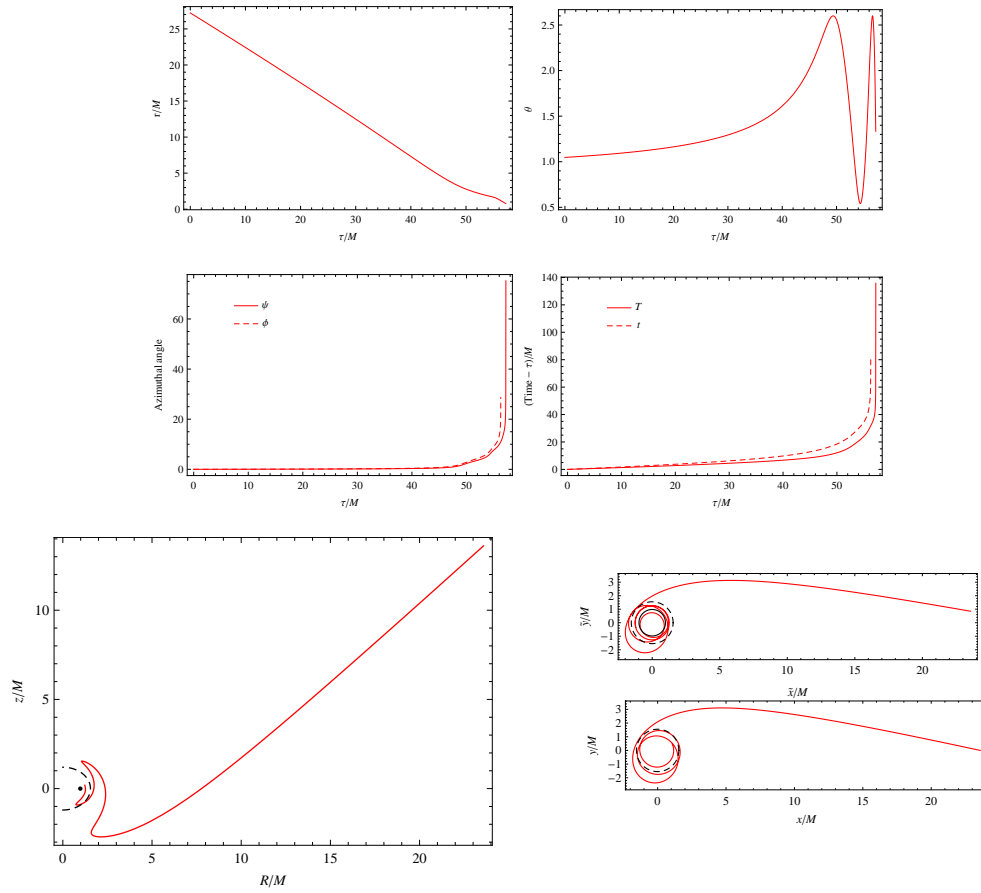


**Figure A.19:** Plunging trajectory for the parameter values  $a = 0.98 M$ ,  $\mathcal{E} = 1.08$ ,  $\ell = 3 M$  and  $Q = 8.5 M^2$ . A black dot in the  $R$ - $z$  projection represents the ring singularity.

## A.4 Orbits off the equatorial plane II

All of the cases analysed in this and the following section correspond to trajectories plunging into the black hole. The aim of this study is to explore a unique characteristic of Kerr spacetime in that, for suitable values of  $a$ ,  $\mathcal{E}$  and  $\ell_z$ , the polar effective potential  $\mathcal{H}(\theta)$  (defined in Eq. 4.5.2) has two local minima symmetrically located about the equator as opposed to the Schwarzschild and Newtonian cases in which it has just one minimum located at  $\theta = \pi/2$ . This possibility was discussed in further detail in Section 4.5 and the locations of the minima,  $\theta_m$  and  $\theta_{m'}$ , were given in Eq. (4.5.8). The condition that  $a$ ,  $\mathcal{E}$  and  $\ell_z$  must satisfy for having two minima is

$$(\mathcal{E}^2 - 1) a^2 > \ell_z^2, \quad (\text{A.4.1})$$

from which it follows that  $\mathcal{E}^2 > 1$ , that is, this feature occurs only for unbound orbits. In this section we consider the trajectories highlighted in Figure A.20, where the polar effective potential  $\mathcal{H}(\theta)$  has been plotted for  $a = 0.9 M$ ,  $\ell_z = 0.05 M$  and  $\mathcal{E} = 1.6$ .

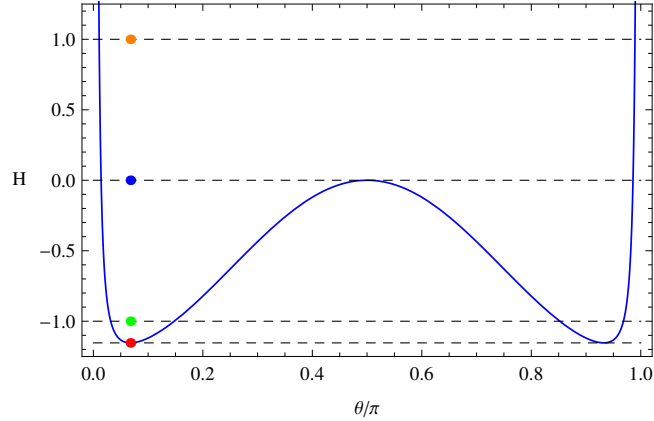


**Figure A.20:** The polar effective potential  $\mathcal{H}(\theta)$  is plotted for  $a = 0.9 M$ ,  $\ell_z = 0.05 M$  and  $\mathcal{E} = 1.6$ . The four horizontal dashed lines correspond to (bottom to top)  $Q/M^2 \approx -1.154, -1, 0, 1$

All of the trajectories considered in this section have a common initial polar angle  $\theta_0 = \theta_m \approx 0.212$ , begin from  $r_0 = 20 M$  and co-rotate with the black hole,  $\dot{\psi}_0 > 0$ . The corresponding value of  $Q$  in each case is

- $\mathcal{Q} = \mathcal{H}(\theta_m) \approx -1.15 M^2$ , red orbit
- $\mathcal{Q} = -M^2$ , green orbit
- $\mathcal{Q} = 0$ , blue orbit
- $\mathcal{Q} = M^2$ , yellow orbit

For each of the last three cases we are actually considering two trajectories, one with  $\dot{\theta}_0 > 0$  (solid line) and the other with  $\dot{\theta}_0 < 0$  (dashed line).

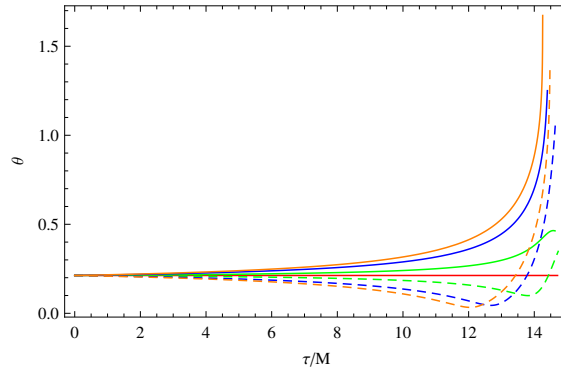


**Figure A.21:** Proper time evolution of the polar angle coordinate for the seven trajectories mentioned above (corresponding to the four values of  $\mathcal{Q}/M^2$  represented in Figure A.20).

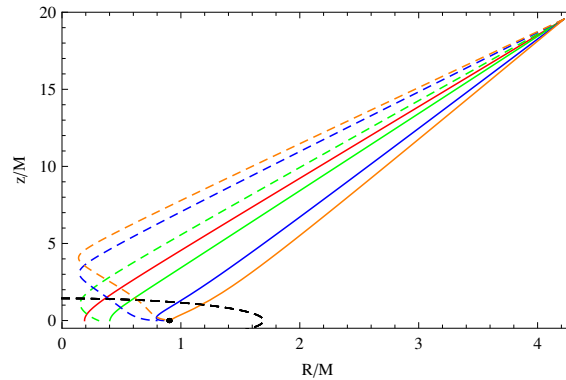


**Figure A.22:** Spatial projection onto the  $R$ - $z$  plane for the same seven trajectories as in Figure A.21. Note that the  $R$  and  $z$  axes have not the same scale.

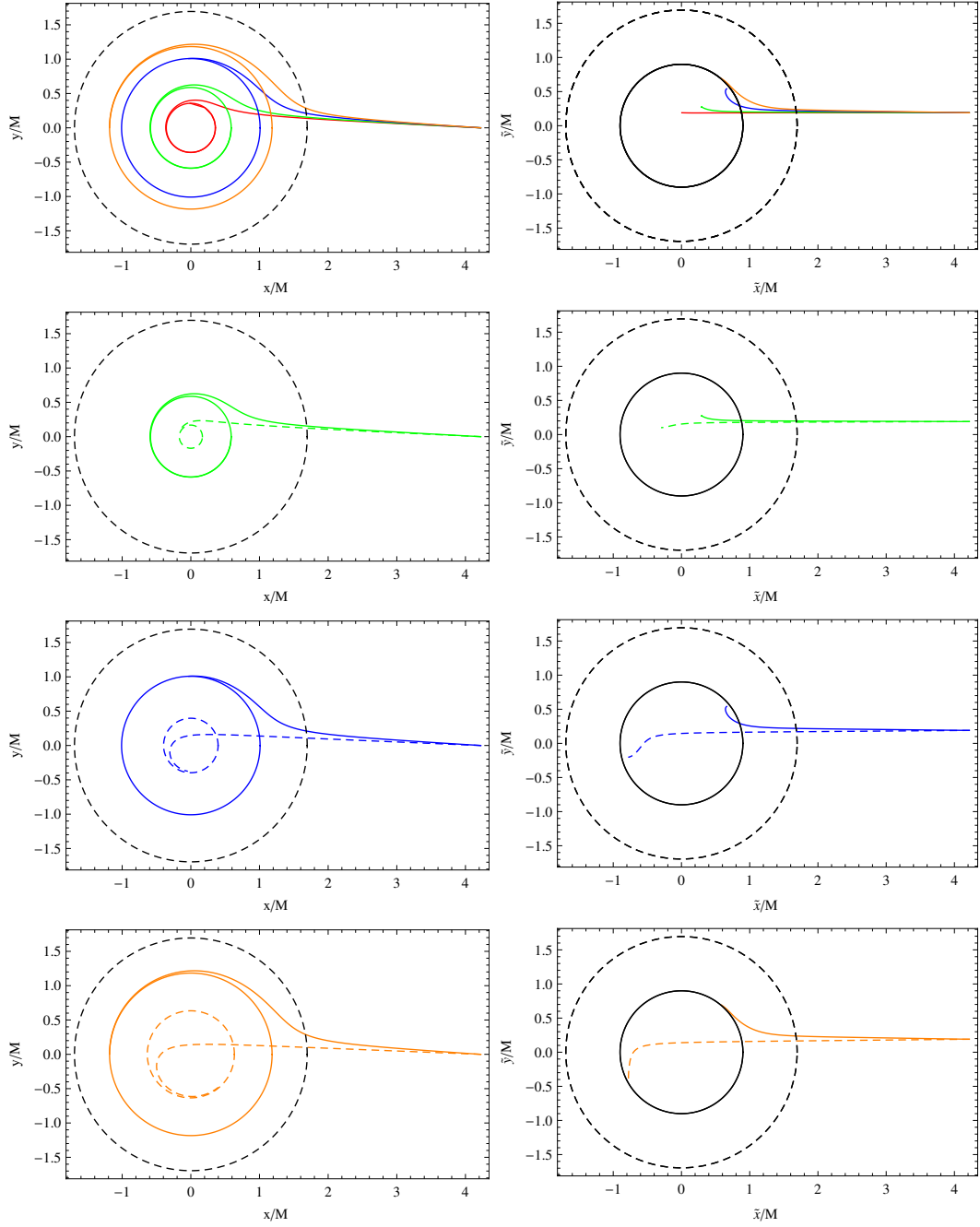


**Figure A.23:** Projection onto the  $x$ - $y$  and  $\tilde{x}$ - $\tilde{y}$  planes. In the BL description (left) the trajectory never crosses the outer event horizon and stays there, going infinitely around a circular orbit. In the  $x$ - $y$  projection the radius of this circle is given by  $r = r_+ \sin \theta_+$ , where  $\theta_+$  is the polar angle at which the trajectory reaches  $r_+$ . Note that in the KS representation (right) we have followed the trajectories until the point at which  $r$  becomes negative and the particle crosses into another asymptotically flat spacetime.

## A.5 Orbits off the equatorial plane III

In this section we consider the trajectories highlighted in Figure A.24. As in the previous case, here we take the following parameter values  $a = 0.9 M$ ,  $\ell_z = 0.05 M$  and  $\mathcal{E} = 1.6$ .

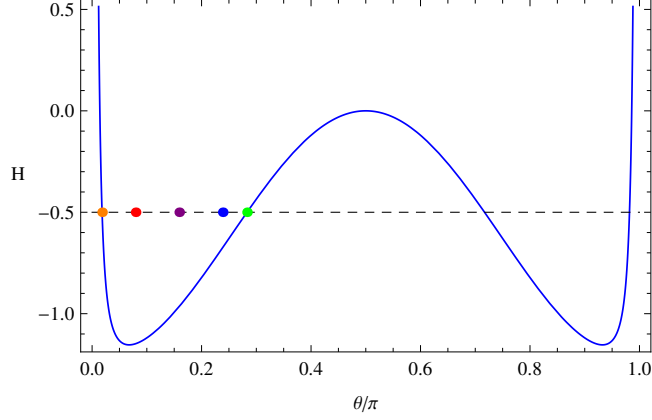


**Figure A.24:** The polar effective potential  $\mathcal{H}(\theta)$  is plotted for  $a = 0.9 M$ ,  $\ell_z = 0.05 M$  and  $\mathcal{E} = 1.6$ . The horizontal dashed line corresponds to a constant value of  $\mathcal{Q} = -0.5 M^2$ .

The six trajectories considered in this section are co-rotating, have a common value of  $\mathcal{Q} = -0.5 M^2$  and begin from  $r_0 = 20 M$ . Again, a solid line represents an orbit with  $\dot{\theta}_0 > 0$  and a dashed line one with  $\dot{\theta}_0 < 0$ .<sup>(1)</sup> The initial polar angles being considered are

- $\theta_0 \approx 0.06$  (first root of  $\mathcal{H}(\theta_0) = \mathcal{Q}$ ), yellow trajectory,
- $\theta_0 = 0.25$ , red trajectory,
- $\theta_0 = 0.5$ , purple trajectory,
- $\theta_0 = 0.75$ , blue trajectory,
- $\theta_0 \approx 0.89$  (second root of  $\mathcal{H}(\theta_0) = \mathcal{Q}$ ), green trajectory.

<sup>(1)</sup>We only consider these two orbits for the trajectory starting at  $\theta_0 = 0.5$  as a way of exemplifying the dependence on the sign of  $\dot{\theta}_0$  but without oversaturating with curves the figures in this section.

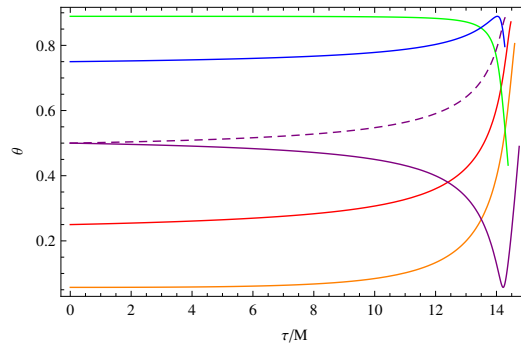


**Figure A.25:** Proper time evolution of the polar angle coordinate for the six trajectories mentioned above (corresponding to the five values of  $\theta_0$  represented in Figure A.24).

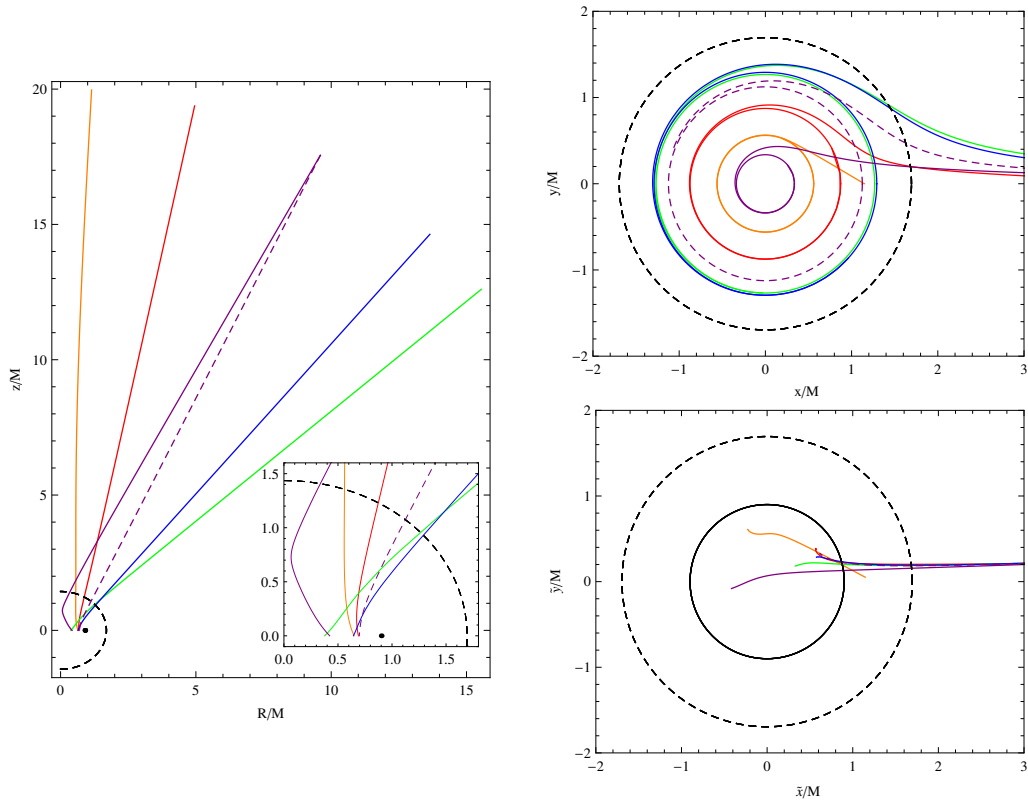


**Figure A.26:** Spatial projections onto the  $R$ - $z$ ,  $x$ - $y$  and  $\tilde{x}$ - $\tilde{y}$  planes of the same six trajectories as in Figure (A.25).

## Appendix B

# Jacobi elliptic functions

In this appendix, we introduce the elliptic integral of the first kind and, in terms of it, we define the Jacobi elliptic functions. A rigorous mathematical definition of these functions is given in Hancock (1917), Cayley (1961) and Lawden (1989), while useful formulae can be found in Abramowitz & Stegun (1970). In what follows, we restrict ourselves to presenting some basic identities for these functions that are relevant for the present study.

In general, elliptic integrals are defined as functions that can be expressed in the form

$$f(x) = \int_0^x R(x', \sqrt{P(x')}) dx', \quad (\text{B.1})$$

where  $R$  is a rational function of its arguments, and  $P(x)$  is a third or fourth order polynomial in  $x$ . In particular, the elliptic integral of the first kind is defined as

$$F(x, k) = \int_0^x \frac{dx'}{\sqrt{(1-x'^2)(1-k^2x'^2)}}, \quad (\text{B.2})$$

where  $k = \text{const.}$  is the so-called modulus. An alternative expression for  $F(x, k)$  is obtained after substituting  $x = \sin \varphi$  in the previous equation, which results in

$$F(\sin \varphi, k) = \int_0^\varphi \frac{d\varphi'}{\sqrt{1-k^2 \sin^2 \varphi'}}. \quad (\text{B.3})$$

The new variable  $\varphi$  is called the Jacobi amplitude. An elliptic integral is said to be complete when  $\varphi = \pi/2$ , i.e.

$$K(k) = F(1, k) = \int_0^{\pi/2} \frac{d\varphi'}{\sqrt{1-k^2 \sin^2 \varphi'}}. \quad (\text{B.4})$$

The function  $K(k)$  is called a complete elliptic integral of the first kind.

The Jacobi elliptic functions can be considered as a natural extension of the trigonometric functions. Just as the inverse of the sine function can be defined by the expression

$$\sin^{-1}(x) = \int_0^x \frac{dx'}{\sqrt{1-x'^2}}, \quad (\text{B.5})$$

the inverse of the Jacobi elliptic function  $\text{sn}(u, k)$  is defined as

$$\text{sn}^{-1}(x, k) = F(x, k) = \int_0^x \frac{dx'}{\sqrt{(1-x'^2)(1-k^2x'^2)}}. \quad (\text{B.6})$$

From Eqs. (B.3)-(B.6) we have that

$$\text{sn}(u, k) = \sin[F^{-1}(u, k)] = \sin \varphi. \quad (\text{B.7})$$

Similarly, two further Jacobi elliptic functions are defined as

$$\text{cn}(u, k) = \cos \varphi, \quad (\text{B.8})$$

$$\text{dn}(u, k) = \sqrt{1 - k^2 \sin^2 \varphi}. \quad (\text{B.9})$$

From Eqs. (B.7)-(B.9) it follows that the functions  $\text{sn}(u, k)$ ,  $\text{cn}(u, k)$  and  $\text{dn}(u, k)$  satisfy

$$\text{sn}^2 u + \text{cn}^2 u = 1, \quad (\text{B.10})$$

$$\text{dn}^2 u + k^2 \text{sn}^2 u = 1, \quad (\text{B.11})$$

$$\text{dn}^2 u - k^2 \text{cn}^2 u = k'^2, \quad (\text{B.12})$$

where, for simplicity, we have dropped  $k$  from the notation and where  $k' = \sqrt{1 - k^2}$  is called the complementary modulus.

From Eq. (B.6), it is simple to see that the Jacobi elliptic functions are related to both trigonometric and hyperbolic functions through

$$\begin{aligned} \text{sn}(u, 0) &= \sin u, & \text{sn}(u, 1) &= \tanh u, \\ \text{cn}(u, 0) &= \cos u, & \text{cn}(u, 1) &= \text{sech } u, \\ \text{dn}(u, 0) &= 1, & \text{dn}(u, 1) &= \text{sech } u. \end{aligned} \quad (\text{B.13})$$

The Jacobi elliptic functions are periodic in  $K(k)$  and  $K'(k) = K(k')$  according to

$$\text{sn}(u + 2mK + 2niK', k) = (-1)^m \text{sn}(u, k), \quad (\text{B.14})$$

$$\text{cn}(u + 2mK + 2niK', k) = (-1)^{m+n} \text{cn}(u, k), \quad (\text{B.15})$$

$$\text{dn}(u + 2mK + 2niK', k) = (-1)^n \text{dn}(u, k). \quad (\text{B.16})$$

Nine further elliptic functions are obtained after taking quotients or reciprocals of the already defined ones

$$\begin{aligned} \text{ns } u &= \frac{1}{\text{sn } u}, & \text{nc } u &= \frac{1}{\text{cn } u}, & \text{nd } u &= \frac{1}{\text{dn } u}, \\ \text{sc } u &= \frac{\text{sn } u}{\text{cn } u}, & \text{cd } u &= \frac{\text{cn } u}{\text{dn } u}, & \text{ds } u &= \frac{\text{dn } u}{\text{sn } u}, \\ \text{cs } u &= \frac{\text{cn } u}{\text{sn } u}, & \text{dc } u &= \frac{\text{dn } u}{\text{cn } u}, & \text{sd } u &= \frac{\text{sn } u}{\text{dn } u}. \end{aligned} \quad (\text{B.17})$$

Some special values of these functions are

$$\begin{aligned}
\operatorname{cn}(0) &= 1, & \operatorname{sn}(0) &= 0, & \operatorname{dn}(0) &= 1, \\
\operatorname{cn}(K) &= 0, & \operatorname{sn}(K) &= 1, & \operatorname{dn}(K) &= k', \\
\operatorname{cn}(2K) &= -1, & \operatorname{sn}(2K) &= 0, & \operatorname{dn}(2K) &= 1, \\
\operatorname{cn}(u+K) &= -k' \operatorname{sd}(u), & \operatorname{sn}(u+K) &= \operatorname{cd}(u), & \operatorname{dn}(u+K) &= k' \operatorname{nd}(u), \\
\operatorname{cn}(u+2K) &= -\operatorname{cn}(u), & \operatorname{sn}(u+2K) &= -\operatorname{sn}(u), & \operatorname{dn}(u+2K) &= \operatorname{dn}(u).
\end{aligned} \tag{B.18}$$

The Jacobi elliptic functions satisfy the following addition theorems

$$\operatorname{sn}(u+v) = \frac{\operatorname{sn} u \operatorname{cn} v \operatorname{dn} v + \operatorname{sn} v \operatorname{cn} u \operatorname{dn} u}{1 - k^2 \operatorname{sn}^2 u \operatorname{sn}^2 v}, \tag{B.19}$$

$$\operatorname{cn}(u+v) = \frac{\operatorname{cn} u \operatorname{cn} v - \operatorname{sn} u \operatorname{sn} v \operatorname{dn} u \operatorname{dn} v}{1 - k^2 \operatorname{sn}^2 u \operatorname{sn}^2 v}, \tag{B.20}$$

$$\operatorname{dn}(u+v) = \frac{\operatorname{dn} u \operatorname{dn} v - k^2 \operatorname{sn} u \operatorname{sn} v \operatorname{cn} u \operatorname{cn} v}{1 - k^2 \operatorname{sn}^2 u \operatorname{sn}^2 v}, \tag{B.21}$$

from where it is simple to get the following identities for double arguments

$$\operatorname{sn} 2u = \frac{2 \operatorname{sn} u \operatorname{cn} u \operatorname{dn} u}{1 - k^2 \operatorname{sn}^4 u}, \tag{B.22}$$

$$\operatorname{cn} 2u = \frac{\operatorname{cn}^2 u - \operatorname{sn}^2 u \operatorname{dn}^2 u}{1 - k^2 \operatorname{sn}^4 u}, \tag{B.23}$$

$$\operatorname{dn} 2u = \frac{\operatorname{dn}^2 u - k^2 \operatorname{sn}^2 u \operatorname{cn}^2 u}{1 - k^2 \operatorname{sn}^4 u}. \tag{B.24}$$

These equations can be inverted as

$$\operatorname{sn}^2 u = \frac{1 - \operatorname{cn} 2u}{1 + \operatorname{dn} 2u}, \tag{B.25}$$

$$\operatorname{cn}^2 u = \frac{\operatorname{cn} 2u + \operatorname{dn} 2u}{1 + \operatorname{dn} 2u}, \tag{B.26}$$

$$\operatorname{dn}^2 u = \frac{\operatorname{dn} 2u + k^2 \operatorname{cn} 2u + k'^2}{1 + \operatorname{dn} 2u}. \tag{B.27}$$

In general, the modulus  $k$  of the elliptic functions can be either a pure real number or a pure imaginary number and can have any magnitude. Nevertheless, it is always possible to transform an elliptic function with an arbitrary modulus into an equivalent combination of elliptic functions with a modulus  $\tilde{k} \in [0, 1]$ . For example, given a non-negative real number  $k$  and defining  $\tilde{u} = \sqrt{1+k^2}u$ ,  $\tilde{k} = k/\sqrt{1+k^2}$ , we have the following transformations

$$k \operatorname{sn}(u, ik) = \tilde{k} \operatorname{sd}(\tilde{u}, \tilde{k}), \tag{B.28}$$

$$\operatorname{cn}(u, ik) = \operatorname{cd}(\tilde{u}, \tilde{k}), \tag{B.29}$$

$$\operatorname{dn}(u, ik) = \operatorname{nd}(\tilde{u}, \tilde{k}), \tag{B.30}$$

while for a modulus  $k > 1$ , with the definitions  $\tilde{u} = k u$ ,  $\tilde{k} = 1/k$ , we have

$$\operatorname{sn}(u, k) = \tilde{k} \operatorname{sn}(\tilde{u}, \tilde{k}), \quad (\text{B.31})$$

$$\operatorname{cn}(u, k) = \operatorname{dn}(\tilde{u}, \tilde{k}), \quad (\text{B.32})$$

$$\operatorname{dn}(u, k) = \operatorname{cn}(\tilde{u}, \tilde{k}). \quad (\text{B.33})$$

Moreover, it is possible to increase or decrease the magnitude of the modulus by means of the so-called, ascending and descending Landen transformations. Defining  $\tilde{u} = (1+k)u/2$  and  $\tilde{k} = 2\sqrt{k}/(1+k)$ , the Landen ascending transformations are given by

$$\operatorname{sn}(u, k) = \frac{2}{1+\tilde{k}} \frac{\operatorname{sn}(\tilde{u}, \tilde{k}) \operatorname{cn}(\tilde{u}, \tilde{k})}{\operatorname{dn}(\tilde{u}, \tilde{k})}, \quad (\text{B.34})$$

$$\operatorname{cn}(u, k) = \frac{1+\tilde{k}}{2\tilde{k}} \frac{\operatorname{dn}^2(\tilde{u}, \tilde{k}) - \frac{1-k}{1+k}}{\operatorname{dn}(\tilde{u}, \tilde{k})}, \quad (\text{B.35})$$

$$\operatorname{dn}(u, k) = \frac{1+\tilde{k}}{2} \frac{\operatorname{dn}^2(\tilde{u}, \tilde{k}) + \frac{1-k}{1+k}}{\operatorname{dn}(\tilde{u}, \tilde{k})}, \quad (\text{B.36})$$

and, if we define  $\tilde{u} = (1+k)u/2$  and  $\tilde{k} = (1-k)/(1+k)$ , the Landen descending transformations are given by

$$\operatorname{sn}(u, k) = \frac{(1+\tilde{k}) \operatorname{sn}(\tilde{u}, \tilde{k})}{1+\tilde{k} \operatorname{sn}^2(\tilde{u}, \tilde{k})}, \quad (\text{B.37})$$

$$\operatorname{cn}(u, k) = \frac{\operatorname{cn}(\tilde{u}, \tilde{k}) \operatorname{dn}(\tilde{u}, \tilde{k})}{1+\tilde{k} \operatorname{sn}^2(\tilde{u}, \tilde{k})}, \quad (\text{B.38})$$

$$\operatorname{dn}(u, k) = \frac{\operatorname{dn}^2(\tilde{u}, \tilde{k}) - (1-\tilde{k})}{(1+\tilde{k}) - \operatorname{dn}^2(\tilde{u}, \tilde{k})}. \quad (\text{B.39})$$

An alternative way of expressing the Landen ascending transformations is obtained by combining Eqs. (B.22)-(B.24) and (B.34)-(B.36), which results in

$$\operatorname{sn} \left[ (1+k)u, \frac{2\sqrt{k}}{1+k} \right] = \frac{(1+k) \operatorname{sn}(u, k)}{1+k \operatorname{sn}^2(u, k)}, \quad (\text{B.40})$$

$$\operatorname{cn} \left[ (1+k)u, \frac{2\sqrt{k}}{1+k} \right] = \frac{\operatorname{cn}(u, k) \operatorname{dn}(u, k)}{1+k \operatorname{sn}^2(u, k)}, \quad (\text{B.41})$$

$$\operatorname{dn} \left[ (1+k)u, \frac{2\sqrt{k}}{1+k} \right] = \frac{1-k \operatorname{sn}^2(u, k)}{1+k \operatorname{sn}^2(u, k)}. \quad (\text{B.42})$$

The argument of the elliptic functions can be any arbitrary complex number. In the case of a pure imaginary number, we have

$$\operatorname{sn}(i u, k) = i \operatorname{sc}(u, k'), \quad (\text{B.43})$$

$$\operatorname{cn}(i u, k) = \operatorname{nc}(u, k'), \quad (\text{B.44})$$

$$\operatorname{dn}(i u, k) = \operatorname{dc}(u, k'), \quad (\text{B.45})$$

where  $u \in \mathbb{R}$  and  $k' = \sqrt{1 - k^2}$ . Bringing together the results in Eqs. (B.19)-(B.21) and Eqs. (B.43)-(B.45), we have that, in the general case,

$$\operatorname{sn}(u + i v, k) = \frac{\operatorname{sn}(u, k) \operatorname{dn}(v, k') + i \operatorname{cn}(u, k) \operatorname{dn}(u, k) \operatorname{sn}(v, k') \operatorname{cn}(v, k')}{\operatorname{cn}^2(v, k') + k^2 \operatorname{sn}^2(u, k) \operatorname{sn}^2(v, k')}, \quad (\text{B.46})$$

$$\operatorname{cn}(u + i v, k) = \frac{\operatorname{cn}(u, k) \operatorname{cn}(v, k') - i \operatorname{sn}(u, k) \operatorname{dn}(u, k) \operatorname{sn}(v, k') \operatorname{dn}(v, k')}{\operatorname{cn}^2(v, k') + k^2 \operatorname{sn}^2(u, k) \operatorname{sn}^2(v, k')}, \quad (\text{B.47})$$

$$\operatorname{dn}(u + i v, k) = \frac{\operatorname{dn}(u, k) \operatorname{cn}(v, k') \operatorname{dn}(v, k') - i k^2 \operatorname{sn}(u, k) \operatorname{cn}(u, k) \operatorname{sn}(v, k')}{\operatorname{cn}^2(v, k') + k^2 \operatorname{sn}^2(u, k) \operatorname{sn}^2(v, k')}. \quad (\text{B.48})$$



# Bibliography

- ABRAMOWICZ, M. A., CZERNY, B., LASOTA, J. P. & SZUSZKIEWICZ, E., 1988. Slim accretion disks. *Astrophysical Journal*, **332**, 646–658.
- ABRAMOWITZ, M. & STEGUN, I., 1970. *Handbook of Mathematical Functions*. New York: Dover, 1970.
- AGUIAR, C. E., KODAMA, T., OSADA, T. & HAMA, Y., 2001. Smoothed particle hydrodynamics for relativistic heavy-ion collisions. *Journal of Physics G Nuclear Physics*, **27**, 75–94.
- ALCUBIERRE, M., 2008. *Introduction to 3+1 Numerical Relativity*. Oxford University Press.
- ARNOWITT, R., DESER, S. & MISNER, C. W., 1959. Dynamical Structure and Definition of Energy in General Relativity. *Physical Review*, **116**, 1322–1330.
- BAADE, W. & ZWICKY, F., 1934. Remarks on Super-Novae and Cosmic Rays. *Physical Review*, **46**, 76–77.
- BALBUS, S. A. & HAWLEY, J. F., 1991. A powerful local shear instability in weakly magnetized disks. I - Linear analysis. II - Nonlinear evolution. *Astrophysical Journal*, **376**, 214–233.
- BARDEEN, J. M., 1970. Kerr Metric Black Holes. *Nature*, **226**, 64–65.
- BARDEEN, J. M., 1973. Timelike and null geodesics in the Kerr metric. In *Black Holes (Les Astres Occlus)*, 215–239.
- BARDEEN, J. M. & PETERSON, J. A., 1975. The Lense-Thirring Effect and Accretion Disks around Kerr Black Holes. *Astrophysical Journal Letters*, **195**, L65.
- BARDEEN, J. M., PRESS, W. H. & TEUKOLSKY, S. A., 1972. Rotating Black Holes: Locally Nonrotating Frames, Energy Extraction, and Scalar Synchrotron Radiation. *Astrophysical Journal*, **178**, 347–370.
- BARNES, J. & HUT, P., 1986. A hierarchical  $O(N \log N)$  force-calculation algorithm. *Nature*, **324**, 446–449.

- BELOBORODOV, A. M. & ILLARIONOV, A. F., 2001. Small-scale inviscid accretion discs around black holes. *Monthly Notices of the Royal Astronomical Society*, **323**, 167–176.
- BIČÁK, J. & STUHLÍK, Z., 1976a. On the latitudinal and radial motion in the field of a rotating black hole. *Bulletin of the Astronomical Institutes of Czechoslovakia*, **27**, 129–133.
- BIČÁK, J. & STUHLÍK, Z., 1976b. The fall of the shell of dust on to a rotating black hole. *Monthly Notices of the Royal Astronomical Society*, **175**, 381–393.
- BLANDFORD, R. D., 1987. Astrophysical black holes. In Hawking, S. W. and Israel, W., ed., *Three Hundred Years of Gravitation*, 277–329.
- BLANDFORD, R. D. & PAYNE, D. G., 1982. Hydromagnetic flows from accretion discs and the production of radio jets. *Monthly Notices of the Royal Astronomical Society*, **199**, 883–903.
- BLANDFORD, R. D. & ZNAJEK, R. L., 1977. Electromagnetic extraction of energy from Kerr black holes. *Monthly Notices of the Royal Astronomical Society*, **179**, 433–456.
- BONDI, H., 1952. On spherically symmetrical accretion. *Monthly Notices of the Royal Astronomical Society*, **112**, 195+.
- BONDI, H. & HOYLE, F., 1944. On the mechanism of accretion by stars. *Monthly Notices of the Royal Astronomical Society*.
- BOYER, R. H. & LINDQUIST, R. W., 1967. Maximal Analytic Extension of the Kerr Metric. *Journal of Mathematical Physics*, **8**(2), 265–281.
- BURROWS, D. N., KENNEA, J. A., GHISELLINI, G., MANGANO, V., ZHANG, B. ET AL., 2011. Relativistic jet activity from the tidal disruption of a star by a massive black hole. *Nature*, **476**, 421–424.
- BYRD, P. & FRIEDMAN, M., 1954. *Handbook of elliptic integrals for engineers and physicists*. Springer.
- CABEZÓN, R. M., GARCÍA-SENZ, D. & RELAÑO, A., 2008. A one-parameter family of interpolating kernels for smoothed particle hydrodynamics studies. *Journal of Computational Physics*, **227**, 8523–8540.
- CARR, B. J. & HAWKING, S. W., 1974. Black holes in the early Universe. *Monthly Notices of the Royal Astronomical Society*, **168**, 399–416.
- CARTER, B., 1968. Global Structure of the Kerr Family of Gravitational Fields. *Physical Review*, **174**(5), 1559–1571.
- CARTER, B., 1971. Axisymmetric Black Hole Has Only Two Degrees of Freedom. *Physical Review Letters*, **26**, 331–333.

- CAYLEY, A., 1961. *An elementary treatise on elliptic functions*. New York : Dover, 1961.
- CELOTTI, A., MILLER, J. C. & SCIAMA, D. W., 1999. Astrophysical evidence for the existence of black holes. *Classical and Quantum Gravity*, **16**, A3–A21.
- CHANDRASEKHAR, S., 1931. The Maximum Mass of Ideal White Dwarfs. *Astrophysical Journal*, **74**, 81.
- CHANDRASEKHAR, S., 1983. *The Mathematical Theory of Black Holes*. Oxford University.
- CHOW, E. & MONAGHAN, J. J., 1997. Ultrarelativistic SPH. *Journal of Computational Physics*, **134**, 296–305.
- DAN, M., ROSSWOG, S., GUILLOCHON, J. & RAMÍREZ-RUIZ, E., 2012. How the merger of two white dwarfs depends on their mass ratio: orbital stability and detonations at contact. *Monthly Notices of the Royal Astronomical Society*, **422**, 2417–2428.
- DE FELICE, F. & CALVANI, M., 1972. Orbital and vortical motion in the Kerr metric. *Nuovo Cimento B Serie*, **10**, 447–458.
- DE FELICE, F. & PRETI, G., 1999. On the meaning of the separation constant in the Kerr metric. *Classical and Quantum Gravity*, **16**, 2929–2935.
- DRASCO, S. & HUGHES, S. A., 2004. Rotating black hole orbit functionals in the frequency domain. *Physical Review D*, **69**(4), 044015.
- DUBINSKI, J., KIM, J., PARK, C. & HUMBLE, R., 2004. GOTPM: a parallel hybrid particle-mesh treecode. *New Astronomy*, **9**, 111–126.
- DYMNKOVA, I. G., 1986. Motion of particles and photons in the gravitational field of a rotating body (In memory of Vladimir Afanas'evich Ruban). *Soviet Physics Uspekhi*, **29**, 215–237.
- EINSTEIN, A., 1915. Die Feldgleichungen der Gravitation. *Sitzungsberichte der Königlich Preußischen Akademie der Wissenschaften (Berlin)*, 844–847.
- FINKELSTEIN, D., 1958. Past-Future Asymmetry of the Gravitational Field of a Point Particle. *Physical Review*, **110**, 965–967.
- FOCK, V. A., 1964. *The theory of space, time and gravitation*. Pergamon Press, Oxford.
- FONT, J. A., 2008. Numerical Hydrodynamics and Magnetohydrodynamics in General Relativity. *Living Reviews in Relativity*, **11**(7). URL <http://www.livingreviews.org/lrr-2008-7>.
- FONT, J. A., IBÁÑEZ, J. M. & PAPADOPOULOS, P., 1999. Non-axisymmetric relativistic Bondi-Hoyle accretion on to a Kerr black hole. *Monthly Notices of the Royal Astronomical Society*, **305**, 920–936.

- FRANK, J., KING, A. & RAINE, D. J., 2002. *Accretion Power in Astrophysics: Third Edition*. Cambridge University Press.
- FROLOV, V. P. & NOVIKOV, I. D., 1998. *Black Hole Physics. Basic Concepts and New Developments*. Kluwer Academic.
- FUJITA, R. & HIKIDA, W., 2009. Analytical solutions of bound timelike geodesic orbits in Kerr spacetime. *Classical and Quantum Gravity*, **26**(13), 135002–+.
- GAFTON, E. & ROSSWOG, S., 2011. A fast recursive coordinate bisection tree for neighbour search and gravity. *Monthly Notices of the Royal Astronomical Society*, **418**, 770–781.
- GALAMA, T. J., VREESWIJK, P. M., VAN PARADIJS, J., KOUVELIOTOU, C., AUGUSTEIJN, T. ET AL., 1998. An unusual supernova in the error box of the  $\gamma$ -ray burst of 25 April 1998. *Nature*, **395**, 670–672.
- GEBHARDT, K., RICH, R. M. & HO, L. C., 2005. An Intermediate-Mass Black Hole in the Globular Cluster G1: Improved Significance from New Keck and Hubble Space Telescope Observations. *Astrophysical Journal*, **634**, 1093–1102.
- GHEZ, A. M., SALIM, S., WEINBERG, N. N., LU, J. R., DO, T., DUNN, J. K., MATTHEWS, K., MORRIS, M. R., YELDA, S., BECKLIN, E. E., KREMENEK, T., MILOSAVLJEVIC, M. & NAIMAN, J., 2008. Measuring Distance and Properties of the Milky Way's Central Supermassive Black Hole with Stellar Orbits. *Astrophysical Journal*, **689**, 1044–1062.
- GILLESSEN, S., EISENHAUER, F., TRIPPE, S., ALEXANDER, T., GENZEL, R., MARTINS, F. & OTT, T., 2009. Monitoring Stellar Orbits Around the Massive Black Hole in the Galactic Center. *Astrophysical Journal*, **692**, 1075–1109.
- GINGOLD, R. A. & MONAGHAN, J. J., 1977. Smoothed particle hydrodynamics - Theory and application to non-spherical stars. *Monthly Notices of the Royal Astronomical Society*, **181**, 375–389.
- GINGOLD, R. A. & MONAGHAN, J. J., 1982. Kernel estimates as a basis for general particle methods in hydrodynamics. *Journal of Computational Physics*, **46**, 429–453.
- GOLD, T., 1968. Rotating Neutron Stars as the Origin of the Pulsating Radio Sources. *Nature*, **218**, 731–732.
- GROSSMAN, R., LEVIN, J. & PEREZ-GIZ, G., 2012. Harmonic structure of generic Kerr orbits. *Physical Review D*, **85**(2), 023012.
- HANCOCK, H., 1917. *Elliptic Integrals*. New York : Dover, 1917.
- HERNQUIST, L. & KATZ, N., 1989. TREESPH - A unification of SPH with the hierarchical tree method. **70**, 419–446.

- HEWISH, A., BELL, S. J., PILKINGTON, J. D. H., SCOTT, P. F. & COLLINS, R. A., 1968. Observation of a Rapidly Pulsating Radio Source. *Nature*, **217**, 709–713.
- HOYLE, F. & LYTTLETON, A., 1939. The effect of interstellar matter on climatic variation. *PCPS*.
- HUGHES, S. A., 2009. Gravitational Waves from Merging Compact Binaries. *Annual Review of Astronomy and Astrophysics*, **47**, 107–157.
- HUGHSTON, L. P., PENROSE, R., SOMMERS, P. & WALKER, M., 1972. On a quadratic first integral for the charged particle orbits in the charged Kerr solution. *Communications in Mathematical Physics*, **27**, 303–308.
- ISRAEL, W., 1967. Event Horizons in Static Vacuum Space-Times. *Physical Review*, **164**, 1776–1779.
- JAROSZYŃSKI, M., ABRAMOWICZ, M. A. & PACZYŃSKI, B., 1980. Supercritical accretion disks around black holes. *Acta Astronomica*, **30**, 1–34.
- KERR, R. P., 1963. Gravitational Field of a Spinning Mass as an Example of Algebraically Special Metrics. *Physical Review Letters*, vol. 11, Issue 5, pp. 237–238, **11**, 237–238.
- KHEYFETS, A., MILLER, W. A. & ZUREK, W. H., 1990. Covariant smoothed particle hydrodynamics on a curved background. *Physical Review D*, **41**, 451–454.
- KING, A., 1995. Accretion in close binaries. In W. H. G. Lewin, J. van Paradijs, & E. P. J. van den Heuvel, ed., *X-ray Binaries*, 419–456.
- KING, A., 2003. Black Holes, Galaxy Formation, and the  $M_{BH}$ - $\sigma$  Relation. *Astrophysical Journal Letters*, **596**, L27–L29.
- KLEBESADEL, R. W., STRONG, I. B. & OLSON, R. A., 1973. Observations of Gamma-Ray Bursts of Cosmic Origin. *Astrophysical Journal Letters*, **182**, L85.
- KOBAYASHI, S., LAGUNA, P., PHINNEY, E. S. & MÉSZÁROS, P., 2004. Gravitational Waves and X-Ray Signals from Stellar Disruption by a Massive Black Hole. *Astrophysical Journal*, **615**, 855–865.
- KRANIOTIS, G. V., 2004. Precise relativistic orbits in Kerr and Kerr (anti) de Sitter spacetimes. *Classical and Quantum Gravity*, **21**, 4743–4769.
- KRIVENKO, O. P., PIRAGAS, K. A. & ZHUK, I. T., 1976. On the second integrals of geodesics in the Kerr field. *Astrophysics and Space Science*, **40**, 39–61.
- LAGUNA, P., MILLER, W. A. & ZUREK, W. H., 1993. Smoothed particle hydrodynamics near a black hole. *Astrophysical Journal*, **404**, 678–685.

- LANDAU, L. & LIFSHITZ, E., 1975. *The Classical Theory of Fields*, vol. 2 of *Course of Theoretical Physics*. Pergamon, 4th ed.
- LAPLACE, P. S., 1796. *Exposition du Système du Monde*. Paris.
- LAWDEN, D. F., 1989. *Elliptic Functions and Applications*. Springer.
- LEE, W. H. & RAMÍREZ-RUIZ, E., 2006. Accretion Modes in Collapsars: Prospects for Gamma-Ray Burst Production. *Astrophysical Journal*, **641**, 961–971.
- LEMAÎTRE, G., 1933. L’Univers en expansion. *Annales de la Societe Scientifique de Bruxelles*, **53**, 51.
- LENSE, J. & THIRRING, H., 1918. Über den Einfluß der Eigenrotation der Zentralkörper auf die Bewegung der Planeten und Monde nach der Einsteinschen Gravitationstheorie. *Physikalische Zeitschrift*, **19**, 156.
- LEVIN, J. & PEREZ-GIZ, G., 2008. A periodic table for black hole orbits. *Physical Review D*, **77**(10), 103005.
- LODATO, G. & PRICE, D. J., 2010. On the diffusive propagation of warps in thin accretion discs. *Monthly Notices of the Royal Astronomical Society*, **405**, 1212–1226.
- LODATO, G. & PRINGLE, J. E., 2006. The evolution of misaligned accretion discs and spinning black holes. *Monthly Notices of the Royal Astronomical Society*, **368**, 1196–1208.
- LÖFFLER, F., FABER, J., BENTIVEGNA, E., BODE, T., DIENER, P., HAAS, R., HINDER, I., MUNDIM, B. C., OTT, C. D., SCHNETTER, E., ALLEN, G., CAMPANELLI, M. & LAGUNA, P., 2012. The Einstein Toolkit: a community computational infrastructure for relativistic astrophysics. *Classical and Quantum Gravity*, **29**(11), 115001.
- LÓPEZ-CÁMARA, D., LEE, W. H. & RAMÍREZ-RUIZ, E., 2009. Gamma-Ray Burst Production and Supernova Signatures in Slowly Rotating Collapsars. *Astrophysical Journal*, **692**, 804–815.
- LOUBÈRE, R., MAIRE, P.-H., SHASHKOV, M., BREIL, J. & GALERA, S., 2010. ReALE: A reconnection-based arbitrary-Lagrangian-Eulerian method. *Journal of Computational Physics*, **229**, 4724–4761.
- LUCY, L. B., 1977. A numerical approach to the testing of the fission hypothesis. *Astronomical Journal*, **82**, 1013–1024.
- MANN, P. J., 1993. A finite element method in space and time for relativistic spherical collapse. *Computer Physics Communications*, **75**, 10–30.
- MARGOLIN, L., 1997. Introduction to “An Arbitrary Lagrangian Eulerian Computing Method for All Flow Speeds”. *Journal of Computational Physics*, **135**, 198–202.

- MCCCLINTOCK, J. E. & REMILLARD, R. A., 2006. *Black hole binaries*, 157–213. Cambridge University Press.
- MENDOZA, S., TEJEDA, E. & NAGEL, E., 2009. Analytic solutions to the accretion of a rotating finite cloud towards a central object - I. Newtonian approach. *Monthly Notices of the Royal Astronomical Society*, **393**, 579–586.
- MICHEL, F. C., 1972. Accretion of Matter by Condensed Objects. *Astrophysics and Space Science*, **15**, 153–160.
- MICHELL, J., 1784. On the Means of Discovering the Distance, Magnitude, &c. of the Fixed Stars, in Consequence of the Diminution of the Velocity of Their Light, in Case Such a Diminution Should be Found to Take Place in any of Them, and Such Other Data Should be Procured from Observations, as Would be Farther Necessary for That Purpose. by the Rev. John Michell, B. D. F. R. S. I a Letter to Henry Cavendish, Esq. F. R. S. and a. S. *Philosophical Transactions of the Royal Society*, **74**, 35–57.
- MILLER, J. M., 2007. Relativistic X-Ray Lines from the Inner Accretion Disks Around Black Holes. *Annual Review of Astronomy and Astrophysics*, **45**, 441–479.
- MINO, Y., 2003. Perturbative approach to an orbital evolution around a supermassive black hole. *Physical Review D*, **67**(8), 084027.
- MISNER, C. W., THORNE, K. S. & WHEELER, J. A., 1973. *Gravitation*. San Francisco: W.H. Freeman and Co., 1973.
- MONAGHAN, J. J., 1992. Smoothed particle hydrodynamics. *Annual Review of Astronomy and Astrophysics*, **30**, 543–574.
- MONAGHAN, J. J., 2005. Smoothed particle hydrodynamics. *Reports on Progress in Physics*, **68**, 1703–1759.
- MONAGHAN, J. J. & PRICE, D. J., 2001. Variational principles for relativistic smoothed particle hydrodynamics. *Monthly Notices of the Royal Astronomical Society*, **328**, 381–392.
- MUKHOPADHYAY, B. & MISRA, R., 2003. Pseudo-Newtonian Potentials to Describe the Temporal Effects on Relativistic Accretion Disks around Rotating Black Holes and Neutron Stars. *Astrophysical Journal*, **582**, 347–351.
- NAKAR, E., 2007. Short-hard gamma-ray bursts. *Physics Reports*, **442**, 166–236.
- NARAYAN, R., 2005. Black holes in astrophysics. *New Journal of Physics*, **7**, 199.
- NELSON, R. P. & PAPALOIZOU, J. C. B., 1994. Variable Smoothing Lengths and Energy Conservation in Smoothed Particle Hydrodynamics. *Monthly Notices of the Royal Astronomical Society*, **270**, 1.

- NEWMAN, E. T., COUCH, E., CHINNAPARED, K., EXTON, A., PRAKASH, A. & TORRENCE, R., 1965. Metric of a Rotating, Charged Mass. *Journal of Mathematical Physics*, **6**, 918–919.
- NOVIKOV, I. D. & THORNE, K. S., 1973. Astrophysics of black holes. In C. Dewitt & B. S. Dewitt, ed., *Black Holes (Les Astres Occlus)*, 343–450. Gordon and Breach, New York.
- NOYOLA, E., GEBHARDT, K. & BERGMANN, M., 2008. Gemini and Hubble Space Telescope Evidence for an Intermediate-Mass Black Hole in  $\omega$  Centauri. *Astrophysical Journal*, **676**, 1008–1015.
- OECHSLIN, R., ROSSWOG, S. & THIELEMANN, F.-K., 2002. Conformally flat smoothed particle hydrodynamics application to neutron star mergers. *Physical Review D*, **65**(10), 103005.
- OPPENHEIMER, J. R. & SNYDER, H., 1939. On Continued Gravitational Contraction. *Physical Review*, **56**, 455–459.
- OPPENHEIMER, J. R. & VOLKOFF, G. M., 1939. On Massive Neutron Cores. *Physical Review*, **55**, 374–381.
- PACZYŃSKY, B. & WITA, P. J., 1980. Thick accretion disks and supercritical luminosities. *Astronomy and Astrophysics*, **88**, 23–31.
- PENROSE, R., 1965. Gravitational Collapse and Space-Time Singularities. *Physical Review Letters*, **14**, 57–59.
- PENROSE, R., 1969. Gravitational Collapse: the Role of General Relativity. *Rivista del Nuovo Cimento*, **1**, 252.
- PEREGO, A., DOTTI, M., COLPI, M. & VOLONTERI, M., 2009. Mass and spin co-evolution during the alignment of a black hole in a warped accretion disc. *Monthly Notices of the Royal Astronomical Society*, **399**, 2249–2263.
- PIRAN, T., 2004. The physics of gamma-ray bursts. *Reviews of Modern Physics*, **76**, 1143–1210.
- POPHAM, R., WOOSLEY, S. E. & FRYER, C., 1999. Hyperaccreting Black Holes and Gamma-Ray Bursts. *Astrophysical Journal*, **518**, 356–374.
- PRENDERGAST, K. H. & BURBIDGE, G. R., 1968. On the Nature of Some Galactic X-Ray Sources. *Astrophysical Journal*, **151**, L83+.
- PRICE, D. J., 2004. *Magnetic fields in Astrophysics*. Ph.D. thesis, Institute of Astronomy, Cambridge, UK.
- PRICE, D. J., 2012. Smoothed particle hydrodynamics and magnetohydrodynamics. *Journal of Computational Physics*, **231**, 759–794.

- PRICE, D. J. & BATE, M. R., 2009. Inefficient star formation: the combined effects of magnetic fields and radiative feedback. *Monthly Notices of the Royal Astronomical Society*, **398**, 33–46.
- PRICE, D. J. & MONAGHAN, J. J., 2007. An energy-conserving formalism for adaptive gravitational force softening in smoothed particle hydrodynamics and N-body codes. *Monthly Notices of the Royal Astronomical Society*, **374**, 1347–1358.
- PRICE, D. J. & ROSSWOG, S., 2006. Producing Ultrastrong Magnetic Fields in Neutron Star Mergers. *Science*, **312**, 719–722.
- PRINGLE, J. E., 1981. Accretion discs in astrophysics. *Annual Review of Astronomy and Astrophysics*, **19**, 137–162.
- REES, M. J., 1984. Black Hole Models for Active Galactic Nuclei. *Annual Review of Astronomy and Astrophysics*, **22**, 471–506.
- REES, M. J., 1988. Tidal disruption of stars by black holes of 10 to the 6th–10 to the 8th solar masses in nearby galaxies. *Nature*, **333**, 523–528.
- RHOADES, C. E. & RUFFINI, R., 1974. Maximum Mass of a Neutron Star. *Physical Review Letters*, **32**, 324–327.
- ROBINSON, D. C., 1975. Uniqueness of the Kerr black hole. *Physical Review Letters*, **34**, 905.
- ROSSWOG, S., 2009. Astrophysical smooth particle hydrodynamics. *New Astronomy Reviews*, **53**, 78–104.
- ROSSWOG, S., 2010a. Conservative, special-relativistic smoothed particle hydrodynamics. *Journal of Computational Physics*, **229**, 8591–8612.
- ROSSWOG, S., 2010b. Relativistic smooth particle hydrodynamics on a given background spacetime. *Classical and Quantum Gravity*, **27**(11), 114108.
- ROSSWOG, S., RAMÍREZ-RUIZ, E. & HIX, W. R., 2009. Tidal Disruption and Ignition of White Dwarfs by Moderately Massive Black Holes. *Astrophysical Journal*, **695**, 404–419.
- ROSSWOG, S., TEJEDA, E., GAFTON, E. & MILLER, J. C., 2012. The SPHINCS code: Smoothed Particle Hydrodynamics IN Curved Spacetime. (In preparation).
- SCHMIDT, M., 1963. 3C 273 : A Star-Like Object with Large Red-Shift. **197**, 1040.
- SCHMIDT, W., 2002. Celestial mechanics in Kerr spacetime. *Classical and Quantum Gravity*, **19**, 2743–2764.
- SCHWARZSCHILD, K., 1916. On the Gravitational Field of a Mass Point According to Einstein's Theory. *Abh. Konigl. Preuss. Akad. Wissenschaften Jahre 1906,92, Berlin,1907*, 189–196.

- SHAKURA, N. I. & SUNYAEV, R. A., 1973. Black holes in binary systems. Observational appearance. *Astronomy and Astrophysics*, **24**, 337–355.
- SHAPIRO, S. & TEUKOLSKY, S., 1983. *Black Holes, White Dwarfs and Neutron Stars*. John Wiley & Sons.
- SHAPIRO, S. L., 1974. Accretion onto Black Holes: the Emergent Radiation Spectrum. III. Rotating (kerr) Black Holes. *Astrophysical Journal*, **189**, 343–352.
- SHARP, N. A., 1979. Geodesics in black hole space-times. *General Relativity and Gravitation*, **10**, 659–670.
- SHKLOVSKY, I. S., 1967. On the Nature of the Source of X-Ray Emission of SCO XR-1. *Astrophysical Journal Letters*, **148**, L1.
- SIEGLER, S. & RIFFERT, H., 2000. Smoothed Particle Hydrodynamics Simulations of Ultrarelativistic Shocks with Artificial Viscosity. *Astrophysical Journal*, **531**, 1053–1066.
- SPRINGEL, V., 2005. The cosmological simulation code GADGET-2. *Monthly Notices of the Royal Astronomical Society*, **364**, 1105–1134.
- SPRINGEL, V., 2010. Smoothed Particle Hydrodynamics in Astrophysics. *Annual Review of Astronomy and Astrophysics*, **48**, 391–430.
- SPRINGEL, V., DI MATTEO, T. & HERNQUIST, L., 2005a. Modelling feedback from stars and black holes in galaxy mergers. *Monthly Notices of the Royal Astronomical Society*, **361**, 776–794.
- SPRINGEL, V., WHITE, S. D. M., JENKINS, A., FRENK, C. S., YOSHIDA, N., GAO, L., NAVARRO, J., THACKER, R., CROTON, D., HELLY, J., PEACOCK, J. A., COLE, S., THOMAS, P., COUCHMAN, H., EVRARD, A., COLBERG, J. & PEARCE, F., 2005b. Simulations of the formation, evolution and clustering of galaxies and quasars. *Nature*, **435**, 629–636.
- STEWART, J. & WALKER, M., 1973. Black holes: the outside story. *Springer Tracts in Modern Physics*, **69**, 69–115.
- TAYLOR, P. A., 2008. *Understanding long-duration gamma-ray bursts : modelling collapsars with SPH*. Ph.D. thesis, University of Oxford. Mathematical, Physical and Life Sciences Division.
- TAYLOR, P. A., MILLER, J. C. & PODSIADLOWSKI, P., 2011. Long-duration gamma-ray bursts: hydrodynamic instabilities in collapsar discs. *Monthly Notices of the Royal Astronomical Society*, **410**, 2385–2413.
- TEJEDA, E., MENDOZA, S. & MILLER, J. C., 2012a. Analytic solutions to the accretion of a rotating finite cloud towards a central object - II. Schwarzschild space-time. *Monthly Notices of the Royal Astronomical Society*, **419**, 1431–1441.

- TEJEDA, E., TAYLOR, P. A. & MILLER, J. C., 2012b. An analytic toy model for relativistic accretion in Kerr spacetime. *ArXiv e-prints*.
- WALKER, M. & PENROSE, R., 1970. On quadratic first integrals of the geodesic equations for type {22} spacetimes. *Communications in Mathematical Physics*, **18**, 265–274.
- WILKINS, D. C., 1972. Bound Geodesics in the Kerr Metric. *Physical Review D*, **5**, 814–822.
- WILTSHIRE, D. L., VISSER, M. & SCOTT, S., 2009. *The Kerr spacetime: Rotating black holes in general relativity*. Cambridge, UK: Cambridge University Press.
- WOOSLEY, S. E., 1993. Gamma-Ray Bursts from Stellar Collapse to a Black Hole? In *American Astronomical Society Meeting Abstracts #182*, vol. 25 of *Bulletin of the American Astronomical Society*, 894.
- ZALAMEA, I. & BELOBORODOV, A. M., 2009. Mini-discs around spinning black holes. *Monthly Notices of the Royal Astronomical Society*, **398**, 2005–2011.